BROADBAND WAVEFORM MODELING OF DEEP MANTLE STRUCTURE

by

Michael S. Thorne

A Dissertation Presented in Partial Fulfillment
of the Requirements for the Degree
Doctor of Philosophy

ARIZONA STATE UNIVERSITY

December 2005

BROADBAND WAVEFORM MODELING OF

DEEP MANTLE STRUCTURE

by

Michael S. Thorne

has been approved

October 2005

APPROVED:

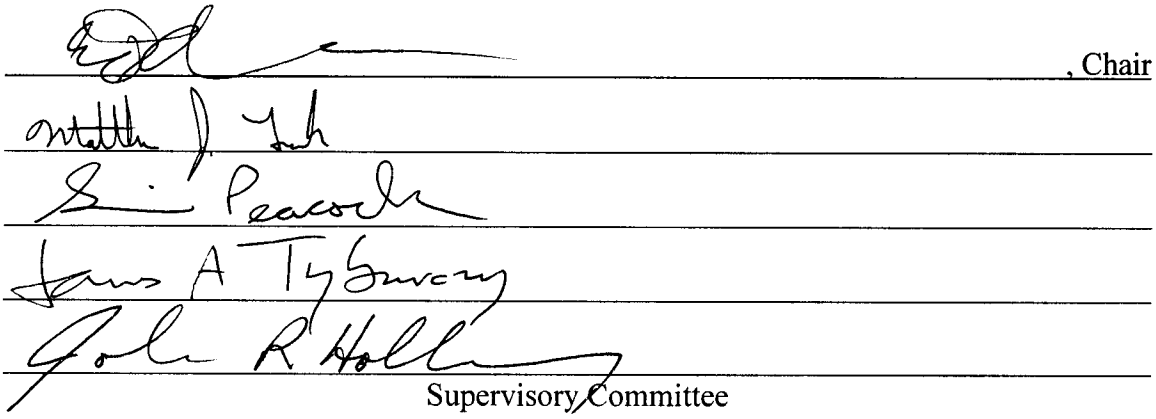

, Chair

Supervisory Committee

ACCEPTED:

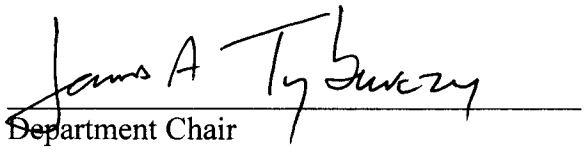

Department Chair

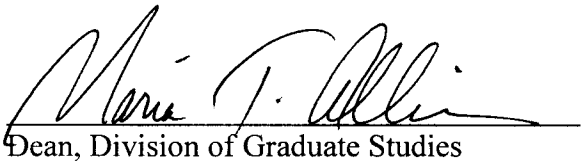

Dean, Division of Graduate Studies

ABSTRACT

The lowermost 200 - 300 km of the mantle, known as the D" region, exhibits some of the strongest seismic heterogeneity in the Earth and plays a crucial role in thermal, chemical and dynamic processes in the mantle. Hot spot volcanism may originate from the deep mantle in regions exhibiting the Earth's most pronounced lateral shear (*S*)-wave velocity gradients. These strong gradient regions display an improved geographic correlation over *S*-wave velocities to surface hot spot locations. The origin of hot spot volcanism may also be linked to ultra-low velocity zone (ULVZ) structure at the core-mantle boundary (CMB). Anomalous boundary layer structure at the CMB is investigated using a global set of broadband *SKS* and *SPdKS* waves from permanent and portable seismometer arrays. The wave shape and timing of *SPdKS* data are analyzed relative to *SKS*, with some *SPdKS* data showing significant delays and broadening. We produce maps of inferred boundary layer structure from the global data and find evidence for extremely fine-scale heterogeneity where our wave path sampling is the densest. These data are consistent with the hypothesis that ULVZ presence (or absence) correlates with reduced (or average) heterogeneity in the overlying mantle. In order to further constrain deep mantle processes, synthetic seismograms for 3-D mantle models are necessary for comparison with data. We develop a 3-D axi-symmetric finite difference (FD) algorithm to model *SH*-wave propagation (SHaxi). In order to demonstrate the utility of the SHaxi algorithm we apply the technique to whole mantle models with random heterogeneity applied to the background model producing whole mantle scattering. We also apply SHaxi to model *SH*-wave propagation through cross-sections

of 3-D lower mantle D" discontinuity models beneath the Cocos Plate derived from recent data analyses. We utilize double-array stacking to assess model predictions of data. 3-D model predictions show waveform variability not observed in 1-D model predictions, demonstrating the importance for the 3-D calculations. An undulating D" reflector produces a double *Scd* arrival that may be useful in future studies for distinguishing between D" volumetric heterogeneity and D" discontinuity topography.

Dedicated to

Peggy Louise Thorne

ACKNOWLEDGMENTS

My greatest appreciation goes to my advisor Ed Garnero. Many thanks for drawing me away from the engineering field and opening my way into seismology. Ed Garnero has proven the best of advisors for many reasons. The exhilaration and interest he displays when shown something new in the seismic wavefield is infectious and inspiring. His creativity in giving suggestions on how to solve problems has always been greatly appreciated. As highly regarded is his hands-off approach in allowing one to arrive at one's own conclusions and in problem solving. Thank you for the constant support, advice, and sometimes silence.

Thanks to my supervisory committee Matt Fouch, Jim Tyburczy, John Holloway and Simon Peacock for many valuable discussions. Special thanks to Matt Fouch for always having an open door and for giving such good advice throughout the years. Additional thanks to Allen McNamara who should have also been on my committee.

Special thanks to Ed's other students and post docs with whom I have shared lab space and a variety of experiences over the years. Thanks to Melissa Moore for continually keeping me entertained with her moaning, whimpering, grunting and general utterances as to how her work progressed. Thanks to Nicholas Schmerr for an enlightening number of years of discussion on the transition zone, tornados, and just about everything else one could imagine. Most notably, thank you for providing ample buffer from the boundless string of flippant GCC neophyte questions. An innumerable amount of thanks must also go to Sean Ford, who has single handedly brought SACLAB into the seismological mainstream, entertained us all with tales of complex signal

analysis dalliances, and kept a positive light over even the darkest of GCC days. A day without Sean is like a day without sunshine. Many more thanks need to go to Sebastian Rost than can be listed here, but thank you in general for all of the discussion and advice given over the years.

I would like to give thanks to those with whom I have become close friends with in my three visits to Bavaria. Special thanks to Markus, Rosemary, Hanna and Martin Treml for all the times you have housed and fed me when I came to Munich. Special thanks to Markus for all of the amazing trips you have taken me on, from hiking in the Alps, to visiting ancient monasteries to spending a day at the Wiesn. Thanks to Gunnar Jahnke for sharing your first version of the SHaxi code with me on the first day we met, and for being such a great collaborator ever since. Thanks to Heiner Igel for support and the willingness to bring me to Munich three times. Thanks to Franz Antwetter for letting me stay one summer in your flat. Thanks to Gilbert Brietzke, Toni Kraft, and Tobi Metz for also making my stays in Munich much more enjoyable and for oftentimes staying out with me until the first U-Bahn train started running in the morning. Thanks to Hubert for making *elefontastic* programming accessible even to me. Thanks to Guoquan Wang for sharing an office with me during the sweltering summer of 2003, for allowing me to open the window from time to time and most notably for sharing the esoteric teachings of The Book of Chinese Seismology with me. Many thanks to the rest of Heiner's students that I have not mentioned above for making my stays in Munich more enjoyable.

Thanks to Artie Rodgers for an enjoyable summer at LLNL. Also thanks to Steve Meyers, Dave Harris and Hrvoje Tkalčić for their technical expertise. Thanks to Clipper

Ford for giving me a place to stay in Livermore and to Bazo for giving me a computer to use while I was there.

I have also received gracious support from many other graduate students over the last few years. Most notably, thanks to John Hernlund, Tarje Nissen-Meyer, and Megan Avants. Thanks to Adam Baig for an especially wild time in the Canadian Northwest. Thanks to the graduate students of Matt Fouch and Allen McNamara with whom I have shared our computer lab and many enjoyable experiences over the last several years, Jesse L. Yoburn, Teresa Lassak, Karen Anglin, and Abby Bull.

I would like to give special thanks to the systems administrators who have served our lab. Somehow they managed, apparently while under great personal duress, to maintain our network and still occasionally manage to install a piece of software for me here or there. Thanks to Bruce Tachoir, Marvin Simkin and Mark Stevens. Also thanks to Christoper Puleo, web designer extraordinaire, for help with web design and various beautiful photoshop art projects. Many thanks to Jeff Lockridge for maintaining our PC's and our PDF library.

Finally I would like to acknowledge Dawn Ashbridge without whom I can't conceive of having finished this dissertation. I would also like to acknowledge my father, Robert Thorne, for his support through this endeavor. And very special thanks to some of my closest friends in Arizona whose companionship in backpacking adventures across the southwest have helped to keep me sane. Special thanks to Todd A. Jones, Stephen T. Wiese, Shinichi Miyazawa, Trevor Graff, and David Downham.

TABLE OF CONTENTS

Page

CHAPTER Page

APPENDIX Page

LIST OF TABLES

LIST OF FIGURES

PREFACE

The format and content of each chapter conform to the author guidelines of Geophysical Journal International. Chapter 2, *Geographic Correlation Between Hot Spots and Deep Mantle Lateral Shear-Wave Velocity Gradients* was published in Physics of the Earth and Planetary Interiors, Volume 146, Issues 1-2, pages 47-63, 2004. Chapter 3, *Inferences on Ultralow-Velocity Zone Structure from a Global Analysis of SPdKS waves* was published in Journal of Geophysical Research – Solid Earth, Volume 109, B08301, doi:10.1029/2004JB003010, pages 1-22, 2004. The first part of Chapter 4, *Computing High Frequency Global Seismograms Using and Axi-Symmetric Finite Difference Approach* describes the mathematics and computation of a new technique for producing synthetic seismograms (SHaxi) and is original to this dissertation. The second part of Chapter 4 describes an application of this SHaxi method for computing synthetic seismograms for models with random velocity perturbations. Some of the results presented in Chapter 4, are submitted to Geophysical Journal International in the paper, *Global SH-Wave Propagation Using a Parallel Axi-Symmetric Finite Difference Scheme* by Gunnar Jahnke, Michael Thorne, Alain Cochard and Heiner Igel. Chapter 5, *3-D Seismic Imaging of the D'' Region Beneath the Cocos Plate* was submitted to Geophysical Journal International in Sept. 2005.

CHAPTER 1

GENERAL INTRODUCTION

Ever since the designation of the D" region (Bullen 1949), consisting of heterogeneous velocity structure in the lowermost 200-300 km of the mantle, researchers have sought to characterize the detailed nature of this boundary layer. The mechanisms responsible for D" heterogeneity, manifested in strong arrival time fluctuations of seismic phases sampling the region, are still poorly constrained. In the past decade increasing evidence suggests that processes responsible for this deep mantle heterogeneity are linked to whole mantle processes and surface features. For example, deep mantle high seismic wave speeds have been linked to regions of past subduction (e.g., Dziewonski, 1984). Recently, seismic tomography has also imaged high seismic velocity structures resembling subducting slabs plunging deep into the mantle (e.g., Grand *et al.* 1997; van der Hilst *et al.* 1997). These subducting slabs may plunge all the way to the core-mantle boundary (CMB) in turn giving rise to the discontinuous increase in seismic velocities 200-300 km above the CMB known of as the D" discontinuity. However, other explanations for the origin of the D" discontinuity abound, and the recent discovery of a deep mantle phase transition from magnesium silicate perovskite to a post-perovskite structure (e.g., Tsuchiya *et al.* 2004) has invigorated the debate. In this dissertation we examine surface features such as hot spot volcanism and compare them to deep mantle seismic observables. Furthermore we analyze broadband seismic energy sampling the deepest mantle in effort to put constraint on the possible origins of deep mantle heterogeneity and its relation to whole mantle processes and surface features.

Hot spot volcanism may originate in the deep mantle. Previous studies have indicated that this volcanism is correlated with regions of the deepest mantle where low *S*-wave velocities are resolved in global tomographic models (e.g., Wen & Anderson, 1997). In Chapter 2 we compare the surface location of hot spots to deep mantle *S*-wave velocities and lateral *S*-wave velocity gradients. We show that hot spot volcanism may originate from the deep mantle in regions exhibiting Earth's most pronounced lateral *S*-wave velocity gradients. These strong gradient regions display an improved geographic correlation over *S*-wave velocities to surface hot spot locations. Furthermore, we find that strong gradient regions typically surround the large lower velocity regions in the base of the mantle, which may indicate a possible chemical, in addition to thermal, component to these regions.

A connection between the origin of mantle plumes in the deep mantle and ultra-low velocity zones (ULVZs) has recently been advanced (e.g., Williams *et al.* 1998). Ultra-low velocity zones are roughly 10-40 km thick regions at the base of the mantle with *S*- and *P*-wave velocity reductions of as much as 40% and 10% respectively. These ULVZs may be regions of partial melt located at the hottest regions of the CMB. In order to understand their relationship with regions of mantle upwelling we analyzed a global dataset of *SKS* and *SPdKS* waveforms. The wave shape and timing of *SPdKS* data are analyzed relative to *SKS*, with some *SPdKS* data showing significant delays and broadening. We find evidence for extremely fine-scale heterogeneity and produce new maps of inferred ULVZ distribution. Furthermore, we show that our data are consistent

with the hypothesis that ULVZ presence (or absence) correlates with reduced (or average) heterogeneity in the overlying mantle.

In Chapter 3 we modeled *SPdKS* waveforms using the 1-D reflectivity technique (Müller, 1985). However, in this modeling endeavor we found it challenging to explain some of the *SPdKS* waveform complexity using a purely 1-D technique. Because short scale-length lateral heterogeneity at the CMB could account for the waveform distortions we sought to utilize techniques at predicting the seismic wavefield in 2- or 3-D. This prompted us to work on techniques for synthesizing waveforms for models of higher-dimensional complexity. In Chapter 4 we discuss one such technique for propagating seismic energy for *SH*-waves in 3-D axi-symmetric models (SHaxi). We discuss solutions to the axi-symmetric wave equation and the numerical application of this technique. Furthermore, we assess the technique's performance on modern distributed memory architectures and discuss the limitations and advantages of using the axi-symmetric assumption.

In order to demonstrate the versatility of the SHaxi technique we apply the method to compute synthetic seismograms for models containing whole mantle random velocity perturbations. Random velocity perturbations or random media, produce scattering of the seismic wavefield. Scattering from random media in turn produces seismic coda or a train of arrivals occurring after the main seismic arrivals. For *S*-wave propagation seismic coda have been extensively studied at high frequency for regional distances (e.g., Sato & Fehler 1998), in which the effects of scattering on the wavefield have been demonstrated to be limited to short period and broadband seismic observations

contributing to the total attenuation of the waveforms. However, the computational cost of performing numerical simulations at high frequencies has prevented computation of synthetic seismograms for global models containing random media. We compute synthetic seismograms for whole mantle random media and examine the effects of random heterogeneity on the seismic waveforms.

As a further application of the SHaxi technique developed in Chapter 4, in Chapter 5 we apply the method to compute synthetic seismograms for recent models of D" discontinuity structure beneath the Cocos Plate region. The D" discontinuity beneath the Cocos Plate region has received a considerable amount of recent attention in the past two years and several possible 3-D models for its structure have been proposed. Yet, these 3-D models have all been constructed using 1-D techniques and have never been benchmarked with synthetics produced with 3-D techniques. We compute synthetic seismograms for these recent models of discontinuity structure and compare them with broadband data. We assess the ability of each model to predict the timing of seismic arrivals traversing the deep mantle and make an analysis of future processing steps necessary in order to gain a finer scale 3-D picture of the deep mantle.

REFERENCES

Bullen, K. E., 1949. Compressibility-pressure hypothesis and the Earth's interior, *Monthly Notes of the Royal Astronomical Society*, Geophysics Supplement, 355-368.

Dziewonski, A.M., 1984. Mapping the lower mantle - Determination of lateral heterogeneity in P-velocity up to degree and order-6. *Journal of Geophysical Research*, **89** (NB7), 5929-5952.

Grand, S.P., van der Hilst, R.D. & Widiyantoro, S., 1997. Global seismic tomography: a snapshot of convection in the Earth. *GSA Today*, **7** (4), 1-7.

Müller, G., 1985. The Reflectivity Method - a Tutorial, *Journal of Geophysics-Zeitschrift Fur Geophysik*, **58** (1-3), 153-174.

Sato, H., & Fehler, M.C., 1998. Seismic Wave Propagation and Scattering in the Heterogeneous Earth, *Springer-Verlag*, New York, 308 pages.

Tsuchiya, T., Tsuchiya, J., Umemoto, K. & Wentzcovitch, R. A., 2004. Phase transition in MgSiO3 perovskite in the Earth's lower mantle, *Earth and Planetary Science Letters*, **224**, 241-248.

Van der Hilst, R.D., Widiyantoro, S., & Engdahl, E.R., 1997. Evidence for deep mantle circulation from global tomography, *Nature*, **386** (6625), 578-584.

Wen, L.X. & Anderson, D.L., 1997. Slabs, hotspots, cratons and mantle convection revealed from residual seismic tomography in the upper mantle. *Phys. Earth Planet. Inter.*, **99** (1-2), 131-143.

Williams, Q., J. Revenaugh, & E. Garnero, 1998. A correlation between ultra-low basal velocities in the mantle and hot spots, *Science*, **281** (5376), 546-549.

CHAPTER 2

GEOGRAPHIC CORRELATION BETWEEN HOT SPOTS AND DEEP MANTLE LATERAL SHEAR-WAVE VELOCITY GRADIENTS

Michael S. Thorne[1], Edward J. Garnero[1], and Stephen P. Grand[2]

[1]*Dept. of Geological Sciences, Arizona State University, Tempe, AZ 85287, USA*
[2]*Dept. of Geological Sciences, University of Texas at Austin, Austin, TX 78712, USA*

SUMMARY

Hot spot volcanism may originate from the deep mantle in regions exhibiting the Earth's most pronounced lateral *S*-wave velocity gradients. These strong gradient regions display an improved geographic correlation over *S*-wave velocities to surface hot spot locations. For the lowest velocities or strongest gradients occupying 10% of the surface area of the core-mantle boundary (CMB), hot spots are nearly twice as likely to overlie the anomalous gradients. If plumes arise in an isochemical lower mantle, plume initiation should occur in the hottest (thus lowest velocity) regions, or in the regions of strongest temperature gradients. However, if plume initiation occurs in the lowest velocity regions of the CMB lateral deflection of plumes or plume roots are required. The average lateral deflections of hot spot root locations from the vertical of the presumed current hot spot location ranges from ~300-900 km at the CMB for the 10-30% of the CMB covered by the most anomalous low *S*-wave velocities. The deep mantle may, however, contain strong temperature gradients or be compositionally heterogeneous, with plume initiation in regions of strong lateral *S*-wave velocity gradients as well as low *S*-wave velocity regions. If mantle plumes arise from strong gradient regions, only half of the lateral deflection from plume root to hot spot surface location is required for the 10-30% of the CMB covered by the most anomalous strong lateral *S*-wave velocities. We find that

strong gradient regions typically surround the large lower velocity regions in the base of the mantle, which may indicate a possible chemical, in addition to thermal, component to these regions.

2.1 Introduction

2.1.1 Seismic evidence for mantle plumes

Morgan (1971) first proposed that hot spots may be the result of thermal plumes rising from the core-mantle boundary (CMB). This plume hypothesis has gained widespread appeal, yet direct seismic imaging of whole mantle plumes through travel-time tomography or forward body wave studies have not yet resolved this issue (e.g., Ji & Nataf 1998b; Nataf 2000). Plume conduits are predicted to be on the order of 100 – 400 km in diameter, with maximum temperature anomalies of roughly 200 – 400 K (Loper & Stacey 1983; Nataf & Vandecar 1993; Ji & Nataf 1998a). Global tomographic models typically possess lower resolution than is necessary to detect a plume in its entirety. Table 2.1 lists the resolution for several recent whole mantle tomographic models. However, a few higher resolution tomographic studies have inferred uninterrupted low velocities from the CMB to the base of the crust. For example, the models of Bijwaard & Spakman (1999) (65 – 200 km and 150 – 400 km lateral resolution in upper and lower mantle, respectively) and Zhao (2001) (5 deg lateral resolution) both show uninterrupted slow *P*-wave velocities beneath Iceland, which have been interpreted as evidence for a whole mantle plume in the region. In addition, the tomographic model S20RTS (Ritsema *et al.* 1999; Ritsema & van Heijst 2000) shows a low *S*-wave velocity anomaly in the

upper mantle beneath Iceland that ends near 660 km depth. High resolution (e.g., block sizes of 75 × 75 × 50 km, Foulger *et al.* 2001) regional tomographic studies have also been used to image plumes in the upper mantle and have shown that some plumes extend at least as deep as the transition zone, but the full depth extent of the inferred plumes remains unresolved (Wolfe *et al.* 1997; Foulger *et al.* 2001; Gorbatov *et al.* 2001). Resolution at even shorter scale lengths is necessary to determine with greater confidence any relationship between continuity of low velocities in the present models and mantle plumes.

Several body wave studies have focused on plume-like structures related to hot spots at the base of the mantle. For example, Ji & Nataf (1998b) used a method similar to diffraction tomography to image a low velocity anomaly northwest of Hawaii that rises at the base of the mantle and extends at least 1000 km above the CMB. Helmberger *et al.* (1998) used waveform modeling to show evidence for a 250 km wide dome-shaped, ultra-low velocity zone (ULVZ) structure beneath the Iceland hot spot at the CMB. Ni *et al.* (1999) used waveform modeling to confirm the existence of an anomalous (approximately up to -4% δVs) low velocity structure beneath Africa extending upward 1500 km from the CMB, which may be related to one or more of the hot spots found in the African region. Several seismic studies have shown evidence for plumes in the mantle transition zone (410 – 660 km), suggesting that hot spots may feed plumes at a minimum depth of the uppermost lower mantle (Nataf & Vandecar 1993; Wolfe *et al.* 1997; Foulger *et al.* 2001; Niu *et al.* 2002; Shen *et al.* 2002). These plumes are not necessary to explain the majority of hot spots on Earth's surface (Clouard & Bonneville

2001), but suggest that some hot spots may be generated from shallow upwelling as implied by layered convection models (e.g., Anderson 1998).

2.1.2 Indirect evidence: correlation studies

The inference that the deepest mantle seismic structure is related to large-scale surface tectonics has been given much attention in the past decade (e.g., Bunge & Richards 1996; Tackley 2000). Several studies suggest that past and present surface subduction zone locations overlay deep mantle high seismic wave speeds (Dziewonski 1984; Su *et al.* 1994; Wen & Anderson 1995), which are commonly attributed to cold subducting lithosphere migrating to the CMB. Recent efforts in seismic tomography have revealed images of planar seismically fast structures resembling subducting lithosphere that may plunge deep into the mantle (Grand 1994; Grand *et al.* 1997; van der Hilst *et al.* 1997; Bijwaard *et al.* 1998; Megnin & Romanowicz, 2000; Gu *et al.* 2001). The final depth of subduction has far reaching implications for the nature of mantle dynamics and composition (Albarede & van der Hilst 2002). This finding, coupled with the spatial correlation of hot spots and deep mantle low seismic velocities, are main constituents of the argument for whole mantle convection (Morgan 1971; Hager *et al.* 1985; Ribe & Devalpine 1994; Su *et al.* 1994; Grand *et al.* 1997; Lithgow-Bertelloni & Richards 1998).

With present challenges in direct imaging of mantle plumes or the source of hot spots, comparison studies of hot spots and deep mantle phenomena have yielded provocative results. Surface locations of hot spots have been correlated to low velocities

(e.g., Wen & Anderson 1997; Seidler *et al.* 1999) and ULVZs (Williams *et al.* 1998) at the CMB. It has also been noted, however, that the locations of hot spots at Earth's surface tend to lie near edges of low-velocity regions, as shown by tomographic models at the CMB (Castle *et al.* 2000; Kuo *et al.* 2000). This correlation has been used to imply that mantle plumes can be deflected by more than 1000 km from their proposed root source of the deepest mantle lowest velocities to the surface, perhaps by the action of "mantle winds" (e.g., Steinberger 2000).

2.1.3 Other mantle plume studies

The wide variability of observed and calculated hot spot characteristics implies that several mechanisms for hot spot genesis may be at work. Modeling of plume buoyancy flux has been carried out for several hot spots (Davies 1988; Sleep 1990; Ribe & Christensen 1994), revealing a wide range in the volcanic output of plumes possibly responsible for many hot spots. Geodynamic arguments suggest some hot spots may be fed by shallow-rooted (e.g., Albers & Christensen 1996) or mid-mantle-rooted (e.g., Cserepes and Yuen 2000) plume structures. Geochemical evidence suggests that different hot spot source regions may exist (Hofmann 1997), as shown by isotopic studies that argue for either transition zone (e.g., Hanan and Graham 1996) or CMB (e.g., Brandon *et al.* 1998; Hart *et al.* 1992) source regions. Further tomographic evidence has been used to argue that several hot spots may be fed by a single large upwelling from the deep mantle (e.g., Goes *et al.* 1999). Hence, the original mantle plume hypothesis

(Morgan 1971), that long-lived thermal plumes rise from the CMB, has expanded to include a wide variety of possible origins of hot spot volcanism.

In this study, we explore statistical relationships between the surface locations of hot spots and seismic heterogeneity observed in the deep mantle. Specifically, we compare hot spot surface locations to low *S*-wave velocity heterogeneities and strong *S*-wave lateral velocity gradients. We evaluate the origin of hot spot related plumes, and examine the implications for deep mantle composition and dynamics.

2.2 Calculation of lateral shear-wave velocity gradients

We analyzed gradients in lateral *S*-wave velocity at the CMB for six global models of *S*-wave velocities. Table 2.1 summarizes the parameterizations of each of the models analyzed. Using bi-cubic interpolation, we resampled models originally parameterized in either spherical harmonics or blocks onto a 1x1 degree grid. Additionally, we smoothed block models laterally by Gaussian cap averaging with a radius of 4 or 8 degrees for comparison with the smoother structures represented by spherical harmonics. We calculated lateral *S*-wave velocity gradients for the deepest layer in each model at every grid point as follows: (a) great circle arc segments were defined with 500 to 2000 km lengths centered on each grid point for every 5 degrees of rotation in azimuth; (b) seismic velocity was estimated at 2, 3, 5, 7, or 9 equally spaced points (by nearest grid point interpolation) along each arc; (c) a least squares best fit line through arc sampling points was applied for each azimuth; and (d) the maximum slope, or gradient, and associated azimuth was calculated for each grid point. This approach

proved versatile for computing lateral velocity gradients for the variety of model parameterizations analyzed (Table 2.1).

In order to compare *S*-wave velocities and lateral *S*-wave velocity gradients between different models, lower mantle *S*-wave velocities and lateral *S*-wave velocity gradients were re-scaled according to CMB surface area. For example, for model S20RTS, *S*-wave velocities at or lower than $\delta Vs = -1.16$, 10% of the surface area of the CMB is covered (herein after referred to as "% CMB surface area coverage"). Similarly, the most anomalous velocities occupying 20% CMB surface area coverage, are lower than $\delta Vs = -0.59$. Lateral *S*-wave velocity gradients are scaled in the same manner, where 10% CMB surface area coverage corresponds to the most anomalous strong gradients. The number of hot spots located within a given percentage of CMB surface area coverage for low *S*-wave velocity or strong lateral gradient are tabulated into hot spot hit counts. In this manner, the spatial distribution of the most anomalous low seismic velocities and strong gradients can be equally compared and correlated to hot spots. For example, the first two columns of Figure 2.2 show velocities and gradients of the model S20RTS (Ritsema & van Heijst 2000), with contours drawn in green around the 10, 20, and 30% most anomalously low shear velocities and strongest lateral *S*-wave velocity gradients scaled by CMB surface area coverage. In the third column (Fig. 2.2), the % CMB surface area coverage contours are filled in solid, with hot spot positions drawn as red circles and hot spot hit counts listed beneath the respective globes.

In order to compare shear velocities and our computed lateral *S*-wave velocity gradients to hot spot surface locations, we used a catalog of 44 hot spots (Steinberger

2000). We used this catalog because it imposed three stringent conditions to qualify as a hot spot. First, each hot spot location must be associated with a volcanic chain, or at least two age determinations must exist indicating a volcanic history of several million years. Second, two out of four of the following conditions must be met: (i) present-day or recent volcanism, (ii) distinct topographic elevation, (iii) associated volcanic chain, or (iv) associated flood basalt. Third, all subduction zone related volcanism was excluded as being related to hot spots. Table 2.2 and Figure 2.1 show the hot spots and their respective locations used in this study.

This is not a comprehensive list of all possible hot spots (e.g., compare with 19 hot spots of Morgan 1972, 37 of Sleep 1990 or 117 of Vogt 1981). Also, we do not presume that plumes rooted in the CMB necessarily produce each of these hot spots. As noted by Steinberger (2000), this list does not include any hot spots in Asia due to difficulty in recognition. Therefore, Table 2.2 gives a representative group of Earth's most prominent hot spots.

2.3 Results

For the 10% of the CMB surface area covered by lowest velocities or strongest gradients, nearly twice as many hot spots are found within 5 degrees of strong gradients. For example, this observation is apparent in the third column of Figure 2.2 for model S20RTS. In this model, 23 hot spots – over half of all hot spots – overlie the strongest gradients, compared to 12 hot spots for low velocities. At 20% CMB surface area coverage 22 hot spots (50%) are found over low velocities, whereas 35 (~80%) are found

over strong gradients. Increasing the coverage to greater than one-fourth of the CMB decreases this disparity. For example, for 30% of the CMB covered by lowest velocities or strongest gradients, model S20RTS has ~61% of all hot spots over the lowest velocities and ~84% over the strongest gradients. The most striking disparity in hot spot hit count is seen in the 10 – 40% CMB surface area coverage range, which holds for all models analyzed.

Figure 2.3 displays the six models analyzed in this study. The first column of Figure 2.3 displays the *S*-wave velocity perturbations, while the second and third columns show low *S*-wave velocity and strong lateral gradient respectively, contoured and shaded on the basis of CMB surface area coverage. The number of hot spots located within a surface area contour for low shear velocity or strong lateral gradient are tabulated into hot spot hit counts, incrementing CMB surface area coverage in one percent intervals. In computing hot spot correlations to these distributions, we allowed for hot spot root lateral deflections by experimenting with a variable radius search bin centered on each hot spot to tabulate lowest velocity or strongest gradient within. Figure 2.4 displays the hot spot hit counts for the model S20RTS, for a 5-degree radius search bin (approximately 300 km radius centered on each hot spot). Steinberger (2000) determined hot spot root locations due to mantle winds using three tomographic models, and estimated average lateral deflections from present day hot spot surface locations averaging ~12 degrees (~734 km) at the CMB. A 5-degree radius search bin is the largest used in our calculations, which corresponds to less than half of this. However, Steinberger (2000) assumed a thermal origin to seismic heterogeneity, with the result of hot spot roots being located near the

hottest temperatures and thus near the lowest velocities. We will first address the statistical correlations between hot spots and low *S*-wave velocities and then hot spots and strong gradients, and further discuss possible scenarios that relate to the origin of lower mantle heterogeneity.

2.4. Discussion

The number of hot spots nearest the strongest velocity gradients is significantly greater than for the lowest velocities in the deep mantle. This is demonstrated in Figure 2.2 for model S20RTS, and is also seen in Figure 2.4 which shows hot spot hit counts for either velocities or gradients versus percent coverage of the CMB for this model. Figure 2.4 also displays the disparity seen in the range of 10 – 40% CMB surface area coverage between low velocities and strong gradients. That is, the correlation between hot spots and velocity gradients is highest for the strongest gradients in this surface area coverage range.

In our analysis of velocity gradients, variations in hot spot hit count occur for ranges of arc length and search radius. We explored up to 2000 km arc lengths for gradient estimations. Figure 2.4 shows a slightly better hot spot count for gradient calculations with a 500 km arc length than for 1000 km, however there is no significant difference between them. Gradient estimations over dimensions larger than 1000 km result in more similar hot spot hit counts between low velocities and strong gradients, which is expected because short wavelength heterogeneity is smoothed out relative to shorter arc length calculations. Hot spot counts also depend on the size of the radius

search bin used to collect the gradient and velocity values. Decreasing the search radius size reduces hot spot counts for both the velocity and gradient calculations. In particular, gradient hot spot counts decrease disproportionately relative to velocity hot spot counts, as gradients naturally possess smaller wavelength features than the velocity data from which they are derived. Conversely, increasing the size of the radius search bin, in accordance with the hot spot plume deflection calculations of Steinberger (2000), increases hot spot counts for the strongest gradients rather than the lowest velocities.

Overall hot spot hit counts for the six *S*-wave models analyzed are given in Tables 2.3 and 2.4. For example, a value of 5 in Table 2.3 signifies that the hot spot overlies D" *S*-wave heterogeneity with the magnitude ranked at 5% of the lowest velocities on Earth (i.e., 0% corresponds to the lowest velocity in D" and 100% corresponds to the highest velocity in D"). Similarly, a value of 5 in Table 2.4 signifies the hot spot overlies D" *S*-wave velocity lateral gradient with the magnitude ranked at 5% of the strongest gradients on Earth. (Again, 0% corresponds to the strongest D" lateral velocity gradients, and 100% corresponds to the weakest gradients). These values are presented in Figure 2.5 for percent CMB surface area coverage's between 10 and 30%. This range displays a higher number of hot spots above strong gradients than for low velocities. The 10% coverage cutoff shows the greatest difference between gradient and velocity counts with an average over all models showing 49% and 46% of all hot spots falling within the gradient cutoff for 500 and 1000 km gradient measurement arcs, respectively. In comparison, only 26% of all hot spots are within 5 degrees of the 10% of the CMB occupied by the lowest velocities.

Using the Steinberger (2000) hot spot root locations, we also calculated correlations between hot spots and either low velocities or strong gradients. As expected, hot spot roots lie closer to the lowest *S*-wave velocities than to strong gradients, since the roots were obtained using the assumption of a density driven flow model, where shear-wave velocities were linearly mapped to densities. The mantle wind estimates using this assumption place the source of mantle plumes near the lowest densities, corresponding to the lowest seismic velocities.

We compared the strength of correlation to hot spot buoyancy flux estimates (Sleep 1990; Steinberger 2000). It has been argued that flux should relate to depth of plume origin (e.g., Albers & Christensen 1996). However, we did not observe a clear dependence on flux in the correlations for either *S*-wave velocities or lateral *S*-wave velocity gradients. This is not surprising, because hot spots with relatively weak flux estimates, as compared to the Hawaiian hot spot (hot spot # 18 in Figure 2.1), also display hot spot traces that accurately follow plate motions. For example, Duncan & Richards (1991) pointed out that the East Australia, Tasmanid, and Lord Howe hot spots (hot spots # 12, 39, and 24, Figure 2.1), each with volume flux estimates of 900 kg/s (compared with 6500 kg/s for the Hawaiian hot spot, Steinberger 2000), accurately represent the Australian-Indian plate motion, suggesting a common source for each of them. Additionally, in the Steinberger (2000) calculation of hot spot lateral deflections, the smallest hot spots (volume flux < 2000 kg/s) show a fairly even distribution of deflections ranging from 200 to 1400 km. Some of the largest hot spots (Tahiti, Marquesas, and Pitcairn, hot spots # 38, 28, and 31, Figure 2.1) show relatively little

deflection, yet Hawaii and Macdonald (hot spot # 26, Figure 2.1) show as much as 700 to 800 km of lateral deflection.

Statistical significance testing of our correlations were performed by comparing the correlation between hot spot locations and the strength of the velocity or gradient anomaly within the radius search bin beneath them. The correlation with hot spots in their current location was compared with the correlation calculated for 10,000 pseudo-random rotations of the hot spots about three Euler angles, with the relative position between hot spots maintained. For the 10% of the CMB overlain by strongest gradients averaged over all six models tested, the percentage of random hot spot locations that show a lower correlation than current hot spot locations is 94.3%. The final number in each row of Figure 2.2 shows the percentage of random hot spot locations with lower correlations than current hot spot current locations for model S20RTS. For example, at 10% CMB surface area coverage, ~89% (~11%) of randomly rotated hot spot locations show lower (higher) correlations than hot spot present locations over low velocities. Similarly, 99.8% (0.2%) of randomly rotated hot spot locations show lower (higher) correlations than hot spot present locations over strong gradients. This statistical significance testing shows that spatial grouping of current hot spot locations does not bias our results.

Our calculations for lateral *S*-wave velocity gradients display some model dependency, especially at shorter length scales. In order to characterize the variability of the tomographic models used, the standard deviation of the magnitude of *S*-wave velocities at each latitude and longitude (as scaled by CMB surface area coverage) was

calculated (Figure 2.6). There is good agreement between each of the models for the most anomalous low and high velocities. Model discrepancy is highest in regions with the lowest amplitude of heterogeneity. Overall, the CMB surface percent coverage (shown in Tables 2.3 and 2.4) underlying each hot spot displays consistency across all velocity models. These averages show high standard deviations for several hot spots, indicating the degree to which the tomographic models differ in these locations, and may provide indication of an upper mantle source.

As arc lengths ranging from 500 – 1500 km yield the same result for a given model, our gradient calculations are most reliable at this length scale. Calculations of gradients over smaller arc lengths tend to display more incoherency, and may only serve to highlight the small-scale differences between the different tomographic models. Longer arc lengths smooth out short wavelength heterogeneity producing more similar hot spot counts between velocity and gradient. For 500 to 1500 km arc lengths, all of the models display strong gradients surrounding low velocity regions, as well as coherence between the different models (Figure 2.6). Nevertheless, some uncertainty exists due to variability in model resolution.

While we do not attempt to reconcile the many issues present regarding hot spot genesis, our results show that hot spot locations are better correlated with lateral *S*-wave velocity gradients than with *S*-wave velocities. This correlation does not mandate that mantle plumes feeding hot spots originate from the CMB, but it does call for further discussion regarding the possible scenarios relating to the CMB-source hypothesis. In this light, we discuss briefly several possibilities and corresponding implications of our

results for plumes possibly originating at the CMB in either an isochemical or chemically heterogeneous lower mantle.

2.4.1 Plumes rising from an isochemical lower mantle

Hot spots may be the result of whole mantle plumes rooted at the CMB in an isochemical lower mantle. The lowest velocities in an isochemical lower mantle should be associated with the highest temperatures, with the consequence of mantle plume formation in those locations. If the tomographic models evaluated in this study are of high enough resolution to resolve CMB plume roots, several observations may be made in light of our results.

Some plumes may be rising vertically from low velocity regions detected by tomography, which may be associated with a ULVZ structure with partial melt origin (Williams & Garnero 1996). Our results indicate that all hot spots are not necessarily located over low *S*-wave velocities; therefore, not all hot spots may be the result of vertically rising plumes from a dynamically static isochemical lower mantle. However, plumes may be deflected in the mantle under the action of mantle winds. Alternatively, if lower mantle viscosity is too low to keep plume roots fixed, they may wander, or advect, in response to the stress field induced by whole mantle convection (Loper 1991; Steinberger 2000). Steinberger's (2000) calculations show density driven horizontal flow in the lower mantle that is directed inward with respect to the African and Pacific low velocity anomalies. This flow field allows for plume roots based in the lowest velocities, but through lower mantle advection are no longer underlying the surface hot spot

locations. Our results are reconcilable with the possibility of upper or lower mantle advective processes shifting the plume root or surface location to non-vertical alignment. However, in the six models we analyzed the average amount of lateral deflection of all hot spot roots is ~300 to 900 km (~5 to 15 deg) for the 10-30% lowest *S*-wave velocities at the CMB (Figure 2.7, top panel). The large uncertainties in the time for a plume to rise from the CMB makes it difficult to quantify the uncertainties in the magnitude of lateral plume deflection calculations.

Tomographic models may lack the resolution to detect lower mantle plume roots in an isochemical lower mantle, unless all plumes originate from the degree-two low velocity features. These degree-two low velocity features are linked to large low velocity structures rising from the CMB under Africa and the south-central Pacific, and may generate observed hot spot volcanism in those regions (Romanowicz & Gung 2002). However, unmapped localized ULVZ structure of partial melt origin may relate to plume genesis, which would also go undetected in current tomographic studies. The observations of ULVZs (Garnero & Helmberger 1998) and strong *PKP* precursors in regions not associated with anomalously low velocities in tomographic models (Wen 2000; Niu & Wen 2001) supports the possibility that plumes are generated at currently unmapped ULVZ locations. The recent observation of strong *PKP* scatterers underneath the Comores hot spot (hot spot #9, Figure 2.1; Wen 2000) also supports this idea. ULVZs and strong *PKP* precursors have been found in regions of strong lateral *S*-wave gradients. However, spatial coverage of either ULVZ variations or *PKP* scatterers is far from global, which precludes comparison to global lower mantle velocities or gradients.

An isochemical lower mantle cannot be completely ruled out, however, as plumes may also be initiated at strong, short-scale, lateral temperature gradients in an isochemical lower mantle (Zhao 2001; Tan *et al.* 2002). Tan *et al.* (2002) suggests that if subducting slabs are able to reach the CMB, then they will push aside hot mantle material and plumes will preferentially be initiated from their edges. Tomographic models may currently lack the resolution needed to characterize such short-scale variations. Nonetheless, strong short scale temperature gradients in an isochemical lower mantle should be associated with strong lateral *S*-wave gradients. Tan *et al.* (2002) suggest that lateral temperature anomalies of ~500º C may exist between subducted slabs and ambient mantle material, which is comparable to temperature anomalies that may be inferred across our gradient estimation calculations (Stacey 1995; Oganov *et al.* 2001). One challenge is that the strongest velocity gradients surround the lowest velocities, which are typically well separated from the high velocity D" features typically associated with subduction. However, it is an intriguing possibility, especially considering the work of Steinberger (2000), who suggests that the lower mantle flow field is being directed inward towards the Pacific and African low velocity anomalies. It is conceivable that this lower mantle flow field could be the result of ancient subduction, and is suggested for hot spots east of South America (Ni & Helmberger 2001). We further discuss lateral deflection of hot spot roots in the next section.

2.4.2 Plumes rising from a compositionally heterogeneous lower mantle

Evidence for deep mantle compositional variations has also been proposed using a variety of seismic methods at a number of spatial scales, (e.g., Sylvander & Souriau 1996; Breger & Romanowicz 1998; Ji & Nataf 1998a; Ishii & Tromp 1999; van der Hilst & Karason 1999; Wysession *et al.* 1999; Garnero & Jeanloz 2000; Masters *et al.* 2000; Breger *et al.* 2001; Saltzer *et al.* 2001) as well as from mineralogical (e.g., Knittle & Jeanloz 1991; Manga & Jeanloz 1996) considerations. Dynamical simulations have also argued for either thermo-chemical boundary layer structure in D" (e.g., Gurnis 1986; Tackley 1998, Kellogg *et al.* 1999) or argued for deep mantle compositional variation (Forte & Mitrovica 2001). As discussed above, however, isochemical slab penetration into the deep mantle can result in plume initiation (Zhong & Gurnis, 1997; Tan *et al.* 2002). If lateral velocity variations are solely thermal in origin, then these strong lateral gradient regions may imply implausibly strong thermal gradients, with peak-to-peak variations possibly nearing 2000 K (Oganov *et al.* 2001). This observation raises the possibility that the degree 2 low velocity features in the deep mantle have a compositional, as well as thermal, origin. To a first approximation, the strongest lateral gradients are associated with the perimeter of the lowest velocity regions, as exhibited in Figure 2.2 by the strongest gradients surrounding the Pacific and southern Africa low velocity anomalies. In a compositionally heterogeneous lower mantle, many possibilities are present that relate to plume genesis.

One possibility is that compositionally distinct lower mantle material of reduced density will rise due to increased buoyancy, which may relate to plume initiation (e.g.,

Anderson 1975). If the mineral phases present near the edges of such compositionally distinct features allow for eutectic melting or solvus formation, then a new post-mixing composition, if less dense, may trigger instabilities that lead to plumes. Alternatively, compositionally distinct bodies of higher thermal conductivity may increase heat transfer from the outer core, with plume formation occurring above it. Another possibility is that plume initiation may be triggered near the lowermost mantle edges of higher thermally conductive bodies. In this model, adjacent mantle material will be heated both from the CMB and the conducting chemical anomaly. However, the topography of the conductive body may extensively modify where plume conduits rise (e.g., Kellogg *et al.* 1999; Tackley 2000).

Jellinek & Manga (2002) performed tank experiments indicating that a dense, low viscosity layer at the base of the mantle can become fixed over length scales longer than the rise-time of a plume. Flow driven by lateral temperature variations allows for buoyant material to rise easiest along the sloping interfaces of topographic highs of the dense, low viscosity layer. However, Jellinek & Manga (2002) suggest the topographic highs where plume initiation is easiest would to some extent be evenly distributed across an area such as the Pacific low velocity anomaly. Future dynamics experiments should further address possible scenarios that give rise to plume initiation near edges of anomalous layers.

Although our results suggest that surface locations of hot spots are more likely to overlie regions of strong lateral *S*-wave velocity gradients, our results do not preclude other plume source origins. The second panel in Figure 2.7 shows the average lateral

deflections from vertical ascent required to explain all hot spot root locations from the strongest gradients. An average of all hot spots suggests that ~ 150 to ~ 450 km (~ 2.5 to ~7.5 deg) of lateral deflections are required if plume roots originate at the 10 to 30% of the CMB covered by the strongest gradients. Although this amount of deflection is considerably less than that required by deflections from the lowest velocities, some hot spots are found far from either low *S*-wave velocity or strong gradient regions (e.g., the Bowie and Cobb hot spots, hot spot # 3 and 8, Figure 2.1), indicating that some plumes may also be initiated in upper or mid-mantle source regions, or that estimations of lateral deflection are grossly underestimated.

We have also compared hot spot counts at the CMB to three other depths in the mantle: 605, 725, and 1375 km (depth slices are shown in Supplemental Figures 2A-2E). These depths were chosen as being representative of the mantle transition zone, and of the upper and mid-lower mantle. Figure 2.8 shows the number of hot spots overlying the 20% strongest gradients or lowest velocities, by surface area coverage of each of these three depth zones. The results are averaged across each of the models explored in this study (with the exclusion of the D" model Kuo12). The highest correlation is seen for hot spot surface locations and lateral gradients in the deepest layer. Additionally, the greatest disparity between hot spot counts for gradients and low *S*-wave velocities is also seen for the deepest layer. However, for *S*-wave velocities, the mid-lower mantle appears to have the highest correlation to hot spots. Figure 2.8 shows that more hot spots overlie lowermost mantle low *S*-wave velocities than low *S*-wave velocities in the upper part of the lower mantle or in the transition zone.

2.5 Conclusions

We have shown that hot spots are more likely to overlie strong *S*-wave velocity lateral gradients rather than low *S*-wave velocity regions in the lower mantle. Nearly twice as many hot spots overlie strong gradients than low velocities occupying 10% of the surface area of the CMB. An isochemical lower mantle source to plume formation requires the presence of mantle winds and/or lower mantle advection to reconcile our correlations, unless plumes are being initiated at the edges of subducted slab material. If plumes are initiated in the lowest *S*-wave velocity regions of the CMB, average lateral deflections of hot spot root locations from ~300-900 km at the CMB for the 10-30% of the CMB covered by the most anomalous low velocities are required. If this model of plume formation is correct, continuing improvements in whole mantle travel-time tomography and forward body wave studies will further elucidate the fine structure of such plumes. Challenges remain, however, to better document ULVZ structure, which may be related to partial melt (Williams & Garnero 1996), as the source of mantle plumes. Further efforts to provide a more global coverage of ULVZ locations will help to resolve this issue.

On the other hand, we find that the strongest lateral *S*-wave velocity gradients tend to surround the large-scale lower velocity regions, with the strong gradient regions possibly signifying lateral boundaries in the deepest mantle between large-scale chemically distinct bodies, or thermal slabs. One possible origin to a compositionally distinct lower mantle is iron enrichment, which may create compositionally distinct features, resulting in a few percent reductions in velocity (Duffy & Ahrens 1992;

Wysession *et al.* 1992; Williams & Garnero 1996) and produce a stable dense feature with relatively sharp edges around its perimeter. Plumes arising from strong gradient regions would require average lateral deflections from the vertical of hot spot root locations of ~ 150 to 450 km at the CMB for the 10-30% of the CMB covered by the most anomalous strong gradients. This amount of lateral deflection is significantly less than that required if plumes initiate at the lowest velocities at the CMB, however, many hot spots may not have a lower mantle source.

Plume source regions may also be located in the mid or upper mantle (Albers & Christensen 1996; Anderson 1998; Cserepes & Yuen 2000), which may or may not be coupled to lower mantle dynamics. The number of possible plume genesis scenarios in the upper or mid-mantle is as varied as they are for the lower mantle. We have presented a better correlation between present surface locations of hot spots and deep mantle lateral *S*-wave velocity gradients than with *S*-wave velocities, and have discussed possible scenarios as to the origins of plumes that may arise from the deep mantle. However, given the wide range of uncertainties it is still impossible to ascertain the true depth origin of mantle plumes that may be responsible for surface hot spot volcanism. This issue may not be resolved until complete high-resolution images of plumes from top to bottom are successfully obtained.

ACKNOWLEDGEMENTS

The authors thank B. Romanowicz, G. Laske, J. Ritsema, and Y. Gu for providing the most recent iterations of their tomographic models. We also thank S. Peacock, J. Tyburczy, M. Fouch, T. Lay, M. Gurnis, and D. Zhao for manuscript review and helpful discussion. This research was supported in part by NSF Grant's EAR-9996302 and EAR-9905710.

REFERENCES

Albarede, F. & van der Hilst, R.D., 2002. Zoned mantle convection. *Philos. Trans. R. Soc. Lond. Ser. A-Math. Phys. Eng. Sci.*, **360** (1800), 2569-2592.

Albers, M. & Christensen, U.R., 1996. The excess temperature of plumes rising from the core-mantle boundary. *Geophys. Res. Lett.*, **23** (24), 3567-3570.

Anderson, D.L., 1975. Chemical plumes in mantle. *Geol. Soc. Am. Bull.*, **86** (11), 1593-1600.

Anderson, D.L., 1998. The scales of mantle convection. *Tectonophysics*, **284** (1-2): 1-17.

Bijwaard, H., Spakman, W. and Engdahl, E.R., 1998. Closing the gap between regional and global travel time tomography. *J. Geophys. Res.-Solid Earth*, **103** (B12), 30055-30078.

Bijwaard, H. & Spakman, W., 1999. Tomographic evidence for a narrow whole mantle plume below Iceland. *Earth Planet. Sci. Lett.*, **166** (3-4), 121-126.

Brandon, A.D., Walker, R.J., Morgan, J.W., Norman, M.D. & Prichard, H.M., 1998. Coupled Os-186 and Os-187 evidence for core-mantle interaction. *Science*, **280** (5369), 1570-1573.

Breger, L. & Romanowicz, B., 1998. Three-dimensional structure at the base of the mantle beneath the central Pacific. *Science*, **282** (5389), 718-720.

Breger, L., Romanowicz, B. & Ng, C., 2001. The Pacific plume as seen by S, ScS, and SKS. *Geophys. Res. Lett.*, **28** (9), 1859-1862.

Bunge, H.P. & Richards, M.A., 1996. The origin of large scale structure in mantle convection: Effects of plate motions and viscosity stratification. *Geophys. Res. Lett.*, **23** (21), 2987-2990.

Castle, J.C., Creager, K.C., Winchester, J.P. & van der Hilst, R.D., 2000. Shear wave speeds at the base of the mantle. *J. Geophys. Res.-Solid Earth*, **105** (B9), 21543-21557.

Clouard, V. & Bonneville, A., 2001. How many Pacific hotspots are fed by deep-mantle plumes? *Geology*, **29** (8), 695-698.

Cserepes, L. & Yuen, D.A., 2000. On the possibility of a second kind of mantle plume. *Earth Planet. Sci. Lett.*, **183** (1-2), 61-71.

Davies, G.F., 1988. Ocean bathymetry and mantle convection .1. Large-scale flow and hotspots. *Journal of Geophysical Research-Solid Earth and Planets*, **93** (B9), 10467-10480.

Duffy, T.S. & Ahrens, T.J., 1992. Sound velocities at high-pressure and temperature and their geophysical implications. *J. Geophys. Res.-Solid Earth*, **97** (B4), 4503-4520.

Duncan, R.A. & Richards, M.A., 1991. Hotspots, mantle plumes, flood basalts, and true polar wander. *Rev. Geophys.*, **29** (1), 31-50.

Dziewonski, A.M., 1984. Mapping the lower mantle - Determination of lateral heterogeneity in P-velocity up to degree and order-6. *Journal of Geophysical Research*, **89** (B7), 5929-5952.

Forte, A.M. & Mitrovica, J.X., 2001. Deep-mantle high-viscosity flow and thermochemical structure inferred from seismic and geodynamic data. *Nature*, **410** (6832), 1049-1056.

Foulger, G.R., Pritchard, M.J., Julian, B.R., Evans, J.R., Allen, R.M., Nolet, G., Morgan, W.J., Bergsson, B.H., Erlendsson, P., Jakobsdottir, S., Ragnarsson, S., Stefansson, R. & Vogfjörd, K., 2001. Seismic tomography shows that upwelling beneath Iceland is confined to the upper mantle. *Geophys. J. Int.*, **146** (2), 504-530.

Garnero, E.J. & Helmberger, D.V., 1998. Further structural constraints and uncertainties of a thin laterally varying ultralow-velocity layer at the base of the mantle. *J. Geophys. Res.-Solid Earth*, **103** (B6), 12495-12509.

Garnero, E.J. & Jeanloz, R., 2000. Fuzzy patches on the Earth's core-mantle boundary? *Geophys. Res. Lett.*, **27** (17), 2777-2780.

Goes, S., Spakman, W. & Bijwaard, H., 1999. A lower mantle source for central European volcanism. *Science*, **286** (5446), 1928-1931.

Gorbatov, A., Fukao, Y., Widiyantoro, S. & Gordeev, E., 2001. Seismic evidence for a mantle plume oceanwards of the Kamchatka-Aleutian trench junction. *Geophys. J. Int.*, **146** (2), 282-288.

Grand, S.P., 1994. Mantle shear structure beneath the America and surrounding oceans. *J. Geophys. Res.-Solid Earth*, **99** (B6), 11591-11621.

Grand, S.P., van der Hilst, R.D. & Widiyantoro, S., 1997. Global seismic tomography: a snapshot of convection in the Earth. *GSA Today*, **7** (4), 1-7.

Grand, S.P., 2002. Mantle shear-wave tomography and the fate of subducted slabs. *Philos. Trans. R. Soc. Lond. Ser. A-Math. Phys. Eng. Sci*., **360** (1800), 2475-2491.

Gu, Y.J., Dziewonski, A.M., Su, W.J. & Ekstrom, G., 2001. Models of the mantle shear velocity and discontinuities in the pattern of lateral heterogeneities. *J. Geophys. Res.-Solid Earth*, **106** (B6), 11169-11199.

Gurnis, M. & Davies, G.F., 1986. Mixing in numerical-models of mantle convection incorporating plate kinematics. *Journal of Geophysical Research-Solid Earth and Planets*, **91** (B6), 6375-6395.

Hager, B.H., Clayton, R.W., Richards, M.A., Comer, R.P. & Dziewonski, A.M., 1985. Lower mantle heterogeneity, dynamic topography and the geoid. *Nature*, **313** (6003), 541-546.

Hanan, B.B. & Graham, D.W., 1996. Lead and helium isotope evidence from oceanic basalts for a common deep source of mantle plumes. *Science*, **272** (5264), 991-995.

Hart, S.R., Hauri, E.H., Oschmann, L.A. & Whitehead, J.A., 1992. Mantle Plumes and Entrainment - Isotopic Evidence. *Science*, **256** (5056), 517-520.

Helmberger, D.V., Wen, L. & Ding, X., 1998. Seismic evidence that the source of the Iceland hotspot lies at the core-mantle boundary. *Nature*, **396** (6708), 251-255.

Hofmann, A.W., 1997. Mantle geochemistry: The message from oceanic volcanism. *Nature*, **385** (6613), 219-229.

Ishii, M. & Tromp, J., 1999. Normal-mode and free-air gravity constraints on lateral variations in velocity and density of Earth's mantle. *Science*, **285** (5431), 1231-1236.

Jellinek, A.M. & Manga, M., 2002. The influence of a chemical boundary layer on the fixity, spacing and lifetime of mantle plumes. *Nature*, **418** (6899), 760-763.

Ji, Y. & Nataf, H.C., 1998a. Detection of mantle plumes in the lower mantle by diffraction tomography: theory. *Earth Planet. Sci. Lett.*, **159** (3-4), 87-98.

Ji, Y. & Nataf, H.C., 1998b. Detection of mantle plumes in the lower mantle by diffraction tomography: Hawaii. *Earth Planet. Sci. Lett.*, **159** (3-4), 99-115.

Kellogg, L.H., Hager, B.H. & van der Hilst, R.D., 1999. Compositional stratification in the deep mantle. *Science*, **283** (5409), 1881-1884.

Knittle, E. & Jeanloz, R., 1991. Earths Core-Mantle Boundary - Results of experiments at high- pressures and temperatures. *Science*, **251** (5000), 1438-1443.

Kuo, B.Y., Garnero, E.J. & Lay, T., 2000. Tomographic inversion of S-SKS times for shear velocity heterogeneity in D": Degree 12 and hybrid models. *J. Geophys. Res.-Solid Earth*, **105** (B12), 28139-28157.

Li, X.D. & Romanowicz, B., 1996. Global mantle shear velocity model developed using nonlinear asymptotic coupling theory. *J. Geophys. Res.-Solid Earth*, **101** (B10), 22245-22272.

Lithgow-Bertelloni, C. & Richards, M.A., 1998. The dynamics of Cenozoic and Mesozoic plate motions. *Rev. Geophys.*, **36** (1), 27-78.

Loper, D.E. & Stacey, F.D., 1983. The dynamical and thermal structure of deep mantle plumes. *Phys. Earth Planet. Inter.*, **33** (4), 304-317.

Loper, D.E., 1991. Mantle Plumes. *Tectonophysics*, **187** (4), 373-384.

Manga, M. & Jeanloz, R., 1996. Implications of a metal-bearing chemical boundary layer in D" for mantle dynamics. *Geophys. Res. Lett.*, **23** (22), 3091-3094.

Masters, G., Laske, G., Bolton, H. & Dziewonski, A.M., 2000. The relative behavior of shear velocity, bulk sound speed, and compressional velocity in the mantle: implications for chemical and thermal structure, *Earth's Deep Interior: Mineral Physics and Tomography From the Atomic to the Global Scale*. American Geophysical Union, Washington DC, pp. 63-87.

Megnin, C. & Romanowicz, B., 2000. The three-dimensional shear velocity structure of the mantle from the inversion of body, surface and higher-mode waveforms. *Geophys. J. Int.*, **143** (3), 709-728.

Morgan, W.J., 1971. Convection plumes in the lower mantle. *Nature*, **230**, 42-43.

Morgan, W.J., 1972. Deep mantle convection plumes and plate motions. *American Association of Petroleum Geologists Bulletin,* **56** (2), 203-213.

Nataf, H.C. & Vandecar, J., 1993. Seismological detection of a mantle plume. *Nature*, **364** (6433), 115-120.

Nataf, H.C., 2000. Seismic imaging of mantle plumes. *Annu. Rev. Earth Planet. Sci.*, **28**, 391-417.

Ni, S.D., Ding, X.M., Helmberger, D.V. & Gurnis, M., 1999. Low-velocity structure beneath Africa from forward modeling. *Earth Planet. Sci. Lett.*, **170** (4), 497-507.

Ni, S.D. & Helmberger, D.V., 2001. Horizontal transition from fast to slow structures at the core- mantle boundary; South Atlantic. *Earth Planet. Sci. Lett.*, **187** (3-4), 301-310.

Niu, F.L. & Wen, L.X., 2001. Strong seismic scatterers near the core-mantle boundary west of Mexico. *Geophys. Res. Lett.*, **28** (18), 3557-3560.

Niu, F.L., Solomon, S.C., Silver, P.G., Suetsugu, D. & Inoue, H., 2002. Mantle transition-zone structure beneath the South Pacific Superswell and evidence for a mantle plume underlying the Society hotspot. *Earth Planet. Sci. Lett.*, **198** (3-4), 371-380.

Oganov, A.R., Brodholt, J.P. & Price, G.D., 2001. The elastic constants of MgSiO3 perovskite at pressures and temperatures of the Earth's mantle. *Nature*, **411** (6840), 934-937.

Ribe, N.M. & Devalpine, D.P., 1994. The global hotspot distribution and instability of D". *Geophys. Res. Lett.*, **21** (14), 1507-1510.

Ribe, N.M. & Christensen, U.R., 1994. 3-dimensional modeling of plume-lithosphere interaction. *J. Geophys. Res.-Solid Earth*, **99** (B1), 669-682.

Ritsema, J., van Heijst, H.J. & Woodhouse, J.H., 1999. Complex shear wave velocity structure imaged beneath Africa and Iceland. *Science*, **286** (5446), 1925-1928.

Ritsema, J. & van Heijst, H.-J., 2000. Seismic imaging of structural heterogeneity in Earth's mantle: evidence for large-scale mantle flow. *Science Progress*, **83**, 243-259.

Romanowicz, B. & Gung, Y.C., 2002. Superplumes from the core-mantle boundary to the lithosphere: Implications for heat flux. *Science*, **296** (5567), 513-516.

Saltzer, R.L., van der Hilst, R.D. & Karason, H., 2001. Comparing P and S wave heterogeneity in the mantle. *Geophys. Res. Lett.*, **28** (7), 1335-1338.

Seidler, E., Jacoby, W.R. & Cavsak, H., 1999. Hotspot distribution, gravity, mantle tomography: evidence for plumes. *J. Geodyn.*, **27** (4-5), 585-608.

Shen, Y., Solomon, C., Bjarnsson, I. Th., Nolet, G., Morgan, W.J., Allen, R.M., Vogfjörd, K., Jakobsdottir, R., Stefansson, R., Julian, B.R. & Foulger, G.R., 2002. Seismic evidence for a tilted mantle plume and north-south mantle flow beneath Iceland. *Earth Planet. Sci. Lett.*, **197** (3-4), 261-272.

Sleep, N.H., 1990. Hotspots and mantle plumes - Some phenomenology. *Journal of Geophysical Research-Solid Earth and Planets*, **95** (B5), 6715-6736.

Stacey, F.D., 1995. Theory of thermal and elastic properties of the lower mantle and core. *Phys. Earth Planet. Inter.*, **89** (3-4), 219-245.

Steinberger, B., 2000. Plumes in a convecting mantle: Models and observations for individual hotspots. *J. Geophys. Res.-Solid Earth*, **105** (B5), 11127-11152.

Su, W.J., Woodward, R.L. & Dziewonski, A.M., 1994. Degree-12 model of shear velocity heterogeneity in the mantle. *J. Geophys. Res.-Solid Earth*, **99** (B4), 6945-6980.

Sylvander, M. & Souriau, A., 1996. P-velocity structure of the core-mantle boundary region inferred from PKP(AB)-PKP(BC) differential travel times. *Geophys. Res. Lett.*, **23** (8), 853-856.

Tackley, P.J., 1998. Three-dimensional simulations of mantle convection with a thermochemical CMB boundary layer: D"? In: M. Gurnis, M.E. Wysession, E. Knittle and B.A. Buffet (Editors), *The Core-Mantle Boundary Region*. American Geophysical Union, Washington DC, pp. 231-253.

Tackley, P.J., 2000. Mantle convection and plate tectonics: Toward an integrated physical and chemical theory. *Science*, **288** (5473), 2002-2007.

Tan, E., Gurnis, M. & Han, L.J., 2002. Slabs in the lower mantle and their modulation of plume formation. *Geochemistry Geophysics Geosystems*, **3**, art. no.-1067.

van der Hilst, R.D., Widiyantoro, S. & Engdahl, E.R., 1997. Evidence for deep mantle circulation from global tomography. *Nature*, **386** (6625), 578-584.

van der Hilst, R.D. & Karason, H., 1999. Compositional heterogeneity in the bottom 1000 kilometers of Earth's mantle: Toward a hybrid convection model. *Science*, **283** (5409), 1885-1888.

Vogt, P.R., 1981. On the Applicability of Thermal Conduction Models to Mid-Plate Volcanism - Comments. *Journal of Geophysical Research*, **86** (B2), 950-960.

Wen, L.X. & Anderson, D.L., 1995. The Fate of Slabs Inferred from Seismic Tomography and 130 Million Years of Subduction. *Earth Planet. Sci. Lett.*, **133** (1-2), 185-198.

Wen, L.X. & Anderson, D.L., 1997. Slabs, hotspots, cratons and mantle convection revealed from residual seismic tomography in the upper mantle. *Phys. Earth Planet. Inter.*, **99** (1-2), 131-143.

Wen, L.X., 2000. Intense seismic scattering near the Earth's core-mantle boundary beneath the Comoros hotspot. *Geophys. Res. Lett.*, **27** (22), 3627-3630.

Williams, Q. & Garnero, E.J., 1996. Seismic evidence for partial melt at the base of Earth's mantle. *Science*, **273** (5281), 1528-1530.

Williams, Q., Revenaugh, J. & Garnero, E., 1998. A correlation between ultra-low basal velocities in the mantle and hot spots. *Science*, **281** (5376), 546-549.

Wolfe, C.J., Bjarnason, I.T., VanDecar, J.C. & Solomon, S.C., 1997. Seismic structure of the Iceland mantle plume. *Nature*, **385** (6613), 245-247.

Wysession, M.E., Okal, E.A. & Bina, C.R., 1992. The Structure of the core-mantle boundary from diffracted waves. *J. Geophys. Res.-Solid Earth*, **97** (B6), 8749-8764.

Wysession, M.E., Langenhorst, K., Fischer, M., Al-eqabi, G.I., Shore, P.J., Fouch, M.J., & Clarke, T.J., 1999. Mantle flow inferred from lateral variations in compressional/shear velocities at the base of the mantle. *Science*, **284** (5411), 120-125.

Zhao, D., 2001. Seismic structure and origin of hotspots and mantle plumes. *Earth Planet. Sci. Lett.*, **192** (3), 251-265.

Zhong, S. & Gurnis, M., 1997. Dynamic interaction between tectonic plates, subducting slabs, and the mantle. *Earth Interactions*, **1**.

TABLES

Table 2.1 *S*-wave velocity models analyzed in this study.

Model	Lateral Parameterization	Lateral Dimensions	Radial Parameterization	Reference
SAW12D	Spherical Harmonics	Up to deg 12 (~1800 km*)	Legendre Polynomials	(Li and Romanowicz, 1996)
S14L18	Equal Area Blocks	4 deg × 4 deg (~240 km*)	200 km thick deepest layer	(Masters et al., 2000)
Kuo12	Spherical Harmonics	Up to deg 12 (~1800 km*)	1 Layer 250 km thick	(Kuo et al., 2000)
S20RTS	Spherical Harmonics	Up to deg 20 (~1000 km*)	21 Vertical splines	(Ritsema and van Heijst, 2000)
S362C1	Spherical B Splines	Roughly deg 18 (~1200 km*)	14 Cubic B splines	(Gu et al., 2001)
TXBW	Equal Area Blocks	~2.5 deg × ~2.5 deg (~150 km*)	240 km thick deepest layer	(Grand, 2002)

* Approximate resolution at CMB

Table 2.2 Hot Spots used with Locations (after Steinberger 2000)

	Hot Spot	Latitude	Longitude		Hot Spot	Latitude	Longitude
1	Azores	38.5	-28.4	23	Kerguelen	-49.0	69.0
2	Balleny	-66.8	163.3	24	Lord Howe	-33.0	159.0
3	Bowie	53.0	-135.0	25	Louisville	-51.0	-138.0
4	Cameroon	4.2	9.2	26	Macdonald	-29.0	-140.2
5	Canary	28.0	-18.0	27	Marion	-46.9	37.8
6	Cape Verde	15.0	-24.0	28	Marquesas	-11.0	-138.0
7	Caroline	5.0	164.0	29	Meteor	-52.0	1.0
8	Cobb	46.0	-130.0	30	New England	28.0	-32.0
9	Comores	-11.8	43.3	31	Pitcairn	-25.0	-129.0
10	Darfur	13.0	24.0	32	Raton	37.0	-104.0
11	East Africa	6.0	34.0	33	Reunion	-21.2	55.7
12	East Australia	-38.0	143.0	34	St. Helena	-17.0	-10.0
13	Easter	-27.1	-109.3	35	Samoa	-15.0	-168.0
14	Eifel	50.0	7.0	36	San Felix	-26.0	-80.0
15	Fernando	-4.0	-32.0	37	Socorro	18.7	-111.0
16	Galapagos	-0.4	-91.5	38	Tahiti	-17.9	-148.1
17	Guadelupe	27.0	-113.0	39	Tasmanid	-39.0	156.0
18	Hawaii	19.4	-155.3	40	Tibesti	21.0	17.0
19	Hoggar	23.0	6.0	41	Trindade	-20.5	-28.8
20	Iceland	65.0	-19.0	42	Tristan	-38.0	-11.0
21	Jan Mayen	71.1	-8.2	43	Vema	-33.0	4.0
22	Juan Fernandez	-34.0	-82.0	44	Yellowstone	44.6	110.5

Table 2.3 *S*-wave Velocity Percent Coverage of CMB Surface Area Overlain by Each Hot Spot

	% CMB Coverage δVs							
Hot Spot	SAW12D	Kuo12	S362C1	TXBW	S20RTS	S14L18	Average	St Dev.
1 Azores	10.00	22.00	43.00	28.00	32.00	16.00	25.17	11.81
2 Balleny	29.00	71.00	59.00	70.00	64.00	55.00	58.00	15.49
3 Bowie	48.00	62.00	82.00	49.00	65.00	64.00	61.67	12.47
4 Cameroon	26.00	20.00	15.00	3.00	3.00	18.00	14.17	9.37
5 Canary	14.00	3.00	13.00	3.00	4.00	3.00	6.67	5.32
6 Cape Verde	16.00	7.00	10.00	3.00	8.00	11.00	9.17	4.36
7 Caroline	5.00	10.00	11.00	3.00	1.00	1.00	5.17	4.40
8 Cobb	47.00	19.00	43.00	48.00	77.00	47.00	46.83	18.44
9 Comores	44.00	28.00	40.00	23.00	26.00	22.00	30.50	9.25
10 Darfur	18.00	20.00	12.00	5.00	10.00	24.00	14.83	7.05
11 East Africa	4.00	45.00	18.00	8.00	15.00	28.00	19.67	14.95
12 East Australia	34.00	31.00	58.00	59.00	43.00	69.00	49.00	15.27
13 Easter	17.00	5.00	18.00	14.00	15.00	9.00	13.00	5.02
14 Eifel	66.00	27.00	83.00	34.00	31.00	39.00	46.67	22.56
15 Fernando	16.00	41.00	20.00	35.00	25.00	33.00	28.33	9.58
16 Galapagos	9.00	29.00	26.00	26.00	47.00	26.00	27.17	12.09
17 Guadelupe	14.00	10.00	35.00	48.00	42.00	49.00	33.00	17.06
18 Hawaii	15.00	38.00	7.00	17.00	13.00	10.00	16.67	11.04
19 Hoggar	24.00	15.00	33.00	11.00	14.00	28.00	20.83	8.80
20 Iceland	5.00	24.00	31.00	26.00	22.00	29.00	22.83	9.33
21 Jan Mayen	14.00	29.00	33.00	28.00	30.00	33.00	27.83	7.08
22 Juan Fernandez	58.00	13.00	35.00	40.00	56.00	28.00	38.33	17.10
23 Kerguelen	13.00	7.00	2.00	2.00	6.00	19.00	8.17	6.68
24 Lord Howe	5.00	19.00	24.00	24.00	36.00	37.00	24.17	11.82
25 Louisville	54.00	35.00	17.00	28.00	18.00	22.00	29.00	13.97
26 Macdonald	66.00	41.00	56.00	27.00	45.00	50.00	47.50	13.34
27 Marion	13.00	14.00	23.00	14.00	16.00	17.00	16.17	3.66
28 Marquesas	10.00	10.00	6.00	4.00	4.00	7.00	6.83	2.71
29 Meteor	22.00	17.00	15.00	5.00	23.00	19.00	16.83	6.52
30 New England	39.00	28.00	28.00	15.00	19.00	14.00	23.83	9.62
31 Pitcairn	7.00	6.00	18.00	5.00	5.00	7.00	8.00	4.98
32 Raton	65.00	24.00	79.00	64.00	40.00	62.00	55.67	19.95
33 Reunion	16.00	19.00	24.00	7.00	16.00	21.00	17.17	5.85
34 St. Helena	5.00	1.00	4.00	2.00	1.00	2.00	2.50	1.64
35 Samoa	14.00	3.00	4.00	17.00	2.00	2.00	7.00	6.69
36 San Felix	65.00	22.00	33.00	58.00	46.00	32.00	42.67	16.61
37 Socorro	14.00	15.00	47.00	49.00	46.00	55.00	37.67	18.22
38 Tahiti	15.00	6.00	12.00	6.00	1.00	3.00	7.17	5.34
39 Tasmanid	14.00	27.00	48.00	45.00	48.00	81.00	43.83	22.76
40 Tibesti	24.00	28.00	26.00	17.00	18.00	22.00	22.50	4.37
41 Trindade	25.00	31.00	14.00	25.00	31.00	23.00	24.83	6.27
42 Tristan	7.00	7.00	10.00	4.00	16.00	13.00	9.50	4.42
43 Vema	35.00	4.00	4.00	1.00	2.00	2.00	8.00	13.28
44 Yellowstone	68.00	22.00	78.00	47.00	62.00	87.00	60.67	23.37

Table 2.4 Lateral Gradient Percent Coverage of CMB Surface Area Overlain by Each Hot Spot

		% CMB Coverage ∇ (δVs)							
	Hot Spot	SAW12D	Kuo12	S362C1	TXBW	S20RTS	S14L18	Average	St Dev.
1	Azores	4.00	44.00	24.00	6.00	13.00	10.00	16.83	15.05
2	Balleny	20.00	29.00	2.00	15.00	17.00	58.00	23.50	19.02
3	Bowie	56.00	2.00	48.00	29.00	38.00	18.00	31.83	19.86
4	Cameroon	18.00	13.00	8.00	1.00	2.00	7.00	8.17	6.49
5	Canary	13.00	7.00	20.00	4.00	3.00	7.00	9.00	6.42
6	Cape Verde	8.00	5.00	7.00	1.00	4.00	3.00	4.67	2.58
7	Caroline	64.00	41.00	47.00	38.00	2.00	8.00	33.33	23.80
8	Cobb	52.00	2.00	7.00	46.00	62.00	15.00	30.67	25.69
9	Comores	3.00	26.00	11.00	12.00	13.00	9.00	12.33	7.58
10	Darfur	17.00	3.00	8.00	3.00	2.00	22.00	9.17	8.42
11	East Africa	20.00	36.00	6.00	7.00	3.00	8.00	13.33	12.55
12	East Australia	1.00	54.00	63.00	6.00	18.00	31.00	28.83	25.37
13	Easter	12.00	12.00	35.00	9.00	4.00	5.00	12.83	11.37
14	Eifel	6.00	19.00	27.00	5.00	27.00	16.00	16.67	9.69
15	Fernando	3.00	36.00	18.00	19.00	5.00	26.00	17.83	12.51
16	Galapagos	2.00	17.00	1.00	2.00	1.00	1.00	4.00	6.39
17	Guadelupe	1.00	3.00	18.00	43.00	16.00	34.00	19.17	16.68
18	Hawaii	5.00	4.00	5.00	32.00	8.00	2.00	9.33	11.27
19	Hoggar	66.00	10.00	59.00	3.00	12.00	10.00	26.67	28.01
20	Iceland	14.00	2.00	36.00	23.00	9.00	28.00	18.67	12.64
21	Jan Mayen	12.00	2.00	31.00	3.00	8.00	22.00	13.00	11.42
22	Juan Fernandez	68.00	8.00	43.00	9.00	35.00	11.00	29.00	24.16
23	Kerguelen	41.00	13.00	2.00	6.00	6.00	75.00	23.83	28.78
24	Lord Howe	7.00	5.00	7.00	8.00	7.00	2.00	6.00	2.19
25	Louisville	61.00	47.00	2.00	6.00	8.00	34.00	26.33	24.61
26	Macdonald	1.00	61.00	57.00	2.00	66.00	7.00	32.33	31.96
27	Marion	5.00	6.00	3.00	2.00	3.00	54.00	12.17	20.55
28	Marquesas	2.00	53.00	13.00	9.00	21.00	17.00	19.17	17.83
29	Meteor	7.00	7.00	7.00	0.00	3.00	18.00	7.00	6.10
30	New England	4.00	9.00	5.00	1.00	2.00	2.00	3.83	2.93
31	Pitcairn	20.00	12.00	14.00	13.00	7.00	5.00	11.83	5.34
32	Raton	11.00	6.00	12.00	46.00	9.00	12.00	16.00	14.87
33	Reunion	1.00	18.00	1.00	1.00	2.00	20.00	7.17	9.20
34	St. Helena	38.00	2.00	35.00	7.00	5.00	11.00	16.33	15.92
35	Samoa	26.00	1.00	47.00	16.00	16.00	15.00	20.17	15.38
36	San Felix	57.00	3.00	47.00	25.00	16.00	5.00	25.50	22.23
37	Socorro	1.00	3.00	21.00	13.00	11.00	34.00	13.83	12.24
38	Tahiti	34.00	38.00	43.00	10.00	21.00	56.00	33.67	16.28
39	Tasmanid	6.00	11.00	40.00	6.00	52.00	10.00	20.83	19.96
40	Tibesti	52.00	5.00	15.00	28.00	4.00	29.00	22.17	18.15
41	Trindade	3.00	56.00	29.00	28.00	17.00	29.00	27.00	17.47
42	Tristan	14.00	16.00	7.00	5.00	12.00	25.00	13.17	7.14
43	Vema	26.00	17.00	34.00	3.00	27.00	18.00	20.83	10.76
44	Yellowstone	36.00	2.00	3.00	25.00	19.00	9.00	15.67	13.44

FIGURES

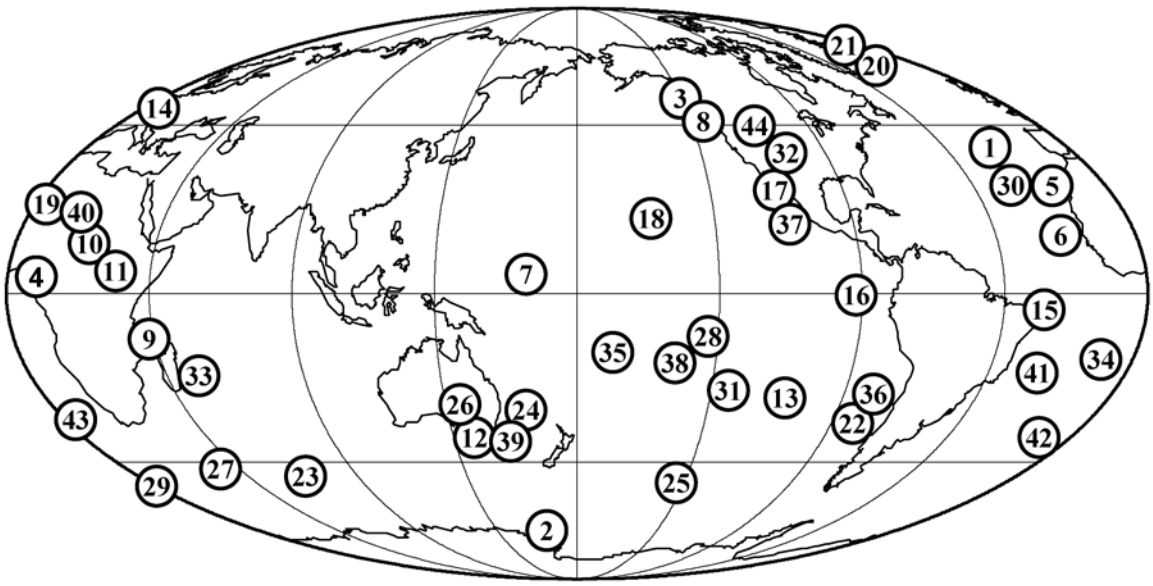

Figure 2.1 Locations of hot spots used in this study are plotted as closed circles. Numbers correspond to the number listed next to each hot spot in Tables 2.2, 2.3, and 2.4.

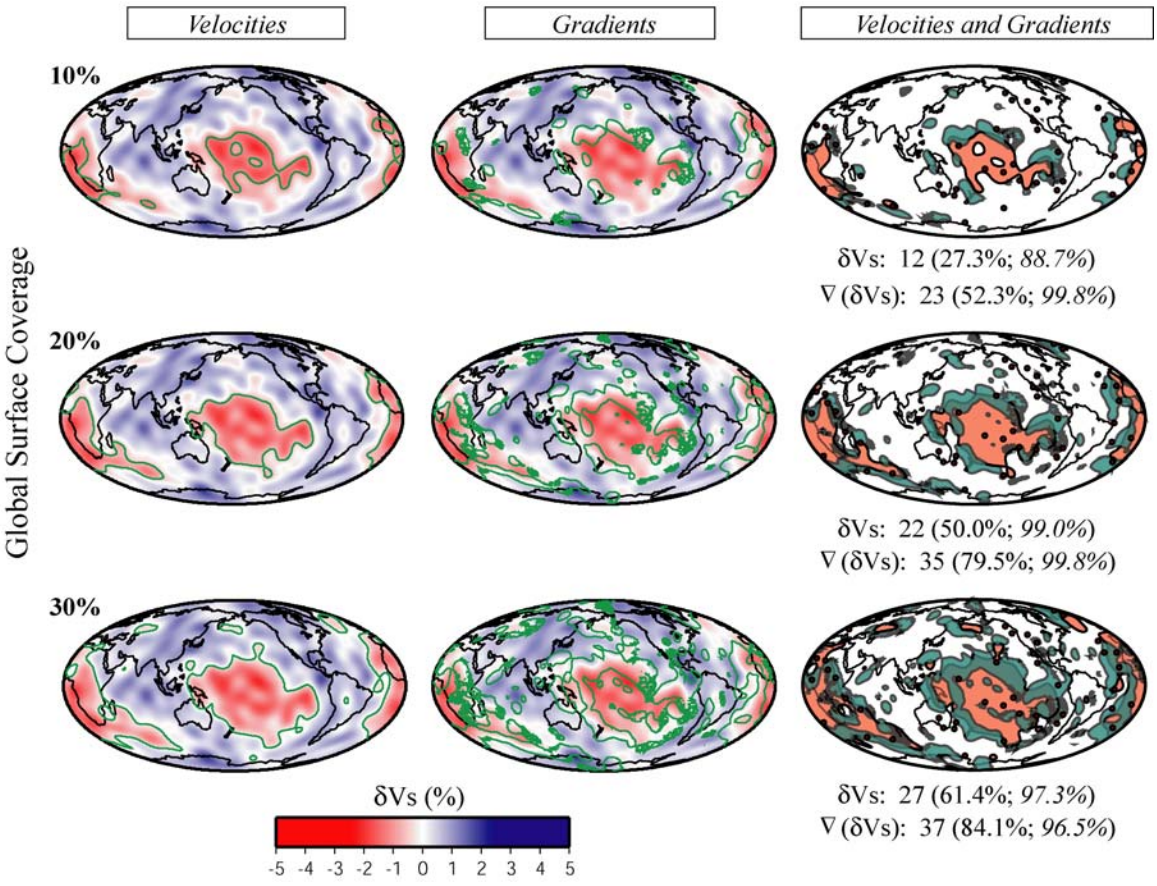
Velocities
Gradients
Velocities and Gradients
10%
20%
30%
Global Surface Coverage
δVs: 12 (27.3%; 88.7%)
∇(δVs): 23 (52.3%; 99.8%)
δVs: 22 (50.0%; 99.0%)
∇(δVs): 35 (79.5%; 99.8%)
δVs: 27 (61.4%; 97.3%)
∇(δVs): 37 (84.1%; 96.5%)
δVs (%)
-5 -4 -3 -2 -1 0 1 2 3 4 5

Figure 2.2 Hot spot counts are shown for model S20RTS. The first column shows contour lines (green) drawn around 10, 20, and 30% CMB surface area coverage for the most anomalous low velocities. The second column has contour lines drawn around 10, 20, and 30% CMB surface area coverage for lateral *S*-wave velocity gradients for a 1000 km arc length with five sample points. The third column shows the CMB percent surface area coverage, contoured in the first two columns, with lowest velocities filled in red and strongest gradients filled in green. The surface locations of hot spots are plotted as red circles. The numbers beneath each drawing show for both *S*-wave velocity and gradient, the hot spot count and, in parenthesis, the percentage of the total amount of hot spots and the percentage of randomly rotated hot spot locations having a weaker correlation within the CMB percent surface coverage contour. All numbers are obtained using a five-degree radius bin centered on the hot spot.

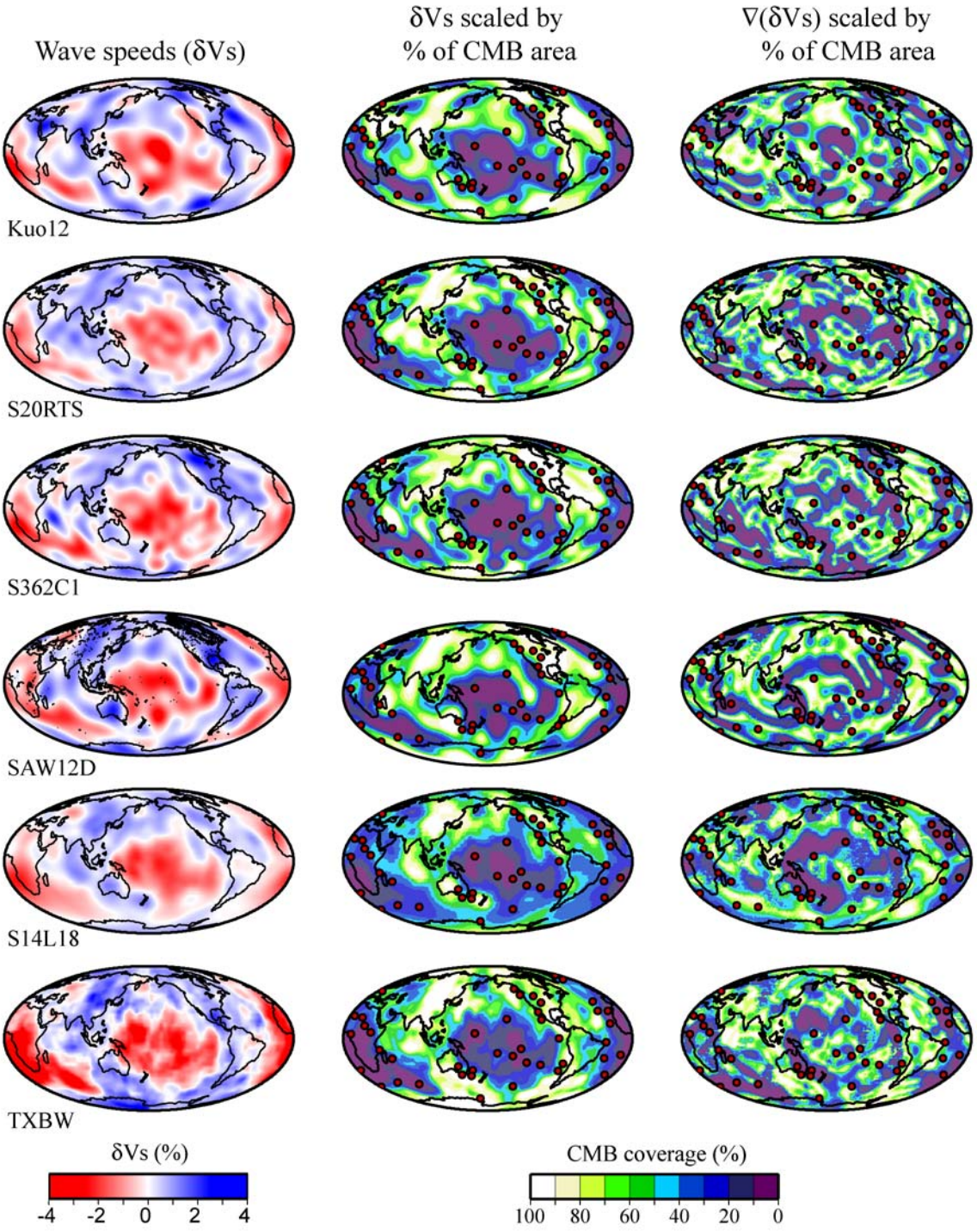
Wave speeds (δVs)
δVs scaled by
% of CMB area
∇(δVs) scaled by
% of CMB area
Kuo12
S20RTS
S362C1
SAW12D
S14L18
TXBW
δVs (%)
-4
-2
0
2
4
CMB coverage (%)
100
80
60
40
20
0

Figure 2.3 The first column displays the raw *S*-wave velocity perturbations of the six models analyzed. The second column shows the *S*-wave velocity models contoured by surface area coverage of the CMB, where the most anomalous low velocities are represented by the lowest percentages. The third column shows lateral *S*-wave velocity gradients contoured by surface area coverage of the CMB, where the strongest gradients are represented by the lowest percentages. Lateral velocity gradients shown here are calculated for a 1000 km length of arc with five sample points used in the least square approximation. Hot spot surface locations are plotted as red circles in the second and third columns. Models are as in Table 2.1.

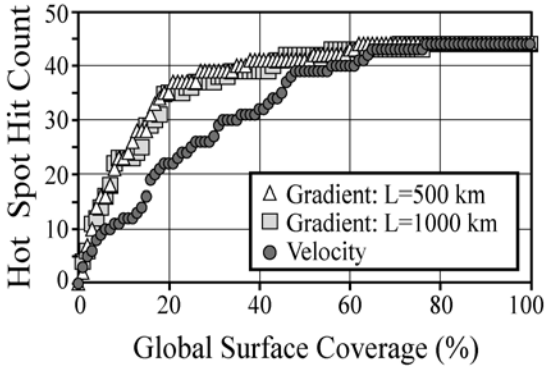

Figure 2.4 The number of hot spots falling within the percentage of CMB surface area coverage are shown for model S20RTS. The triangles show the number of hot spots for a lateral velocity gradient calculation with a 500 km arc length, while the squares show the number of hot spots for a gradient calculation with a 1000 km arc length. Both gradient calculations were done with five points used in the least square approximation. The circles show the number of hot spots within the percentage of CMB surface area coverage for velocity.

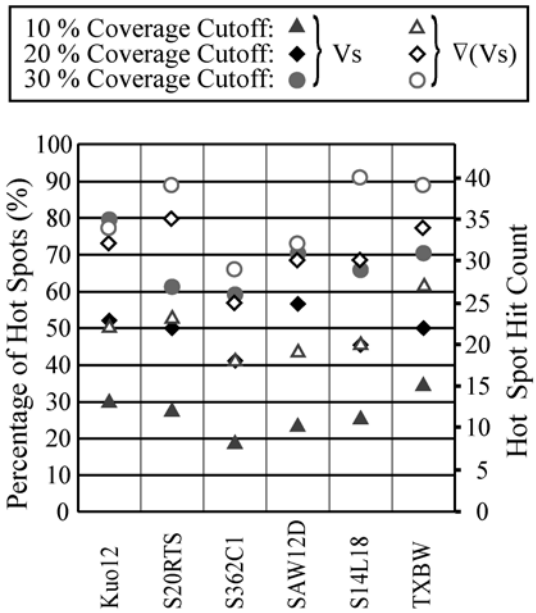

Figure 2.5 The number of hot spots (hot spot hit count and percentage of total amount of hot spots) that fall within 10, 20, and 30 % CMB surface area coverage for all six *S*-wave velocity models. The solid-fill and open-fill symbols show the number of hot spots falling inside the CMB percent surface area coverage for velocity and lateral *S*-wave velocity gradient respectively. Hot spot hit counts are shown using a five-degree radius bin centered on the hot spot. Gradient calculations were done using a 500 km arc length.

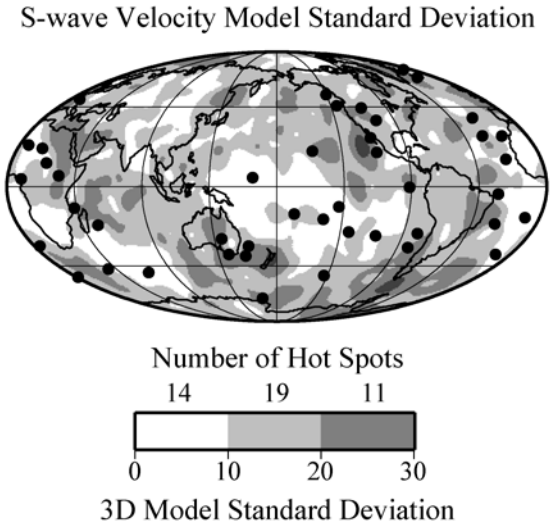

Figure 2.6 The standard deviation of the six *S*-wave models analyzed is shown, where the magnitude of *S*-wave velocities are scaled by CMB surface area coverage. The number of hot spots overlying the ranges of standard deviation 0-10%, 10-20%, and 20-30% is indicated above the scale-bar. All standard deviation values greater than 30% (corresponding to < 1% CMB surface area coverage) are shaded the darkest. Hot spots are drawn as black circles.

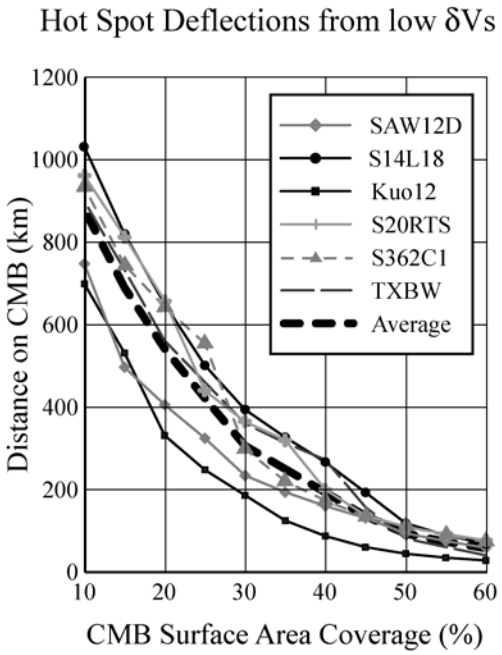
Hot Spot Deflections from low δVs
Distance on CMB (km)
CMB Surface Area Coverage (%)
SAW12D
S14L18
Kuo12
S20RTS
S362C1
TXBW
Average
0
200
400
600
800
1000
1200
10
20
30
40
50
60

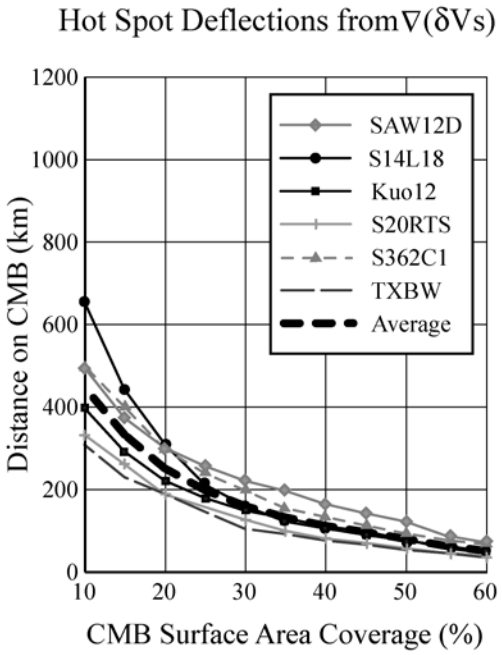
Hot Spot Deflections from∇(δVs)
Distance on CMB (km)
CMB Surface Area Coverage (%)
SAW12D
S14L18
Kuo12
S20RTS
S362C1
TXBW
Average
0
200
400
600
800
1000
1200
10
20
30
40
50
60

Figure 2.7 The top panel shows, for each of the six tomographic models analyzed, the average distance on the CMB for all hot spots to the specified percentage of CMB surface area coverage for low *S*-wave velocities. The bottom panel shows the average distance on the CMB for all hot spots to the specified percentage of CMB surface area coverage from strong lateral *S*-wave velocity gradients.

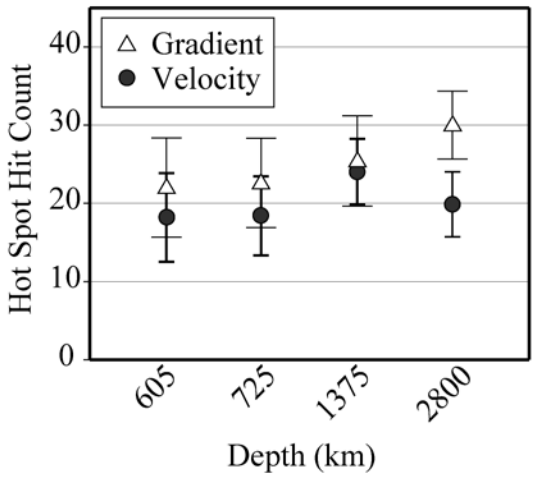

Figure 2.8 Average hot spot hit counts for four zones in the mantle are shown. The black circles and white triangles respectively show the number of hot spots that overlie the most anomalous low *S*-wave velocities and strongest lateral *S*-wave velocity gradients that cover 20% of the surface area of the indicated zone. The hit counts were averaged over all models analyzed, with the exception of the D" model Kuo12 that is only used in the deepest zone. The bars represent the standard deviation of the hot spot hit counts in each zone.

SUPPLEMENTAL FIGURES

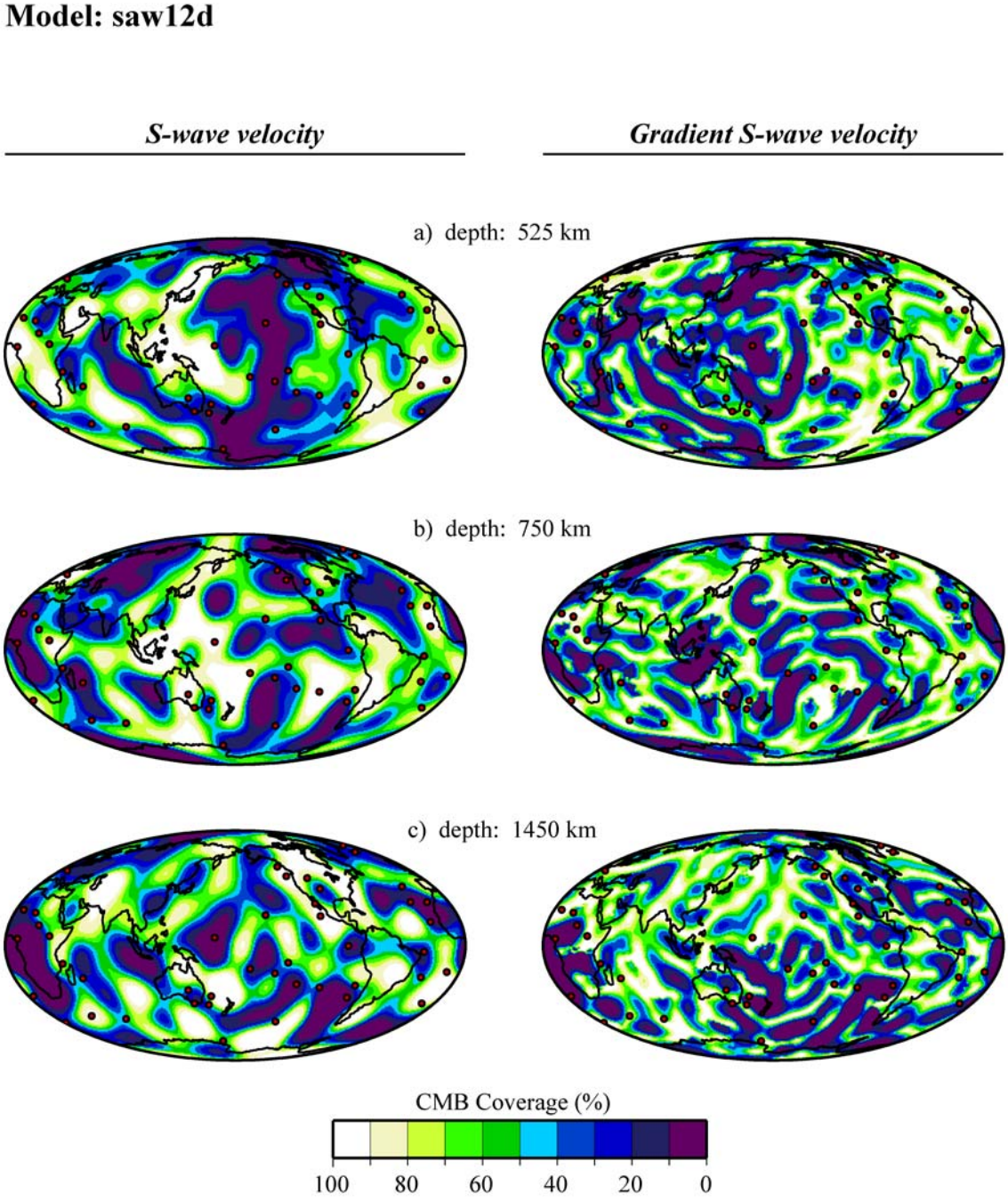

Supplement 2A The first column shows the *S*-wave velocity model saw12d contoured by surface area coverage of the CMB, where the most anomalous low velocities are represented by the lowest percentages. The second column shows lateral *S*-wave velocity gradients contoured by surface area coverage of the CMB, where the strongest gradients are represented by the lowest percentages. Lateral velocity gradients shown here are calculated for a 1000 km length of arc with five sample points used in the least square approximation. Hot spot surface locations are plotted as red circles in the second and third columns. Three depth slices are shown corresponding to depths in the transition zone, slightly deeper than the transition zone, and the mid-lower mantle. Models are as in Table 2.1.

Model: s14l18

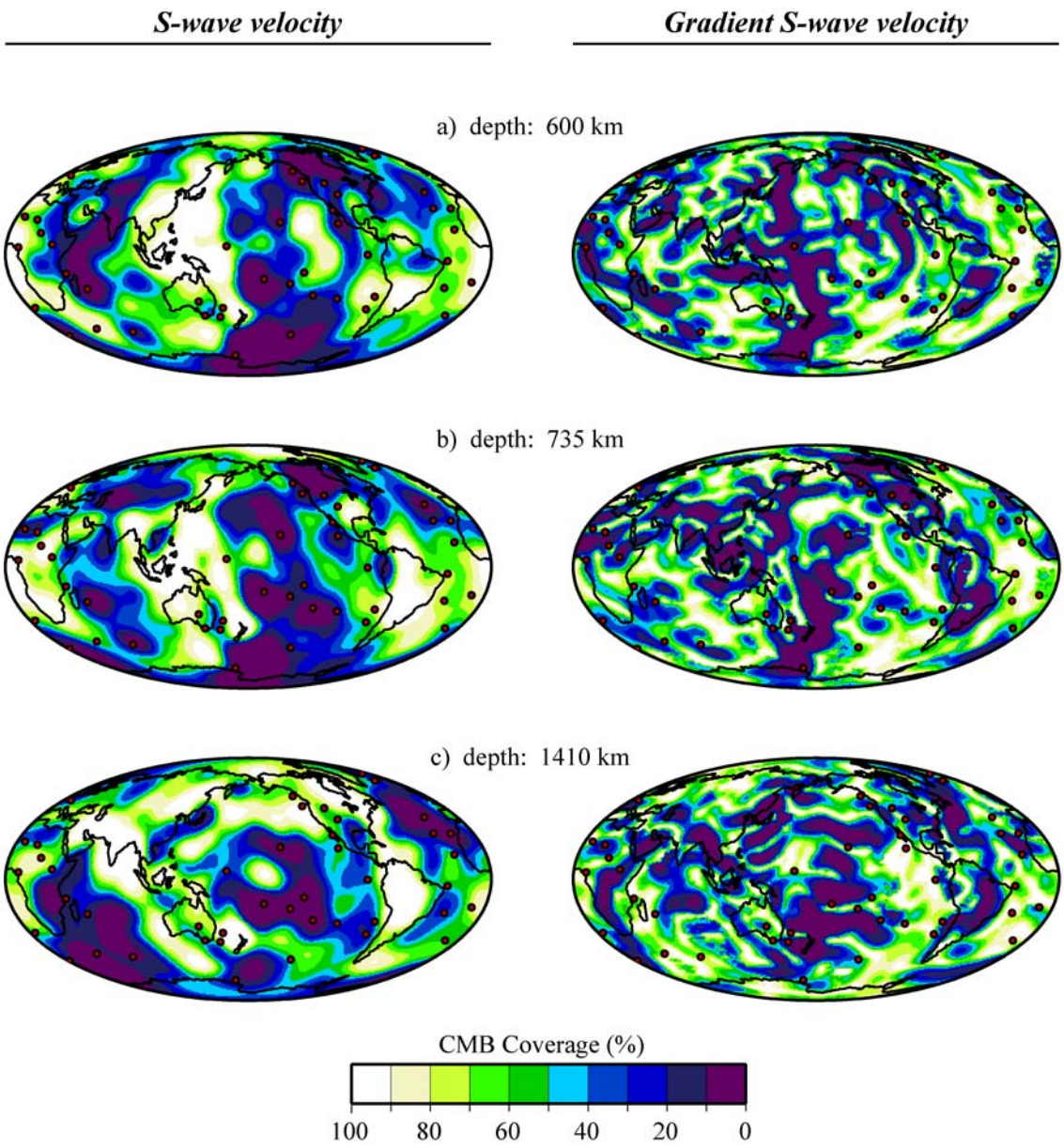

Supplement 2B The first column shows the *S*-wave velocity model s14l18 contoured by surface area coverage of the CMB, where the most anomalous low velocities are represented by the lowest percentages. The second column shows lateral *S*-wave velocity gradients contoured by surface area coverage of the CMB, where the strongest gradients are represented by the lowest percentages. Lateral velocity gradients shown here are calculated for a 1000 km length of arc with five sample points used in the least square approximation. Hot spot surface locations are plotted as red circles in the second and third columns. Three depth slices are shown corresponding to depths in the transition zone, slightly deeper than the transition zone, and the mid-lower mantle. Models are as in Table 2.1.

Model: s20rts

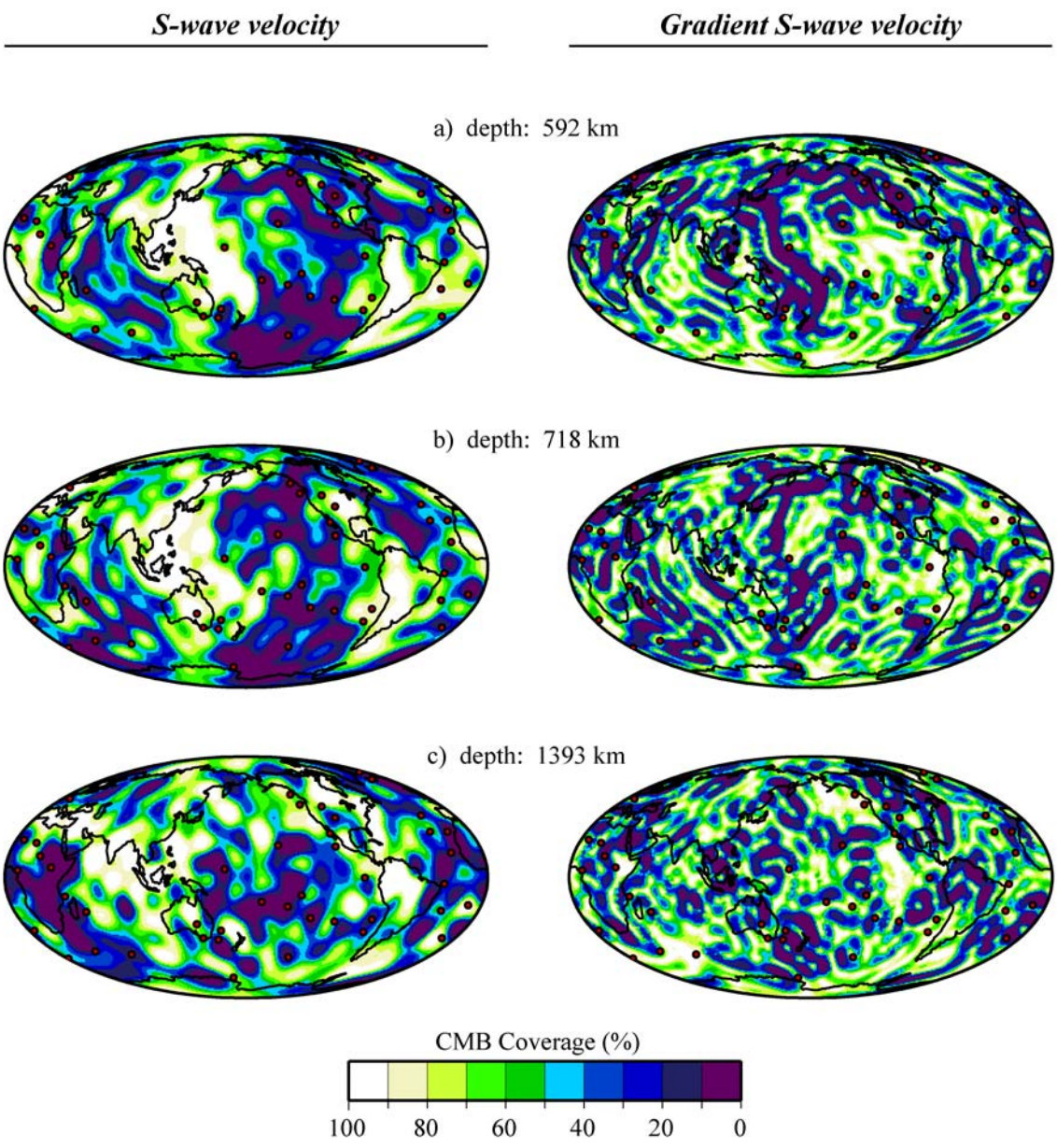

Supplement 2C The first column shows the *S*-wave velocity model s20rts contoured by surface area coverage of the CMB, where the most anomalous low velocities are represented by the lowest percentages. The second column shows lateral *S*-wave velocity gradients contoured by surface area coverage of the CMB, where the strongest gradients are represented by the lowest percentages. Lateral velocity gradients shown here are calculated for a 1000 km length of arc with five sample points used in the least square approximation. Hot spot surface locations are plotted as red circles in the second and third columns. Three depth slices are shown corresponding to depths in the transition zone, slightly deeper than the transition zone, and the mid-lower mantle. Models are as in Table 2.1.

Model: s362c1

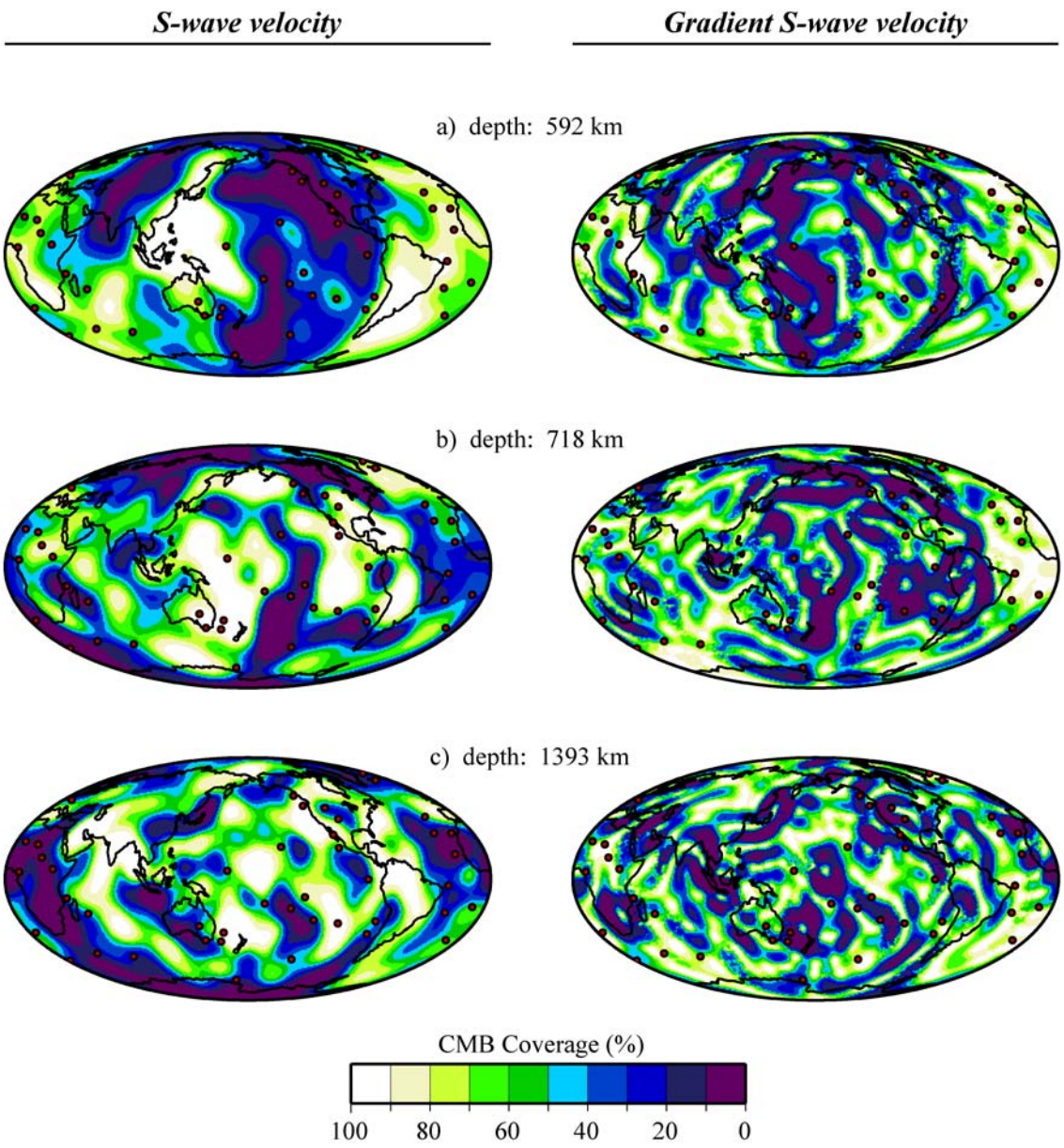

Supplement 2D The first column shows the *S*-wave velocity model s362c1 contoured by surface area coverage of the CMB, where the most anomalous low velocities are represented by the lowest percentages. The second column shows lateral *S*-wave velocity gradients contoured by surface area coverage of the CMB, where the strongest gradients are represented by the lowest percentages. Lateral velocity gradients shown here are calculated for a 1000 km length of arc with five sample points used in the least square approximation. Hot spot surface locations are plotted as red circles in the second and third columns. Three depth slices are shown corresponding to depths in the transition zone, slightly deeper than the transition zone, and the mid-lower mantle. Models are as in Table 2.1.

Model: TXBW

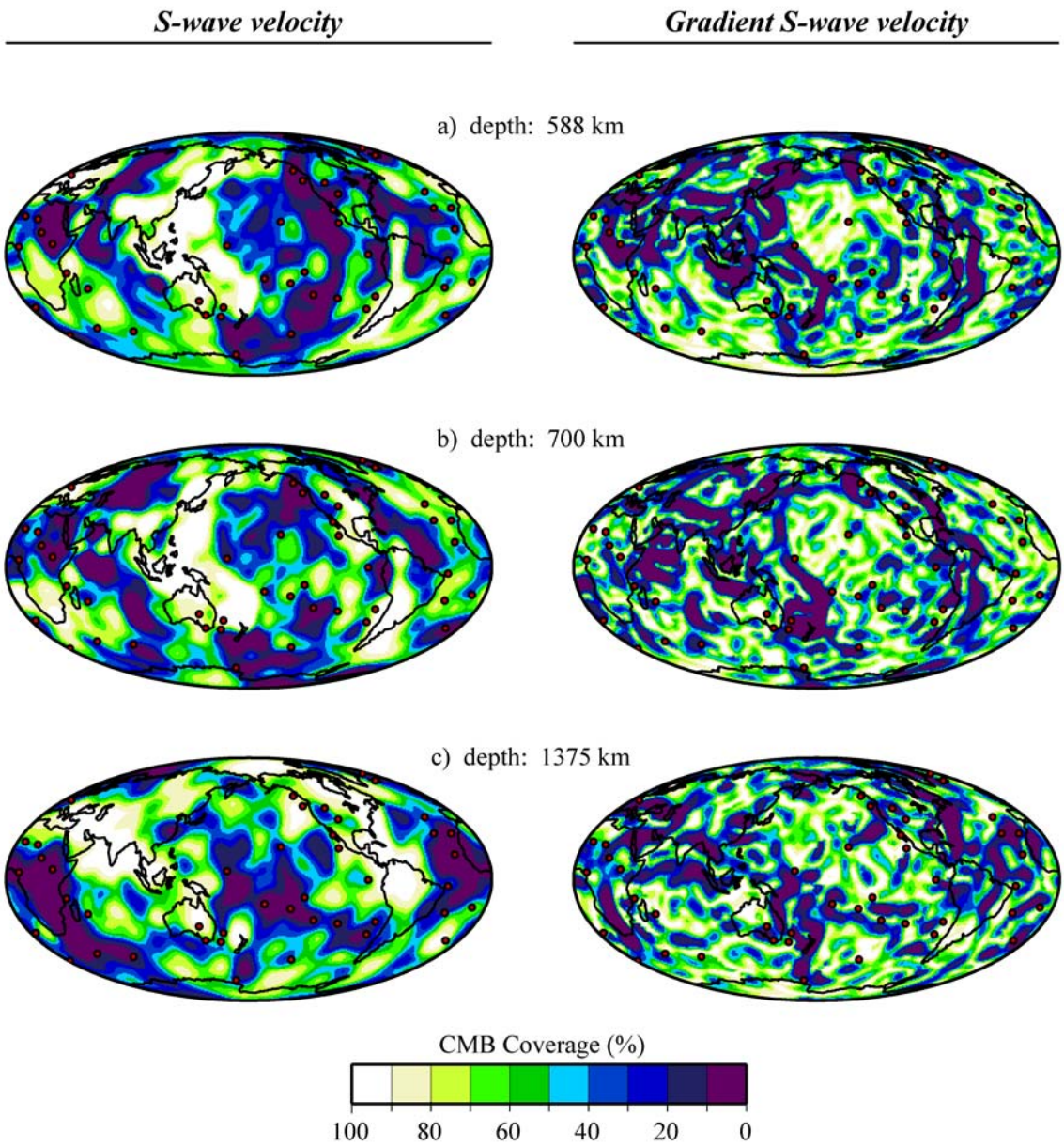
S-wave velocity
Gradient S-wave velocity
a) depth: 588 km
b) depth: 700 km
c) depth: 1375 km
CMB Coverage (%)
100
80
60
40
20
0

Supplement 2E The first column shows the *S*-wave velocity model TXBW contoured by surface area coverage of the CMB, where the most anomalous low velocities are represented by the lowest percentages. The second column shows lateral *S*-wave velocity gradients contoured by surface area coverage of the CMB, where the strongest gradients are represented by the lowest percentages. Lateral velocity gradients shown here are calculated for a 1000 km length of arc with five sample points used in the least square approximation. Hot spot surface locations are plotted as red circles in the second and third columns. Three depth slices are shown corresponding to depths in the transition zone, slightly deeper than the transition zone, and the mid-lower mantle. Models are as in Table 2.1.

CHAPTER 3

INFERENCES ON ULTRA-LOW VELOCITY ZONE STRUCTURE FROM A GLOBAL ANALYSIS OF SPdKS WAVES

Michael S. Thorne[1] and Edward J. Garnero[1]

[1]*Dept. of Geological Sciences, Arizona State University, Tempe, AZ 85287, USA*

SUMMARY

Anomalous boundary layer structure at the core-mantle boundary (CMB) is investigated using a global set of broadband *SKS* and *SPdKS* waves from permanent and portable broadband seismometer arrays. *SPdKS* is an *SKS* wave that intersects the CMB at the critical angle for *ScP*, thus initiating a diffracted *P*-wave (P_{diff}) along the CMB at the core entry and exit locations. The wave shape and timing of *SPdKS* data are analyzed relative to *SKS*, with some *SPdKS* data showing significant delays and broadening. Broadband data from several hundred deep focus earthquakes were analyzed; retaining data with simple sources and high signal-to-noise ratios resulted in 53 high quality earthquakes. For each earthquake, an empirical source was constructed by stacking pre-*SPdKS* distance range *SKS* pulses (~90° – 100°). These were utilized in our synthetic modeling process, whereby reflectivity synthetic seismograms are produced for three classes of models: (1) mantle-side ultra-low velocity zones (UVLZ), (2) underside-CMB core rigidity zones (CRZ), and (3) core mantle transition zones (CMTZ). For ULVZ structures, ratios of *P*-to-*S* velocity reductions of 1:1 and 1:3 are explored, where 1:3 is appropriate for a partial melt origin of ULVZ. Over 330 unique CMB boundary layer models have been constructed and tested, corroborating previous work suggesting strong trade-offs between the three model spaces. We produce maps of inferred boundary layer

structure from the global data, and find evidence for extremely fine-scale heterogeneity where our wave path sampling is the densest. While uncertainties are present relating to the source- versus receiver-sides of the *SPdKS* wave path geometry, our data are consistent with the hypothesis that ULVZ presence (or absence) correlates with reduced (or average) heterogeneity in the overlying mantle.

3.1 Introduction

Evidence for strong *P*- and *S*- wave velocity reductions at the core-mantle boundary (CMB) has been reported for over two decades. Here we briefly summarize these past efforts, from early CMB heterogeneity and tomography studies to more recent work specifically aimed at characterization of ultra-low velocity zone (ULVZ) structure, then discuss the geographic distribution and possible origin of ULVZs presented in past work. This provides the basis for the work we report in this paper.

3.1.1 Early indirect evidence for ULVZ: CMB topography studies

The first studies reporting strong velocity reductions as well as lateral variations at the CMB were aimed at resolving CMB topography. For example, models of CMB topography derived from the inversion of core phases that cross or reflect off of the CMB (e.g., *PKP*, *PcP*) map CMB undulations of up to ± 10 km (e.g., Creager & Jordan 1986; Morelli & Dziewonski 1987). Additionally, travel time variations of core-reflected *PcP* waves referenced to *PKP* have suggested CMB topography as large as ± 15 km (e.g., Rodgers & Wahr 1993). Consensus on the exact distribution or patterns of CMB

topography, as well as peak-to-peak topography amplitude, is lacking at present (e.g., Rodgers & Wahr 1993; Garcia & Souriau 2000), and subsequent identification of thin zones of ultra-low velocities further complicate efforts to constrain CMB topography, due to the strong trade-off between volumetric heterogeneity and CMB topography. Peak-to-peak amplitudes of CMB topography inferred from seismic studies (up to ±15 km) are considerably larger than those from dynamical considerations (roughly ±0.5-3 km; e.g., see Hager *et al.* 1985; Bowin 1986; Hide *et al.* 1993). This discrepancy may in fact be due to a mismapping of ULVZ signal. We note that the likely existence of CMB topography does not strongly contaminate ULVZ studies.

Volumetric heterogeneity in the D" region may help reconcile discrepancies in mapped CMB peak-to-peak amplitudes. By observing the amplitude decay of long-period *Pdiff* and *Sdiff* and short-period *Pdiff*, Doornbos, (1983) concluded that the CMB might have significant lateral variations within a relatively thin (<100 km) low velocity boundary layer. Subsequently, Doornbos and Hilton, (1989) inverted *PcP*, *PKP*, and *PnKP* for CMB topography to support relatively reduced CMB topography (± 4 km), and argued that lateral variations in travel time residuals of *PcP* and *PKP* can be best modeled by a laterally varying lowermost mantle boundary layer (in the form of variable layer thickness, velocity fluctuations, or some combination of the two), with average layer thickness of ~20 km, and *P*-wave velocity heterogeneity perturbations up to ±7.3%. While the thickness of their solution layer is not well constrained because there is a direct trade-off with velocity heterogeneity in the layer, the inference for thin zones of strong reductions was made. A recent demonstration of this trade-off arose in a joint inversion

for peak-to-peak topography and D" heterogeneity using the seismic phases *PcP*, *PKP*, and *PKKP*: Sze & van der Hilst (2003) found that ±13 km CMB undulations are necessary if no D" velocity variations are invoked. This reduces to CMB topography amplitude of ± 3 km if ± 5% D" variations (lowermost 290 km) in *P*-wave velocities are considered. Further evidence for this trade-off was reported by Garcia & Souriau (2000); they present evidence for peak-to-peak topography from 1.5-4.0 km with lateral scales of 300-1500 km. These recent models are in greater agreement with dynamical models in terms of peak-to-peak topography values. We note that shorter scale CMB topography or roughness may be superimposed on this longer wavelength CMB topography (Earle & Shearer 1997; Shearer *et al.* 1998; Garcia & Souriau 2000).

A multitude of studies over the last 15-20 years have put forth evidence for strong deep mantle heterogeneity. These efforts may have similarly mapped ULVZ signal into larger scale D" heterogeneity. This may be especially relevant for lower mantle structure from tomographic studies. Currently, the highest resolution modeling efforts have presented heterogeneity at lateral and vertical scales on the order of 500+ km (e.g., Masters *et al.* 2000; Megnin & Romanowicz 2000; Grand 2002). Small scale ULVZ structure likely maps into these velocity predictions, though to what extent is extremely difficult to assess, because it is quite likely that strong D" heterogeneity exists in addition to ULVZ structure (see, for example, review by Garnero 2000).

3.1.2 Recent probes of ULVZ structure

Recent efforts have been aimed at looking directly for ULVZ structure. A summary of these studies is provided in Table 3.1. The probes used can be organized as follows: precursors to the core-reflected phases *PcP* and *ScP*, scattering from the core wave *PKP*, and travel time and/or waveform anomalies of a variety of mantle and core waves, including *ScS*, *SPdKS*, *PcP*, and *PKP*.

Analysis of precursors to the core-reflected phases *PcP* and *ScP* has proven extremely valuable in mapping detailed structure of boundary layer structure at the CMB. These studies have predominantly utilized short-period array data, revealing a wide variety of observations from a simple CMB with no evident precursors (Vidale & Benz 1992; Castle & van der Hilst 2000), to highly anomalous zones characterized as ULVZ or thin core-side layering with finite rigidity (a "core-rigidity zone", or CRZ) with small-scale lateral variations on the order of 10's of kilometers (e.g., Garnero & Vidale 1999; Rost & Revenaugh 2001; Rost & Revenaugh 2003). These studies also highlight apparent contradictions in some geographic locales where evidence for and against anomalous boundary layer structure have been put forth. For example, using short-period *PcP* stacks, Mori & Helmberger (1995) and Revenaugh & Meyer (1997) both observed precursors in the Central Pacific that indicated the presence of a ULVZ. However, these two studies disagree as to whether a ULVZ exists in a location in the East Pacific. The recent use of broadband data is helping to reconcile these contradictions, as well as better constrain the limits on sharpness of the structural features responsible for precursors (Havens & Revenaugh 2001; Rondenay & Fischer 2003).

Small scale scatterers in D" can give rise to *PKP* precursors, and have also been used to map anomalous ULVZ and CMB structure (e.g., Vidale & Hedlin 1998; Wen & Helmberger 1998b). *PKP* precursors attributed to ULVZ structure have been observed in short-period, long-period, and broadband data (see Table 3.1). The presence of short- and long-period *PKP* precursors in data from a given region can be attributed to variable scatterer scale lengths, from 10's of km up to 100-300 km (Wen & Helmberger 1998b). Additionally, migration techniques have been employed to locate scatterers with scale lengths of ~ 10-50 km (Thomas *et al.* 1999). The presence of large *S*-wave velocity reductions relative to *P*-wave reductions, as predicted by the partial melt origin of the ultra-low velocities (Williams & Garnero 1996; Berryman 2000), produces observable *SKS* precursors for ULVZ layer thickness greater than ~15 km (if velocity reductions are 10 and 30% for *P* and *S*, respectively). However, these have not yet been identified or documented (Stutzmann *et al.* 2000). Such precursors would go undetected if either (a) partial melt layering is thinner than 10-15 km, or (b) the *P* and *S* wave reductions are less than 10 and 30%, respectively, such as 5 and 15% or less.

In addition to studying precursors, a wide variety of studies have inferred ULVZ presence from differential travel time and waveform anomalies of *SPdKS* waves referenced to *SKS* (Table 3.1). One advantage in using *SPdKS* is greatly increased global sampling. However, inherent trade-offs exist in constraining ULVZ elastic parameters as well as geographic location, which are discussed in detail in this paper. Additionally, travel-time and waveform studies of *ScS* relative to *S* have proven significant in revealing

ULVZ structure in regions not sampled by *SPdKS* (Simmons & Grand 2002; Ni & Helmberger 2003b).

3.1.3 Geographic distribution of ULVZ

Most ULVZ studies have utilized the abundance of deep focus earthquakes from the Pacific rim, which has resulted in CMB structure beneath three areas being extensively studied: 1) the Southwest Pacific, 2) Central America, and 3) the Northeast Pacific. Figure 3.1 summarizes the results of previous studies under the Southwest Pacific and Central America regions. The Southwest Pacific region is dominated by a large low-velocity anomaly prominent in models of shear-wave tomography (e.g., see Masters *et al.* 2000), and may also contain the source of several hotspots (e.g., see Sleep 1990; Steinberger 2000; Montelli *et al.* 2004; Thorne *et al.* 2004). In contrast to this, the Central America region may be home to remnants of the subducted Farallon slab as indicated by relatively high shear-wave velocities (e.g., Grand *et al.* 1997). Evidence for a small-scale, high attenuation, low-velocity anomaly has also been put forth for the Caribbean region (Wysession *et al.* 2001; Fisher *et al.* 2003), as well as short scale lateral heterogeneity (Tkalčić & Romanowicz 2002). Additionally, the source of the Galapagos, Guadelupe, and Socorro hotspots may lie in the west of this region. Lightly shaded patches represent *SPdKS* Fresnel zones: pink denotes ULVZ detection; light blue indicates that no ULVZ was detected (Garnero *et al.* 1998). These zones predominantly characterize long wavelength structure. Shorter scale length ULVZ phenomena are provided from core reflected precursors or scattering studies: a high degree of variability

is observed, as can be seen in the southwest Pacific (symbols, lines, Figure 3.1a). For example, observations of *ScP* precursors that indicate anomalous boundary layer structure are co-located with normal *ScP* waveforms (Garnero & Vidale 1999; Reasoner & Revenaugh 2000; Rost & Revenaugh 2001; Rost & Revenaugh 2003). Disagreement between the long wavelength ULVZ map (Garnero *et al.* 1998) and the short-scale results shown in Figure 3.1 are due to (a) ULVZ heterogeneity existing at wavelengths shorter than *SPdKS* Fresnel zones, (b) uncertainties due to the source-receiver side ambiguity of the source of *SPdKS* anomalies (which we address later in this paper) and (c) possible sensitivity to different ULVZ structure features.

3.1.4 Origin of ULVZ anomalies

Several explanations have been proposed for the origin of ULVZ structure. These fall into the categories of (a) chemically unique material on the mantle-side of the CMB (e.g., Manga & Jeanloz 1996; Stutzmann *et al.* 2000), (b) partial melt of some component of the lowermost mantle right at/above the CMB (e.g., Williams & Garnero 1996; Revenaugh & Meyer 1997; Helmberger *et al.* 1998; Vidale & Hedlin 1998; Williams *et al.* 1998; Zerr *et al.* 1998; Berryman 2000; Wen 2000), (c) material with finite rigidity pooling at the underside of the CMB, for example, beneath CMB topographical highs (e.g., Buffett *et al.* 2000; Rost & Revenaugh 2001), (d) some form of blurring of the CMB, such as a transition between core and mantle material from some form of mixing or chemical reactions (Garnero & Jeanloz 2000a; Garnero & Jeanloz 2000b), and (e) any combination of the above (Rost & Revenaugh 2001). Increased resolution is necessary

for better characterization of boundary layer structure at the CMB. This is additionally important as it may relate to the source regions of whole mantle plumes responsible for hotspot volcanism (Williams *et al.* 1998), the frequency of magnetic field reversals (Glatzmaier *et al.* 1999), and nutation of Earth's rotation axis (Buffett *et al.* 2000). At a minimum, the patches or zones of ultra-low velocities are likely related to deep mantle dynamics and chemistry. To more accurately constrain elastic properties of boundary layer structure at the CMB, we improve CMB coverage in this paper as sampled by broadband *SPdKS* data, which we hope can contribute to future analyses using the various other probes (e.g., Table 3.1).

3.2 *SPdKS* Data

This study utilizes a global set of broadband *SPdKS* data. *SPdKS* is an *SKS* wave, where the down-going *S*-wave intersects the CMB at the critical angle for diffraction generating *P*-diffracted (*Pdiff*) segments propagating on the mantle-side of the CMB. The complementary phase *SKPdS* has the *Pdiff* leg occurring on the receiver side, where the up-going *P*-wave intersects the CMB at the critical angle. For the PREM model (Dziewonski & Anderson 1981), *SPdKS* initiates at ~104°, however, the bifurcation between *SKS* and *SPdKS* is not observable in broadband waveforms until ~110°. Ray path geometries are shown for four distances in the top row of Figure 3.2, with both *SPdKS* and *SKPdS* being displayed. As the source-receiver distance increases, the length of *Pdiff* segments on the CMB increases, which is the only alteration to *SPdKS*+*SKPdS* paths with distance. For example, for PREM, *Pdiff* segments are 420 and 1000 km, for

110° and 120° source-receiver distances respectively (see middle row of Figure 3.2). The distance between the core entry (exit) locations of *SKS* and *SPdKS* (*SKPdS*) at the CMB also increases with distance. For example, for PREM, the *SKS – SPdKS* separation increases from 60 to 210 km for a source-receiver distance increase of 110° to 120° (see middle row of Figure 3.2). Example synthetic seismograms (for PREM) for the four distances are shown in the bottom row in Figure 3.2. Data with source-receiver distances of 110°–115° are most useful as strong waveform distortions are observed, particularly near 110° where interference with *SKS* results in diagnostic waveform shapes. Source-receiver geometries with distances of near 120° (and greater) have broader *SPdKS* pulses due to long *Pdiff* segments. These are less useful for modeling detailed short-scale ULVZ structure, because CMB and D" structure is averaged over fairly large distances. If the mantle structure encountered on both the source and receiver side CMB crossing location is identical, *SPdKS* and *SKPdS* have coincident arrival times. However, differing source- and receiver-side mantle structure should affect the timing, amplitude, and wave shape of *SPdKS* and *SKPdS* (e.g., Rondenay & Fischer 2003). Yet, it is not generally possible to distinguish *SPdKS* from *SKPdS* in observed waveforms. We note one recent array analysis using the phase stripping method of eigenimage decomposition has been able to separately identify the source and receiver contributions to the combined wave fields (Rondenay & Fischer 2003). For convenience, the combined *SPdKS* plus *SKPdS* energy is referred to as *SPdKS* throughout this paper.

Figure 3.2 also shows the phase *SKiKS*, which is an *SKS* wave that reflects off the inner core boundary (ray path geometry shown in the top row of Figure 3.2). The bottom

row of Figure 3.2 shows the *SKiKS* arrival at four distances. Most notably, for the PREM model, *SKiKS* arrives coincident with *SPdKS* at a distance of ~120° and may interfere with the *SPdKS* arrival.

Data used in this study were collected from the publicly available Incorporated Research Institutions for Seismology Data Management Center (IRIS DMC). Initially, we conducted a global search for earthquakes using IRIS's Fast Archive Recovery Method (FARM) catalog. We searched for earthquakes with depths greater than 100 km, and moment magnitudes (Mw) greater than 6.0, for events occurring between the years 1990 and 2000. This resulted in a collection of 321 events. To further augment our data set we also obtained broadband data for several earthquakes from the Observatories and Research Facilities for European Seismology (ORFEUS) Data Center (ODC), the Canadian National Seismic Network (CNSN), and PASSCAL data available from the IRIS DMC.

All data were instrument-deconvolved to displacement using the Seismic Analysis Code (SAC) (Goldstein *et al.* 1999) transfer function, and the pole-zero response files obtained from the IRIS DMC, with a band pass window from 0.01 to 1.0 Hz. Resultant displacement files were then rotated to great circle path radial and transverse components and resampled to a 0.1 sec time interval. We retained radial component seismograms, for analysis of *SPdKS* relative to *SKS*.

All data were visually inspected to determine data quality; initial criteria leading to data rejection were: 1) no stations in the epicentral distance range of 90º to 125º, or 2) it was not possible to clearly distinguish the seismic phase *SKS* above the background

noise level. Using these criteria, the number of events reduced from 321 to 53. In total, records were examined for 182 unique stations in the distance range 105º to 125º, resulting in 443 unique records used in this study. Table 3.2 displays the resulting 53 events used in this study. The most notable CMB sampling is beneath the southwest Pacific, the Americas, eastern Eurasia, northern Africa and Europe, and the southern Indian Ocean.

A distance profile for each event was visually inspected for possible anomalous source structure effects, where events with exceedingly complex sources were discarded. Profiles for four events used in this study are displayed in Figure 3.3. All traces are normalized in time and amplitude to the *SKS* peak (solid line at zero seconds). The dashed and dotted lines show predicted arrivals for *SPdKS* and *SKiKS*, respectively, using the PREM model. Clean and impulsive *SKS* can be observed in these profiles for records from 100º to 110º, with the exception of the highly anomalous records in panel (d) at stations CCM, FFC, TIXI, and WMQ (Cathedral Caves, Missouri, USA; Flin Flon, Canada; Tiksi, Russia; Urumqi, Xinjiang, China). These anomalous records may be attributable to CMB structure, as the anomalous waveform behavior is not observed in other traces for the same event, as long as site effects can also be ruled out. Beyond 110º, the separation of *SPdKS* from *SKS* becomes apparent. *SPdKS* often arrives as predicted by PREM, however, several delayed *SPdKS* arrivals are also observed. Additionally, Figure 3.3 displays several smaller peaks having arrivals coincident with the PREM prediction for *SKiKS*, which is highly suggestive of *SKiKS* interference (or contamination) with the *SKS* and *SPdKS* arrivals.

To determine if site effects are contributing to anomalous waveforms, *SPdKS* behavior at individual stations has been studied. Figure 3.4 shows distance profiles for four broadband stations. Three extremely anomalous records are seen for station CCM around 107º (Figure 3.4a). These anomalous traces show *SPdKS* (right-shoulder) with higher amplitudes than *SKS* (left-shoulder), which is not predicted by the PREM model. Because other traces at CCM do not show two distinct shoulders, site effects are ruled out; also, these anomalous effects are not seen for these 3 events at other stations (not shown), ruling out source mechanism effects.

SKS and *SPdKS* are extremely close throughout the mantle, except where the *Pdiff* segments occur in *SPdKS*; therefore the source of the anomalous waveforms is attributed to structure at the CMB, once source mechanism and site effects are ruled out (as discussed above). Similarly, highly anomalous records can be seen in Figure 3.4b near 112º for station WMQ; again, site effects can be ruled out. One of the anomalous WMQ records is observed in Figure 3.3d, where several records display anomalous waveforms. However, most records for that event have an impulsive *SKS* peak, suggesting that the anomaly observed at WMQ is likely attributable to CMB structure and not source mechanism effects. The additional anomalous records seen in Figure 3.3d (CCM, FFC, SUR) also suggest anomalous CMB structure, somewhere along the *Pdiff* paths.

3.3 Synthetic seismograms

A large bank of CMB boundary layer models (ULVZ, CRZ, CMTZ) were constructed for computation of synthetic seismograms to compare to our data, using the

1-D reflectivity method (Fuchs & Müller 1971; Müller 1985). Helmberger *et al.* (1996) found that the properties of 1-D synthetics were similar to those of 2-D synthetics. The main drawback in the 1-D approach is that boundary layer modeling cannot address structure confined to one side of the *SPdKS* path (i.e., the core entry versus exit location where *Pdiff* occurs). Furthermore, using the 1-D approach, we cannot take into account focusing/defocusing effects of ULVZ or CMB topography, or volumetric heterogeneity, as can be modeled in 2- or 3-dimensions (e.g., Wen & Helmberger 1998a). Effects of D" anisotropy are also excluded from modeling in the 1-D case, however we don't expect this to affect our data. In addition, the reflectivity method makes use of the Earth flattening approximation, which may also affect the validity of large distance synthetic seismograms of core phases in the *P-SV* system (Choy *et al.* 1980). Nevertheless, as we are documenting relative changes in waveform behavior of *SPdKS* to *SKS*, we are still able to document the relative boundary layer anomalies responsible for the waveform changes by using the 1-D method. Furthermore, documentation of modeling trade-offs is straightforward, whereas this becomes increasingly difficult with 2-D or 3-D methods due to the increase in modeling degrees of freedom.

In accordance with proposed models of boundary layer structure at the CMB, we created synthetic seismograms for CMTZ, CRZ and ULVZ model spaces, using PREM as the reference model throughout the rest of the Earth. Synthetic seismograms were produced for a fine discretization in epicentral distance and source depth so every observation could be compared to predictions from every model. The types of models we used are summarized in Figure 3.5. We specifically explored variations in boundary

layer thickness ("h", Figure 3.5), *P*- and *S*-wave velocity reductions, and density (ρ) increases; a summary of the ranges explored is given in Table 3.3. For ULVZ structures, two classes of models were considered: 1) an equal reduction of V_P and V_S (δV_P and δV_S respectively), and 2) δV_S equal to three times δV_P. The first class of models is representative of a chemically distinct solid ULVZ, whereas the second corresponds to a partial melt origin of the ULVZ (Williams & Garnero 1996). For both cases, δV_P, δV_S, ρ, and ULVZ thickness were allowed to vary (Figure 3.5a). We created CRZ models by assuming there is a small finite rigidity at the top of the core. To accommodate this assumption CRZ models were created by assuming a non-zero value of *S*-wave velocity (V_S) in the outer core, and rigidity (μ) calculated from $\mu=\rho V_S^2$. This non-zero rigidity perturbs the outermost core *P*-wave velocity ($V_P = [(K + 4/3\mu)/\rho]^{½}$) in the CRZ, making it larger than that of PREM (by up to 33%). Hence, with CRZ models, we allowed thickness, density, and V_S to vary, which involve V_P perturbations due to finite μ (Figure 3.5b). CMTZ models were created with a linear gradient from lower mantle properties at the top of the CMTZ layer to outer core properties at the bottom of the CMTZ layer. CMTZ models are centered in depth on the CMB with layer thickness as the only variable (Figure 3.5c).

The parameter range for each model space (Table 3.3) was discretized as follows: for both classes of ULVZ models, ULVZ thickness was modeled as being 2, 5, 10, or 30 km, and lowermost mantle ρ was modeled as a 0, 10, 20, 40, or 60% increase (i.e., relative to the PREM mantle). For class 1, equal δV_P and δV_S reductions ranged from 0, 5, 10, 15, 20, and 30%. For class 2, δV_P and δV_S reductions of 5 and 15%, 10 and 30%,

15 and 45%, or 20 and 60% respectively (i.e., $\delta V_S = 3\delta V_P$), were tested. This resulted in 200 unique ULVZ models. CRZ models were discretized in 1.0 km thickness increments, resulting in 4 unique CRZ thicknesses. Additionally, the CRZ layer contained non-zero V_S between 1.0 and 5.0 km/sec in 1.0-km/sec increments, and outer-core density reductions by up to –50% in 10% increments. Therefore, our CRZ model space consisted of 4 thicknesses × 5 V_S values × 6 ρ reductions, equaling 120 distinct CRZ models. For CMTZ models, thickness (the only variable) was discretized in 0.25 km increments, resulting in 11 unique models. Thus, our model space consisted of synthetic seismograms for 333 distinct models that span the range of parameters in Table 3.3. Synthetic seismogram construction for each model for a range of source depths and distances resulted in nearly 200,000 synthetic seismograms in our model space database to be compared to data traces.

Previous modeling of ULVZ structure has shown evidence for low quality factor (Q) values (Havens & Revenaugh 2001), which may be expected if the ULVZ structure is composed of partial melt. However, in creating this synthetic model space we do not consider variations in Q. This is primarily an effort to limit the number of parameters, noting that extremely low Q (e.g., $Q_\mu = 5$, $Q_K = 5$) variations will lower *SPdKS* amplitudes but roughly retain relative *SKS*-*SPdKS* timing (Garnero & Helmberger 1998). Nevertheless, future efforts should consider Q, especially for probes that demonstrate a first-order sensitivity to it.

3.4 Modeling approach

In order to compare *SPdKS* observations to synthetic predictions, we first constructed an empirical source for each of the events used in this study (Table 3.2). On an event-by-event basis, *SKS* pulses were stacked if (a) they were at pre-*SPdKS* distances between 90º-100º; (b) they were clean and impulsive; and (c) they had a high degree of waveform similarity, manifest in a high cross-correlation (CC) coefficient with other records for that event. Figure 3.6 shows an example empirical source construction, where 24 individual *SKS* records between 90º-100º (Fig. 3.6a) are summed (Fig. 3.6b) for event #30 (Table 3.2). The dashed gray line is the resulting linear stack and is shown overlain on the original 24 traces. For each event, the following steps were carried out to best incorporate the empirical source in our synthetic modeling: (1) We conducted a systematic grid search for a triangle function that when convolved with a pre-*SPdKS* distance PREM synthetic seismogram returned the best CC coefficient with our empirical source function (Figure 3.6c, step 3). We created triangle functions by starting with a delta function, and then alternately varying the right- and left-hand width of the triangle in 0.1 sec increments, which included both symmetric and asymmetric triangle functions. Truncated triangle functions were also considered. (2) The best fitting triangle function was convolved with all synthetic seismograms in our model space. (3) A 45 sec time window containing *SKS* and *SPdKS* for all data and synthetics (at appropriate source depths and distances) was constructed. Each data record was cross-correlated with the appropriate depth and distance synthetic seismogram of all of the 333 models. The

resulting CC coefficient was stored for all possible combinations, and visual inspection of results was also made from graphical overlays of all data-model comparisons.

SKS waveforms used for empirical source construction (recorded between 90°-100°) intersect the CMB at a supercritical angle resulting in a small phase shift, thus introducing a slight shoulder in our waveforms (observable on individual traces in Fig 3.6). For distances greater than that for *SPdKS* inception this phase shift disappears. This does not strongly affect our source construction, as the width of the central *SKS* peak is well fit by our model. However, the shoulder introduces a slight asymmetry of our triangle functions to the right-hand side. Where the asymmetry became too large, we shortened the window over which we calculated the CC coefficient so as to not include the shoulder, thus retaining symmetric empirical source functions.

We grouped records into four basic categories, based on data-synthetic CC coefficients. (1) PREM waveforms: the observation-PREM synthetic CC coefficient ranked higher than all other data-synthetic combinations (we note that the use of the term "PREM" here and hereafter is simply meant to signify the lack of any significant low velocity boundary layering at the CMB, the 1-D reference model is unimportant). (2) Probable low velocity zone (PLVZ) waveforms: the highest data-synthetic CC coefficients correspond to synthetic models having very thin boundary layers (typically < 5 km in thickness), but do not differ significantly from the PREM CC coefficient. We chose a relative percent difference of CC coefficients of 5% as our cutoff. That is, if the CC coefficient of the PREM model was within 5% of the CC coefficient of the best fitting model, the record was classified as PLVZ. (3) Boundary layer structure (ULVZ)

waveforms: the highest data-synthetic CC coefficients are from significant CMB boundary layer model synthetics (hereafter we refer to these waveforms as simply "ULVZ" although CRZ, or CMTZ models may apply as well). For this case, the PREM CC coefficient normalized to that of the best fitting model is below 95%. (4) Extreme waveforms: observations are not adequately fit by any synthetic in our model space – typically, these waveforms exhibited much higher amplitudes of *SPdKS* relative to *SKS* (as seen in Figure 3.4a, 108º) than are present in any of our models. In some cases this may be indicative of 2- or 3-D structure causing focusing effects, however, further investigation is needed in order to explain these records. Records of this class are assumed to sample an extreme low-velocity zone, or ELVZ. No CC coefficient-based modeling for ELVZ waveforms is made, due to the high degree of variability of these records (and subsequent CC coefficients). The lack of a well-defined basis for classification of ELVZ records does not produce problems in our analyses, as we only use the ELVZ characterization in searching for spatial groupings of *Pdiff* segments that display similar properties, and may elucidate highly anomalous regions of the CMB.

Figure 3.7 shows examples of comparisons between data (bold lines) and synthetics (thin lines). Figure 3.7(a-c) presents observed waveforms best fit by the PREM model. Observation-prediction comparisons are shown for PREM along with 11 models having the next highest cross-correlation coefficient. Cross-correlation coefficients are displayed to the right of each overlay, and model properties are listed in Table 3.4. Due to the fine-discretization of the model space (i.e., models span properties that are only slight perturbations from PREM, up to more extreme ULVZ structures), only a gradual

degradation in fit from the best fit PREM prediction is seen. Nonetheless, PREM is the best fit. For example, Figure 3.7a shows that slight CMB perturbations result in *SPdKS* delays relative to *SKS*, which degrades the CC goodness of fit. Figure 3.7(d-f) shows examples of the PLVZ observations and predictions. The 11 best fitting synthetics are overlain on the data, and the 12th overlay is the data and PREM. All waveform complexities are better reproduced by models with a thin anomalous boundary layer, though the PREM fit only slightly differs from the fits with higher cross-correlation coefficients. For example, the best fit-normalized CC coefficient for PREM for Figure 3.7d is 100 × (1 - 96.48/97.13) or ~ 0.7%; these data are thus grouped into the PLVZ category. Figure 3.7(g,h) shows data and synthetic comparisons for the boundary layer structure category (ULVZ). The data are fit by significant (> 5% relative difference in CC coefficients) low velocity CMB layering (contrast with the PREM synthetic at the bottom of each panel); and Figure 3.7i displays a comparison for the ELVZ waveform category. This record could not be explained adequately by any of our models constructed, and was thus grouped into the extreme category.

It is noteworthy that the model giving the highest cross-correlation coefficient does not necessarily fit the observation the best in terms of *SPdKS* amplitude and timing. For example, in Figure 3.7e for station BDFB (Brasilia, Brazil), *SPdKS* is observed to arrive slightly later than predicted by the model with the highest CC coefficient. This *SPdKS* arrival time may be better predicted by one of the models with a lower ranking cross-correlation coefficient, however the downswing between *SKS* and *SPdKS* is over-predicted. Furthermore, notable model parameter trade-offs can be seen between models

ranked nearly the same in CC coefficient. These 1-D model trade-offs between thickness, density and velocity variations have been explored in previous work (Garnero & Helmberger 1998; Garnero & Jeanloz 2000a), and show the difficulty in uniquely constraining model parameters. Thus, determination of the best model parameters describing an individual record is difficult and potentially subject to personal bias. This is a primary motivation for grouping our observations into the previously described four categories. We note that the CC method is both useful, in that it aids in large data set processing, and has shortcomings, given that important waveform subtleties are difficult to address.

In modeling *SPdKS* observations, additional considerations must also be taken into account. First, *SPdKS* waveforms may undergo constructive and destructive interference with the phase *SKiKS* that is observable in broadband data. Figure 3.8 shows PREM synthetics and sample records that may exhibit interference from *SKiKS*. The shaded distance range shows the region of maximum potential interference of *SKiKS* as predicted by PREM for an event with a 400 km source depth. The distance range represented by this gray box can shift to greater distances (by 1-2º) with the presence of low velocity CMB structure. Several traces seem to be affected by this interference as evidenced by broadened *SPdKS* arrivals (e.g., near 120º in Figure 3.8b). This interference further complicates the waveform modeling, and must be considered in modeling of broadband *SPdKS* waveforms as in this study.

Finally, the uniqueness of model fit is highly dependent on epicentral distance. Records from the *SPdKS* inception distance up to ~112º contain the most diagnostic wave

shape distortions, due to *SPdKS* modulating the peak, shoulder, and downswing of *SKS*. Larger distance recordings are more difficult to uniquely constrain, as *SPdKS* is a longer period pulse that has sampled a much longer path along the CMB, as well as structure above the CMB. These records, even in regions known to contain strong CMB anomalies, often appear PREM-like. This can be observed in Figure 3.7f, for station CTAO (Charters Towers, Australia) at 123.9º, models with large ULVZ characteristics do not remarkably vary from PREM (< 5% CC coefficient difference), whereas for station SSPA (Standing Stone, Pennsylvania, USA) at 112.7º (Figure 3.7g), the boundary layer models show characteristics of wave-shape distortions that are quite distinguishable from PREM (> 5% CC coefficient difference).

The dependency of uniqueness-of-fit on epicentral distance is further explored in Figure 3.9. Most of the *SPdKS* distance range studied here is densely sampled (Figure 3.9a). The CC coefficient between each observation and PREM was divided by the cross-correlation coefficient of the best fitting synthetic for that record. This normalized PREM-data CC coefficient is averaged in 2.5° distance bins and shown in Figure 3.9b. The error bars represent 1 standard deviation of the mean. In Figure 3.9b, a value of 1 represents the best fit synthetic and PREM being indistinguishable. The bin between 105° and 110° are close to PREM as for most of the global data, *SPdKS* anomalies are typically not yet manifested as *SKS* waveform distortions. Between 110º and 115º, however, these distortions are easily viewed, and start to degrade the CC coefficient between data and PREM. The large increase in the standard deviation indicates the ability to better distinguish between models for this distance range. At larger distances,

both the timing and amplitude of *SPdKS* do not differ that remarkably from PREM, resulting in the average normalized CC coefficient again approaching the PREM value (thus, indicating the reduction in ability of the data beyond 115º to strongly constrain CMB boundary layer structure).

3.5 Inferred ULVZ distribution

3.5.1 Quantifying ULVZ strength and trade-offs

Our synthetic seismogram model space spans three classes of models: ULVZ, CRZ, and CMTZ (Figure 3.5). Each record (of collected data) was compared to synthetics of every model in each of these model classes. As mentioned previously (Section 3.4) there are strong modeling trade-offs between the different model types, particularly for the larger distance data. And only relatively subtle changes exist between associated CC coefficients between data and best fit ULVZ, CRZ, or CMTZ synthetics for the larger distances. This often precludes constraining whether any particular model class best explains a given record. Nonetheless, it is still possible to characterize how anomalous data are in a relative sense, by looking at geographical trends in data best fit by PREM (i.e., normal mantle), probable low velocity zones (PLVZ), or anomalous boundary layer structure (ULVZ), where we use "ULVZ" to represent moderate ULVZ, CRZ, or CMTZ. We have thus classified best fitting models of each observation in this fashion: (a) PREM, (b) PLVZ, (c) ULVZ, and (d) ELVZ. Although, we are not able to constrain specific boundary layer properties (e.g., layer thickness, density, and velocity

perturbation) due to trade-offs, we infer structure in terms of relative waveform behavior by the four listed categories.

By looking at the distribution of *SPdKS Pdiff* segments on the CMB, we are able to observe the geographical distribution of waveform behavior for individual records. Figure 3.10 shows two regions of the CMB (the same regions presented in Figure 3.1) with *Pdiff* segments color-coded based on our waveform behavior classification scheme. Several *Pdiff* segments best modeled as having ULVZ-like structure are in close proximity to *Pdiff* segments best modeled as exhibiting PREM-like structure. A high degree of lateral heterogeneity is observed, where in some cases the *Pdiff* CMB entry point for ULVZ- and PREM-type waveforms is only on the order of 10's of kilometers apart. Lateral heterogeneity at such short scale-lengths has been observed in previous studies (Garnero & Helmberger 1996; Rost & Revenaugh 2001; Wen 2001; Rost & Revenaugh 2003) and is consistent with a CMB environment of high variability and complexity.

Despite the close proximity of *Pdiff* segments grouped into PREM or ULVZ categories, to first order there does exist localized groupings of similarly characterized *Pdiff* segments. For example, Figure 3.10a shows that east of the Tonga and Kermadec Trenches, the majority of *Pdiff* segments are characterized as ULVZ, to the south most segments are characterized as PLVZ. To the west (at ~ -15º latitude) there exists a tight grouping of segments classified as ULVZ that transitions into PREM and PLVZ to north and northwest. The predominance of *Pdiff* segments (on the source-side) characterized as ULVZ to the west of the Tonga and Kermadec Trenches are also manifested in a close

grouping of ULVZ classified segments (on the receiver-side) under Central North America (~30º latitude; Figure 3.10b). However, without crossing coverage we are unable to constrain if an ULVZ exists under the Southwest Pacific, North America, or both regions.

3.5.2 ULVZ likelihood maps

Even in the presence of extremely short scale heterogeneity, it is useful to address the intermediate- to long-wavelength geographical distribution of ULVZ heterogeneity. Here we describe an averaging scheme that maps the likelihood of any part of the CMB sampled by our data being best characterized with or without anomalous low velocity boundary layering. For this purpose we have divided the CMB into 5º × 5º cells. To best quantify ULVZ existence/non-existence, the number of *SPdKS Pdiff* segments that pass through each grid cell have been tabulated, and assigned "*SPdKS* values" as follows: PREM-like *SPdKS* segments have been assigned a value of 0.0 (thus zero "ULVZ-likelihood"), PLVZ-like segments have also been assigned a value of 0.0, ULVZ-like segments have been assigned a value of 1.0 (i.e., maximum ULVZ-likelihood), and ELVZ-like segments have also been assigned a value of 1.0 (where waveforms with extreme *SPdKS* anomalies are assumed to be due to boundary layer structure). This enables a cell-by-cell average that permits assessment of solution structure uniformity, as well as geographical ULVZ distribution.

We define the ULVZ-likelihood for each cell sampled, by averaging all *SPdKS* values in each cell. That is, we sum the "*SPdKS* value" of all *Pdiff* segments, based on

PREM predicted ray paths, passing through one of our 5º × 5º cells, and weight the sum by the total number of rays that passed through the cell. If all *SPdKS Pdiff* segments passing through a given cell were classified as ULVZ-like, then its ULVZ-likelihood would correspond to 1.0. If all data were classified as PREM-like, its ULVZ-likelihood would correspond to 0.0. Figure 3.11 shows the resulting ULVZ likelihood for our *SPdKS* data set. Figure 3.12a shows our entire data set with PREM predicted source- and receiver-side *Pdiff* segments colored red and blue respectively. In section 3.4 we noted that records in the epicentral distance range between 110º and 115º provide the greatest uniqueness of fit (Figure 3.9). For longer source-receiver distances the uniqueness of fit degrades. Figure 3.11b shows our data coverage for each 5º × 5º cell for our most distinctive data (restricted between 110º and 120º), where we have colored each grid cell by the number of *Pdiff* segments passing through a cell, and Figure 3.11c shows the ULVZ-likelihood for this restricted range.

When comparing this ULVZ likelihood map (Figure 3.11c) with a comparable likelihood map utilizing all data (available as additional supplementary information from the JGR website[1]) the two ULVZ likelihood maps critically depend on how uniquely *SKS-SPdKS* waveform characteristics can reveal CMB structure. While both maps agree with each other to first-order at long wavelength, distinct differences exist for some regions. Restricting the distance range has enhanced ULVZ likelihood in many regions,

[1] Supporting material is available via Web browser or via Anonymous FTP from ftp://ftp.agu.org/apend/ (Username = "anonymous", Password = "guest"); subdirectories in the ftp site are arranged by journal and paper number. Information on searching and submitting electronic supplements is found at http://ww.agu.org/pubs/esupp_about.html.

by discarding the longest distance (poorly constrained) PREM-fit data. We consider the first map (Figure 3.11c) to be the more constrained estimation of ULVZ likelihood.

The ULVZ likelihood maps reveal regional scale ULVZ patterns. For example, the southwest Pacific region and Central American region show high ULVZ likelihood. Strong ULVZ likelihood is observed under the Indian Ocean although we do not have complete coverage here. On the other hand, the Central East Asia region is extremely well sampled and shows no ULVZ likelihood. The central and eastern African CMB region also shows lesser likelihood of ULVZ, although we note that this is not well sampled. The area beneath (and west of) Kamchatka displays evidence for ULVZ existence, which is a region where no ULVZ has previously been observed. Other regions, such as the area east of the Philippines, are dominated by moderate to low ULVZ likelihood (midway between ULVZ and PREM). These regions likely contain a high degree of heterogeneity as suggested by the multiple *Pdiff* segments of varying classifications passing through each cell (also see Figure 3.10).

Many studies have focused on the Southwest Pacific and Central American regions (Figure 3.1, Table 3.1). The Southwest Pacific region has displayed compelling evidence for ULVZs utilizing varied approaches. To the west and northwest of the Tonga and Kermadec Trenches, short scale-length heterogeneity has been argued in studies utilizing short-period precursors to the phase *ScP* (studies 5,7,10 and 11 in Table 3.1 and Figure 3.1). These studies show *ScP* bounce points located within 10's of km on the CMB displaying waveforms indicative of both existence and non-existence of ULVZ structure. Our study also shows this high degree of lateral heterogeneity in these regions, with

ULVZ likelihood in the range of 0.5 to 0.8 (Figure 3.11c). Studies focusing west of the Tonga and Kermadec Trenches have agreed on positive ULVZ sighting. This region also contains some of our highest ULVZ likelihood values. Yet, we also observe intermingled PREM- and PLVZ- like waveforms suggesting that this region is more complicated than previously suggested. A variety of results have emerged from studies looking at the Central American Region. Nearly all of our data for this region displays either ULVZ or PLVZ-like waveforms. Of special note is the tight grouping of ULVZ- and ELVZ- like waveforms just to the east of the Galapagos Islands supporting the findings of studies 4 and 18 (Table 3.1, Figure 3.1).

Several studies have searched for ULVZ structures in regions not encompassed in Figure 3.1. The Northeast Pacific region has received much attention from studies of short-period precursors to core reflected phases (see Table 3.1), although the majority of these studies have not shown any evidence of ULVZ structure. Our likelihood map is in agreement with no ULVZ under the Northeast Pacific, however we only sparsely sample this region. Wen, (2001) studied the southern Indian Ocean using travel times and waveform analysis of *S*, *ScS*, *SHdiff* and *Pdiff* from four events, and found a trend of PREM-like lowermost mantle in the south to ULVZ-like structure in the north. This finding coincides remarkably well with the likelihood transition at the southeast tip of Africa for our most constrainable data (Figure 3.11c). Here we only use data from one of the four events used by Wen (2001). Additionally, Helmberger *et al.* (2000) suggests that ULVZ structure exists beneath Iceland and the East Africa Rift. Our averaging scheme does not result in the highest ULVZ likelihood (1.0) in either region, but is > 0.5 under

Iceland and displays some evidence under the East Africa Rift corroborating this possibility. However, as noted above, our data coverage is sparse beneath most of Africa. Further evidence has been supplied that ULVZ structure exists under the Southern Atlantic Ocean from studies of *S-ScS* travel times and waveform anomalies (Simmons & Grand 2002; Ni & Helmberger 2003b). However, we have no data coverage there.

As noted, seemingly conflicting results have been reported for the existence/non-existence of ULVZs for a given region. The ULVZ-likelihood approach is useful for identifying regions that display variability in solution models, that often depend on the wavelength of the energy modeled (e.g., short-period versus broadband data). We stress that the exact sampling location and dominant wavelength of observation is extremely important for model determination. The likelihood map presented in Figure 3.11 provides a better estimation of where ULVZ structure may exist than the simple binary distributions previously presented (e.g., Garnero *et al.* 1998).

Fresnel zones of the *Pdiff* segments of *SPdKS* can also be used in ULVZ map construction (Garnero *et al.* 1998). Figure 3.12 shows *SPdKS Pdiff* Fresnel zones (¼ wavelength, 10 sec dominant period, calculated for a ULVZ model with a 10% reduction in V_P), where the shading represents ULVZ likelihood (as in Figure 3.11). Light shading corresponds to high likelihood of having ULVZ structure and dark shading indicates low likelihood. While using Fresnel zones are extremely useful for accommodating likely wavelengths of wave field sensitivity, caution must be taken in subsequent interpretation, because significant sub-Fresnel zone variability exists (Figure 3.10). This was a pitfall of the final ULVZ distribution figure of Garnero *et al.* (1998) that utilized Fresnel zones –

as with Figure 3.12, and the spatial averaging used in Figure 3.11 – lateral variations in boundary layer structure appears to exist at wavelengths much shorter than Fresnel zones or our grid cell sizes.

3.6 Discussion

In this paper, we present a method to assign best fit 1-D models to high quality broadband *SPdKS* data. Our main focus has been to identify likely regions of anomalous CMB structure. While this data set and method greatly improve our earlier efforts, several uncertainties are still present. In this section we discuss important sources of uncertainty and the relationship between likely ULVZ presence and overlying mantle heterogeneity.

3.6.1 Uncertainties in mapping ULVZ structure

Perhaps the most significant uncertainty associated with *SPdKS* analyses is the difficulty in attributing anomalous *SPdKS* signals to either the *SPdKS* core entry or exit (or both) locations. This is identical to trade-offs in *PKP* precursor analyses aimed at D" scatterer modeling (e.g., Hedlin & Shearer 2000). Some crossing paths help to reduce these uncertainties, but many regions lack any azimuthal sampling.

While static displacements of the CMB do not affect our results, small-scale topography (e.g., domes, etc.) can act to focus or defocus energy and may play a significant role in perturbing *SPdKS* relative to *SKS* (or vice versa), resulting in erroneous mapping of structure. Data coverage at present is not adequate to address this issue

globally. Some regional efforts (as in Wen & Helmberger 1998a) may have dense enough sampling to constrain such features.

In most *SPdKS* modeling to date, synthetic predictions assume that *SKS* also propagates through the ULVZ structure, resulting in an *SKS* delay. For example, a 20 km thick ULVZ with a 10% δV_P reduction results in an *SKS* delay of ~0.3 sec. In 1-D modeling, *SKS* travels through the ULVZ structure twice, thus a 0.6 sec anomaly accumulates. If in fact *SKS* does not traverse any ULVZ, then a 0.6 sec bias has been folded into the modeling, which amounts to an underestimation of *SPdKS* delays (because *SKS* has been artificially delayed, and *SPdKS* is analyzed relative to *SKS*). This affect should only minimally affect our results, because (a) most of our best fit models are thinner than this example, and (b) a 0.6 sec differential time error will only result in a minor mismapping of ULVZ strength. Nonetheless, future efforts need to focus beyond 1-D methods.

Our modeling has assumed constant anomalous property layering (except the CMTZ models), for a single layer. More recent work has suggested multiple ULVZ layers in two localized regions: beneath the central Pacific (Avants *et al.* 2003), and beneath North America (Rondenay & Fischer 2003). Some of our regions may entail much greater complexity than this first effort at global ULVZ characterization.

Because of the various modeling trade-offs, the absolute velocity reductions, density increases, or thickness cannot be constrained in this study. However, average ULVZ properties (e.g., thickness) can be pursued for specific model assumptions. Table 3.5 presents the average ULVZ thickness for a variety of model types. For each model,

we: (1) extracted the best fitting thickness of that model type for every *SPdKS* observation; (2) discarded records having a CC coefficient (for that specific model) below 5% of that of the overall best fit synthetic to that observation; and (3) averaged the resulting thicknesses for all records that fulfilled requirement (2) (this was done separately for both PLVZ and ULVZ model characterizations). The average thickness is given in Table 3.5 with the number of qualifying records listed in parenthesis to the right. It is notable that the number of qualifying records for each of the models presented is approximately equal (for either PLVZ or ULVZ), which is further indication of the modeling trade-offs. Nonetheless, several key generalizations can be made from these modeling summaries:

I. For ULVZ models:

- Doubling the velocity reduction (where $\delta V_S = \delta V_P$) results in an average ULVZ thickness roughly halved.
- Doubling the density increase reduces ULVZ thickness by roughly 20%.
- Equal δV_S and δV_P reductions have the greatest average ULVZ thickness (for the parameter space we explored with $\delta V_S = \delta V_P$).
- For $\delta V_S = 3\delta V_P$ (representing the partial melt scenario), greater thicknesses can be achieved if the velocity reductions are relatively mild. In our model space, the thickest partially molten ULVZ (~ 8 km) occurs for (δV_S = -15%, δV_P = -5%, $\delta\rho$= +0%).
- Increasing velocity reductions or density increases for $\delta V_S = 3\delta V_P$, the average ULVZ thickness significantly decreases, e.g., < 5 km average thickness results for (δV_S = -30%, δV_P = -10%, $\delta\rho$ = +0%).

II. For CRZ models:

- Increasing V_S or ρ decreases CRZ thickness.

III. For CMTZ models:

- The average thickness is less than 2.0 km.

If we assume a specific model type (e.g., as in Table 3.5), boundary layer distribution and thickness maps can be constructed. Figure 3.11d shows the average thickness of one ULVZ model (δV_S = -15%, δV_P = -5%, δρ = +5%), averaged onto 5º×5º grid cells. Additionally, Figures 3.11e,f show the average thickness of one CRZ model (δV_S = -59%, δV_P = -34%, δρ = +42%), and for CMTZ. These maps are produced by averaging best fitting thicknesses in each grid cell, for all data characterized by a CC coefficient within 5% of the best fitting record (for that specific model). This figure does not include thickness averages for waveforms classified as PLVZ, and thus represents a maximum thickness for the sampled regions. Interestingly, thick ULVZ is exhibited (Figure 3.11d) in the East African Rift Area and under Iceland, as suggested by Helmberger *et al.* (2000), where only moderate ULVZ likelihood was suggested (Figure 3.11c). Approximate thicknesses for other ULVZ model properties may be estimated to first order from the present map, and Table 3.5. For example, for an ULVZ model with δV_S = -30%, δV_P = -10%, and δρ = +0%, the average thickness of each cell would be reduced by approximately half. We note that our complete list of model parameters, cross-correlation coefficients, and ULVZ likelihood maps, are available in ASCII format as additional supplementary information from the JGR website.

3.6.2 Relating ULVZ and mantle heterogeneity

We have compared these likelihood maps to several *P*- and *S*-wave tomography models (Boschi & Dziewonski 1999; Megnin & Romanowicz 2000; Ritsema & van Heijst 2000; Gu *et al.* 2001; Kárason & van der Hilst 2001; Zhao 2001; Grand 2002). However, there is no significant correlation between strong ULVZ-likelihood and lowermost mantle velocities from these tomographic models. This may be expected due to the source-receiver ambiguity of *SPdKS*. For example, tomographic models of shear-wave velocity display strong degree-2 heterogeneity, with low velocities below the Pacific and Africa, and high velocities in the circum-Pacific region. All of our records originate in sources along deep subduction zones circling the Pacific. For example, a record originating in the Fiji-Tonga subduction complex and recorded in North America or Asia may have *Pdiff* segments on the source-side encountering low shear-wave velocities in the Pacific and high shear-wave velocities on the receiver-side in the North American or Asian regions. Because we cannot distinguish between source- or receiver-side ULVZ anomalies, ULVZ likelihood estimations in both locales are affected. This causes an averaging effect in comparing likelihood to tomography results. Thus, while ULVZ structure may strongly relate to lowermost mantle velocities, the correlation between our likelihood maps and lowermost mantle velocities may be blurred due to the source– versus receiver-side of path ambiguity (which is explored in greater detail in the following section). As data coverage and crossing path sampling increases, future efforts will better minimize uncertainties due to the source receiver ambiguity in *SPdKS* modeling.

However, there is a correlation with tomographic models of shear-wave velocity and the source-side *Pdiff* segments used in this study. For each record in our study we have determined the lowest velocity encountered on each *Pdiff* segment for both source- and receiver-side arcs, for four models of *S*-wave tomography (Megnin & Romanowicz 2000; Ritsema & van Heijst 2000; Gu *et al.* 2001; Grand 2002) and three models of *P*-wave tomography (Boschi & Dziewonski 1999; Kárason & van der Hilst 2001; Zhao 2001). The most notable correlation occurs for *Pdiff* segments from data in the distance range of 110º–120º. Figure 3.13 shows averages of the lowest tomographic velocities along either source- or receiver-side *Pdiff* segments, for the different model classifications of PREM, PLVZ, or ULVZ (ELVZ waveforms are combined with the ULVZ waveforms for this analysis). For both the *P*- and *S*-wave models, the lowest velocities encountered by the *SPdKS Pdiff* segments are predominantly on the source-side and approximately zero on the receiver side of the path. No clear trend is found between average *P*-wave velocities and *SPdKS* anomalies (i.e., PREM, PLVZ, or ULVZ data), with the exception of model kh2000pc (Kárason & van der Hilst 2001). For model kh2000pc, the *Pdiff* segments on the source-side typically encounter higher velocities for PREM than for PLVZ (slightly lower), and for ULVZ (lower yet), than for the receiver-side of the path. This trend is apparent for all *S*-wave models analyzed. That is, considering the source-side segments for all *S*-wave models, the PREM-like waveforms encounter the higher velocities on average than those classified as ULVZ. Also, PLVZ-classified waveforms on average encounter *S*-wave velocities in-between PREM and

ULVZ data. The velocity averages for receiver-side *Pdiff* segments do not show any apparent trend relating to our waveform classification.

As our inferred structure varies on rather small length-scales, we have attempted to make our comparisons with global structures with the shortest wavelength variations. However, no apparent agreement in correlation is evident in the *P*-wave models, which may be related to the general disagreement between the models, and indicate a necessity to utilize models specifically aimed at determining D" structure or at more detailed regional maps (e.g., Valenzuela *et al.* 2000, Tkalčić *et al.* 2002, Tkalčić & Romanowicz 2002). Of the *P*-wave models analyzed here, only kh2000pc utilizes *Pdiff*, which may result in the better correlation to the ULVZ results than for the other *P* structures. As longer distance records may inappropriately be classified as PREM-like (see Section 3.5.2), correspondence of low tomographically derived V_S and source-side *Pdiff* arcs is less apparent when using our entire data set (in comparison to using the 110°-120° subset). As expected, more PREM-like averages of tomographic velocities encountered result from inclusion of the largest distance data (i.e., > 120°). Because the main source region of events used in this study lie in the Southwest Pacific, and the majority of receiver locations are in Eastern Asia and North America (Figure 3.11a) rays from the same event are more likely to sample bins on the source-side, whereas bins nearest the receiver-side are more likely to be sampled by rays from a wide range of events. Hence the limited coverage enforced by source-receiver geometry inadequacy may introduce a geographical bias in our low V_S and source-side *Pdiff* arc correspondence.

3.6.3 SPdKS ray path uncertainties

In our one-dimensional modeling efforts, boundary layer structure exists at both the source and receiver sides of the *SPdKS* path. But, ULVZ structure may be confined to only one side, and may only partially interact with the *Pdiff* segments on that side. Figure 3.14 illustrates three different ULVZ localizations on the source-side. In panel (a), the *SPdKS Pdiff* segment initiates, propagates, then exits completely within the ULVZ (solid line ray path). For reference, the dotted line indicates the ray path for PREM. Of first note, the critical angle for *ScP* converting to a *Pdiff* segment increases for a ULVZ, as compared to that for PREM . All diffracted waves within a ULVZ exit into the core at the same model dependent critical angle. The *Pdiff* inception location (i.e., where *P*-diffraction initiates) is closer to the earthquake source for the ULVZ model than for PREM, resulting in longer diffraction distances (to reach the same receiver).

Panel (b) depicts the situation where *Pdiff* initiates in PREM mantle, then propagates in a ULVZ before diving into the core. In this case, the diffraction length is larger than for pure PREM paths. The opposite geometry is also possible, that is, the *Pdiff* inception can occur in an isolated ULVZ, exit the ULVZ into PREM-like mantle, and then dive into the core from PREM mantle. It is also possible the *Pdiff* passes through one or several ULVZ structures of a much smaller scale than the *Pdiff* arcs. In this case, travel time anomalies associated with *SPdKS* may be abrogated by wavefront healing making their existence difficult to establish.

3.6.4 2- and 3-D synthetics

In the three cases of Figure 3.14, the length of diffraction, as well as the *Pdiff* inception and termination locations vary significantly. Synthetic waveforms that account for structure in two- or three-dimensions are desired (e.g., by utilizing methods such as presented in Igel & Weber 1996; Helmberger *et al.* 1996; Wen & Helmberger 1998). Helmberger *et al.* (1996) studied the effects of two-sided structures, with PREM-like mantle on one side and a ULVZ structure on the opposite side of the *SPdKS* path. Two distinct waveform effects (relative to 1-D modeling) were noticed: (1) a decrease in *SPdKS* amplitude near 110°-112° occurs, as the anomalous signal comes from only half of the geometric path, and (2) at larger distances, two distinct arrivals are apparent, one for *SPdKS* and *SKPdS*. The source versus receiver side of path ambiguity is nevertheless still present.

3.6.5 Other considerations

A significant amount of waveforms have been characterized as PLVZ, which raises the possibility that a thin (< 5 km) ULVZ structure may exist throughout much of Earth's D" layer. Williams & Garnero (1996) suggested that if ULVZs are of partial melt origin, they might arise if the geotherm is close to the solidus of silicate mantle. For this case, ULVZs should be a global feature (as the CMB should be isothermal), but could be very thin in colder regions. At present it may be difficult to detect such a possibility. Even with array methods, it is difficult to resolve "typical" ULVZ boundary layering (e.g., $\delta V_S = \delta V_P = -10\%$) much thinner than ~3 km (e.g., Rost & Revenaugh 2003). A

gradational top to the ULVZ may further hinder ULVZ detection in such studies. However, one may expect greater *SPdKS* delays in higher frequency data as *Pdiff* may be more efficiently trapped inside a ULVZ. Thus, using shorter-period data may prove useful in future characterizations of ULVZ structure.

As global coverage increases, particularly through combining results of the other important ULVZ probes, comparisons between better constrained global ULVZ maps and other related phenomena will be important, such as possible preferred magnetic field reversal paths (e.g., Laj *et al.* 1991; Brito *et al.* 1999; Kutzner & Christensen 2004), or the geographic distribution of hotspots (e.g., Williams *et al.* 1998a).

3.7 Conclusions

We have investigated anomalous boundary layer structure at the core-mantle boundary using a global set of broadband *SKS* and *SPdKS* waves. In attempt to circumvent the strong modeling trade-offs we have produced ULVZ likelihood maps, inferring regional patterns in ULVZ structure. The Southwest Pacific, Central America, Indian Ocean and Northeast Asia regions indicate the highest likelihood of ULVZ existence, whereas the North America, Central East Asia, and Africa regions display the lowest likelihood. Although there exists ambiguity over whether anomalous boundary layer structure exists on the source- or receiver-side of the *SPdKS* paths, there exists an apparent correlation with lower mantle *S*-wave velocity as inferred from tomography. This finding is consistent with ULVZ structure predominantly existing on the source-side of *SPdKS* paths. Additionally, broadband *SPdKS* data is determined to be most sensitive

to boundary layer structure in the distance range of 110º-115º. We observe very short-scale heterogeneity, with P_{diff} segments separated by 10's of kilometers, consistent with past studies. A partial melt origin to ULVZs implies a global average ULVZ thickness of < 10 km for δV_S = -15%, δV_P = -5%, and $\delta\rho$ = +0%. Stronger velocity reductions or density increases results in an even thinner ULVZ. Better constraint on structural specifics is necessary; combining *SPdKS* analyses with other ULVZ probes (both short-period and broadband) in addition to modeling waveforms with higher dimensional methods will greatly advance our ability to constrain ULVZ layer properties and geographical distribution (including the possibility of an ubiquitous ULVZ layer).

ACKNOWLEDGEMENTS

The authors thank T. Lay and S. Rost for useful discussions, the IRIS, ORPHEUS, and CNSN data agencies for the broadband data, and M. Fouch for helping with data processing. The authors also thank J. Revenaugh, S. Rondenay, and H. Tkalčić for constructive review and suggestions. MT and EG were partially supported by NSF grants EAR-9905710, and EAR-0135119. Most figures were generated using the Generic Mapping Tools freeware package (Wessel & Smith 1998). Actual waveform data used in this study is available at http://ulvz.asu.edu

REFERENCES

Avants, M.S., T. Lay, & E. Garnero, 2003. Determining shear velocity structure of ULVZs using stacked ScS data, *EOS Trans. AGU*, **84** (46).

Berryman, J.G., 2000 Seismic velocity decrement ratios for regions of partial melt in the lower mantle, *Geophys. Res. Lett.*, **27** (3), 421-424.

Boschi, L., & A.M. Dziewonski, 1999. High- and low-resolution images of the Earth's mantle: Implications of different approaches to tomographic modeling, *J. Geophys. Res.-Solid Earth*, **104** (B11), 25567-25594.

Bowers, D., D.A. McCormack, & D.S. Sharrock, 2000. Observations of PKP(DF) and PKP(BC) across the United Kingdom: implications for studies of attenuation in the Earth's core, *Geophys. J. Int.*, **140** (2), 374-384.

Bowin, C., 1986 Topography at the Core Mantle Boundary, *Geophys. Res. Lett.*, **13** (13), 1513-1516.

Brito, D., J. Aurnou, & P. Olson, 1999. Can heterogeneous core-mantle electromagnetic coupling control geomagnetic reversals?, *Phys. Earth Planet. Inter.*, **112** (3-4), 159-170.

Buffett, B.A., E.J. Garnero, & R. Jeanloz, 2000. Sediments at the top of Earth's core, *Science*, **290** (5495), 1338-1342.

Castle, J.C., & R.D. van der Hilst, 2000. The core-mantle boundary under the Gulf of Alaska: No ULVZ for shear waves, *Earth Planet. Sci. Lett.*, **176** (3-4), 311-321.

Choy, G.L., V.F. Cormier, R. Kind, G. Muller, & P.G. Richards, 1980. A Comparison of Synthetic Seismograms of Core Phases Generated by the Full-Wave Theory and by the Reflectivity Method, *Geophysical Journal of the Royal Astronomical Society*, **61** (1), 21-39.

Creager, K.C., & T.H. Jordan, 1986. Aspherical Structure of the Core-Mantle Boundary from PKP Travel-Times, *Geophys. Res. Lett.*, **13** (13), 1497-1500.

Doornbos, D.J., 1983 Present Seismic Evidence for a Boundary-Layer at the Base of the Mantle, *Journal of Geophysical Research*, **88** (B4), 3498-3505.

Doornbos, D.J., & T. Hilton, 1989. Models of the Core-Mantle Boundary and the Travel-Times of Internally Reflected Core Phases, *Journal of Geophysical Research-Solid Earth and Planets*, **94** (B11), 15741-15751.

Dziewonski, A.M., & D.L. Anderson, 1981. Preliminary Reference Earth Model, *Phys. Earth Planet. Inter.*, **25** (4), 297-356.

Earle, P.S., & P.M. Shearer, 1997. Observations of PKKP precursors used to estimate small-scale topography on the core-mantle boundary, *Science*, **277** (5326), 667-670.

Fisher, J.L., M.E. Wysession, & K.M. Fischer, 2003. Small-scale lateral variations in D" attenuation and velocity structure, *Geophys. Res. Lett.*, **30** (8).

Fuchs, K., & G. Müller, 1971. Computation of Synthetic Seismograms with Reflectivity Method and Comparison with Observations, *Geophysical Journal of the Royal Astronomical Society*, **23** (4), 417-433.

Garcia, R., & A. Souriau, 2000. Amplitude of the core-mantle boundary topography estimated by stochastic analysis of core phases, *Phys. Earth Planet. Inter.*, **117** (1-4), 345-359.

Garnero, E., J. Revenaugh, Q. Williams, T. Lay, & L.H. Kellogg, 1998. Ultralow Velocity Zone at the Core-Mantle Boundary, in *The Core-Mantle Boundary Region*, edited by M. Gurnis, M.E. Wysession, E. Knittle, and B.A. Buffet, pp. 319-334, American Geophysical Union, Washington, D.C.

Garnero, E.J., S.P. Grand, & D.V. Helmberger, 1993. Low P-Wave Velocity at the Base of the Mantle, *Geophys. Res. Lett.*, **20** (17), 1843-1846.

Garnero, E.J., & D.V. Helmberger, 1995. A Very Slow Basal Layer Underlying Large-Scale Low-Velocity Anomalies in the Lower Mantle beneath the Pacific - Evidence from Core Phases, *Phys. Earth Planet. Inter.*, **91** (1-3), 161-176.

Garnero, E.J., & D.V. Helmberger, 1996. Seismic detection of a thin laterally varying boundary layer at the base of the mantle beneath the central-Pacific, *Geophys. Res. Lett.*, **23** (9), 977-980.

Garnero, E.J., & D.V. Helmberger, 1998. Further structural constraints and uncertainties of a thin laterally varying ultralow-velocity layer at the base of the mantle, *J. Geophys. Res.-Solid Earth*, **103** (B6), 12495-12509.

Garnero, E.J., & J.E. Vidale, 1999. ScP; a probe of ultralow velocity zones at the base of the mantle, *Geophys. Res. Lett.*, **26** (3), 377-380.

Garnero, E.J., 2000. Heterogeneity of the lowermost mantle, *Annu. Rev. Earth Planet. Sci.*, **28**, 509-537.

Garnero, E.J., & R. Jeanloz, 2000a. Fuzzy patches on the Earth's core-mantle boundary?, *Geophys. Res. Lett.*, **27** (17), 2777-2780.

Garnero, E.J., & R. Jeanloz, 2000b. Geophysics - Earth's enigmatic interface, *Science*, **289** (5476), 70-71.

Glatzmaier, G.A., R.S. Coe, L. Hongre, & P.H. Roberts, 1999. The role of the Earth's mantle in controlling the frequency of geomagnetic reversals, *Nature*, **401** (6756), 885-890.

Goldstein, P., D. Dodge, & M. Firpo, 1999. SAC2000: Signal processing and analysis tools for seismologists and engineers, in *Invited contribution to the IASPEI International Handbook of Earthquake and Engineering Seismology*, edited by P.C. Jennings, H. Kanamori, C. Kisslinger, and W.H.K. Lee, pp. 1613-1614, Academic, San Diego, Calif.

Grand, S.P., R.D. van der Hilst, & S. Widiyantoro, 1997. Global Seismic Tomography: A Snapshot of Convection in the Earth, *GSA Today*, **7** (4), 1-7.

Grand, S.P., 2002. Mantle shear-wave tomography and the fate of subducted slabs, *Philos. Trans. R. Soc. Lond. Ser. A-Math. Phys. Eng. Sci.*, **360** (1800), 2475-2491.

Gu, Y.J., A.M. Dziewonski, W.J. Su, & G. Ekstrom, 2001. Models of the mantle shear velocity and discontinuities in the pattern of lateral heterogeneities, *J. Geophys. Res.-Solid Earth*, **106** (B6), 11169-11199.

Hager, B.H., R.W. Clayton, M.A. Richards, R.P. Comer, & A.M. Dziewonski, 1985. Lower Mantle Heterogeneity, Dynamic Topography and the Geoid, *Nature*, **313** (6003), 541-546.

Havens, E., & J. Revenaugh, 2001. A broadband seismic study of the lowermost mantle beneath Mexico: Constraints on ultralow velocity zone elasticity and density, *J. Geophys. Res.-Solid Earth*, **106** (B12), 30809-30820.

Hedlin, M.A.H., & P.M. Shearer, 2000. An analysis of large-scale variations in small-scale mantle heterogeneity using Global Seismographic Network recordings of precursors to PKP, *J. Geophys. Res.-Solid Earth*, **105** (B6), 13655-13673.

Helmberger, D., S.D. Ni, L.X. Wen, & J. Ritsema, 2000. Seismic evidence for ultralow-velocity zones beneath Africa and eastern Atlantic, *J. Geophys. Res.-Solid Earth*, **105** (B10), 23865-23878.

Helmberger, D.V., E.J. Garnero, & X. Ding, 1996. Modeling two-dimensional structure at the core-mantle boundary, *J. Geophys. Res.-Solid Earth*, **101** (B6), 13963-13972.

Helmberger, D.V., L. Wen, & X. Ding, 1998. Seismic evidence that the source of the Iceland hotspot lies at the core-mantle boundary, *Nature*, **396** (6708), 251-255.

Hide, R., R.W. Clayton, B.H. Hager, M.A. Spieth, & C.V. Voorhies, 1993. Topographic Core-Mantle Coupling and Fluctuations in the Earth's Rotation, *Geophys. Mono.*, **72**, 113-125.

Igel, H., & M. Weber, 1996. P-SV wave propagation in the Earth's mantle using finite differences: Application to heterogeneous lowermost mantle structure, *Geophys. Res. Lett.*, **23** (5), 415-418.

Kárason, H., & R.D. van der Hilst, 2001. Tomographic imaging of the lowermost mantle with differential times of refracted and diffracted core phases (PKP, P-diff), *J. Geophys. Res.-Solid Earth*, **106** (B4), 6569-6587.

Kohler, M.D., J.E. Vidale, & P.M. Davis, 1997. Complex scattering within D" observed on the very dense Los Angeles region seismic experiment passive array, *Geophys. Res. Lett.*, **24** (15), 1855-1858.

Kutzner, C., & U.R. Christensen, 2004. Simulated Geomagnetic Reversals and Preferred VGP Paths, *Geophys. J. Int.*, **157**, 1105-1118.

Laj, C., A. Mazaud, M. Fuller, R. Weeks, & E. Herrero-Bervera, 1991. Lateral variations at the core-mantle boundary revealed by geomagnetic reversal paths?, *Nature*, **351**, 447.

Luo, S.N., S.D. Ni, & D.V. Helmberger, 2001. Evidence for a sharp lateral variation of velocity at the core- mantle boundary from multipathed PKPab, *Earth Planet. Sci. Lett.*, **189** (3-4), 155-164.

Manga, M., & R. Jeanloz, 1996. Implications of a metal-bearing chemical boundary layer in D" for mantle dynamics, *Geophys. Res. Lett.*, **23 (22)**, 3091-3094.

Masters, G., G. Laske, H. Bolton, & A.M. Dziewonski, 2000. The Relative Behavior of Shear Velocity, Bulk Sound Speed, and Compressional Velocity in the Mantle: Implications for Chemical and Thermal Structure, in *Earth's Deep Interior: Mineral Physics and Tomography From the Atomic to the Global Scale*, pp. 63-87, American Geophysical Union, Washington DC.

Megnin, C., & B. Romanowicz, 2000. The three-dimensional shear velocity structure of the mantle from the inversion of body, surface and higher-mode waveforms, *Geophys. J. Int.*, **143** (3), 709-728.

Montelli, R., G. Nolet, F.A. Dahlen, G. Masters, E.R. Engdahl, & S.H. Hung, 2004. Finite-frequency tomography reveals a variety of plumes in the mantle, *Science*, **303** (5656), 338-343.

Morelli, A., & A.M. Dziewonski, 1987. Topography of the Core-Mantle Boundary and Lateral Homogeneity of the Liquid Core, *Nature*, **325** (6106), 678-683.

Mori, J., & D.V. Helmberger, 1995. Localized Boundary-Layer Below the Mid-Pacific Velocity Anomaly Identified from a PcP Precursor, *J. Geophys. Res.-Solid Earth*, **100** (B10), 20359-20365.

Müller, G., 1985. The Reflectivity Method - a Tutorial, *Journal of Geophysics-Zeitschrift Fur Geophysik*, **58** (1-3), 153-174.

Ni, S., & D.V. Helmberger, 2001a. Probing an Ultra-low velocity zone at the Core Mantle Boundary with P and S Waves, *Geophys. Res. Lett.*, **28** (12), 2345-2348.

Ni, S.D., & D.V. Helmberger, 2001b. Horizontal transition from fast to slow structures at the core- mantle boundary; South Atlantic, *Earth Planet. Sci. Lett.*, **187** (3-4), 301-310.

Ni, S.D., & D.V. Helmberger, 2003a. Seismological constraints on the South African superplume; could be the oldest distinct structure on Earth, *Earth Planet. Sci. Lett.*, **206** (1-2), 119-131.

Ni, S.D., & D.V. Helmberger, 2003b. Ridge-like lower mantle structure beneath South Africa, *J. Geophys. Res.-Solid Earth*, **108** (B2).

Niu, F.L., & L.X. Wen, 2001. Strong seismic scatterers near the core-mantle boundary west of Mexico, *Geophys. Res. Lett.*, **28** (18), 3557-3560.

Persh, S.E., J.E. Vidale, & P.S. Earle, 2001. Absence of short-period ULVZ precursors to PcP and ScP from two regions of the CMB, *Geophys. Res. Lett.*, **28** (2), 387-390.

Reasoner, C., & J. Revenaugh, 2000. ScP constraints on ultralow-velocity zone density and gradient thickness beneath the Pacific, *J. Geophys. Res.-Solid Earth*, **105** (B12), 28173-28182.

Revenaugh, J., & R. Meyer, 1997. Seismic evidence of partial melt within a possibly ubiquitous low-velocity layer at the base of the mantle, *Science*, **277** (5326), 670-673.

Ritsema, J., & H.-J. van Heijst, 2000. Seismic Imaging of Structural Heterogeneity in Earth's Mantle: Evidence for Large-Scale Mantle Flow, *Science Progress*, **83**, 243-259.

Rodgers, A., & J. Wahr, 1993. Inference of Core-Mantle Boundary Topography from Isc Pcp and Pkp Travel-Times, *Geophys. J. Int.*, **115** (3), 991-1011.

Rondenay, S., & K.M. Fischer, 2003. Constraints on localized CMB structure from multichannel, broadband SKS-coda analysis, *Journal of Geophysical Research*, **108** (B11), 2537, doi:10.1029/2003JB002518.

Rost, S., & J. Revenaugh, 2001. Seismic detection of rigid zones at the top of the core, *Science*, **294** (5548), 1911-1914.

Rost, S., & J. Revenaugh, 2003. Small-scale ultralow-velocity zone structure imaged by ScP, *Journal of Geophysical Research*, **108** (B1), 2056, doi:10.1029/2001JB001627.

Shearer, P.M., M.A.H. Hedlin, & P.S. Earle, 1998. PKP and PKKP precursor observations: Implications for the small-scale structure of the deep mantle and core, in *The Core-Mantle Boundary Region*, edited by M. Gurnis, M.E. Wysession, E. Knittle, and B.A. Buffet, pp. 37-55, American Geophysical Union, Washington, D.C.

Simmons, N.A., & S.P. Grand, 2002. Partial melting in the deepest mantle, *Geophys. Res. Lett.*, **29** (11), art. no.-1552.

Sleep, N.H., 1990. Hotspots and Mantle Plumes - Some Phenomenology, *Journal of Geophysical Research-Solid Earth and Planets*, **95** (B5), 6715-6736.

Steinberger, B., 2000. Plumes in a convecting mantle: Models and observations for individual hotspots, *J. Geophys. Res.-Solid Earth*, **105** (B5), 11127-11152.

Stutzmann, E., L. Vinnik, A. Ferreira, & S. Singh, 2000. Constraint on the S-wave velocity at the base of the mantle, *Geophys. Res. Lett.*, **27** (11), 1571-1574.

Sze, E.K.M., & R.D. van der Hilst, 2003. Core mantle boundary topography from short period PcP, PKP, and PKKP data, *Phys. Earth Planet. Inter.*, **135** (1), 27-46.

Thomas, C., M. Weber, C.W. Wicks, & F. Scherbaum, 1999. Small scatterers in the lower mantle observed at German broadband arrays, *J. Geophys. Res.-Solid Earth*, **104** (B7), 15073-15088.

Thorne, M., E. Garnero, & S. Grand, 2004. Geographic correlation between hot spots and deep mantle lateral shear-wave velocity gradients, *Phys. Earth Planet. Inter.*, **146** (1-2), 47-63.

Tkalčić, H., & B. Romanowicz, 2002. Short scale heterogeneity in the lowermost mantle: insights from PcP-P and ScS-S data, *Earth Planet. Sci. Lett.*, **201** (1), 57-68.

Tkalčić, H., B. Romanowicz, & N. Houy, 2002. Constraints on D" structure using PKP(AB-DF), PKP(BC-DF) and PcP-P traveltime data from broad-band records, *Geophys. J. Int.*, **148**, 599-616.

Valenzuela, R.W., M.E. Wysession, M.O. Neustadt, & J.L. Butler, 2000. Lateral Variations at the base of the mantle from profiles of digital S-diff data, *J. Geophys. Res.-Solid Earth*, **105** (B3), 6201-6220.

Vidale, J.E., & H.M. Benz, 1992. A Sharp and Flat Section of the Core Mantle Boundary, *Nature*, **359** (6396), 627-629.

Vidale, J.E., & M.A.H. Hedlin, 1998. Evidence for partial melt at the core-mantle boundary north Tonga from the strong scattering of seismic waves, *Nature*, **391** (6668), 682-685.

Wen, L.X., & D.V. Helmberger, 1998a. A two-dimensional P-SV hybrid method and its application to modeling localized structures near the core-mantle boundary, *J. Geophys. Res.-Solid Earth*, **103** (B8), 17901-17918.

Wen, L.X., & D.V. Helmberger, 1998b. Ultra-low velocity zones near the core-mantle boundary from broadband PKP precursors, *Science*, **279** (5357), 1701-1703.

Wen, L.X., 2000. Intense seismic scattering near the Earth's core-mantle boundary beneath the Comoros hotspot, *Geophys. Res. Lett.*, **27** (22), 3627-3630.

Wen, L.X., 2001. Seismic evidence for a rapidly varying compositional anomaly at the base of the Earth's mantle beneath the Indian Ocean, *Earth Planet. Sci. Lett.*, **194** (1-2), 83-95.

Wessel, P., & W.H.F. Smith, 1998. New, improved version of the Generic Mapping Tools released, *EOS Trans. AGU*, **79** (579).

Williams, Q., & E.J. Garnero, 1996. Seismic evidence for partial melt at the base of Earth's mantle, *Science*, **273** (5281), 1528-1530.

Williams, Q., J. Revenaugh, & E. Garnero, 1998. A correlation between ultra-low basal velocities in the mantle and hot spots, *Science*, **281** (5376), 546-549.

Wysession, M.E., K.M. Fischer, G.I. Al-eqabi, P.J. Shore, & I. Gurari, 2001. Using MOMA broadband array ScS-S data to image smaller-scale structures at the base of the mantle, *Geophys. Res. Lett.*, **28** (5), 867-870.

Zerr, A., A. Diegeler, & R. Boehler, 1998. Solidus of Earth's deep mantle, *Science*, **281** (5374), 243-246.

Zhao, D., 2001. Seismic structure and origin of hotspots and mantle plumes, *Earth Planet. Sci. Lett.*, **192** (3), 251-265.

TABLES

Table 3.1 Core-mantle boundary layer studies.

	Reference	Phases Used[1]	Region	Sighting[2]
		Precursors to Core Reflected Phases		
1	*Vidale and Benz*, [1992]	SP ScP Stacks	NE Pacific	N
2	*Mori and Helmberger*, [1995]	SP PcP Stacks	Central, E Pacific	Y, N
3	*Kohler et al.,* [1997]	SP PcP Stacks	Central Pacific	Y, N
4	*Revenaugh and Meyer,* [1997]	SP PcP Stacks	Central, E, NE Pacific	Y
5	*Garnero and Vidale,* [1999]	SP, BB ScP	SW Pacific	Y, N
6	*Castle and van der Hilst,* [2000]	SP, BB ScP	NE Pacific, Central America	N
7	*Reasoner and Revenaugh,* [2000]	SP ScP Stacks	SW Pacific	Y, N
8	*Havens and Revenaugh,* [2001]	BB PcP Stacks	Central Mexico, W Gulf of Mexico	Y, N
9	*Persh et al.,* [2001]	SP PcP, ScP Stacks	NE Pacific, Central America	N
10	*Rost and Revenaugh,* [2001]	SP ScP Stacks	SW Pacific	Y
11	*Rost and Revenaugh,* [2003]	SP ScP Stacks	SW Pacific	Y, N
		Scattered Core Phases		
12	*Vidale and Hedlin,* [1998]	SP PKP precursors	SW Pacific	Y
13	*Wen and Helmberger,* [1998b]	SP, LP PKP precursors	SW Pacific	Y
14	*Thomas et al.,* [1999]	BB PKP precursors	SW Pacific, N. Europe	Y
15	*Wen,* [2000]	BB PKP precursors	Underneath Comores	Y
16	*Stutzmann et al.,* [2000]	BB SKS precursors	SW Pacific	N
17	*Ni and Helmberger,* [2001a]	BB PKP precursors, SKPdS	Western Africa	Y
18	*Niu and Wen,* [2001]	SP PKP precursors	W. of Mexico	Y
		Travel Time and Waveform Anomalies		
19	*Garnero et al.,* [1993]	LP SPdKS	Central Pacific	Y
20	*Garnero and Helmberger,* [1995]	LP SPdKS, SKS, SVdiff	Pacific, N. America	Y, N
21	*Garnero and Helmberger,* [1996]	LP SPdKS	Central, Circum Pacific	Y, N
22	*Helmberger et al.,* [1996]	SP, LP SPdKS	Central Pacific	Y
23	*Garnero and Helmberger,* [1998]	LP SPdKS	Central Pacific, Circum-Pacific	Y, N
24	*Helmberger et al.,* [1998]	LP SPdKS	Iceland	Y
25	*Wen and Helmberger,* [1998a]	LP SPdKS	SW Pacific	Y
26	*Bowers et al.,* [2000]	BB PKPdf, PKPbc	SW Pacific, E. of Iceland	Y
27	*Helmberger et al.,* [2000]	LP SPdKS	Africa, E. Atlantic	Y
28	*Luo et al.,* [2001]	BB PKPab-PKPdf	Central Pacific	Y
29	*Ni and Helmberger,* [2001b]	BB S,ScS	S. Atlantic	Y
30	*Wen,* [2001]	BB S, ScS, SHdiff, Pdiff, SKS	Indian Ocean	Y
31	*Simmons and Grand,* [2002]	BB ScS-S, PcP-P	S. Atlantic	Y
32	*Ni and Helmberger,* [2003]	LP, BB SKS-S, ScS-S	S. Africa	Y
33	*Rondenay and Fischer,* [2003]	BB SKS coda	N. America	Y

Table 3.2 Earthquakes used in this study

No	Date (yymmdd)	Lat (˚)	Lon (˚)	Depth (km)	Mw
1	900520	-18.1	-175.3	232	6.3
2	900608	-18.7	-178.9	209	6.9
3	910607	-7.3	122.6	563	6.9
4	910623	-26.8	-63.4	581	7.3
5	920802	-7.1	121.7	483	6.6
6	921018	-6.3	130.2	109	6.2
7	930321	-18.0	-178.5	584	6.3
8	930709	-19.8	-177.5	412	6.1
9	930807	26.5	125.6	158	6.4
10	930807	-23.9	179.8	555	6.7
11	940211	-18.8	169.2	204	6.9
12	940331	-22.0	-179.6	591	6.5
13	940429	-28.3	-63.2	573	6.9
14	940510	-28.5	-63.1	605	6.9
15	940713	-7.5	127.9	185	6.5
16	940819	-26.6	-63.4	565	6.5
17	950629	-19.5	169.2	144	6.6
18	950814	-4.8	151.5	126	6.3
19	950823	18.9	145.2	596	7.1
20	950918	-6.95	128.9	180	6.0
21	951006	-20.0	-175.9	209	6.4
22	951225	-6.9	129.2	150	7.1
23	960222	45.2	148.6	133	6.3
24	960317	-14.7	167.3	164	6.7
25	960502	-4.6	154.8	500	6.6
26	960827	-22.6	-179.8	575	6.0
27	961105	-31.2	180.0	369	6.8
28	961201	-30.5	-179.7	356	6.1
29	961222	43.2	138.9	227	6.5
30	970321	-31.2	179.6	449	6.3
31	970611	-24.0	-177.5	164	5.8
32	970904	-26.6	178.3	625	6.8
33	971128	-13.7	-68.8	586	6.7
34	980127	-22.4	179.0	610	6.5
35	980329	-17.5	-179.1	537	7.2
36	980403	-8.1	-74.2	165	6.6
37	980414	-23.8	-179.9	499	6.1
38	980516	-22.2	-179.5	586	6.9
39	980709	-30.5	-179.0	130	6.9
40	981008	-16.1	-71.4	136	6.2
41	981011	-21.0	-179.1	624	5.9
42	981227	-21.63	-176.4	144	6.8
43	990408	43.6	130.4	566	7.1
44	990409	-26.4	178.2	621	6.2
45	990413	-21.4	-176.5	164	6.8
46	990426	-1.6	-77.8	173	6.1
47	990512	43.0	143.8	103	6.2
48	990917	-13.8	167.2	197	6.3
49	000418	-20.7	-176.5	221	6.0
50	000614	-25.5	178.1	605	6.5
51	000616	-33.9	-70.1	120	6.4
52	000815	-31.5	179.7	358	6.6
53	001218	-21.2	-179.1	628	6.6

Table 3.3 Synthetic Model Space Parameter Ranges

Model	min Vs km/s (%)	max Vs km/s (%)	min Vp km/s (%)	max Vp km/s (%)	min ρ g/cm^3 (%)	max ρ g/cm^3 (%)	Thickness km
ULVZ[a]	5.08 (-30)	7.26 (0)	9.60 (-30)	13.72 (0)	5.57 (0)	8.91 (60)	2.0 - 30.0
ULVZ[b]	2.91 (-60)	6.17 (-15)	10.97 (-20)	13.03 (-5)	5.57 (0)	8.91 (60)	2.0 - 30.0
CRZ	1.00 (-86)	5.00 (-31)	8.20 (-40)	10.70 (-22)	4.95 (-11)	9.90 (77)	0.5 - 3.5
CMTZ	NA	NA	NA	NA	NA	NA	0.5 - 3.0

Percentages are referenced to properties on the mantle-side of the CMB relative to PREM.
[a] Indicates ULVZ models with $\delta\ln Vs = \delta\ln Vp$
[b] Indicates ULVZ models with $\delta\ln Vs = 3*\delta\ln Vp$.

Table 3.4 Model Parameters Corresponding to Figure 3.8.

3.8a) KURK *113.8*

No	CCC (%)	Model	-Vs (%)	-Vp (%)	+ρ (%)	h (km)
1	92.13	PREM	-	-	-	-
2	92.06	CRZ	31	22	-11	0.5
3	91.89	ULVZ	5	5	0	2
4	91.88	CRZ	45	28	-11	0.5
5	91.83	CRZ	59	34	-11	0.5
6	91.78	CRZ	72	38	-11	0.5
7	91.65	CMTZ	-	-	-	0.25
8	91.48	CRZ	86	40	-11	0.5
9	91.33	ULVZ	10	10	0	2
10	91.14	ULVZ	15	5	0	2
11	90.64	CMTZ	-	-	-	0.5
12	90.24	ULVZ	15	15	0	2

3.8b) PFO *114.1*

No	CCC (%)	Model	-Vs (%)	-Vp (%)	+ρ (%)	h (km)
1	98.05	PREM	-	-	-	-
2	97.86	CRZ	31	22	-11	0.5
3	97.79	ULVZ	5	5	0	2
4	97.78	CRZ	48	28	-11	0.5
5	97.73	CRZ	59	34	-11	0.5
6	97.68	CRZ	72	38	-11	0.5
7	97.63	CMTZ	-	-	-	0.25
8	97.61	CRZ	86	40	-11	0.5
9	97.33	ULVZ	10	10	0	2
10	97.32	ULVZ	15	5	0	2
11	96.85	CMTZ	-	-	-	0.5
12	96.72	ULVZ	15	15	0	2

3.8c) MM05 *123.4*

No	CCC (%)	Model	-Vs (%)	-Vp (%)	+ρ (%)	h (km)
1	90.40	PREM	-	-	-	-
2	90.11	CRZ	31	22	-11	0.5
3	90.00	ULVZ	5	5	0	2
4	89.99	CRZ	45	28	-11	0.5
5	89.90	CRZ	59	34	-11	0.5
6	89.87	CMTZ	-	-	-	0.25
7	89.87	CRZ	72	38	-11	0.5
8	89.83	CRZ	86	40	-11	0.5
9	89.59	ULVZ	10	10	0	2
10	89.54	ULVZ	15	5	0	2
11	89.30	CMTZ	-	-	-	0.5
12	89.11	ULVZ	15	15	0	2

3.8d) DRG *113.7*

No	CCC (%)	Model	-Vs (%)	-Vp (%)	+ρ (%)	h (km)
1	97.13	CRZ	86	40	7	0.5
2	97.07	CRZ	72	38	24	0.5
3	97.05	CRZ	45	28	42	0.5
4	97.05	ULVZ	15	5	10	2
5	97.04	CRZ	31	22	60	0.5
6	97.04	ULVZ	10	10	10	2
7	97.03	ULVZ	5	5	0	5
8	97.03	CMTZ	-	-	-	0.5
9	97.02	ULVZ	15	15	0	2
10	97.02	CRZ	59	34	42	0.5
11	96.87	ULVZ	20	20	0	2
12	96.48	PREM	-	-	-	-

3.8e) BDFB *117.5*

No	CCC (%)	Model	-Vs (%)	-Vp (%)	+ρ (%)	h (km)
1	94.12	ULVZ	30	10	10	2
2	94.00	CRZ	86	40	78	0.5
3	93.96	ULVZ	45	15	10	2
4	93.95	ULVZ	10	10	60	2
5	93.93	CMTZ	-	-	-	1.25
6	93.92	ULVZ	15	5	10	5
7	93.80	ULVZ	5	5	0	10
8	93.74	ULVZ	60	20	0	2
9	93.70	CRZ	72	38	7	1.5
10	93.64	ULVZ	20	20	40	2
11	93.63	CRZ	59	34	24	1.5
12	92.30	PREM	-	-	-	-

3.8f) CTAO *123.9*

No	CCC (%)	Model	-Vs (%)	-Vp (%)	+ρ (%)	h (km)
1	97.99	CRZ	86	40	78	0.5
2	97.99	CRZ	59	34	7	1.5
3	97.97	ULVZ	15	15	40	2
4	97.97	CMTZ	-	-	-	1
5	97.96	ULVZ	10	10	10	5
6	97.96	CRZ	31	22	42	1.5
7	97.95	ULVZ	20	20	40	2
8	97.95	ULVZ	30	30	10	2
9	97.95	ULVZ	45	15	0	2
10	97.94	ULVZ	30	10	20	2
11	97.91	CRZ	72	38	78	0.5
12	96.78	PREM	-	-	-	-

3.8g) SSPA *112.7*

No	CCC (%)	Model	-Vs (%)	-Vp (%)	+ρ (%)	h (km)
1	95.18	ULVZ	15	5	40	5
2	94.94	ULVZ	5	5	20	10
3	94.83	ULVZ	20	20	0	5
4	94.82	CRZ	31	22	42	2.5
5	94.82	ULVZ	45	15	40	2
6	94.79	CRZ	45	28	60	1.5
7	94.77	ULVZ	15	15	10	5
8	94.76	ULVZ	30	10	60	2
9	94.74	CRZ	59	34	42	1.5
10	94.71	CMTZ	-	-	-	1.75
11	94.67	ULVZ	60	20	20	2
12	79.17	PREM	-	-	-	-

3.8h) NRIL *119.2*

No	CCC (%)	Model	-Vs (%)	-Vp (%)	+ρ (%)	h (km)
1	91.05	ULVZ	30	30	60	2
2	90.67	ULVZ	15	15	20	5
3	90.67	ULVZ	10	10	40	5
4	90.66	CRZ	45	28	78	1.5
5	90.63	ULVZ	20	20	10	5
6	90.59	ULVZ	5	5	40	10
7	90.59	ULVZ	5	5	20	10
8	90.51	ULVZ	30	30	40	2
9	90.42	ULVZ	10	10	60	5
10	90.42	CRZ	31	22	42	1.5
11	90.39	CRZ	45	28	60	2
12	84.32	PREM	-	-	-	-

3.8i) WMQ *112.5*

No	CCC (%)	Model	-Vs (%)	-Vp (%)	+ρ (%)	h (km)
1	84.29	ULVZ	20	20	60	2
2	83.74	ULVZ	30	30	20	2
3	83.50	ULVZ	10	10	20	5
4	83.44	ULVZ	5	5	60	5
5	83.38	ULVZ	15	15	0	5
6	83.21	CRZ	31	22	60	1.5
7	82.04	ULVZ	30	10	40	2
8	81.35	ULVZ	15	5	20	5
9	81.09	ULVZ	45	15	10	2
10	80.57	ULVZ	60	20	0	2
11	70.52	CMTZ	-	-	-	0.5
12	59.05	PREM	-	-	-	-

Table 3.5 Average CMB layer thickness

Model[a]				Average thickness, km – (NR)[b]	
	-δVs (%)	-δVp (%)	+δρ (%)	PLVZ	ULVZ[c]
ULVZ	5	5	0	4.7 - (214)	19.3 - (59)
ULVZ	5	5	20	3.4 - (210)	10.6 - (73)
ULVZ	5	5	40	2.8 - (208)	8.8 - (79)
ULVZ	10	10	0	3.4 - (208)	9.6 - (74)
ULVZ	15	5	0	3.0 - (209)	8.2 - (62)
ULVZ	15	5	20	2.4 - (203)	6.7 - (75)
ULVZ	15	5	40	2.3 - (190)	5.6 - (78)
ULVZ	30	10	0	2.2 - (189)	4.7 - (68)
CRZ	86	40	78	0.5 - (180)	0.9 - (59)
CRZ	72	38	78	0.5 - (188)	1.3 - (72)
CRZ	59	34	78	0.6 - (197)	1.4 - (78)
CRZ	59	34	42	0.6 - (206)	1.8 - (81)
CRZ	59	34	7	0.8 - (210)	2.4 - (73)
CMTZ	NA	NA	NA	0.6 - (214)	1.9 - (82)

[a]Percentages are referenced to properties on the mantle-side of the CMB relative to PREM.

[b]NR – Total number of records for which the average was calculated, and for which the specified model has a CC coefficient within 5% of the best-fitting model.

[c]In this last column, "ULVZ" represents any of the CMB boundary layer types (as in ULVZ, CRZ, and CMTZ of the first column)

FIGURES

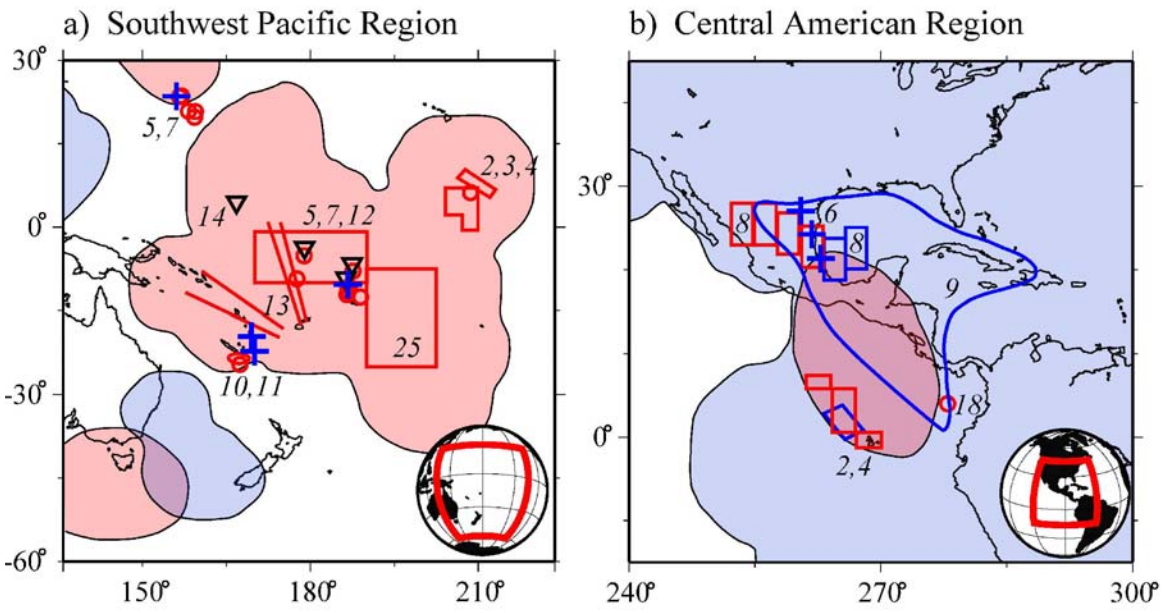

Figure 3.1 Past study results. Panels a) and b) display details of previous studies in the Southwest Pacific and Central American regions of the CMB respectively. The light- red and blue shaded regions correspond to areas where ULVZ have and have not been previously detected (Garnero *et al.* 1998). Red boxes, lines, and circles correspond to locations where anomalous boundary layer structure has been inferred from previous studies as outlined in Table 3.1 (numbers correspond to those of Table 3.1. Blue boxes, crosses, and outlined regions correspond to locations where anomalous boundary layer structure has previously been searched for but not observed. Black triangles correspond to locations where anomalous boundary layer structure may exist, yet data is inconclusive.

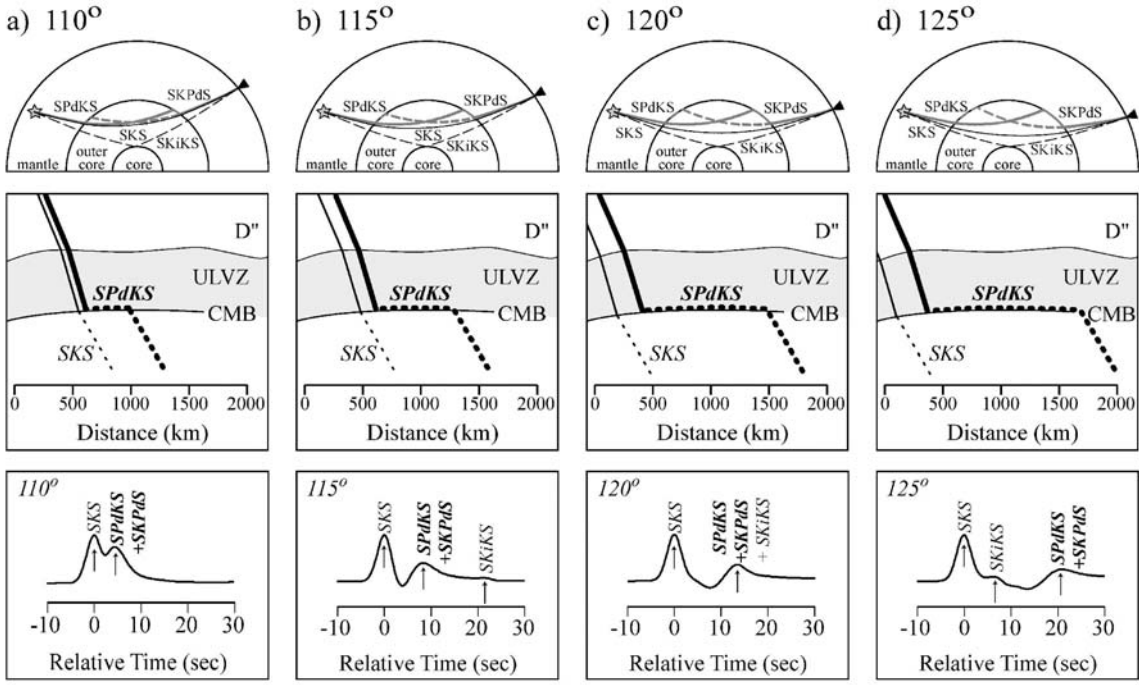

Figure 3.2 Panels a-d show the phases used in this study at four epicentral distances. The top row of each panel shows ray paths for *SKS*, *SPdKS* (both *SPdKS* and *SKPdS*), and *SKiKS*. The center row of each panel zooms in on the ray path of *SKS* and *SPdKS* for each distance. Shown is the lateral distance along the CMB of the P_{diff} portion of *SPdKS* and the amount of lateral separation between *SKS* and *SPdKS* (calculated for the PREM model), with the vertical scale exaggerated. The bottom panel shows PREM synthetic seismograms highlighting the arrivals at each distance.

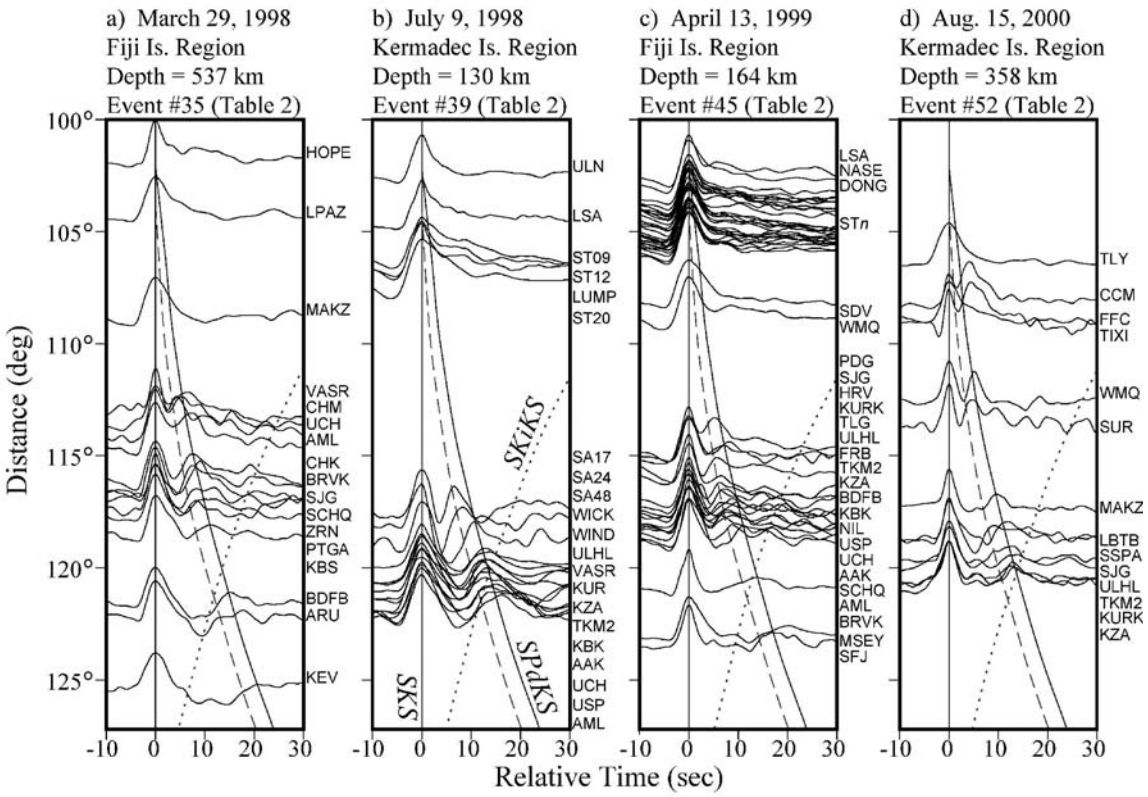

Figure 3.3 Distance profiles for four events. The radial component of displacement is shown. All records are normalized and centered on the *SKS* peak. The predicted *SPdKS* arrival for PREM is a dashed gray line and for a ULVZ model is a solid black line. (ULVZ model: δV_P = -5%, δV_S = -15%, $\delta\rho$ = +10%, thickness = 10 km). The dotted gray line shows the PREM prediction for the phase *SKiKS*. The recording station is shown to the right of each trace. STn in panel c) corresponds to 26 stations from the INDEPTH III PASSCAL experiment.

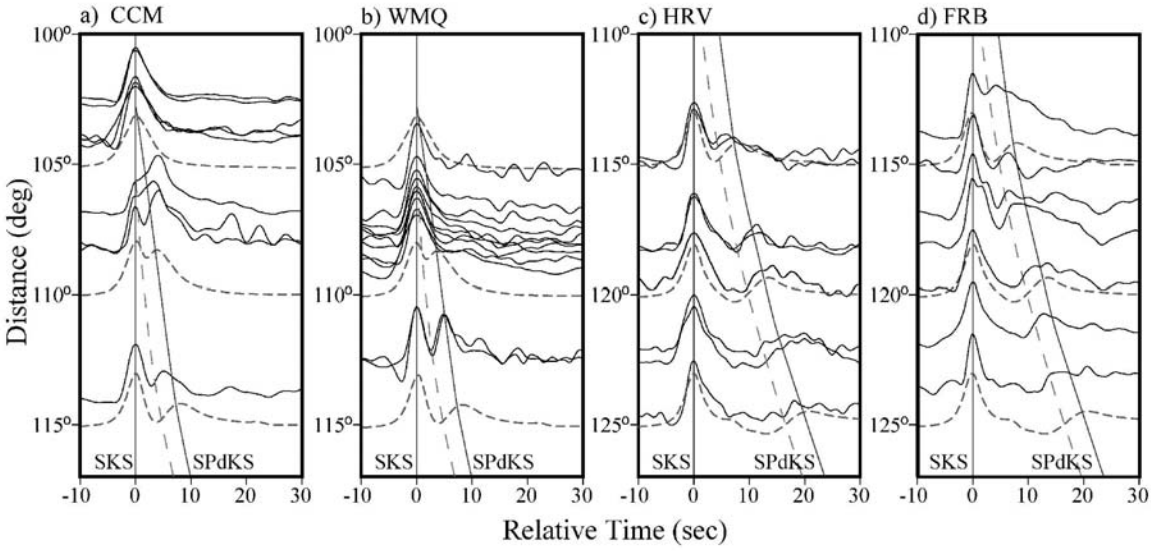

Figure 3.4 The radial component of displacement of four recording stations is shown. All records are normalized and centered on the *SKS* peak. Each record is shifted in distance to accommodate varying source depth. The predicted arrival for *SPdKS* is shown for PREM (dashed gray line) and for a ULVZ model (solid black line; ULVZ model: δV_P = -5%, δV_S = -15%, $\delta\rho$ = +10%, thickness = 10 km). Also shown (dashed lines) are representative synthetic seismograms for this ULVZ model. Stations shown are a) Cathedral Caves, Missouri, USA; b) Urumqi, Xinjiang, China; c) Harvard, Massachusetts, USA; and d) Frobisher Bay, Canada.

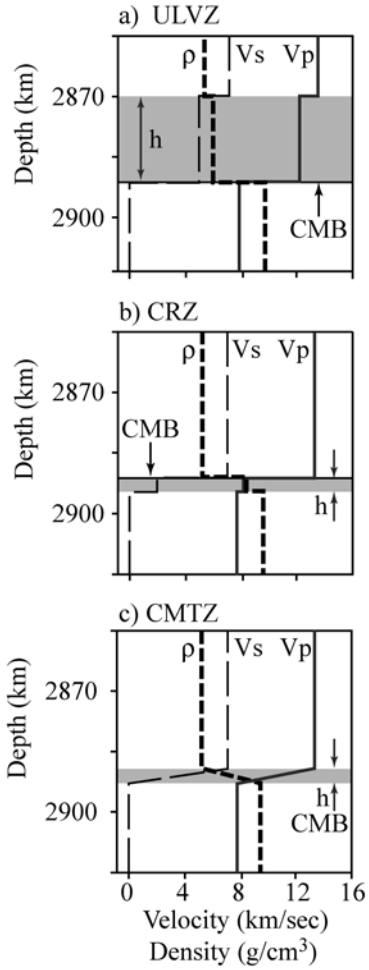

Figure 3.5 Panels a, b, and c show the velocity and density profiles with depth for ULVZ, CRZ, and CMTZ models respectively. In panels a) and b), h represents the thickness over which mantle or core properties are modified for ULVZ or CRZ models. In panel c, h represents the thickness over which the transition between mantle and core properties is modeled. Relevant parameters (compared to PREM on the mantle-side) for models shown are: a) δV_S = -30%, δV_P = -10%, $\delta\rho$ = +10%, h = 20 km; b) δV_S = -72%, δV_P = -38%, $\delta\rho$ = +60%, h= 3 km; and c) h = 3 km.

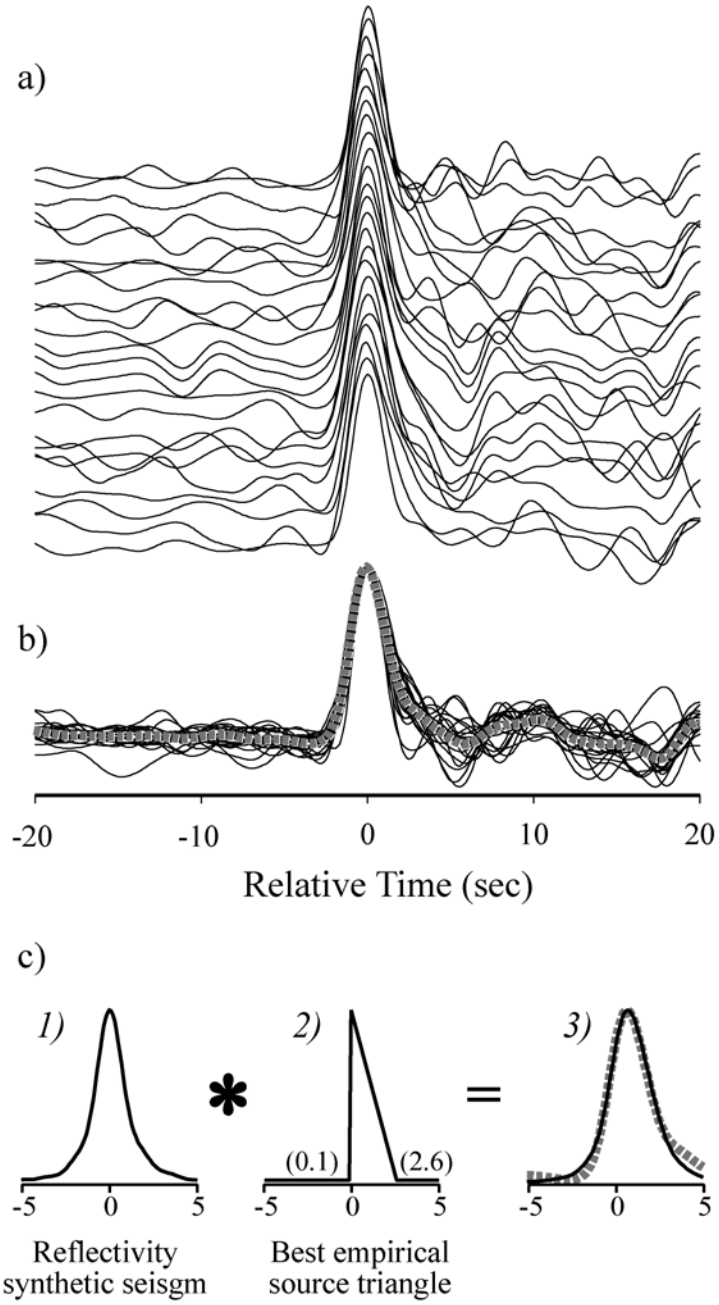
a)
b)
-20
-10
0
10
20
Relative Time (sec)
c)
1)
2)
3)
(0.1)
(2.6)
-5
0
5
Reflectivity
synthetic seisgm
Best empirical
source triangle

Figure 3.6 Empirical source modeling. Panel a) displays 24 records windowed, centered, and normalized on the *SKS* peak for the April 14, 1998 Fiji Islands event (#37 Table 2). The traces are all records accepted for stacking with a cross-correlation coefficient of at least 0.85, in the distance range of 92º - 98º. In panel b), the individual traces are overlain, with the dashed gray line indicating the resulting stack. Panel c) displays the method of determining the empirical source, by 1) taking the synthetic seismogram centered on *SKS* at 95º epicentral distance and, 2) convolving the synthetic with a triangle or truncated triangle function (in this case, a triangle function with width 0.1 sec to the left of zero and 2.6 sec to the right of zero) that best fits the stacked data (dashed gray line) shown in 3.

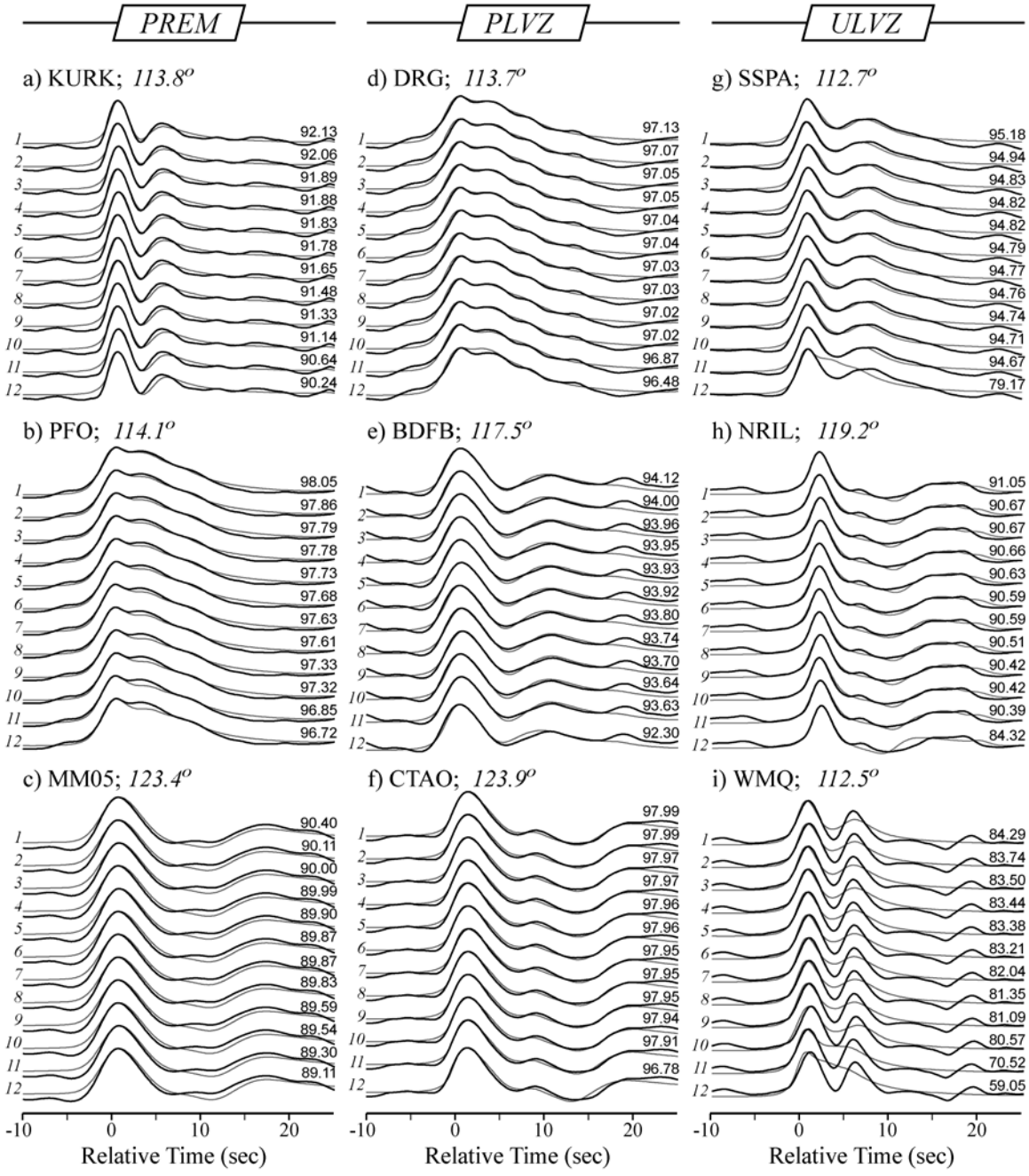
PREM
PLVZ
ULVZ
a) KURK; 113.8°
92.13
92.06
91.89
91.88
91.83
91.78
91.65
91.48
91.33
91.14
90.64
90.24
d) DRG; 113.7°
97.13
97.07
97.05
97.05
97.04
97.04
97.03
97.03
97.02
97.02
96.87
96.48
g) SSPA; 112.7°
95.18
94.94
94.83
94.82
94.82
94.79
94.77
94.76
94.74
94.71
94.67
79.17
b) PFO; 114.1°
98.05
97.86
97.79
97.78
97.73
97.68
97.63
97.61
97.33
97.32
96.85
96.72
e) BDFB; 117.5°
94.12
94.00
93.96
93.95
93.93
93.92
93.80
93.74
93.70
93.64
93.63
92.30
h) NRIL; 119.2°
91.05
90.67
90.67
90.66
90.63
90.59
90.59
90.51
90.42
90.42
90.39
84.32
c) MM05; 123.4°
90.40
90.11
90.00
89.99
89.90
89.87
89.87
89.83
89.59
89.54
89.30
89.11
f) CTAO; 123.9°
97.99
97.99
97.97
97.97
97.96
97.96
97.95
97.95
97.95
97.94
97.91
96.78
i) WMQ; 112.5°
84.29
83.74
83.50
83.44
83.38
83.21
82.04
81.35
81.09
80.57
70.52
59.05
-10
0
10
20
Relative Time (sec)

Figure 3.7 Cross-correlation of records with model synthetics. Panels a,b,c show records classified as PREM; panels d,e,f show example records classified as PLVZ; panels g,h show records classified as ULVZ; and panel i is an example of a record classified as ELVZ. The dark line is data, repeated through each panel compared to the light colored line of the synthetics. Epicentral distances and station names for each record section is shown above the traces. Just above each data/model overlay on the right is the CCC of the record compared to the model synthetic. Model details are contained in Table 4 (numbers to the left of each trace correspond with Table 3.4) Events used to make this figure are for those listed in Table 3.2 for the following dates. KURK: Dec. 18, 2000; PFO: Dec. 25, 1995; MMO5: Aug 14, 1995; DGR: Dec. 25, 1995; BDFB: April 13, 1999; CTAO: May 10, 1994; SSPA: May 16, 1998; NRIL: March 21, 1997; WMQ: Aug 15, 2000.

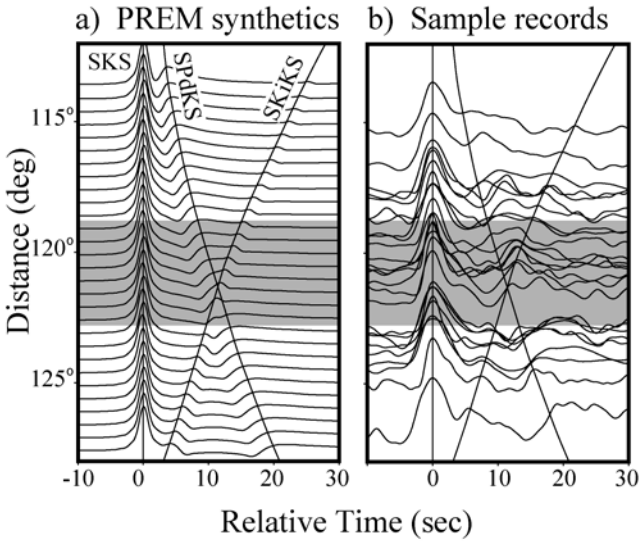

Figure 3.8 Panel a) shows sample PREM synthetic seismograms centered and normalized on *SKS* for a 400 km deep event. Black lines show predicted arrivals for *SPdKS* and *SKiKS*. *SKiKS* is observed to interfere with *SPdKS* waveforms in the dark shaded region. Panel b) shows 26 records from varying events centered on *SKS* and shifted to a common source depth of 400 km.

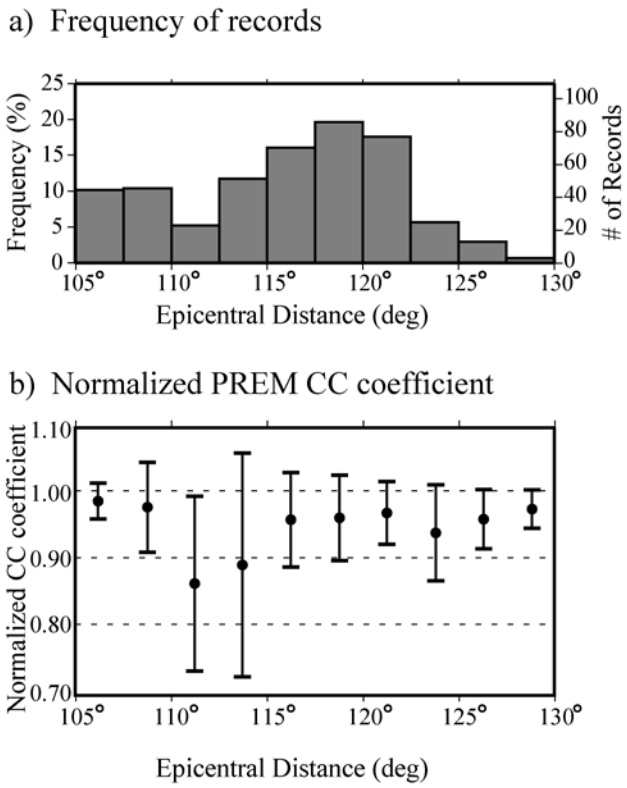

Figure 3.9 Panel a) shows the amount of records used in this study grouped into 2.5º epicentral distance bins. Panel b) shows the average and 1 standard deviation of all normalized cross-correlation coefficients grouped in the same distance bins as in panel a). The normalized cross-correlation coefficient is: cross-correlation coefficient for a PREM synthetic compared to a record/cross-correlation coefficient for the synthetic of the best fitting model for a record.

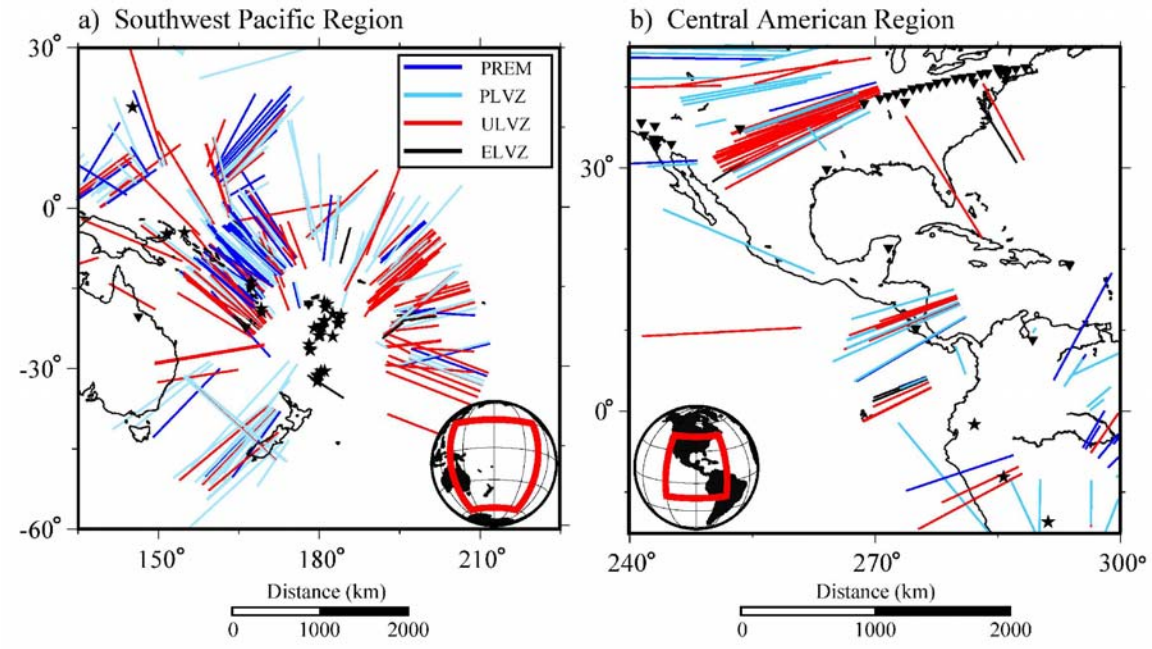

Figure 3.10 Shown in panels a) and b) are regional maps centered in the Southwest Pacific and Central American regions respectively. Lines drawn represent the P_{diff} segments of *SPdKS* on the CMB. Dark blue lines represent paths for which the waveforms behaved as PREM. Light blue lines represent paths that are characterized as PLVZ. Red lines are used for waveforms that are characterized as ULVZ and black lines represent ELVZ waveforms. Stars indicate event locations and triangles represent station locations. The distance scale beneath each panel is the distance at the equator on the CMB.

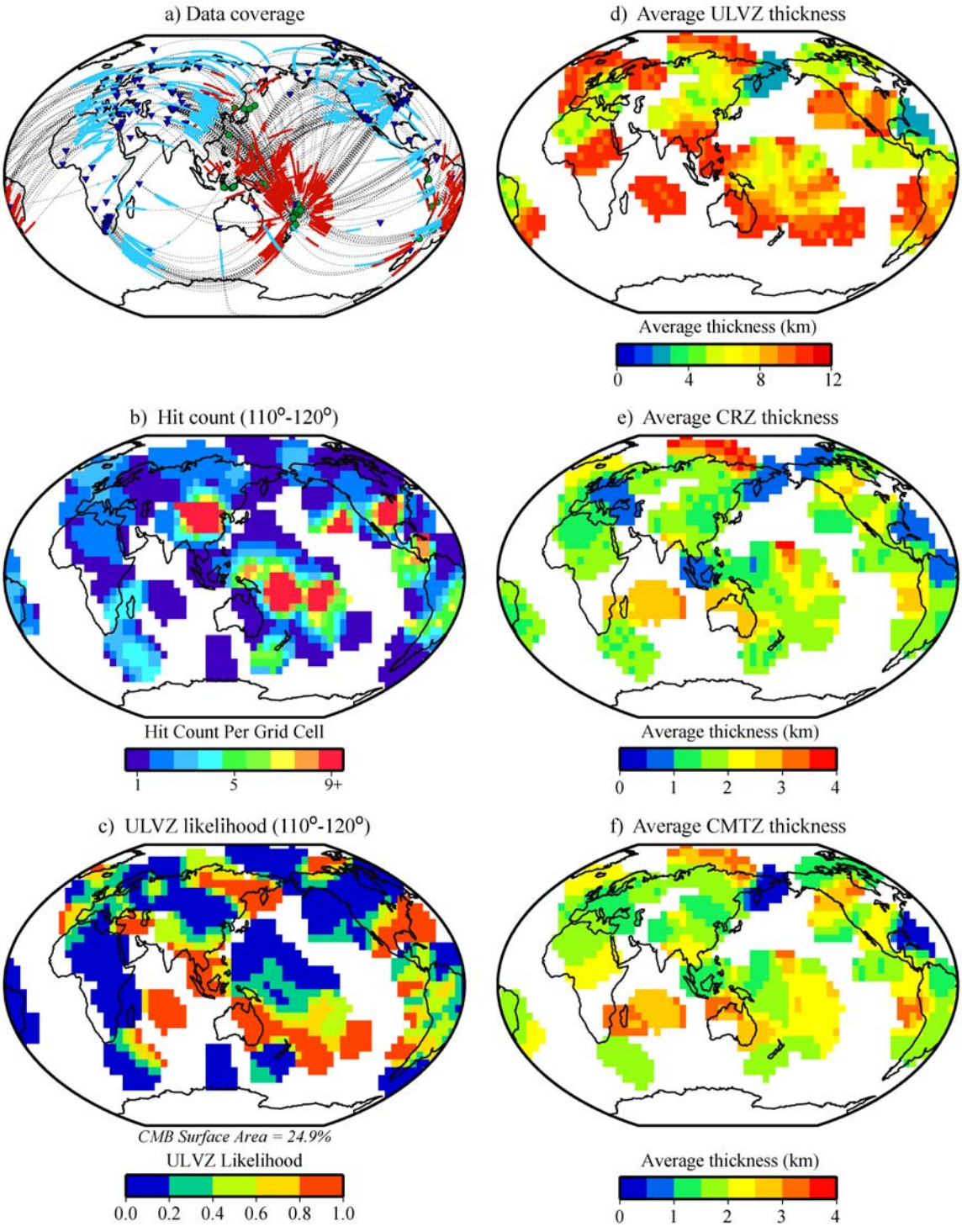
a) Data coverage
d) Average ULVZ thickness
Average thickness (km)
0
4
8
12
b) Hit count (110°-120°)
e) Average CRZ thickness
Hit Count Per Grid Cell
1
5
9+
Average thickness (km)
0
1
2
3
4
c) ULVZ likelihood (110°-120°)
f) Average CMTZ thickness
CMB Surface Area = 24.9%
ULVZ Likelihood
0.0
0.2
0.4
0.6
0.8
1.0
Average thickness (km)
0
1
2
3
4

Figure 3.11 a) Total data coverage. Green circles are stations and blue triangles are events. Dotted lines show great circle paths between events and stations, and solid red and light-blue lines show the P_{diff} portion of *SPdKS* and *SKPdS* on the CMB respectively. Panel b) shows the earth divided into 5° × 5° cells colored by the number of P_{diff} segments on the CMB that pass through each grid cell. Panel c) shows the earth divided into the same grid colored by ULVZ likelihood, where a value of 1.0 signifies that all P_{diff} segments on the CMB passing through the cell had waveforms that behaved as ULVZ, and a value of 0.0 indicates that all P_{diff} segments passing through the cell had waveforms behaving as PREM. The result is shown for the most characteristic data between 110° and 120°. Shown in italics below the projection is the total percentage of CMB surface area of grid cells with P_{diff} segments passing through them. d-f) The average thickness is shown for ULVZ, CRZ and CMTZ models averaged in the same grid spacing. ULVZ model properties in panel d) are δV_S = -15%, δV_P = -5%, $\delta\rho$ = +5%. CRZ model properties in panel e) are δV_S = -59%, δV_P = -34%, $\delta\rho$ = +42%. Model thickness is only averaged for records where the model is within 5% of the best fitting model. For comparison of thickness with other ULVZ models, scaling may be applied as suggested in Table 3.5.

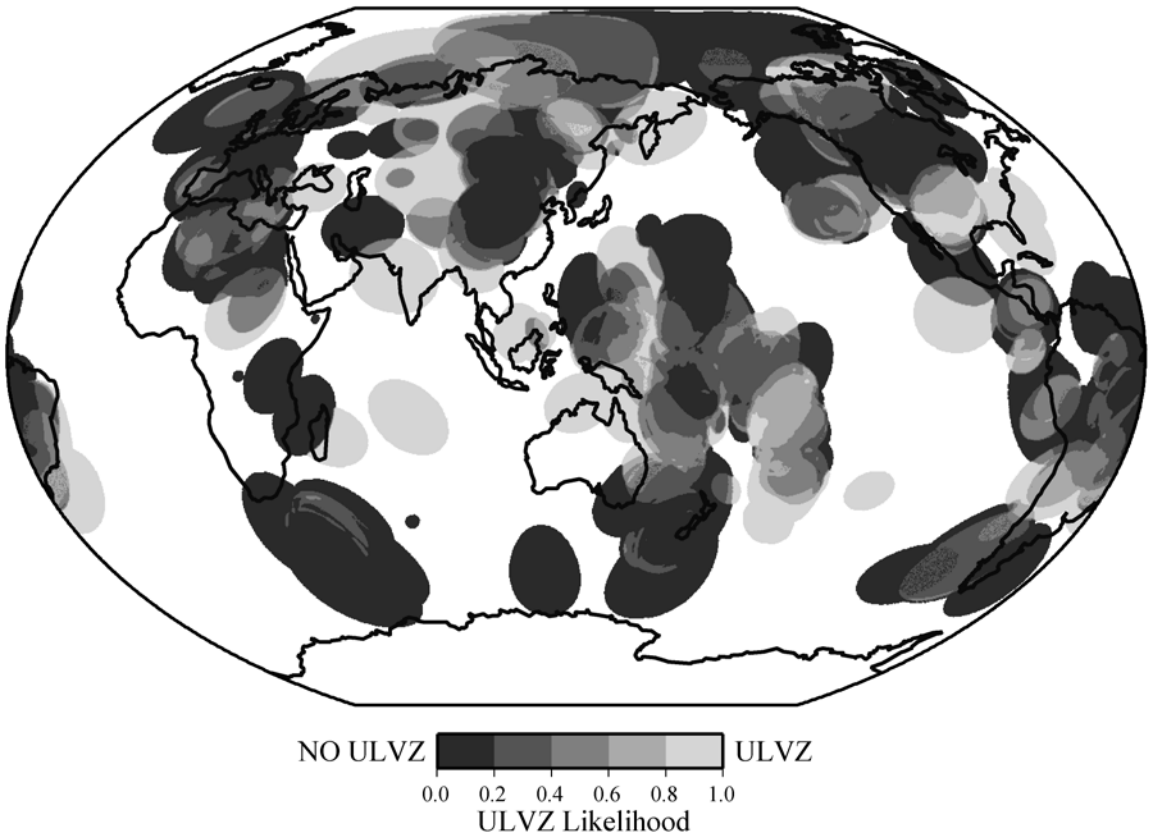

Figure 3.12 Shown are Fresnel zones for P_{diff} segments of *SPdKS* on the CMB shaded by ULVZ likelihood, where ULVZ likelihood is as described in Figure 3.11. Fresnel zones are calculated for ¼ wavelength with a dominant period of 10 sec for a ULVZ model with a V_P reduction of 10%.

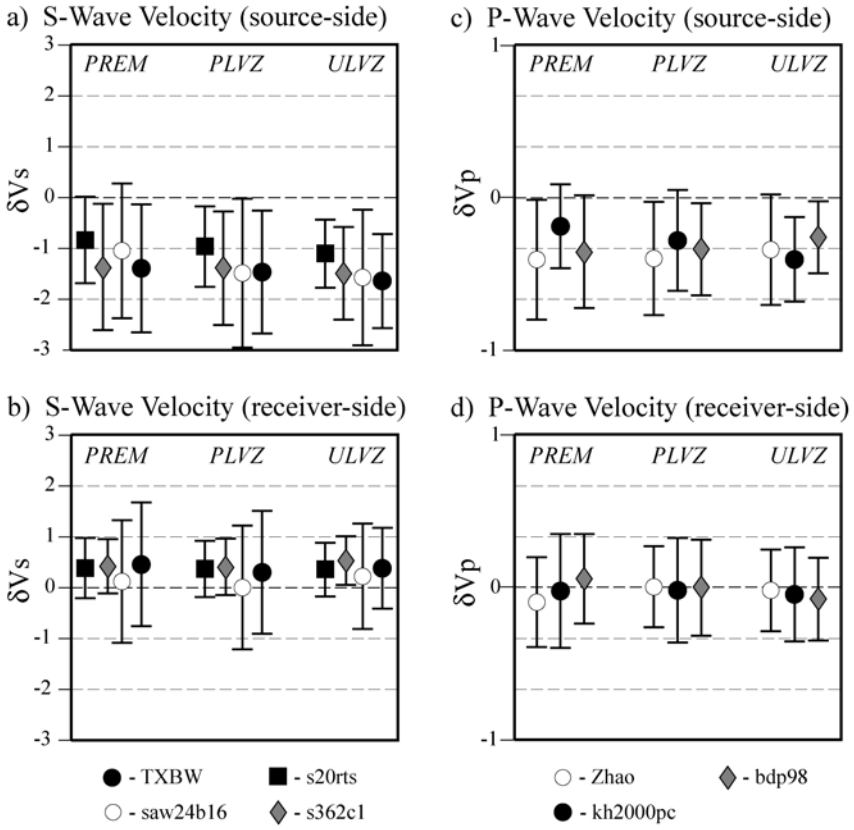

Figure 3.13 Shown is the comparison between *SPdKS* source- and receiver-side arcs with four *S*-wave and three *P*-wave tomography models. The comparison is carried out for all data with source-receiver distances between 110º-120º. For each tomographic model, the average and standard deviation of the lowest velocity encounterd along a P_{diff} segment are shown. Individual model results are grouped into categories of PREM, PLVZ, and ULVZ waveform classifications. *S*-wave models are: TXBW (Grand 2002), saw24b16 (Megnin & Romanowicz 2000), s20rts (Ritsema & van Heijst 2000), and s362c1 (Gu *et al.* 2001). *P*-wave models are: kh2000pc (Kárason & van der Hilst 2001), Zhao (Zhao 2001), bdp98 (Boschi & Dziewonski 1999).

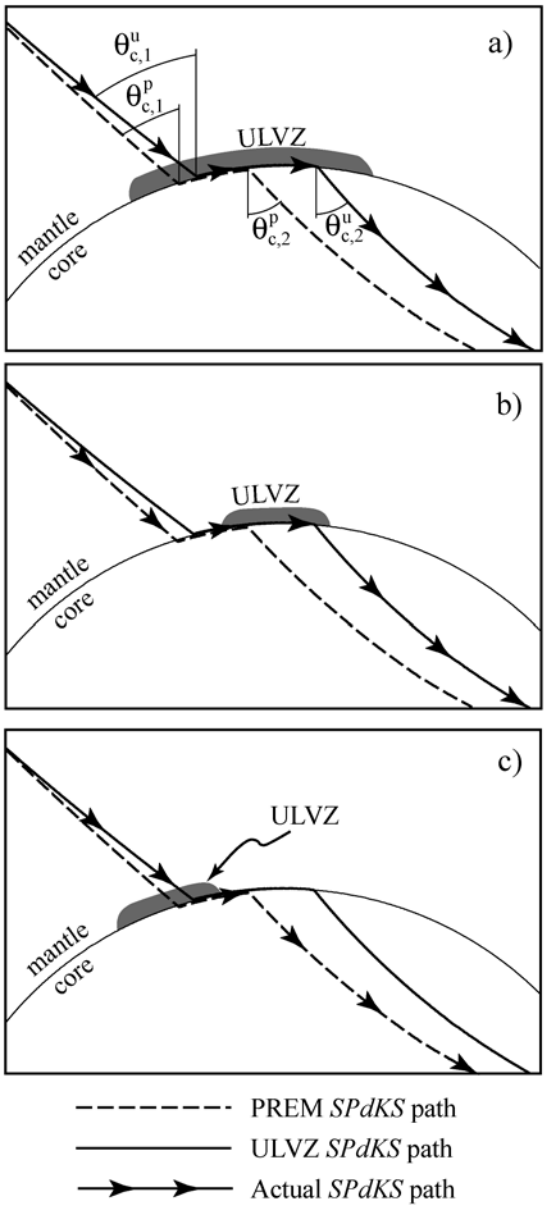
a)
$\theta^u_{c,1}$
$\theta^p_{c,1}$
ULVZ
$\theta^p_{c,2}$
$\theta^u_{c,2}$
mantle
core
b)
ULVZ
mantle
core
c)
ULVZ
mantle
core
PREM *SPdKS* path
ULVZ *SPdKS* path
Actual *SPdKS* path

Figure 3.14 The source-side *SPdKS* ray path geometry is shown for three different possibilities of ULVZ location. The dashed line indicates the path *SPdKS* would take if the mantle were purely PREM, and the solid line indicates the path *SPdKS* would take if there existed a 30 km thick ULVZ (δV_S = -15%, δV_P = -5%, $\delta\rho$ = +0%) at the base of the mantle. Arrows outline the actual path *SPdKS* takes. In panel a), the ray path encounters the ULVZ and becomes critical at an angle of $\theta^u_{c,1}$. The P_{diff} path continues through the ULVZ and exits at the same critical angle $\theta^u_{c,2}$. If the ULVZ did not exist, the ray path would follow the PREM prediction and become critical at angle $\theta^p_{c,1}$ with the P_{diff} path also exiting at that angle ($\theta^p_{c,2}$). In panel b), no ULVZ exists at the inception point of P_{diff} and becomes critical at angle $\theta^p_{c,1}$. However, P_{diff} encounters the ULVZ along its path and thus exits at the critical angle for the ULVZ model $\theta^u_{c,2}$. In panel c) the situation is reversed from panel b). The geometry of the ray paths was calculated for a source-receiver distance of 115° and a source depth of 500 km.

SUPPLEMENTAL FIGURES

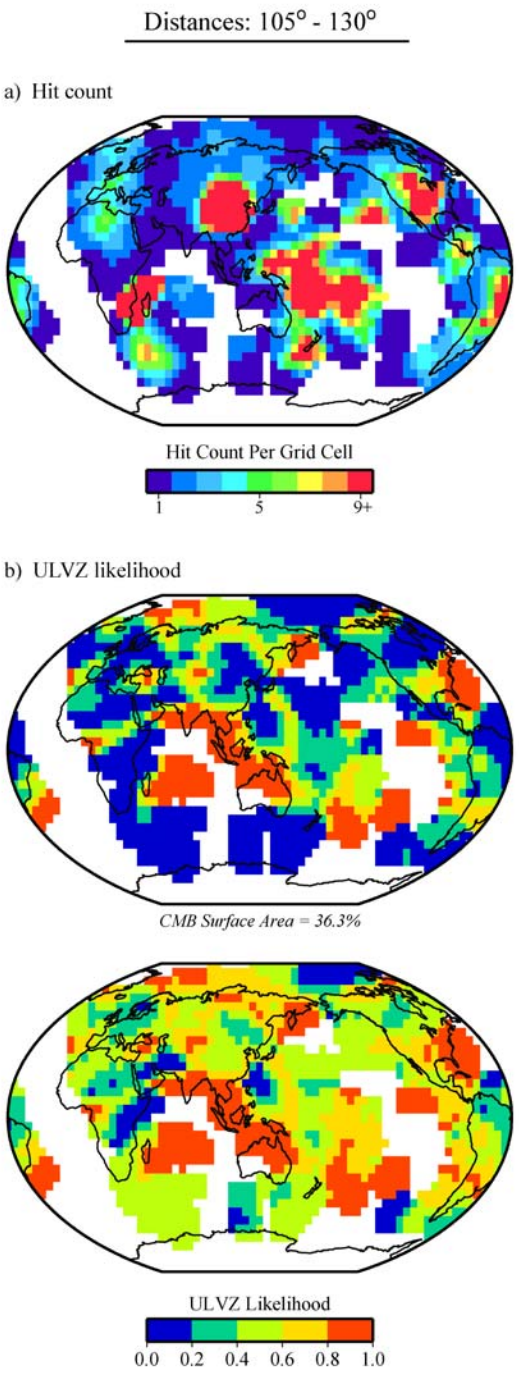

Supplement 3A Panel a shows the earth divided into 5° x 5° cells colored by the number of P_{diff} segments on the CMB that pass through each grid cell. The result is shown for all data used in this study in the distance range 105° to 130°. Panel b shows the earth divided into 5° x 5° cells colored by ULVZ likelihood, where a value of 1.0 signifies that all P_{diff} segments on the CMB passing through the cell had waveforms that behaved as ULVZ, and a value of 0.0 indicates that all P_{diff} segments passing through the cell had waveforms behaving as PREM. The result is shown when all data is included. For the top figure of panel b, ULVZ likelihood calculations were made with PREM- and PLVZ-waveforms given a value=0, and ULVZ- and ELVZ-waveforms given a value=1. For the bottom plot of panel b, PREM-waveforms were given a value=0, PLVZ-waveforms were given a value=0.5, and ULVZ- and ELVZ-waveforms were given a value=1. This figure differs from Figure 3.11, in that PLVZ-waveforms were there given a value=0, and this figure also shows the result when considering our entire data set. The bottom figure of panel b shows the pervasiveness of ULVZ structure that may exist if PLVZ-waveforms actually represent thin ULVZ structure.

CHAPTER 4

COMPUTING HIGH FREQUENCY GLOBAL SYNTHETIC SEISMOGRAMS USING AN AXI-SYMMETRIC FINITE DIFFERENCE APPROACH

Michael S. Thorne[1]

[1]Dept. of Geological Sciences, Arizona State University, Tempe, AZ 85287, USA

4.1 Introduction

Resolving Earth's seismic structure is crucial in order to understand Earth's dynamics, composition, and evolution. Waveform modeling is an exceptional tool for modeling Earth's seismic structure, by comparing real seismograms with synthetic seismograms computed for realistic Earth models. Numerous techniques for computing synthetic seismograms by solving the wave equation for seismic wave propagation have been developed over the last 40 years. Many of these techniques have been based on analytical solutions and/or the assumption of spherical symmetry (e.g., Helmberger 1968; Fuchs & Müller 1971; Woodhouse & Dziewonski 1984). Recently, advances in distributed memory, or cluster, computing have made numerical techniques for solving the wave equation viable, thus allowing computation of synthetic seismograms for a wide range of heterogeneous Earth models at frequencies relevant to broadband and short period waveform modeling.

Numerical techniques are important because synthetic seismograms can be computed for models of a highly heterogeneous nature where analytical solutions may be difficult to obtain. Finite difference (FD) techniques are the most common numerical techniques in practice; however other numerical techniques are also used frequently. The most common numerical techniques currently in use are:

1) pseudo-spectral technique (e.g., Fornberg 1987; Furumura *et al.* 1998; Cormier 2000),

2) spectral element technique (e.g., Komatitsch & Tromp, 2002),

3) finite element technique (e.g., Smith 1975), and

4) finite volume technique (e.g., Dormy & Tarantola 1995).

Each technique has strengths and weaknesses and may be suitable for different styles of problems (see Carcione *et al.* 2002 for a review).

Finite difference techniques have been used to calculate seismic wave propagation for nearly 40 years since the first applications by Alterman & Karal (1968) and Alterman *et al.* (1970). Madariaga (1976) was the first to use a velocity-stress FD formulation, the most common formulation currently in use. The first 2-D Cartesian grid FD simulations were carried out for *SH*-waves by Virieux (1984) and Vidale *et al.* (1985). Virieux (1986) and Levander (1988) carried out the first 2-D Cartesian grid FD simulations for *P-SV* wave propagation. The first 3-D Cartesian grid FD simulations were performed shortly thereafter (e.g., Randall 1989). All of the aforementioned simulations were limited to small regional dimensions, mostly due to limited computational resources. An abundance of studies on FD methods for wave propagation have been developed over the decades and an excellent overview is given in Moczo *et al.* (2004).

In this paper we apply a 3-D axi-symmetric FD approach. First we outline the method, then show an example application of the method by simulating seismic coda waves through models containing randomly distributed heterogeneous *S*-wave velocity

perturbations. This is the first study in which a FD technique has been employed for whole mantle scattering.

4.2 3-D axi-symmetric finite difference wave propagation

The 3-D axi-symmetric FD method for SH-waves (SHaxi) is developed because it is less computationally expensive than fully 3-D methods. This is because axi-symmetry allows the calculation to be performed on a 2-D grid. Hence, we are able to obtain frequencies relevant to broadband waveform modeling (e.g., up to 1 Hz dominant frequencies) that are not currently feasible using 3-D methods. The axi-symmetric approach is also attractive as the correct 3-D geometrical spreading is naturally incorporated which fully 2-D techniques must approximate.

Axi-symmetric FD methods have been applied in the past. Igel & Weber (1995) were the first to compute axi-symmetric wave propagation for *SH*-waves. The technique was then applied to studying long period *SS*-precursors by Chaljub & Tarantola (1997). Igel & Gudmundsson (1997) also used the method to study frequency dependent effects of *S* and *SS* waves. Igel & Weber (1996) developed an axi-symmetric approach for *P-SV* wave propagation. Thomas *et al.* (2000) developed an axi-symmetric method for acoustic wave propagation and applied the technique to studying precursors to *PKPdf*. Recently, Toyokuni *et al.* (2005) have also developed an axi-symmetric method for *SH*-wave propagation.

The axi-symmetric FD technique for *SH*-waves (SHaxi) first developed by Igel & Weber (1995) has recently been expanded to operate on distributed memory computers

and to include higher order FD operators (Jahnke *et al.* 2005). These advances have given the SHaxi technique the ability to compute synthetic seismograms for higher frequencies (up to 1 Hz) than have previously been possible. In this Section we present the technique behind SHaxi. Verification of the SHaxi method is presented in Jahnke *et al.* (2005).

4.2.1 The axi-symmetric wave equation

The displacement-stress formulation of the wave equation in spherical coordinates can be written as follows:

$$\rho\frac{\partial^2 u_r}{\partial^2 t}=\frac{\partial\sigma_{rr}}{\partial r}+\frac{1}{r}\frac{\partial\sigma_{r\theta}}{\partial\theta}+\frac{1}{r\sin\theta}\frac{\partial\sigma_{r\varphi}}{\partial\varphi}+\frac{1}{r}\left(2\sigma_{rr}-\sigma_{\theta\theta}-\sigma_{\varphi\varphi}+\sigma_{r\theta}\cot\theta\right)+f_r \tag{4-1}$$

$$\rho\frac{\partial^2 u_\theta}{\partial^2 t}=\frac{\partial\sigma_{r\theta}}{\partial r}+\frac{1}{r}\frac{\partial\sigma_{\theta\theta}}{\partial\theta}+\frac{1}{r\sin\theta}\frac{\partial\sigma_{\theta\varphi}}{\partial\varphi}+\frac{1}{r}\left(\left(\sigma_{\theta\theta}-\sigma_{\varphi\varphi}\right)\cot\theta+3\sigma_{r\theta}\right)+f_\theta \tag{4-2}$$

$$\rho\frac{\partial^2 u_\varphi}{\partial^2 t}=\frac{\partial\sigma_{r\varphi}}{\partial r}+\frac{1}{r}\frac{\partial\sigma_{\theta\varphi}}{\partial\theta}+\frac{1}{r\sin\theta}\frac{\partial\sigma_{\varphi\varphi}}{\partial\varphi}+\frac{1}{r}\left(3\sigma_{r\varphi}+2\sigma_{\theta\varphi}\cot\theta\right)+f_\varphi\,, \tag{4-3}$$

where ρ is density, u is displacement, σ is stress and *f* is a body force. The coordinate system adopted is displayed in Figure 4.1.

For the case of *SH*-wave propagation we are only concerned with the displacement in the φ-direction therefore only eq. (4-3) is applicable. Because of axi-symmetry the $\partial/\partial\varphi$ terms go to zero and eq. (4-3) reduces to:

$$\rho\frac{\partial^2 u_\varphi}{\partial^2 t}=\frac{\partial\sigma_{r\varphi}}{\partial r}+\frac{1}{r}\frac{\partial\sigma_{\theta\varphi}}{\partial\theta}+\frac{1}{r}\left(3\sigma_{r\varphi}+2\sigma_{\theta\varphi}\cot\theta\right)+f_\varphi\,. \tag{4-4}$$

Vireux (1984) showed that FD simulations can attain greater accuracy using a staggered grid (see Section 4.3.1) and the velocity-stress formulation. The SHaxi method adopts this staggered grid and velocity-stress formulation, thus we are left with the following axi-symmetric wave equation to solve:

$$\rho \frac{\partial v_\varphi}{\partial t} = \frac{\partial \sigma_{r\varphi}}{\partial r} + \frac{1}{r}\frac{\partial \sigma_{\theta\varphi}}{\partial \theta} + \frac{1}{r}\left(3\sigma_{r\varphi} + 2\sigma_{\theta\varphi}\cot\theta\right) + f_\varphi, \tag{4-5}$$

where v, is the velocity.

4.2.2 The strain tensor

Solving the wave equation as presented in eq. (4-5) consists of a two-step procedure. In the first step we update the strain tensor from the velocity field and then calculate the stress tensor from the strain tensor. Once the stress tensor is updated we can update the velocity field in the second step from equation (4-5). Equation 1.56 of Ben-Menahem & Singh (1981) gives the expressions for the strain tensor in spherical coordinates:

$$\varepsilon_{rr} = \frac{\partial u_r}{\partial r} \tag{4-6}$$

$$\varepsilon_{\theta\theta} = \frac{1}{r}\left(\frac{\partial u_\theta}{\partial \theta} + u_r\right) \tag{4-7}$$

$$\varepsilon_{\varphi\varphi} = \frac{1}{r}\left(\frac{1}{\sin\theta}\frac{\partial u_\varphi}{\partial \varphi} + u_r + u_\theta \cot\theta\right) \tag{4-8}$$

$$\varepsilon_{\theta\varphi} = \varepsilon_{\varphi\theta} = \frac{1}{2r}\left(\frac{\partial u_\varphi}{\partial \theta} - u_\varphi \cot\theta + \frac{1}{\sin\theta}\frac{\partial u_\theta}{\partial \varphi}\right) \tag{4-9}$$

$$\varepsilon_{\varphi r} = \varepsilon_{r\varphi} = \frac{1}{2}\left(\frac{1}{r\sin\theta}\frac{\partial u_r}{\partial \varphi} + \frac{\partial u_\varphi}{\partial r} - \frac{u_\varphi}{r} \right) \tag{4-10}$$

$$\varepsilon_{r\theta} = \varepsilon_{\theta r} = \frac{1}{2}\left(\frac{\partial u_\theta}{\partial r} - \frac{u_\theta}{r} + \frac{1}{r}\frac{\partial u_r}{\partial \theta} \right), \tag{4-11}$$

where ε is the strain. For SHaxi we can see from inspection with eq. (4-5) that only $\sigma_{\theta\varphi}$ and $\sigma_{r\varphi}$ need to be calculated. Hence we only need to calculate the strain components $\varepsilon_{\theta\varphi}$ and $\varepsilon_{r\varphi}$ from eqs. (4-9) and (4-10). In the axi-symmetric velocity-stress formulation these two equations reduce to:

$$\frac{\partial \varepsilon_{\theta\varphi}}{\partial t} = \frac{1}{2r}\left(\frac{\partial v_\varphi}{\partial \theta} - v_\varphi \cot\theta \right) \tag{4-12}$$

$$\frac{\partial \varepsilon_{r\varphi}}{\partial t} = \frac{1}{2}\left(\frac{\partial v_\varphi}{\partial r} - \frac{v_\varphi}{r} \right). \tag{4-13}$$

4.2.3 The stress tensor

Once the strain tensor is determined, the stress calculation is straightforward. From Hooke's Law:

$$\sigma_{rr} = \lambda\Delta + 2\mu\varepsilon_{rr} + M_{rr} \tag{4-14}$$

$$\sigma_{\varphi\varphi} = \lambda\Delta + 2\mu\varepsilon_{\theta\theta} + M_{\theta\theta} \tag{4-15}$$

$$\sigma_{\varphi\varphi} = \lambda\Delta + 2\mu\varepsilon_{\varphi\varphi} + M_{\varphi\varphi} \tag{4-16}$$

$$\sigma_{r\theta} = 2\mu\varepsilon_{r\theta} + M_{r\theta} \tag{4-17}$$

$$\sigma_{\theta\varphi} = 2\mu\varepsilon_{\theta\varphi} + M_{\theta\varphi} \tag{4-18}$$

$$\sigma_{r\varphi} = 2\mu\varepsilon_{r\varphi} + M_{r\varphi}, \tag{4-19}$$

where λ and μ are the Lamé parameters (μ is the shear modulus), Δ is the dilatation or trace of the strain tensor, and M is the seismic moment. For the *SH*-case, only eqs. (4-18) and (4-19) need to be calculated. In general seismic sources can be added to the simulation by addition of appropriately scaled moment tensor elements (M_{ij}) in this step (e.g., Coutant 1995; Graves 1996). However, direct application of moment tensor elements may be challenging in SHaxi due to the axi-symmetric boundary condition and we do not concern ourselves with moment tensor addition. A description of how the source is implemented is given in Section 4.3.6.

4.3 Finite difference implementation

4.3.1 Finite difference grid

SHaxi solves the wave equation on a 2-D grid as shown in Figure 4.2. The grid is bound between radii of 3480 to 6371 km, and theta values between 0° and 180°. A few grid points exist outside of these bounds in order to compute the boundary conditions (see Section 4.3.3). Virieux (1986) introduced a staggered grid system for FD simulations of the wave equation, which improved numerical accuracy over other grid systems. As a result most current FD methods for solving the wave equation incorporate the staggered grid formulation (e.g., Coutant *et al.* 1995; Igel & Weber 1995; 1996, Graves 1996; Chaljub & Tarantola, 1997; Igel *et al.* 2001; Takenaka *et al.* 2003). Detail of the staggered FD grid used by SHaxi is shown in Figure 4.3. The correspondence between grids shown in Figures 4.2 and 4.3 can be seen in that each grid point crossing shown in Figure 4.2 corresponds to a velocity (v_φ) grid point in Figure 4.3.

It can be shown that the staggered grid produces more accurate results by considering the error in FD approximations (Igel, 2002). Using a staggered grid system, the spatial derivatives of discrete fields such as velocity or stress, are calculated halfway between the defined grid points. The SHaxi method utilizes a centered difference FD scheme. For example, using a two-point finite difference operator we may approximate the spatial derivative as follows:

$$\frac{\partial f}{\partial x} \approx \frac{f(x+dx) - f(x-dx)}{2dx}. \tag{4-20}$$

If we expand equation 4-2-22 using a Taylor series expansion, recalling that the Taylor series expansion is given by:

$$f(x \pm dx) = f(x) \pm dxf'(x) + \frac{dx^2}{2!} f''(x) \pm \frac{dx^3}{3!} f'''(x) + \frac{dx^4}{4!} f''''(x) \pm \ldots. \tag{4-21}$$

Then we may rewrite 4-2-22 as:

$$\frac{f(x+dx/2) - f(x-dx/2)}{dx} = \frac{1}{dx}\left[dxf'(x) + \frac{dx^3}{3!} f'''(x) + \ldots \right] = f'(x) + O(dx^2). \tag{4-22}$$

The error of the first derivative is of the order dx^2, or is proportional to the size of the FD grid step over which the derivative is approximated. Reducing the size of the grid step by half reduces the error of the approximation by a factor of four.

4.3.2 Boundary Conditions

There are two cases of boundary conditions in SHaxi. The first case occurs at the symmetry axes (located at θ=0° and θ=180°; see Figure 4.2). At the symmetry axes a reflecting boundary condition is defined as:

$$
\begin{aligned}
&v_\varphi\big|_{\theta=0,\theta=\pi} = 0 \\
&v_\varphi\big|_{\theta=-nd\theta} = v_\varphi\big|_{\theta=+nd\theta} \\
&v_\varphi\big|_{\theta=\pi+nd\theta} = v_\varphi\big|_{\theta=\pi-nd\theta} \\
&\sigma_{\theta\varphi}\big|_{\theta=-nd\theta/2} = \sigma_{\theta\varphi}\big|_{\theta=+nd\theta/2} \\
&\sigma_{\theta\varphi}\big|_{\theta=\pi+nd\theta/2} = \sigma_{\theta\varphi}\big|_{\theta=\pi-nd\theta/2},
\end{aligned}
\tag{4-23}
$$

where *n* is an integral number of grid points from the symmetry axis. The second case occurs at the free surface. Here we use the zero-stress condition where $\sigma_{r\varphi}$ must go to zero (e.g., Levander 1988; Graves 1996). The zero-stress condition can be met by giving the v_φ and $\sigma_{r\varphi}$ values above the free surface the opposite of the values below the free surface. Because the CMB is a perfect reflector for *SH*-waves, the zero-stress condition is also used there. The zero-stress boundary condition is defined as:

$$
\begin{aligned}
&v_\varphi\big|_{r=R_E+ndr} = -v_\varphi\big|_{r=R_E-ndr} \\
&v_\varphi\big|_{r=R_{CMB}-ndr} = -v_\varphi\big|_{r=R_{CMB}+ndr} \\
&\sigma_{r\varphi}\big|_{r=R_E+ndr/2} = -\sigma_{r\varphi}\big|_{r=R_E-ndr/2} \\
&\sigma_{r\varphi}\big|_{r=R_{CMB}-ndr/2} = -\sigma_{r\varphi}\big|_{r=R_{CMB}+ndr/2},
\end{aligned}
\tag{4-24}
$$

where *n* is an integer number of grid points from the free surface or CMB.

4.3.3 Source implementation

Because of axi-symmetry, in particular due to the cot θ term in eq. (4-5), the source cannot be placed directly on the symmetry axis but rather must be placed at a grid point adjacent to the symmetry axis. In SHaxi we apply a body force to one of the velocity field grid points. With the reflecting boundary condition, this is seen as a reflection on the velocity grid point directly opposite the source insertion grid point

across the symmetry axis. This source implementation does not produce a seismic source similar to a double-couple, but instead approximates a single-couple. By axi-symmetry the source is effectively rotated in the φ-direction and is thus a ring of single-couples. The source radiation pattern for this type of source is derived in Jahnke *et al.* (2005). The most notable aspect of this type of source is its strong dependence on take-off angle, where the amplitude of the source radiation is proportional to the sine of the take off angle. This is demonstrated in Figure 4.4.

Implementing a source-time function in SHaxi can be accommodated in two ways. The first way is to provide a step-impulse function applied as a body force (*f* in eq. 4-5). As displacement is proportional to the first derivative of the moment function, resulting displacement seismograms are delta functions. This technique propagates energy at all frequencies and after completion of the computation, the synthetic seismograms must be filtered to remove higher frequency content that is invalid for the FD grid. Any source time function can then be implemented by convolving a source-time function with the delta function output, so long as the frequency content of the source-time function is long enough period to be valid. This is our preferred method for implementing sources when synthetic seismograms are the desired output. Alternatively, a smooth function with finite frequency content can be applied directly as a body force. This method is preferred for producing snapshots of wave propagation. The source-time function used in this case is:

$$\begin{aligned} S(t) &= \sin\left(r_n p_i t / p_t\right) - \left(r_n / r_n + 2\right)\sin\left((r_n + 2) p_i t / p_t\right) && [t < p_t] \\ S(t) &= \sin\left(r_n p_i\right) - \left(r_n / (r_n + 2)\right)\sin\left((r_n + 2) p_i\right), && [t \geq p_t] \end{aligned} \tag{4-25}$$

where p_i = 4*atan(1), p_t is the dominant period, and r_n is the number of extrema. To reproduce a smoothly varying step function, appropriate to produce a Gaussian shaped displacement pulse we choose r_n = 0.001.

4.3.4 Parallelization

The SHaxi method is parallelized to operate on distributed memory computer systems. The Message Passing Interface (MPI) is used to control communication between separate processors. The parallelization is implemented as shown in Figure 4.2. The SHaxi grid is subdivided laterally (in the θ-direction) into a user-defined number of separate ranks. Each processor is responsible for updating the wavefield in each rank. Overlapping grid points (in number corresponding to the FD operator length divided by two) are used in the SHaxi grid (located at the maximum θ value for each rank) to accommodate this parallelization. Communication at each time step need only update overlapping grid points.

The advantage of the parallelization is that synthetic seismograms can be computed much more rapidly than on single processor machines allowing computation of relatively high frequency synthetics on modest Linux clusters. Table 4.1 lists some sample grid dimensions, attainable dominant periods, computational memory requirements, and performance for parallel jobs. The values given in Table 4.1 are for a Linux cluster (located at Arizona State University) with Intel® Xeon™ 2.40 GHz CPU's. Values given are for a source-code compiled using the Intel® Fortran Compiler for Linux (ifort v. 9.0) with Single SIMD Extensions (SSE) enabled. From Table 4.1 it can be seen

that the run time is roughly proportional to the number of grid points × the number of timesteps. The slight decrease in performance for larger models is likely due to the limited cache size. The performance listed in Table 4.1 corresponds to simulation times of 2700 sec. It should be noted however, that total run time is not linearly related to simulation time. This is because computation time at each time step increases with increasing simulation time as the wavefield spreads throughout the grid. Many simulations do not need to be computed to 2700 sec (e.g., 1700 sec is appropriate for the models discussed in Chapter 5) and much quicker performance is attained. SHaxi also has the ability to perform the calculation on a limited domain size in the θ-direction. That is, an absorbing boundary can be placed at an arbitrary grid location. For example, placing an absorbing boundary at 90° would reduce the total grid size by half and dramatically reduce computation time. The total run times listed in Table 4.1 are for longer simulations and represent the higher end of SHaxi's computational demands.

4.3.5 3-D Axi-symmetric model structure

Although SHaxi implements models on a 2-D grid, the formulation of the wave equation (eqs. 4-5, 4-12, 4-13) is for 3-D axi-symmetry or model invariance in the φ-direction. This means that models are constructed along the great-circle arc plane between source and receiver with no model variation off of the great-circle arc plane. In essence, the model placed on the 2-D grid is rotated about the φ-direction. To understand this, consider placing *S*-wave velocity anomalies on SHaxi's grid as shown in Figure 4.5. Rotating this model in the φ-direction produces the model shown in Figure 4.6. The

result of this model construction is that seismic amplitudes may be over- or under-predicted from amplitudes expected from fully 3-D models. For example, if the high-velocity anomaly (blue filled area) of Figure 4.5 were actually spherically shaped (and not ring-shaped as in Figure 4.6), the seismic wavefield would be slowed down in its path around the off great-circle arc plane in the presence of this anomaly. Therefore, the amplitudes of the latter portion of the arrival would be diminished. Despite this introduction of ring-like anomalies, the absolute arrival time information is not corrupted.

4.3.6 PREM Synthetic Seismograms

As an example of using the SHaxi method we show synthetic seismograms computed for the PREM model (Dziewonski & Anderson 1981). One advantage of the SHaxi method is the ease in which snapshots of wave propagation can be produced. Snapshots at three time steps are shown in Figure 4.7. Five-second dominant period synthetic seismograms for this run are shown in Figure 4.8. Here we show a small window of the wavefield between 70º and 85º encompassing the *S* and *SS* arrivals. A clear advantage of numerical techniques can be seen in Figure 4.8, in that the entire wavefield is calculated. This can be seen by all of the minor arrivals apparent in between the dominant arrivals that are labeled, corresponding to crustal and mid-crustal reverberations, reflections from first-order discontinuities, etc. An exhaustive list of arrivals apparent in Figure 4.8 is beyond the scope of this chapter (For a list of some of the arrivals apparent in a narrow time window of Figure 4.8 see Supplement 5A in Chapter 5).

4.4 Application: Whole mantle scattering

4.4.1 Seismic scattering in the mantle

Propagating seismic waves lose energy due to geometrical spreading, intrinsic attenuation and scattering attenuation. The scattering, or interaction with small spatial variations of material properties, of seismic waves affects all seismic observables including amplitudes and travel-times and also gives rise to seismic coda waves. Seismic coda are wave trains that trail dominant seismic arrivals. For example, high frequency *P*-waves exhibit energy decaying over hundreds of seconds after the direct arrival.

Much of seismic analysis is done where the length scales of velocity perturbations are much larger than the wavelength of the seismic phase of interest. In this case, ray theoretical approaches such as seismic tomography have dominated seismic analyses and have provided large-scale length views of Earth's seismic properties (e.g., Ritsema & van Heijst 2000; Grand 2002). Aki (1969) first demonstrated that seismic coda waves might be produced by random heterogeneity with length scales of velocity perturbations on the order of the wavelength of the seismic phase. Analysis of seismic coda waves has thus provided a method to quantify small-scale seismic properties that cannot be determined through travel-time analysis or ray theoretical approaches.

Many techniques have been developed to study the properties of seismic scattering (see Sato & Fehler, 1998 for a discussion on available techniques). Recently, advances in computational speed have allowed numerical methods such as FD techniques to be utilized in analyzing seismic scattering (e.g., Frankel & Clayton 1984, 1986; Frankel 1989; Wagner 1996). The majority of FD studies have thus far focused on *S*-

wave scattering in regional settings with source-receiver distances of just a few hundred kilometers. This has greatly improved our understanding of scattering in the lithosphere where strong scattering is apparent with *S*-wave velocity perturbations on the order of 5 km in length and 5% RMS velocity fluctuations (e.g., Saito *et al.* 2003).

Recently, small-scale scattering has been observed near the core-mantle boundary (CMB). Cleary & Haddon (1972) first recognized that precursors to the phase *PKP* might be due to small-scale heterogeneity near the CMB. Hedlin *et al.* (1997) also modeled *PKP* precursors with a global data set. They concluded that the precursors are best explained by small-scale heterogeneity throughout the mantle instead of just near the CMB. Hedlin *et al.*'s (1997) finding suggests scatterers exist throughout the mantle with correlation length scales of roughly 8 km and 1% RMS velocity perturbation. Margerin & Nolet (2003) also modeled *PKP* precursors corroborating the Hedlin *et al.* (1997) study that whole mantle scattering best explains the precursors. Although Margerin & Nolet suggest a slightly smaller RMS perturbations of 0.5% on length scales from 4 to 24 km. Recently, Lee *et al.* (2003) examined scattering from *S* and *ScS* waves beneath central Asia finding that scattering from *ScS* waves may dominate over the scattering from *S* waves at dominant periods greater than 10 sec and that as much as 80% of the total attenuation of the lower mantle may be due to scattering attenuation. Because Lee *et al.* (2003) utilized radiative transfer theory to model scattering coefficient; it is not possible to directly translate the scattering coefficients determined in their study to correlation length scales or RMS perturbations (personal communication, Haruo Sato, 2005) for comparison with the studies of Hedlin *et al.* (1997) or Margerin & Nolet (2003).

Nevertheless, their conclusion is important in that whole mantle scattering is necessary to model their data.

Baig & Dahlen (2004) sought to constrain the maximum allowable RMS heterogeneity in the mantle as a function of scale length. Their study also suggests as much as 3% RMS *S*-wave velocity perturbations are possible for the entire mantle for scale lengths less than roughly 50 km. Baig & Dahlen (2004) also suggest that in the upper 940 km of the mantle scattering may be twice as strong as in the lower mantle. The suggestion of stronger upper mantle scattering is also supported by Shearer & Earle (2004). Shearer & Earle (2004) find that in the lower mantle 8 km scale length heterogeneity with 0.5% RMS perturbations can explain *P* and *PP* coda for earthquakes deeper than 200 km. They find that shallower earthquakes require stronger upper mantle scattering with 4-km scale lengths and 3-4% RMS perturbations.

Although, a growing body of evidence suggests whole mantle scattering is necessary to explain many disparate seismic observations, the characteristic scale lengths and RMS perturbations are determined using analytical and semi-analytical techniques which in many cases are based on single-point scattering approximations and do not synthesize waveforms. As whole mantle scattering may affect all aspects of seismic waveforms, it is thus important to synthesize global waveforms with the inclusion of scattering effects. The first attempt at synthesizing global waveforms was by Cormier (2000). He utilized a 2-D Cartesian pseudo-spectral technique to demonstrate that the D" discontinuity may due to an increase in the heterogeneity spectrum. Cormier (2000)

suggests that as much as 3% RMS perturbations may be possible for length scales down to roughly 6 km.

4.4.2 Construction of random velocity perturbations – Summary

Random velocity perturbations (we refer to models of random velocity perturbations as random media hereafter) are characterized by their spatial autocorrelation function, the Fourier transform of which equals the power spectrum of the velocity perturbations. Construction of random media for FD simulations is implemented using a Fourier based method (e.g., Frankel & Clayton 1986; Ikelle *et al.* 1993; Sato & Fehler 1998). In this section we provide an outline of the method. The basic steps in creating random velocity perturbations are outlined below:

1) Create a matrix of uncorrelated random numbers $\theta(x,y)$ on the interval $[0, 2\pi]$.

2) Create an autocorrelation matrix *auto(x,y)* with the same dimensions as θ.

3) Fast Fourier Transform (FFT) θ and *auto* into the wavenumber domain.

4) In the wavenumber domain, multiply θ and *auto*, corresponding to convolution.

5) Inverse FFT the random media back to the spatial domain.

6) Window the velocity variations so as to not be outside of the range of the FD numerical stability.

In what follows we describe the six steps outlined above in greater detail.

4.4.3 Construction of random velocity perturbations - Details

1) A matrix of uncorrelated random numbers *(θ)* is generated with a Gaussian probability distribution with dimensions equal to the model size. The random distributions are also scaled on the interval [0,2π] so that they do not individually need to be Fourier transformed later. Figure 4.9 shows 2 realizations of initial random matrices.

2) The spectral characteristics of random inhomogeneities are described by autocorrelation functions (ACF). The most popular choice of ACF's are defined:

Gaussian: $$auto(x,y) = e^{-r^2/a^2} \tag{4-26}$$

Exponential: $$auto(x,y) = e^{-r/a} \tag{4-27}$$

von Karman: $$auto(x,y) = \frac{1}{2^{m-1}\Gamma(m)}\left(\frac{r}{a}\right)^m K_m\left(\frac{r}{a}\right), \tag{4-28}$$

where r is the offset or spatial lag: $r = \sqrt{x^2 + y^2 + z^2}$, and a is the autocorrelation length (ACL). The ACFs given in eqs. (4-26) through (4-28) are shown in Fig. 4.11. These three ACFs are most predominantly used, however many other choices also exist (e.g., Klimeš 2002a; 2002b).

The definition of the von Karman ACF given in eq. (4-28) is taken from Frankel & Clayton (1986), where $K_m(x)$ is a modified Bessel function of the second kind of order m and $\Gamma(m)$ is the gamma function. Modified Bessel functions are solutions to the following differential equation:

$$x^2 \frac{\partial^2 y}{\partial^2 x} + x\frac{\partial y}{\partial x} - (x^2 + m^2)y = 0. \tag{4-29}$$

The general solution to this differential equation is:

$$y(x) = c_1 I_m(x) + c_2 K_m(x), \tag{4-30}$$

where $I_m(x)$ and $K_m(x)$ are the modified Bessel functions of the first and second kind respectively. Frankel and Clayton (1986) limit their discussion to Bessel functions of order $m = 0$, yet the order can vary between 0.0-0.5. In the case of order $m = 0.5$, the von Karman ACF is identical to the Exponential ACF. Fig. 4.10 shows Bessel functions of the second kind.

The ACF definitions given in eqs. (4-26) through (4-28) represent isotropic ACFs because the ACLs are the same in the three principal directions. Ikelle *et al.* (1993) also define an anisotropic exponential ACF, which they refer to as an Ellipsoidal ACF. Ikelle *et al.* (1993) considers 2-D media and their definition allows for ACLs in the x- and y-principal directions to be different from each other. We generalize their definition for the ACFs listed in eqs. (4-26) through (4-28) to allow for anisotropic ACLs in all three dimensions for each ACF:

Gaussian: $$auto(x,y) = e^{-\left(\frac{x^2}{alx^2}+\frac{y^2}{aly^2}+\frac{z^2}{alz^2}\right)} \tag{4-31}$$

Exponential: $$auto(x,y) = e^{-\sqrt{\frac{x^2}{alx^2}+\frac{y^2}{aly^2}+\frac{z^2}{alz^2}}} \tag{4-32}$$

von Karman: $$auto(x,y) = \frac{1}{2^{m-1}\Gamma(m)}\left(\sqrt{\frac{x^2}{alx^2}+\frac{y^2}{aly^2}+\frac{z^2}{alz^2}}\right)^m K_m\left(\sqrt{\frac{x^2}{alx^2}+\frac{y^2}{aly^2}+\frac{z^2}{alz^2}}\right), \tag{4-33}$$

where *alx*, *aly*, and *alz* are the ACLs in the x-, y-, and z- principal directions.

3) Once an autocorrelation matrix has been created the realization of random media is accommodated in the wavenumber domain by FFT. This is because the Fourier transform of the autocorrelation function is equal to the power spectrum of the random media (e.g., Frankel 1989).

The primary difference between ACFs is defined by their roughness. The power spectrum of an ACF is flat out to a corner wavenumber that is roughly proportional to the inverse of the ACL. From the corner wavenumber the power spectrum asymptotically decays. The roughness is a measure of how fast the rate of fall of is. In order to examine the ACF's roughness we must first describe the FFT of an ACF and then describe how the random media is realized.

The Fourier Transform is typically defined in terms of a time-frequency transform. Nevertheless, the Fourier Transform is also valid in the distance-wavenumber domain. In the frequency domain we define the continuous time Fourier Transform as:

$$H(f) = \int_{-\infty}^{\infty} h(t) e^{2\pi i f t} dt, \tag{4-34}$$

where f is the frequency with units [sec^{-1} or Hz]. In the space-wavenumber domain we replace ω with radial wavenumber k with units [rad/m]. As with the temporal case $\omega = 2\pi f$ we also have a spatial counterpart $k = 2\pi K$ where K is the wavenumber [m^{-1}]. Hence if we are concerned with spatial variations we can write the Fourier Transform as:

$$H(K) = \int_{-\infty}^{\infty} h(r) e^{2\pi i K r} dr, \tag{4-35}$$

and the inverse transform as:

$$h(r) = \int_{-\infty}^{\infty} H(K) e^{-2\pi i K r} dK \,. \tag{4-36}$$

Because the Fourier transform of the ACF determines the power spectrum of the random media it is worthwhile to look at the power spectrum of the three classes of ACFs. First we will derive the Fourier transform of the 1-D isotropic exponential ACF. Substituting equation (4-27) into (4-35) we obtain:

$$H(K) = \int_{-\infty}^{\infty} e^{-|r|/a} e^{2\pi i k r} dr \tag{4-37}$$

$$\Rightarrow H(K) = \int_{-\infty}^{0} e^{r/a} e^{2\pi i K r} dr + \int_{0}^{\infty} e^{-r/a} e^{2\pi i K r} dr \tag{4-38}$$

$$\Rightarrow H(K) = \frac{a}{1 + 2\pi i K a} + \frac{a}{1 - 2\pi i K a} \tag{4-39}$$

$$\Rightarrow H(K) = \frac{2a}{1 + 4\pi^2 K^2 a^2} \tag{4-40}$$

Or, because $k=2\pi K \Rightarrow k^2=4\pi^2K^2$, and we can write:

$$H(k) = \frac{2a}{1 + k^2 a^2} \tag{4-41}$$

Frankel & Clayton (1986) define the Fourier transform for 1-D and 2-D isotropic ACFs. These Fourier transforms are:

1-D Isotropic ACF Fourier Transforms:

Gaussian: $$H(k) = (\pi)^{1/2} a e^{-k^2 a^2/4} \tag{4-42}$$

Exponential: $$H(k) = \frac{2a}{1 + k^2 a^2} \tag{4-43}$$

von Karman (Order=0): $$H(k) = \frac{a}{\left(1 + k^2 a^2\right)^{1/3}} \tag{4-44}$$

2-D Isotropic ACF Fourier Transforms:

Gaussian: $$H(k) = \frac{a^2}{2} e^{-k_r^2 a^2/4} \tag{4-45}$$

Exponential: $$H(k) = \frac{a^2}{(1 + k_r^2 a^2)^{3/2}} \tag{4-46}$$

von Karman (Order=0): $$H(k) = \frac{a^2}{1 + k_r^2 a^2} \tag{4-47}$$

4) Once we have the autocorrelation function (*auto*) and the random matrix (θ) in the wavenumber domain creating the random media is done by a 2- or 3-D convolution, which is simply a multiplication in the wavenumber domain.

5) Now to realize the random media, we need to inverse Fourier transform the product of *auto* with θ. The top row of Figure 4.12 shows three realizations of random media once inverse Fourier transformed into the spatial domain. Each realization in Fig. 4.12 is created with an ACL of 16 km and an identical initial random matrix (θ). The difference in roughness between each of the three ACFs is readily observed. For example, one can see that the Gaussian ACF produces the smoothest perturbations. In Fig. 4.13 we show the power spectrum for the three realizations of random media shown in Fig. 4.12. From the power spectrum we can see that the Gaussian ACF decreases most rapidly, producing the smoothest velocity perturbations in Fig. 4.12. It is also apparent that the shape of the power spectrum of the Exponential ACF and the von Karman ACF is similar, except that the von Karman ACF has more power at shorter wavelengths. This

is also observed in Fig. 4.12 where we can see stronger variation at short wavelengths for the von Karman ACF than in the Exponential ACF. The most important factor that the roughness of the ACF affects is the frequency dependence of scattering (e.g., Wu 1982). For example, a von Karman type ACF will produce more scattering at shorter periods than a Gaussian ACF because the von Karman ACF contains more power of heterogeneity at shorter wavelengths.

6) Because we must be careful in FD simulations to ensure that we do not violate the stability criterion of the simulation we must ensure that we do not have velocity perturbations that are too strong. In the bottom row of Fig. 4.12 we show the distribution of velocity perturbations for each model. The velocity perturbations are Gaussian distributed with a standard deviation set to 1% δV_S in the model creation. Here we clip the velocity perturbations to keep them within ±3%. This does not strongly affect the statistical properties of the medium.

The ACFs shown in Figure 4.12 are for the isotropic case. However, as shown in equations (4-31) through (4-33), anisotropic ACFs can also be considered. Anisotropic ACFs produces lens-like, lamellae-like or layered random media as shown in Figure 4.14. This class of random media has been shown to produce forward scattering and is often more consistent with observations of lithospheric scattering (e.g., Wagner 1996).

4.4.4 Wave propagation through random media - Regional studies

Figure 4.15 shows a *P*-wave propagating through a homogeneous medium. Shown in Figure 4.16 is the identical case of Figure 4.15 except that random velocity perturbations have been added to the homogeneous medium. As the circular *P*-wave propagates through the random medium part of it is scattered behind the main *P*-wavefront. This scattered energy behind the direct *P*-wave is the coda. Energy is lost by the direct *P*-wave to the coda. Additionally, energy is converted by the scattering into *S*-wave energy (not shown).

4.4.5 Wave propagation through random media – Global SH- case

Challenges arise in implementing random media in SHaxi as the Fourier technique outlined above, is defined for a Cartesian grid and not the spherical grid used in SHaxi. We cannot simply create our media onto SHaxi's grid using the Fourier technique as we would introduce spatially anisotropic ACF's onto SHaxi's grid in the radial- and θ-directions. This can be understood in that a spatially isotropic ACF on a Cartesian grid would result in an ACF that has increasing length in the lateral direction for increasing radius. To implement random media in SHaxi we create models of random media on a 2-D Cartesian grid with total model size of 6371 × 12742 km. The entire SHaxi grid fits within this Cartesian grid, and we hence overlay the SHaxi grid onto the Cartesian grid and interpolate the velocity perturbations onto the SHaxi grid using a near neighbor algorithm. The random velocity perturbations are then applied to the PREM background model. Analysis of the statistical properties of the original random media on the Cartesian grid and the interpolated random media on SHaxi's grid show no significant

difference. Figure 4.17 shows an example of random media interpolated onto SHaxi's grid.

Fully 3-D random media cannot be incorporated in SHaxi because of the axi-symmetric approximation. Figure 4.18 shows an example how random perturbations appear to the wavefield in SHaxi. As explained in Section 4.3.5 model invariance in the φ-direction causes the random perturbations to effectively be infinite in this direction (as in the anisotropic case drawn in Figure 4.14c). The effect of this apparent anisotropic ACF in SHaxi will likely be to produce less scattering than for fully 3-D models (e.g., Makinde *et al.* 2005).

We compute synthetic seismograms for a suite of realizations of random media with ACL's of 8, 16, and 32 km and RMS *S*-wave velocity perturbations of 1, 3, and 5%. We analyze the effect of these random velocity perturbations on *S* and *ScS* waves in the distance range 65° to 75° for a source depth of 200 km.

The frequency dependence of scattering is displayed in Figure 4.19. Here synthetics computed for an epicentral distance of 75° are shown for a Gaussian ACF with 3% RMS perturbations and ACL of 16 km overlain on top of synthetics computed for the PREM model. The effects of scattering are most pronounced for the shortest dominant period synthetics. Here the direct *S*-arrival is broadened with a delay of the peak energy of roughly two seconds. A similar effect is observed for the *ScS* arrival. Substantial energy is also seen between the *S* and *ScS* arrivals that do not appear in the PREM synthetics. However, as we move to longer period waveforms, these scattering effects become less apparent, and by the time we reach 20 sec dominant periods the PREM and

Gaussian ACF synthetics are nearly identical. This is due to the short-scale length of the random perturbations applied to the model. As the dominant wavelength of the propagating energy increases to values greater than the dominant wavelength of the random media the propagating energy can much easier heal around the perturbations.

The effect of ACL on the waveform shape is demonstrated in Figure 4.20 for models produced with Gaussian ACFs. The largest amount of scattering is observed for the largest ACL of 32 km. Here the absolute amplitude of the *S* arrival is most significantly reduced as more energy is robbed from the direct *S*-wave to go into later arrivals. Significant delay in *S*-wave peak arrival time is also apparent which may strongly affect the results of cross-correlation techniques at picking arrival times.

Figure 4.20 also shows strong energy between the direct *S* and *ScS* arrivals. The arrivals in this time window are reminiscent of the crustal and mid-crustal arrivals in the PREM model. However, the arrivals are shifted by several seconds. Receiver function studies may be strongly affected by this shifting. That is, it appears as though these crustal discontinuities would be significantly mismapped for an ACL of 8 km and RMS *S*-wave velocity perturbation of 3%. Lithospheric studies suggest ACLs of 5 km and RMS *S*-wave velocity perturbations of 5% is consistent with data. However, whole mantle scattering may not have RMS *S*-wave velocity perturbations as strong as 3% and it is thus difficult from the present study to ascertain whether the apparent mismapping would occur for a multi-layered model with low RMS perturbations (e.g., 0.5 to 1.0%) in the lower mantle and high perturbations in the lithosphere. Smaller whole mantle RMS

variations (e.g., 1%) do not produce a strong affect on timing of the PREM crustal arrivals.

The results shown in Figures 4.19 and 4.20 are for models of whole mantle scattering. Although, whole mantle scattering has been inferred it is likely that ACL and RMS velocity perturbations also vary with depth or laterally. It is difficult to implement multi-layered models using the Fourier technique. Different models have to be constructed on Cartesian grids and then interpolated onto the SHaxi grid. This construction with a Fourier technique will also produce first-order discontinuities in between layers with different scattering properties, which is undesirable. We are currently working on a new method to produce random media embedded in arbitrary grids without the problems of the Fourier technique. This new method will be reported on shortly.

4.5 Conclusions

The SHaxi technique is an important tool for modeling synthetic waveforms at high frequencies. Although the SHaxi technique is not a fully 3-D technique it provides greater degrees of freedom than 1-D techniques and accounts for correct 3-D geometric spreading which purely 2-D techniques cannot. Just as 1-D techniques are important in gaining an understanding of wavefield characteristics, SHaxi can provide important intuition into the wavefield for higher dimensional geometries. Many situations also exist in which SHaxi provides a better alternative to fully 3-D techniques. For example, if velocity variations off of the great circle arc plane are not significant within a couple of

wavelengths of the dominant seismic energy there is no need to compute 3-D synthetics. In such cases the SHaxi method provides correct fully 3-D synthetic seismograms at a much lower computational cost, and potentially much shorter periods than currently possible with full 3-D methods.

Scattering in the mantle affects all parts of the seismic waveform and may account for a significant portion of the total attenuation we map to in the lower mantle. We have implemented scattering in a global numerical method, however much work needs to be done in comparing our results with data and in producing more realistic models of mantle scattering. For example, models with anisotropic ACFs in the lateral direction or models with differing ACLs or ACFs in different layers of the mantle may provide better approximations to Earth structure. SHaxi is currently the best numerical technique for which models of whole mantle scattering can be implemented. Although fully 3-D techniques exist, it is impossible to model scattering in 3-D because of current computational limits. Furthermore, the SHaxi method provides a better alternative to finite frequency approximations of scattering as the entire wavefield is computed and there is no reliance on single-point scattering approximations.

ACKNOWLEDGEMENTS

Most figures were generated using the Generic Mapping Tools freeware package (Wessel & Smith 1998). M.T. thanks Gunnar Jahnke, Heiner Igel, and Markus Treml for coding, discussions and support in working on the SHaxi method. The SHaxi source code is openly available at http://www.spice-rtn.org/.

REFERENCES

Aki, K., 1969. Analysis of seismic coda of local earthquakes as scattered waves, *Journal of Geophysical Research*, **74**, 615-631.

Alterman, Z., Aboudi, J., & Karal, F.C., 1970. Pulse propagation in a laterally heterogeneous solid elastic sphere, *Geophysical Journal of the Royal Astronomical Society*, **21**, 243-260.

Alterman, Z., & Karal, F.C., 1968. Propagation of elastic waves in layered media by finite difference methods, *Bulletin of the Seismological Society of America*, **58**, 367-398.

Baig, A.M., Dahlen, F.A., & Hung, S.-H., 2003. Traveltimes of waves in three-dimensional random media. *Geophysical Journal International*, **153**, 467-482.

Baig, A.M., & Dahlen, F.A., 2004. Traveltime biases in random media and the *S*-wave discrepancy, *Geophysical Journal International*, **158**, 922-938.

Ben-Menahem., & Singh, S.J., 1981. Seismic Waves and Sources. *Dover Publications, Inc.,* Mineola, New York, 1102 pages.

Carcione, J.M., Herman, G.C., & ten Kroode, A.P.E., Seismic modeling, *Geophysics*, **67** (4), 1304-1325.

Chaljub, E. & Tarantola, A., 1997. Sensitivity of SS precursors to topography on the upper-mantle 660-km discontinuity. *Geophysical Research Letters*, **24** (21), 2613-2616.

Cleary, J.R., & Haddon, R.A.W., 1972. Seismic wave scattering near core-mantle boundary – new interpretation of precursors to PKP, *Nature*, 240 (5383), 549.

Cormier, V.F., 2000. D" as a transition in the heterogeneity spectrum of the lowermost mantle. *Journal of Geophysical Research*, **105**, 16193-16205.

Countant O., Virieux, J., & Zollo, A., 1995. Numerical source implementation in a 2D finite difference scheme for wave propagation. *Bulletin of the Seismological Society of America*, **85** (5), 1507-1512.

Dormy, E., & Tarantola, A., 1995. Numerical simulation of elastic wave propagation using a finite volume method. *Journal of Geophysical Research*, **100**, 2123-2133.

Dziewonski, A.M., & Anderson, D.L., 1981. Preliminary Reference Earth Model, *Physics of the Earth and Planetary Interiors*, **25** (4), 297-356.

Fornberg, B., 1987. The pseudospectral method: Comparison with finite differences for the elastic wave equation. *Geophysics*, **52**, 483-501.

Frankel, A., & Clayton, R.W., 1984. A Finite Difference Simulation of Wave Propagation in Two-dimensional Random Media, *Bulletin of the Seismological Society of America*, **74** (6), 2167-2186.

Frankel, A., & Clayton, R.W., 1986. Finite Difference Simulations of Seismic Scattering: Implications for the Propagation of Short-Period Seismic Waves in the Crust and Models of Crustal Heterogeneity, *Journal of Geophysical Research*, **91** (B6), 6465-6489.

Frankel, A., 1989. A Review of Numerical Experiments on Seismic Wave Scattering, *Pure and Applied Geophysics*, **131** (4), 639-685.

Fuchs, K., & Müller, G., 1971. Computation of synthetic seismograms with the reflectivity method and comparison with observations. *Geophysical Journal of the Royal Astronomical Society*, **23**, 417-433.

Furumura, T., Kennett, B.L.N., & Furumura, M., 1998. Seismic wavefield calculation for laterally heterogeneous whole Earth models using the pseudospectral method, *Geophysical Journal International*, **135**, 845-860.

Grand, S. P., 2002. Mantle shear-wave tomography and the fate of subducted slabs, *Philosophical Transactions of the Royal Society of London Series a-Mathematical Physical and Engineering Sciences*, **360**, 2475-2491.

Graves, R.W., 1996. Simulating seismic wave propagation in 3D elastic media using staggered-grid finite differences. *Bulletin of the Seismological Society of America*, **86** (4), 1091-1106.

Hedlin, M.A.H, Shearer, P.M., & Earle, P.S., 1997. Seismic evidence for small-scale heterogeneity throughout Earth's mantle. *Nature*, **387**, 145.

Helmberger, D.V., 1968. The crust-mantle transition in the Bering Sea. *Bulletin of the Seismological Society of America*, **58**, 179-214.

Igel, H., & Weber, M., 1995. SH-wave propagation in the whole mantle using high-order finite differences, *Geophysical Research Letters*, **22** (6), 731-734.

Igel, H., & Weber, M., 1996. P-SV wave propagation in Earth's mantle using finite differences: Application to heterogeneous lowermost mantle structure. *Geophysical Research Letters*, **23** (5), 415-418.

Igel, H., & Gudmundsson, O., 1997. Frequency-dependent effects on travel times and waveforms of long-period S and SS waves, *Physics of the Earth and Planetary Interiors*, **104**, 229-246.

Igel, H., Nissen-Meyer, T., & Jahnke, G., 2001. Wave propagation in 3-D spherical sections: effects of subduction zones. Physics of the Earth and Planetary Interiors, **132**, 219-234.

Igel, H. 2002. Numerical methods in the earth sciences. Unpublished lecture notes.

Ikelle, L.T., Yung, S.K., & Daube, F., 1993. 2-D random media with ellipsoidal autocorrelation functions. *Geophysics*, **58** (9), 1359-1372.

Jahnke, G., Thorne, M., Cochard, A., & Igel, H., 2005. Global SH-wave propagation using a parallel axi-symmetric finite difference scheme. *Geophysical Journal International*, submitted 2005.

Klimeš, Luděk, 2002a. Correlation Functions of random media. *Pure and Applied Geophysics,* **159**, 1811-1831.

Klimeš, Luděk, 2002b. Estimating the correlation function of a self-affine random medium, *Pure and Applied Geophysics*, **159**, 1833-1853.

Komatitsch, D. & Tromp, J., 2002. Spectral-element simulations of global seismic wave propagation - I. Validation, *Geophysical Journal International*, **149**, 390-412.

Lee, W.S., Sato, H., & Lee, K., 2003. Estimation of S-wave scattering coefficient in the mantle from envelope characteristics before and after the ScS arrival, *Geophysical Research Letters*, **30** (24), doi:10.1029/2003GL018413.

Levander, A.R., 1988. Fourth-order finite-difference P-SV seismograms. *Geophysics*, **53** (11), 1425-1436.

Madariaga, R., 1976. Dynamics of an expanding circular fault. *Bulletin of the Seismological Society of America*, **66**, 163-182.

Makinde, W., Favretto-Cristini, N., & de Bazelaire, E., 2005. Numerical modeling of interface scattering of seismic wavefield from a random rough interface in an acoustic medium: comparison between 2D and 3D cases. *Geophysical Prospecting*, **53**, 373-397.

Margerin, L., & Nolet, G., 2003. Multiple scattering of high-frequency seismic waves in the deep Earth: Modeling and numerical examples. *Journal of Geophysical Research,* **108** (B5), doi:10.1029/2002JB001974.

Moczo, P., Kristek, J., & Halada, L., 2004. The finite difference method for seismologists: An introduction. *Cormenius University*, Bratislava, 150 pages.

Randall, C.J., 1989. Absorbing boundary condition for the elastic wave equation: velocity-stress formulation, *Geophysics*, **54**, 1141-1152.

Ritsema, J. & van Heijst, H.-J., 2000. Seismic imaging of structural heterogeneity in Earth's mantle: Evidence for Large-Scale Mantle Flow, *Science Progress*, **83**, 243-259.

Saito, T., Sato, H., Fehler, M., & Ohtake, M. 2003. Simulating the envelope of scalar waves in 2D random media having power-law spectra of velocity fluctuation, Bulletin of the Seismological Association of America, **93** (1), 240-252.

Sato, H., & Fehler, M.C., 1998. Seismic Wave Propagation and Scattering in the Heterogeneous Earth, *Springer-Verlag*, New York, 308 pages.

Sato, H., Fehler, M., & Wu, R.-S., 2002. Scattering and Attenuation of Seismic Waves in the Lithosphere, *International Handbook of Earthquake and Engineering Seismology*, **81A**, 195-208.

Shearer, P.M., & Earle, P.S., 2004. The global short-period wavefield modeled with a Monte Carlo seismic phonon method. *Geophysical Journal International*, **158**, 1103-1117.

Smith, W.D., 1975. The application of finite-element analysis to body wave propagation problems, *Geophysical Journal of the Royal Astronomical Society*, **42**, 747-768.

Takenaka, H., Tanaka, H., Okamoto, T., & Kennett, B.L.N., 2003. Quasi-cylindrical 2.5D wave modeling for large-scale seismic surveys. *Geophysical Research Letters*, **30** (21), 2086, doi:10.1029/2003GL018068.

Thomas, C., Igel, H., Weber, M., & Scherbaum, F., 2000. Acoustic simulation of *P*-wave propagation in a heterogeneous spherical earth: numerical method and application to precursor waves to *PKPdf*, *Geophysical Journal International*, **141**, 307-230.

Toyokuni, G., Takenaka, H., Wang, Y., & Kennett, B.L.N., Quasi-Spherical Approach for Seismic Wave Modeling in a 2D Slice of a Global Earth Model with Lateral Heterogeneity, *Geophysical Research Letters*, **32** (9), L09305.

Vidale, J., Helmberger, D.V., & Clayton, R.W., 1985. Finite-Difference Seismograms for *SH* Waves, *Bulletin of the Seismological Society of America*, **75** (6), 1765-1782.

Virieux, J., 1984. SH-wave propagation in heterogeneous media: Velocity-stress finite-difference method, *Geophysics*, **49** (11), 1933-1957.

Virieux, J., 1986. P-SV wave propagation in heterogeneous media: Velocity-stress finite-difference method, *Geophysics*, **51**, 889-901.

Wagner, G.S., 1996. Numerical Simulations of Wave Propagation in Heterogeneous Wave Guides with Implications for Regional Wave Propagation and the Nature of Lithospheric Heterogeneity, *Bulletin of the Seismological Society of America*, **86** (4), 1200-1206.

Wessel, P., and W. H. F. Smith, 1998. New, improved version of the Generic Mapping Tools released, *Eos Trans. AGU*, 79, 579.

Woodhouse, J.H., & Dziewonski, A.M., 1984. Mapping the upper mantle: three-dimensional modeling of Earth structure by inversion of seismic waveforms, *Journal of Geophysical Research*, **89**, 5953-5986.

Wu, R.-S., 1982. Attenuation of Short-period Seismic Waves due to Scattering, *Geophysical Research Letters*, **9**, 9-12.

Wu, R.-S., & Aki, K., 1988. Introduction: Seismic Wave Scattering in Three-dimensionally Heterogeneous Earth. *Pure and Applied Geophysics*, **128**, 1-6.

TABLES

Table 4.1 Example SHaxi parameters and performance.

Grid Size				Number of Time Steps	Memory Usage[c] (Mb)	Dominant Period[d] (sec)				Run Time[e]
npts[a] (θ)	dθ[b] (km)	npts (r)	dr (km)			*S* (40º)	*S* (80º)	*SS* (120º)	*SS* (160º)	
5000/24	4.0/2.2	1000	2.9	16894	17	16	18	25	30	19 m
10000/24	2.0/1.1	1800	1.6	33785	52	10	12	17	19	2 h 9 m
15000/24	1.3/0.7	2900	1.0	50758	122	8	10	12	15	7 h 39 m
20000/24	1.0/0.5	3800	0.76	67649	210	6	8	10	11	17 h 33 m
30000/24	0.7/0.4	5200	0.55	101512	428	5	6	8	9	2 d 6 h 21 m

[a]Values are: Total number of grid points / Number of processors used.
[b]Values are: dθ (at Earth surface) / dθ (at CMB)
[c]Memory is reported as total memory (code size + data size + stack size) for one processor. Code size is ~800 kb.
[d]Dominant Period based on phase and epicentral distance listed for a source depth of 500 km.
[e]Total run time is based on 2700.0 sec of simulation time.

FIGURES

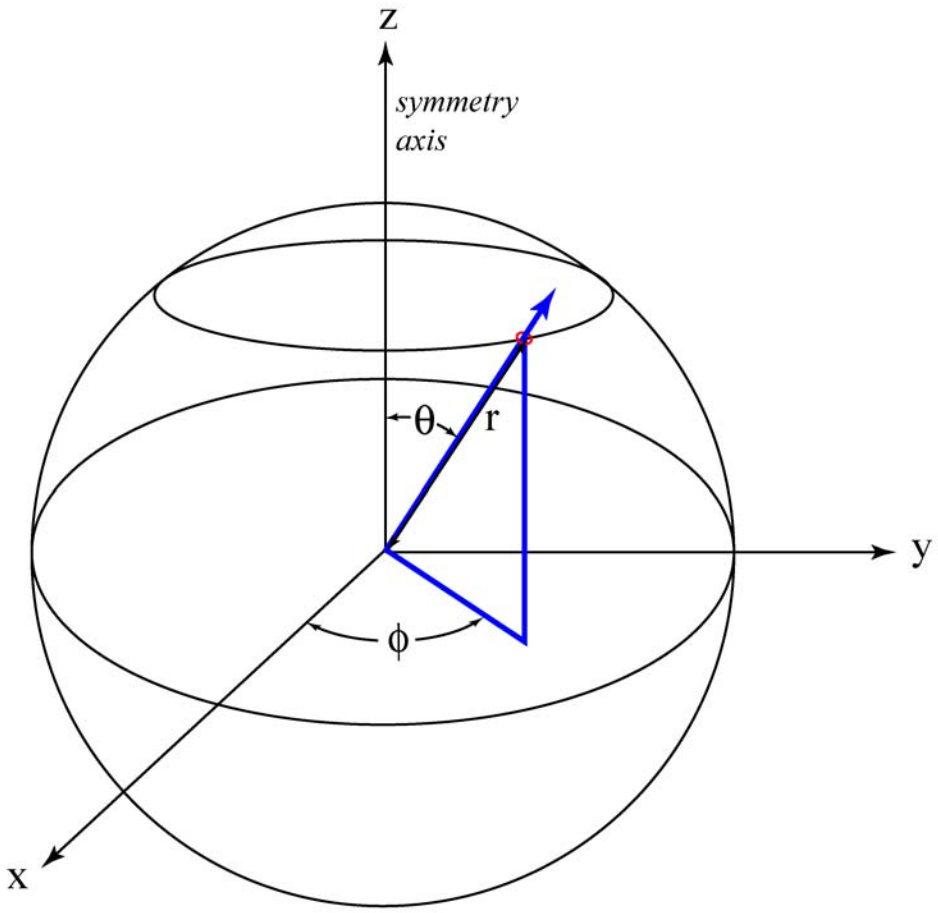

Figure 4.1 Spherical coordinate system used in description of SHaxi method. The axis of symmetry, where the seismic source is located, is placed along the z-axis in this figure. In the axi-symmetric system, there is no model dependence in the φ-direction.

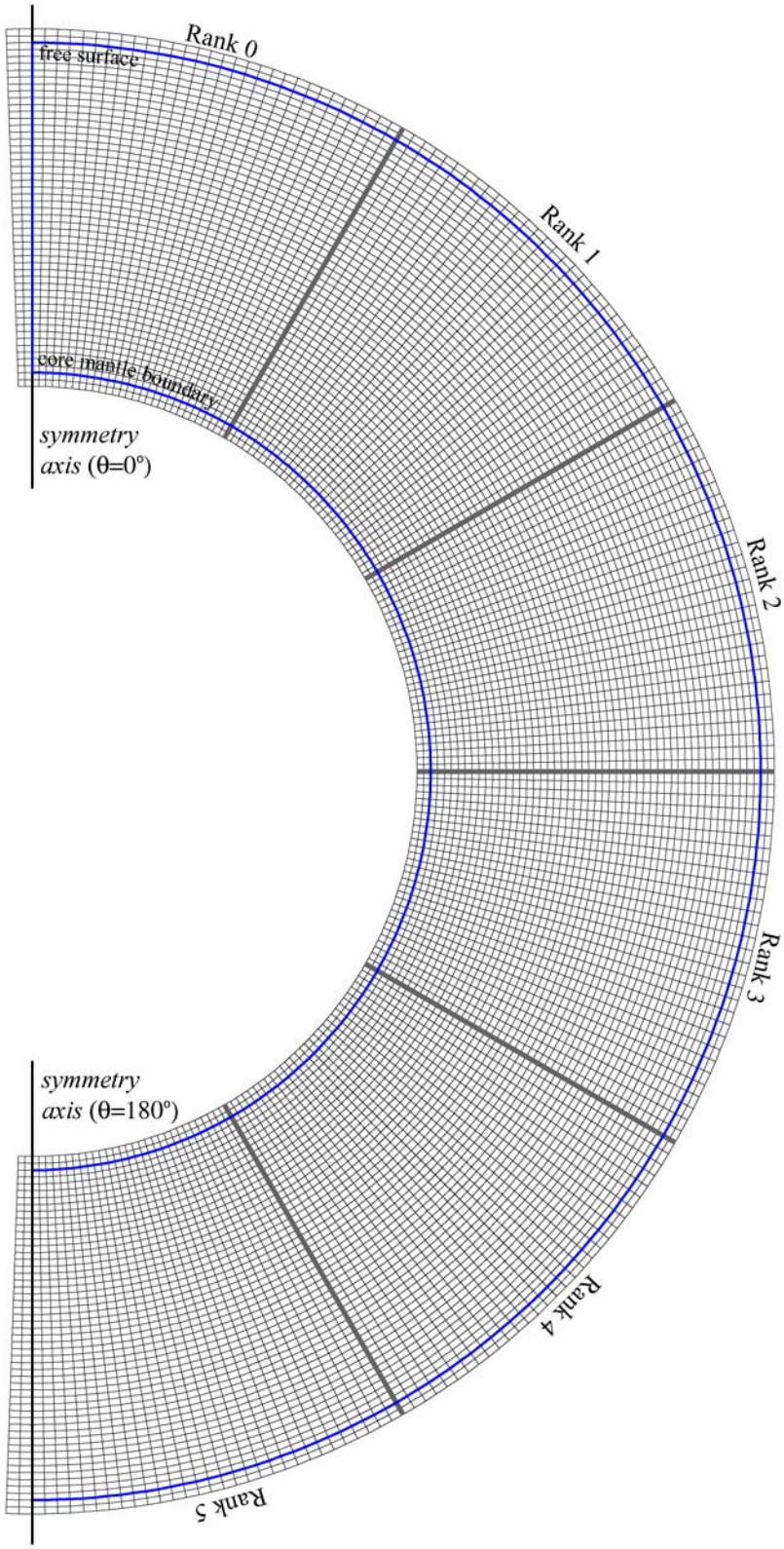
Rank 0
free surface
Rank 1
core mantle boundary
symmetry
axis (θ=0°)
Rank 2
Rank 3
symmetry
axis (θ=180°)
Rank 4
Rank 5

Figure 4.2 Schematic representation of SHaxi grid. The SHaxi grid is defined in two dimensions ranging in theta from 0° to 180° and in radius from 3480 to 6371 km (area encompassed by blue lines). A few grid points above Earth's surface and below the CMB are defined in order to compute the free surface boundary condition. Similarly, extra grid points are defined with $\theta < 0°$ and with $\theta > 180°$ in order to compute the reflecting boundary condition at the symmetry axes. The SHaxi method is parallelized by splitting the calculation into several ranks. The parallel rank boundaries are shown (gray lines) for the case of six ranks.

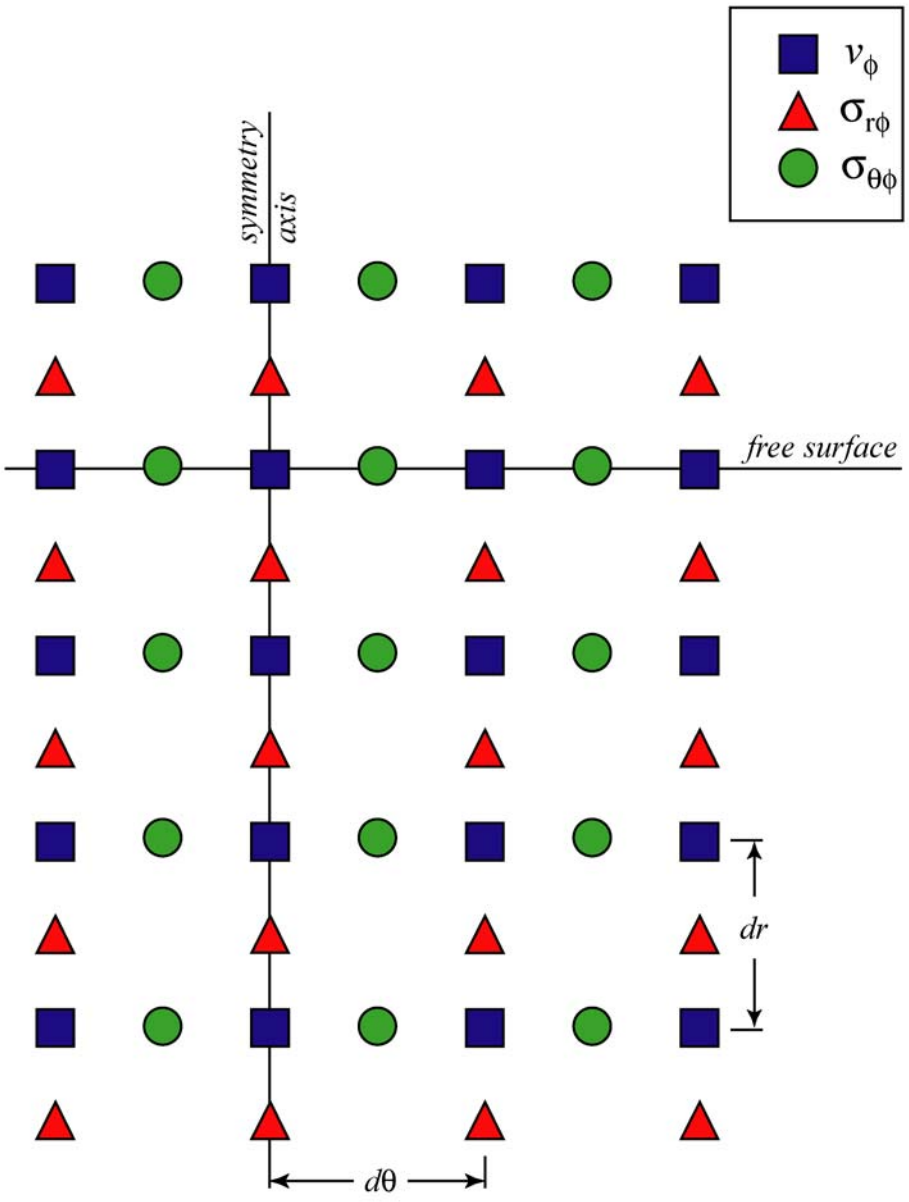

Figure 4.3 Detail of SHaxi grid. Location of velocity (v_φ) and stress ($\sigma_{r\varphi}$ and $\sigma_{\theta\varphi}$) grid points in the SHaxi staggered grid.

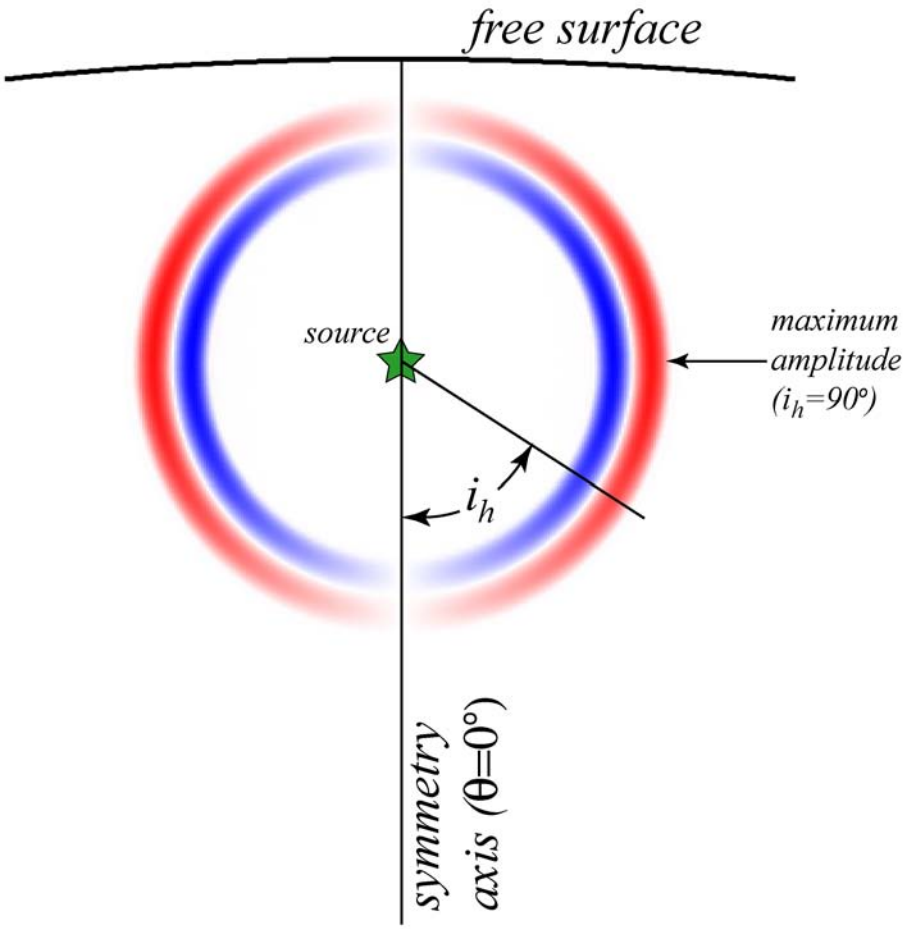

Figure 4.4 The SHaxi source radiation pattern is shown for a 500 km deep event in a homogeneous background model. The amplitude of the *SH*-velocity wavefield is colored red (positive) and blue (negative) with the strength of color saturation representing the amplitude. The amplitude of the source radiation is proportional to the sine of the takeoff angle: sin(i_h). This provides a minimum in amplitude at i_h=0° where no *SH*-wavefield is observable and a maximum at i_h=90° where the red and blue amplitude scaling is saturated. The computation is shown for a dominant period of 12 sec.

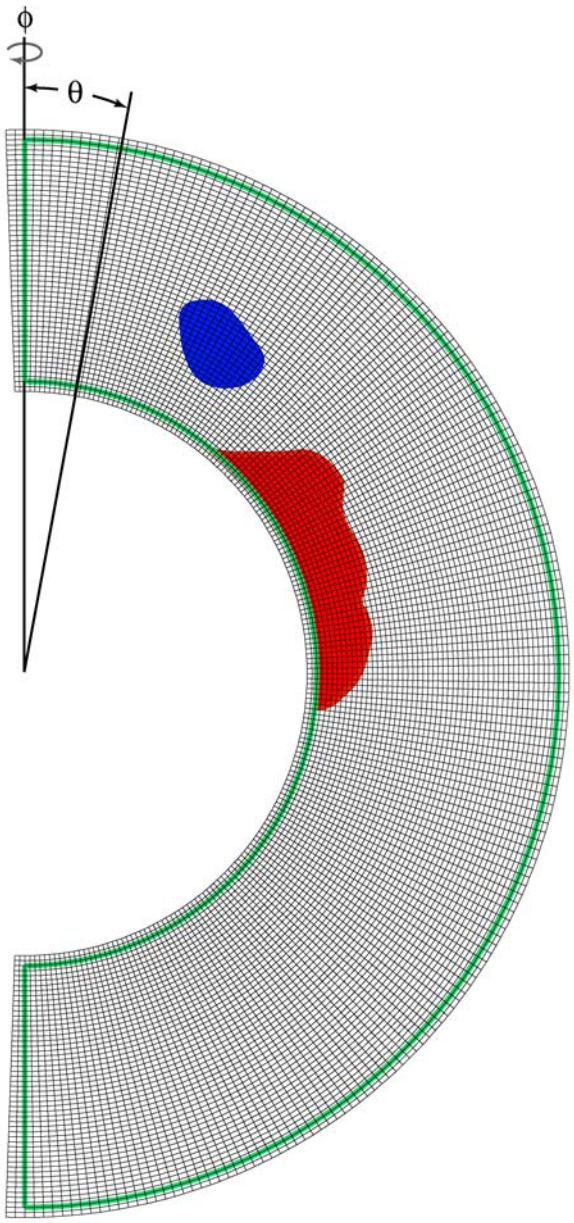

Figure 4.5 Hypothetical low- and high- velocity anomaly (red and blue filled areas respectively) placed onto the 2-D SHaxi grid. The corresponding 3-D axi-symmetric velocity structure is shown in Figure 4.6.

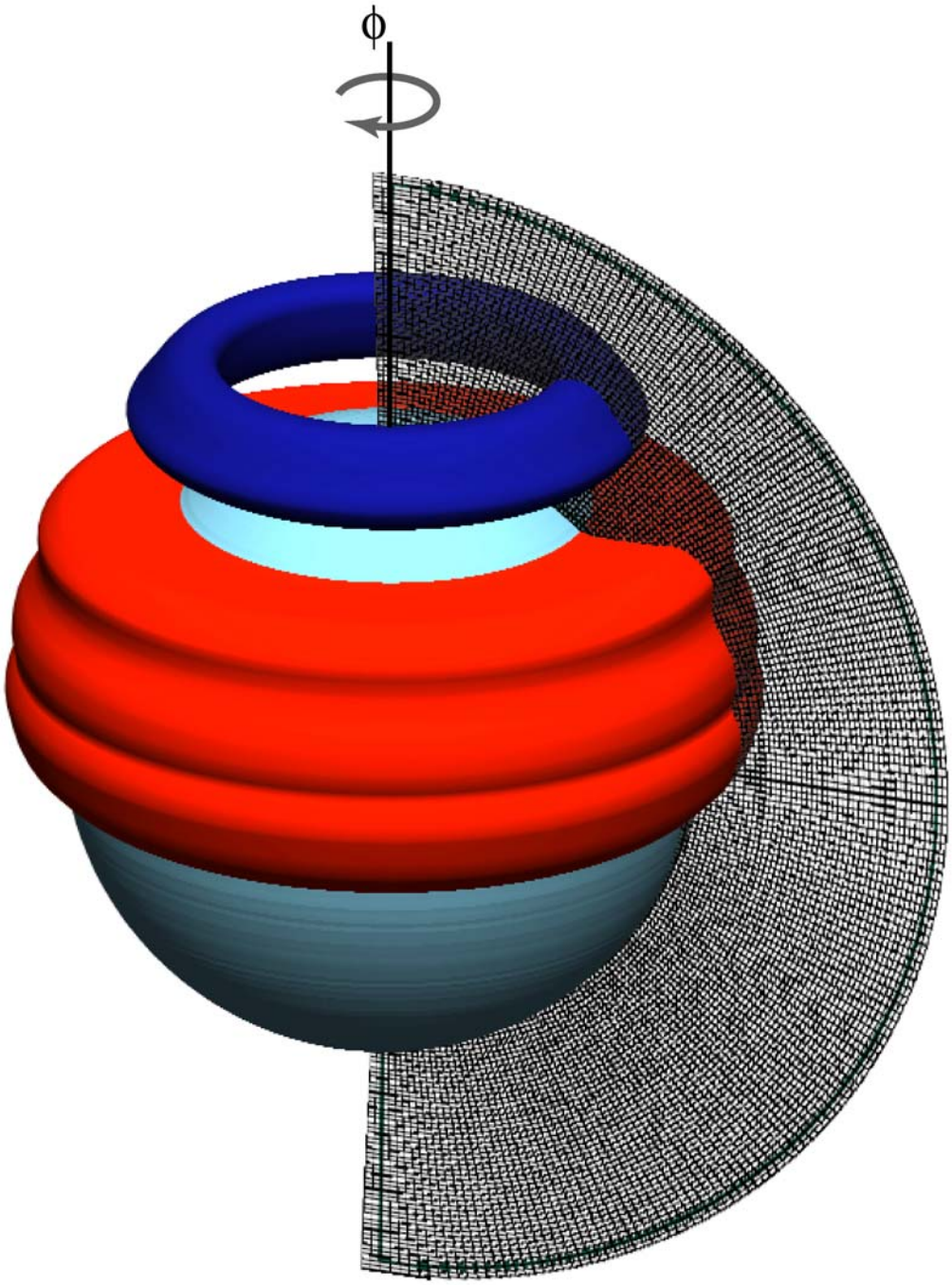

Figure 4.6 Corresponding 3-D axi-symmetric structure of velocity anomalies placed on grid of Figure 4.5.

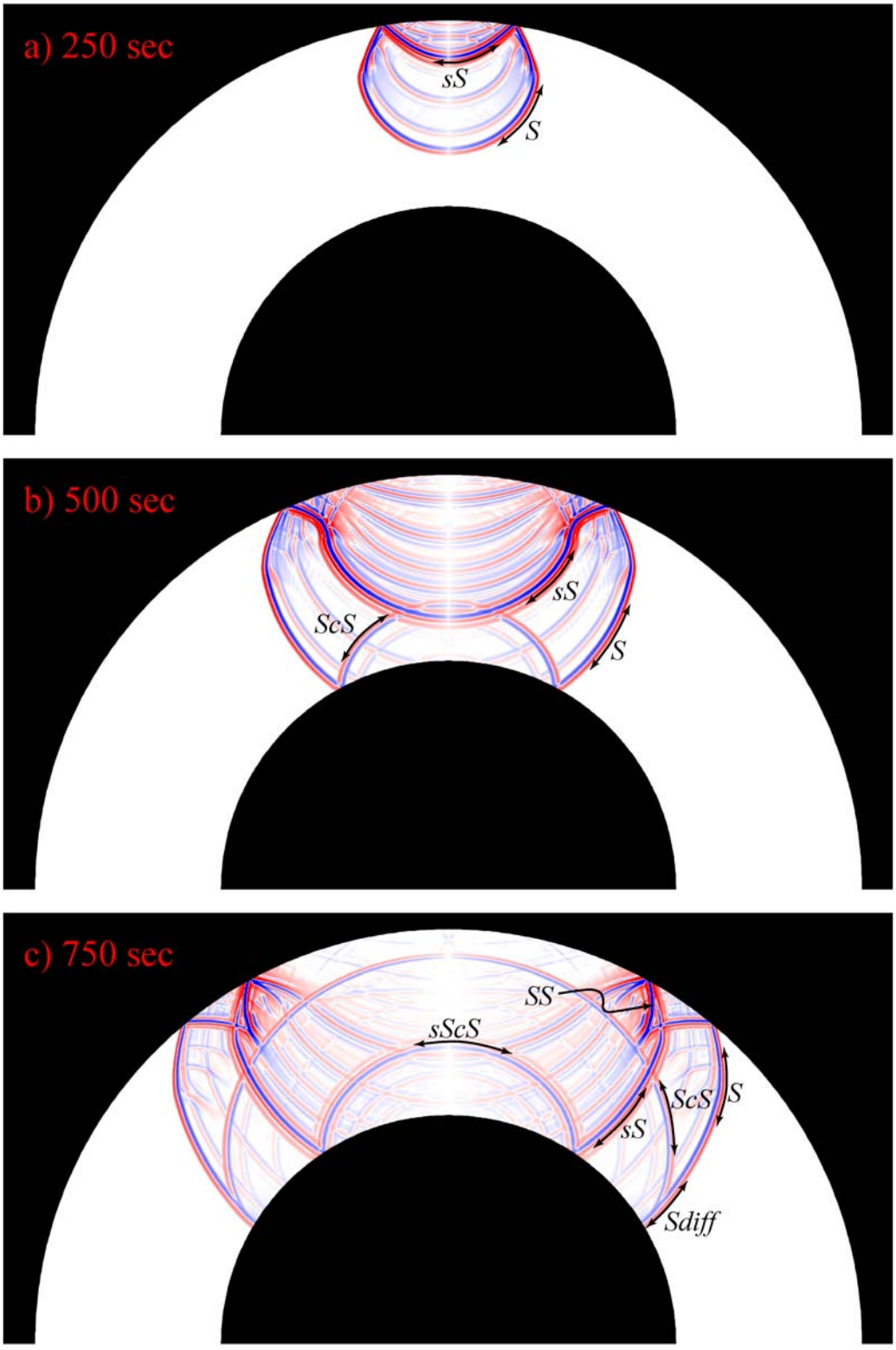
a) 250 sec
sS
S
b) 500 sec
ScS
sS
S
c) 750 sec
SS
sScS
ScS
S
sS
Sdiff

Figure 4.7 The *SH*-velocity wavefield is shown for three snapshots (simulation time of 250, 500, and 750 seconds) of a SHaxi simulation for the PREM model. Computation is for a 500 km event depth. Wavefield is shown for a dominant period of 20 sec. Major seismic phases are labeled with double sided arrows.

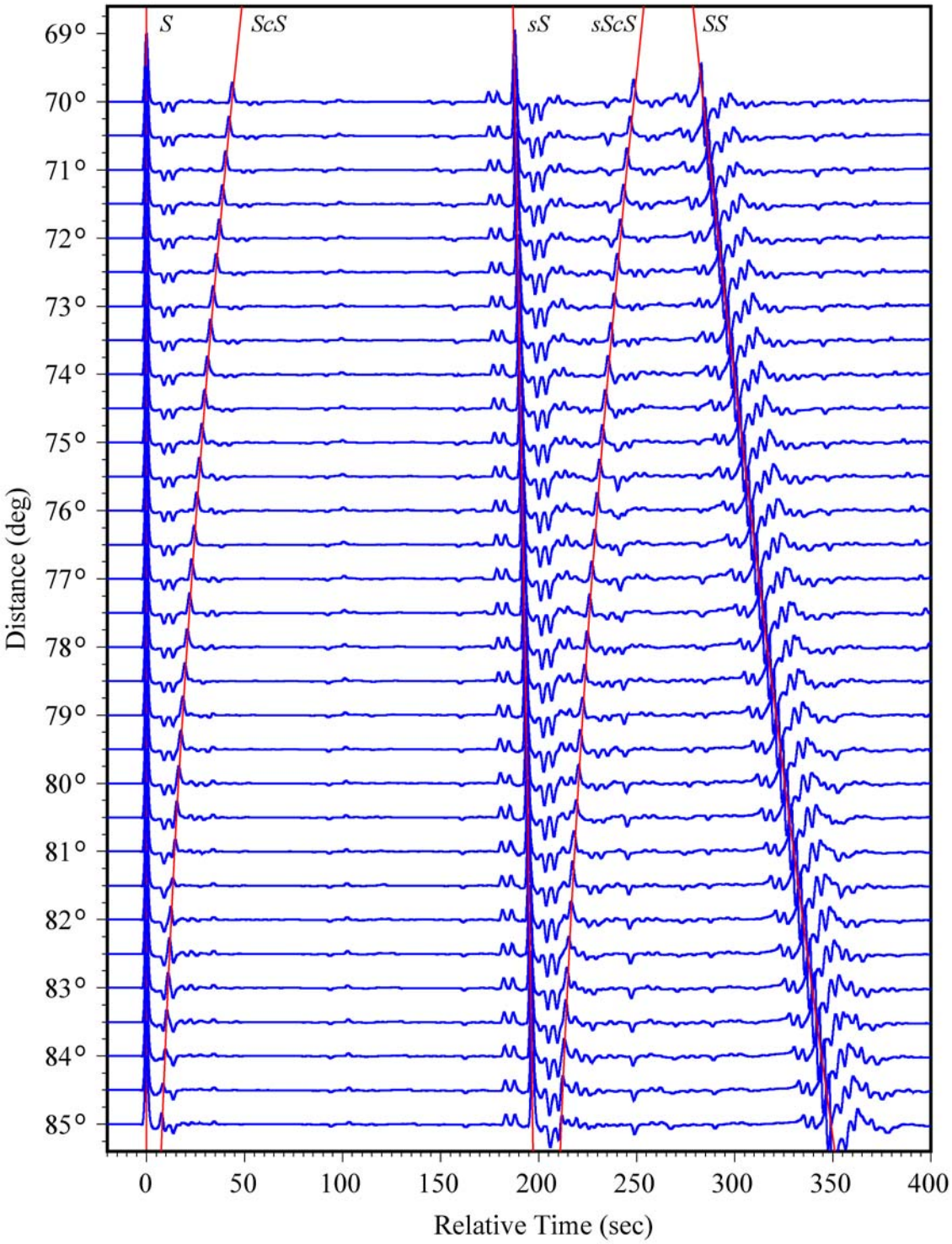
S
ScS
sS
sScS
SS
69°
70°
71°
72°
73°
74°
75°
76°
77°
78°
79°
80°
81°
82°
83°
84°
85°
Distance (deg)
0
50
100
150
200
250
300
350
400
Relative Time (sec)

Figure 4.8 PREM tangential component displacement synthetic seismograms. Seismograms are aligned and normalized to unity on the *S* arrival. Computation for a 500 km deep source with 5 sec dominant period. Red lines show PREM predicted arrival times for select phases.

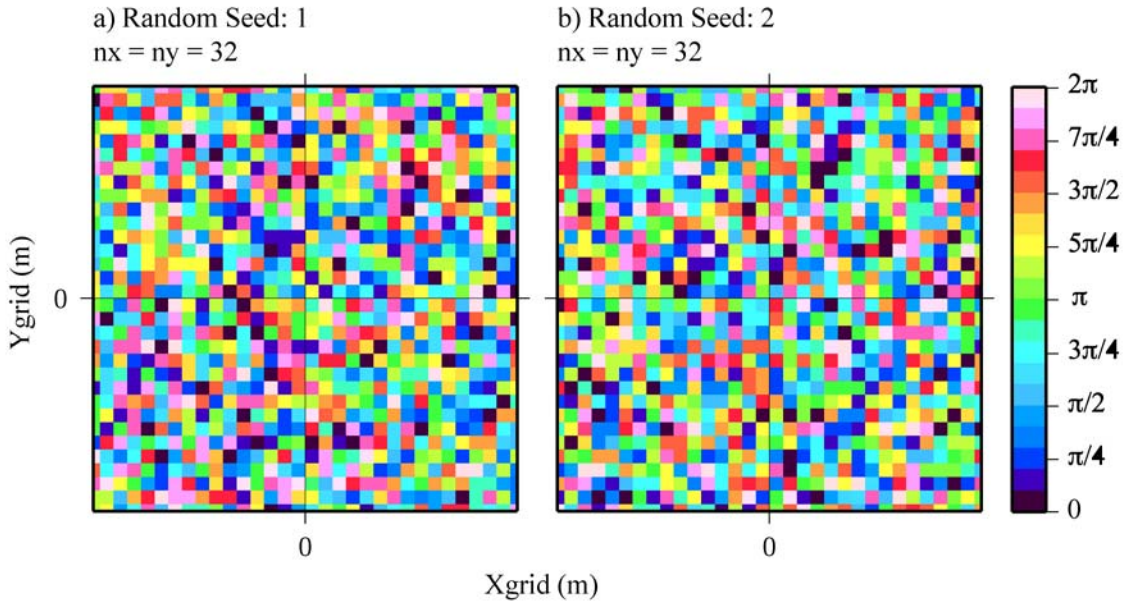

Figure 4.9 Random seed matrices (θ) scaled on the interval [0,2π].

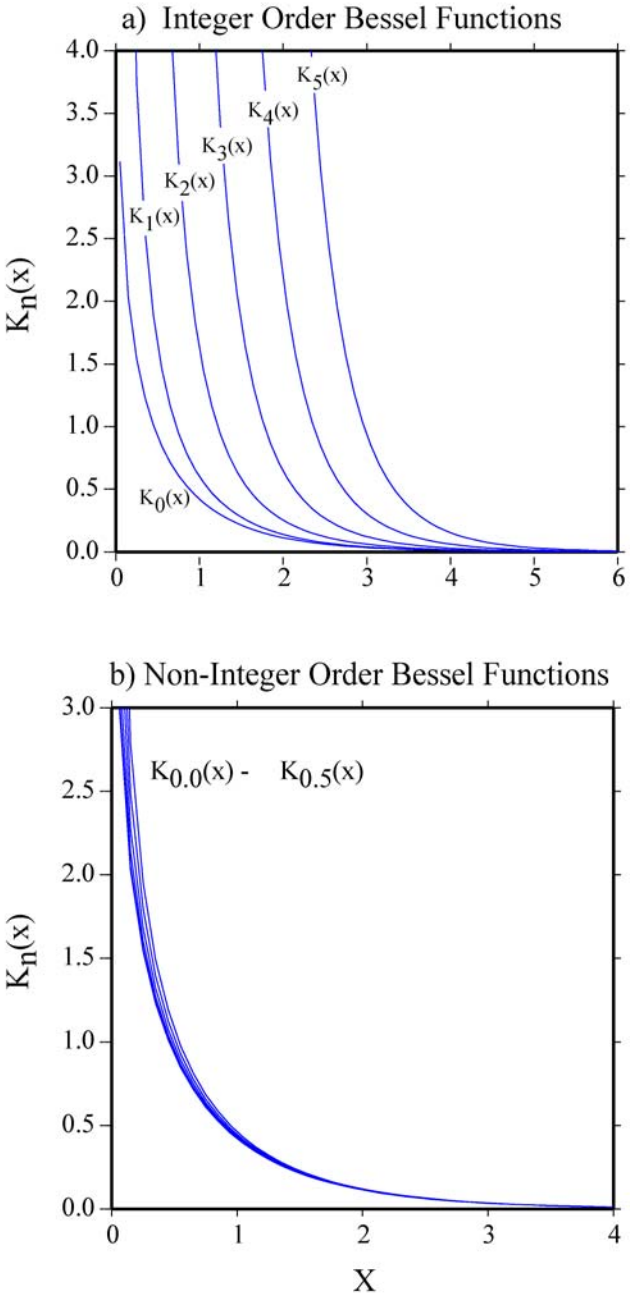

Figure 4.10 Bessel functions of the second kind. Panel a displays integer order Bessel functions. The von Karman autocorrelation function uses non-integer order Bessel functions with order (*m*) between 0.0 and 0.5 (panel b).

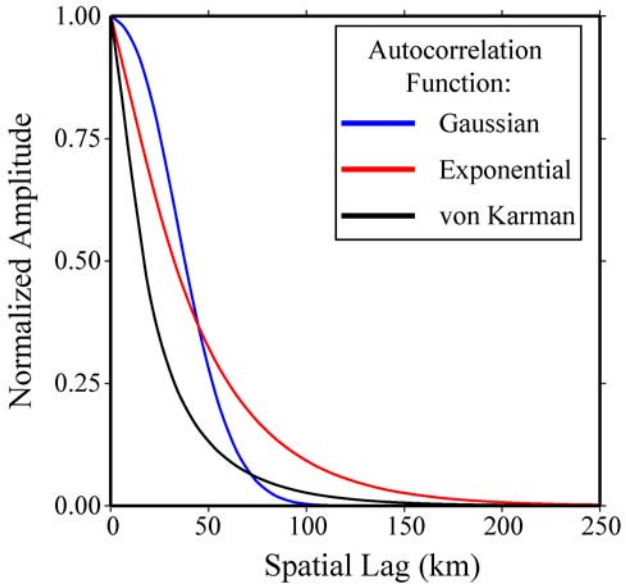

Figure 4.11 Autocorrelation functions shown in 1-D for a 32 km autocorrelation length. The shape of the von Karman autocorrelation function is given for order m=0.0. The peak amplitude is normalized to unity for each autocorrelation function.

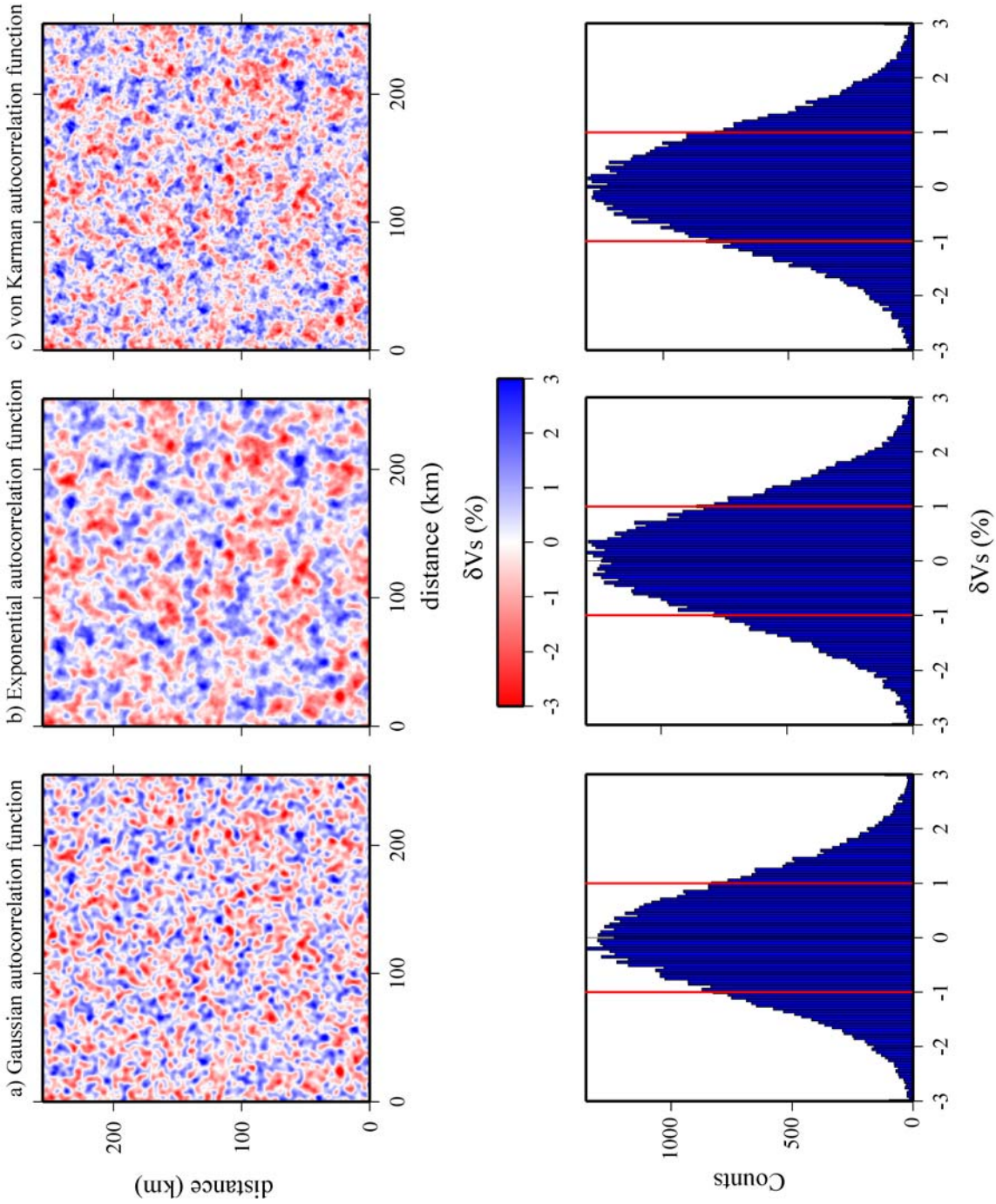
a) Gaussian autocorrelation function
b) Exponential autocorrelation function
c) von Karman autocorrelation function
distance (km)
δVs (%)
Counts
δVs (%)

Figure 4.12 Three realizations of isotropic random media using the same initial random seed matrix. The top row shows the realization of the *S*-wave velocity perturbation for three types of autocorrelation functions. The random media is constructed with an autocorrelation length of 16 km and a RMS velocity perturbation of 1%. The bottom row shows the frequency histogram of the three realizations of the first row. In each case the histogram is Gaussian distributed. The red lines show the region encompassing 1 standard deviation of the velocity perturbation. Velocity perturbations are clipped at ±3% in order to avoid extreme perturbations that may affect the finite difference simulations stability.

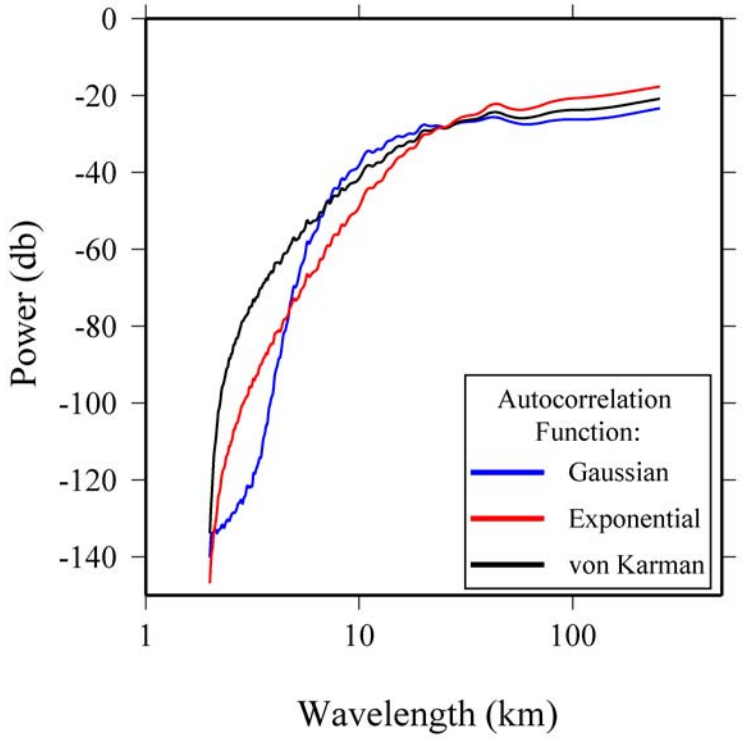

Figure 4.13 Power spectra of random media shown in Figure 4.11. The von Karman type autocorrelation function (ACF) shows the most roughness, as it decays the slowest at shorter wavelengths. The Gaussian ACF displays the smoothest variation (compare with Fig. 4.11) as indicated by the fastest decay to shorter wavelengths.

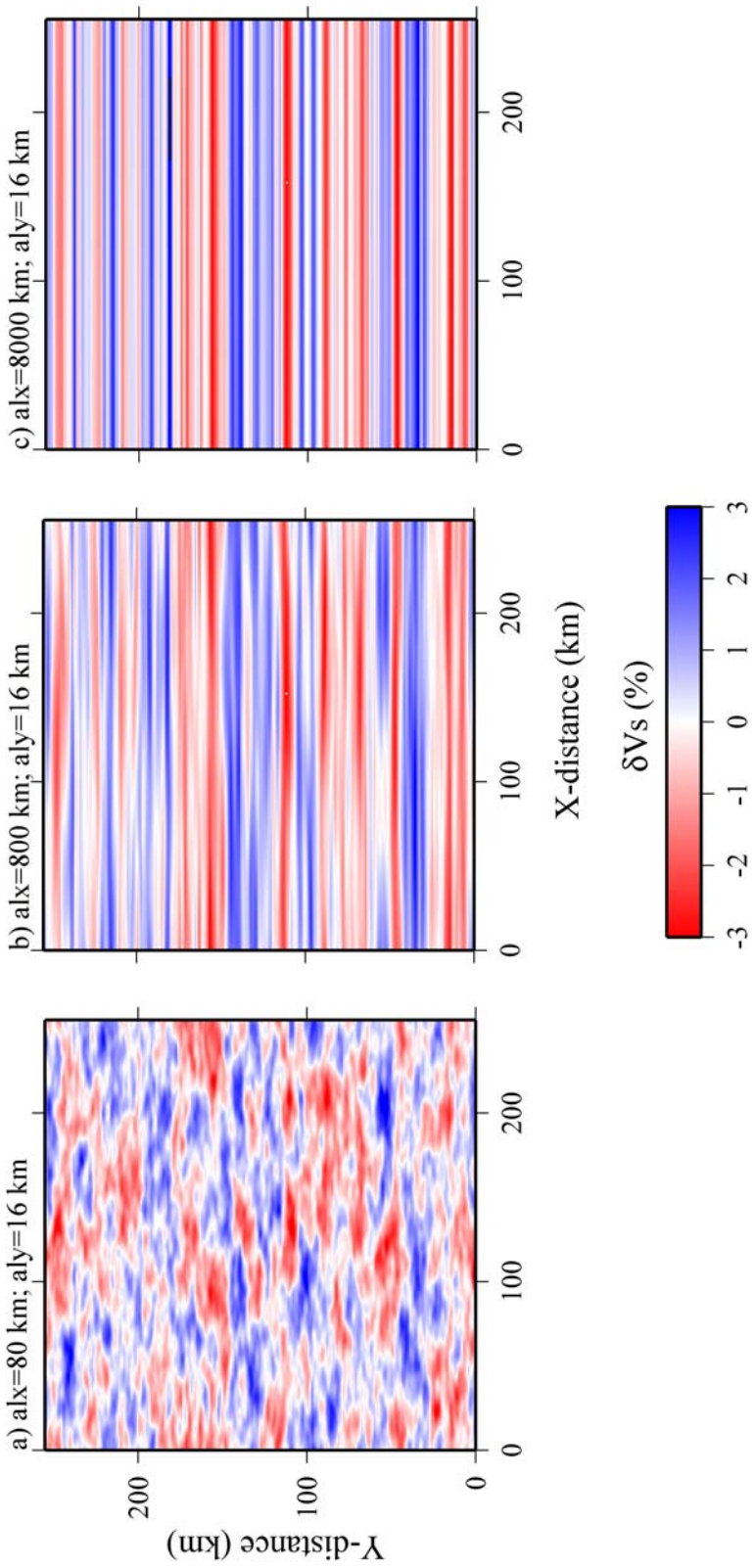
a) alx=80 km; aly=16 km
b) alx=800 km; aly=16 km
c) alx=8000 km; aly=16 km
Y-distance (km)
X-distance (km)
δVs (%)
0
100
200
-3
-2
-1
0
1
2
3

Figure 4.14 Three realizations of anisotropic random media computed for a von Karman autocorrelation function. The same random seed is used in each case. The autocorrelation lengths in the x- and y- directions (alx and aly respectively) are listed above each panel.

a) 500 sec

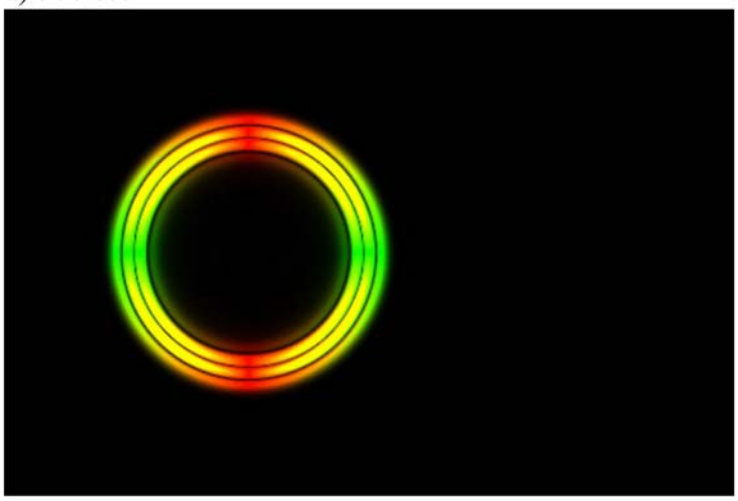

b) 1000 sec

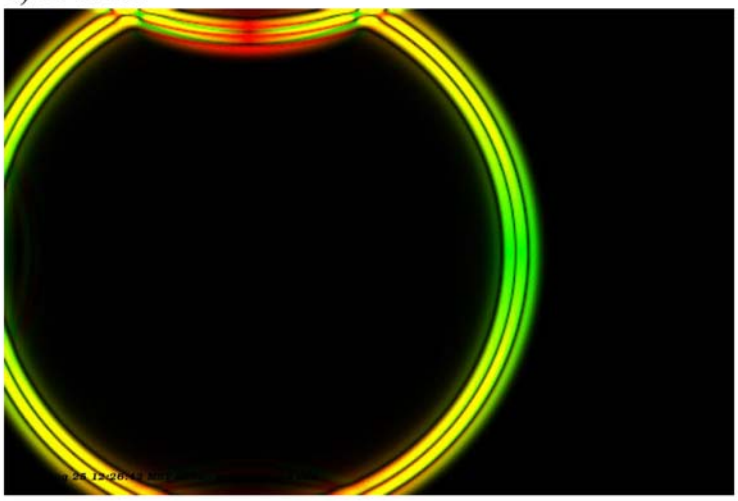

c) 1500 sec

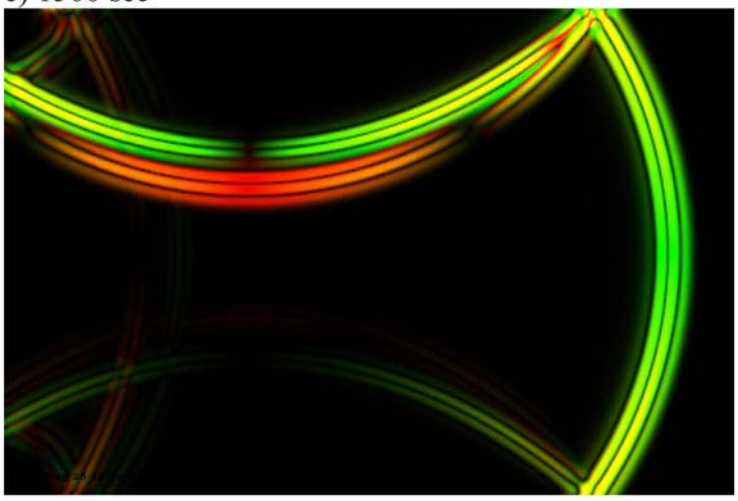

Figure 4.15 Wave propagation in a homogeneous media produced with E3D. Computation is for a 1 sec dominant period explosion source placed at 40 km depth and 40 km away from the left grid boundary. A Ricker wavelet is used for the source-time function. The homogeneous background model has the properties: V_S=4.0 km/sec; V_P=5.0 km/sec; density=3.0 g/cm^3. The arrival amplitudes are scaled showing red on the vertical component and green on the horizontal component. The final snapshot (panel c) displays artificial reflections from an imperfect radiating boundary layer. Also, the conversion from *P*-to-*S* at the free surface reflection (top edge of grid) is observed in panel c. Total grid dimensions are 80 × 120 km.

a) 500 sec

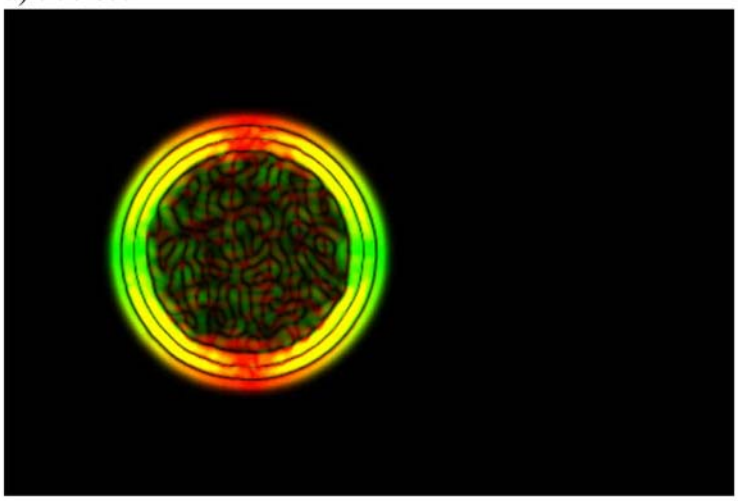

b) 1000 sec

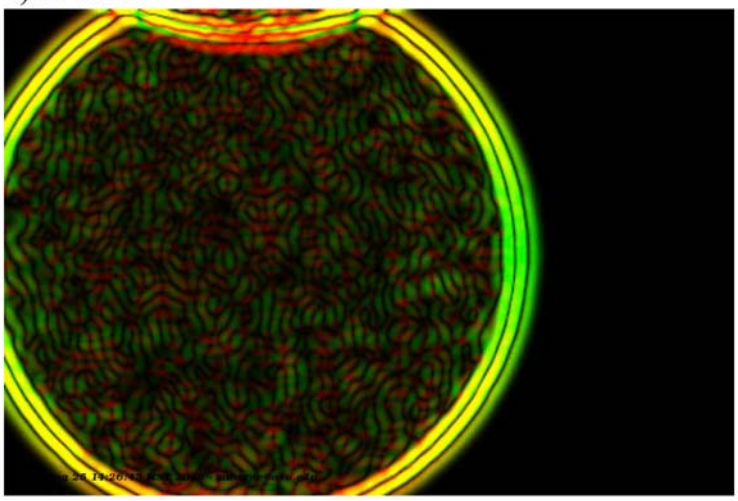

c) 1500 sec

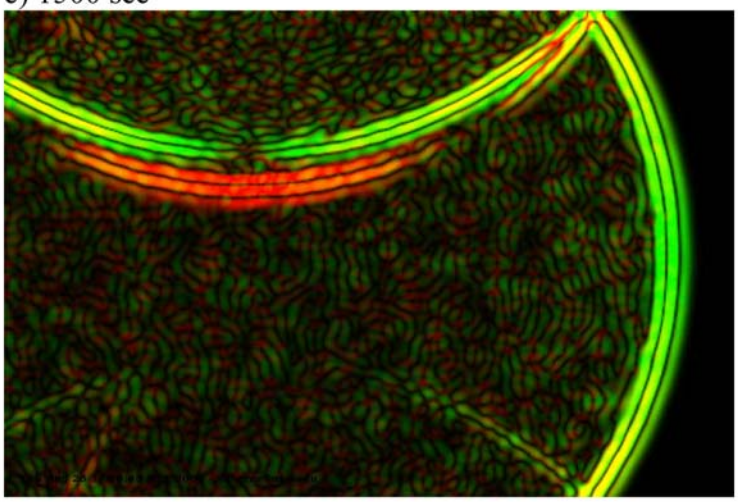

Figure 4.16 Three snapshots of wave propagations through random media are shown. The model is the homogeneous model of Figure 4.15 with 3% RMS *P*-wave velocity perturbations applied to the model. A von Karman autocorrelation function with 1 km autocorrelation length is used to construct the random media. As opposed to purely homogeneous case of Fig. 4.15 strong coda development is observed as a result of the random velocity perturbations. The source and grid parameters are the same as in Fig. 4.15.

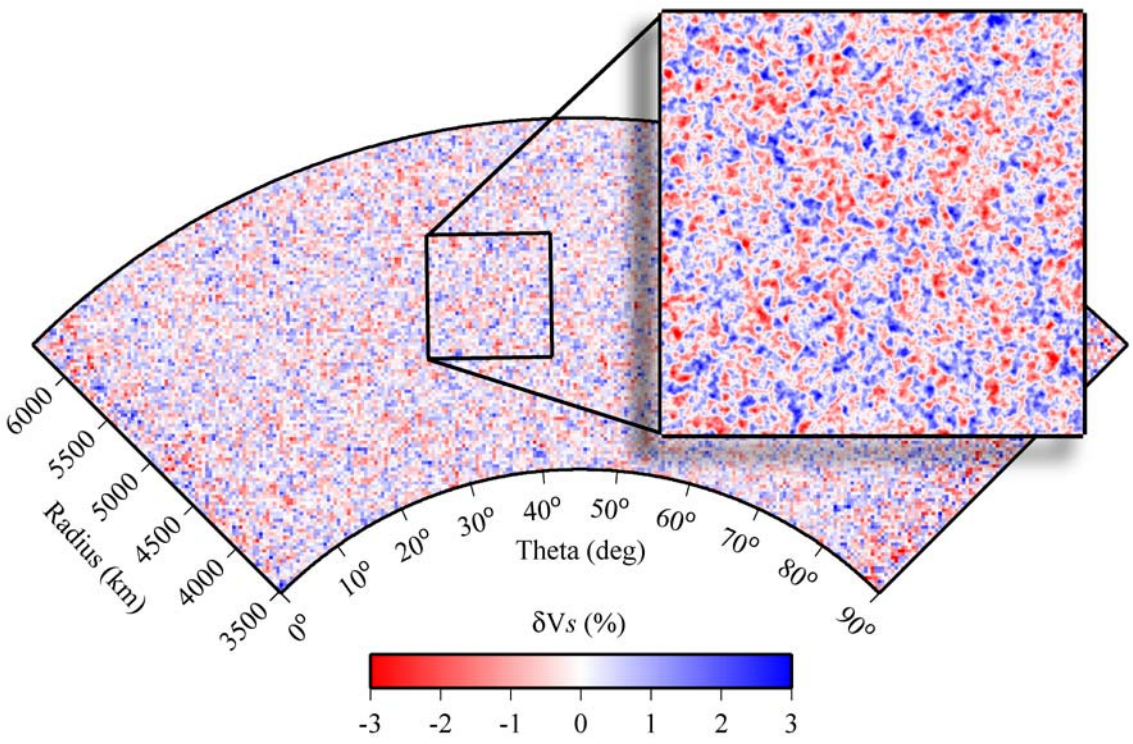

Figure 4.17 Shown is a realization of random velocity perturbations in SHaxi. An exponential autocorrelation function is used with a corner correlation wavelength of 32 km. RMS *S*-wave velocity perturbation is 1%.

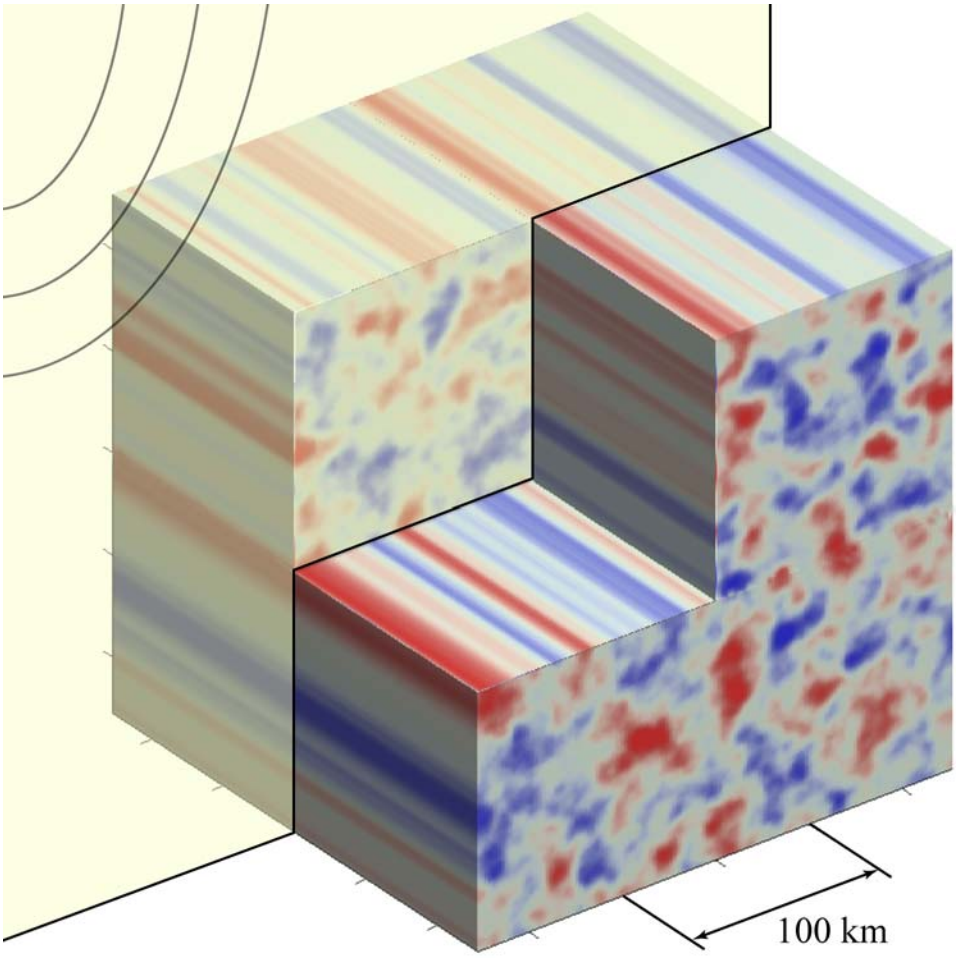

Figure 4.18 Detail of representation of random media in SHaxi. Because of axi-symmetry random velocity perturbations are anisotropic (e.g., see Fig. 4.14) with the perturbation being stretched in the φ-direction. The realization shown is for a 32 km autocorrelation length and an exponential autocorrelation function.

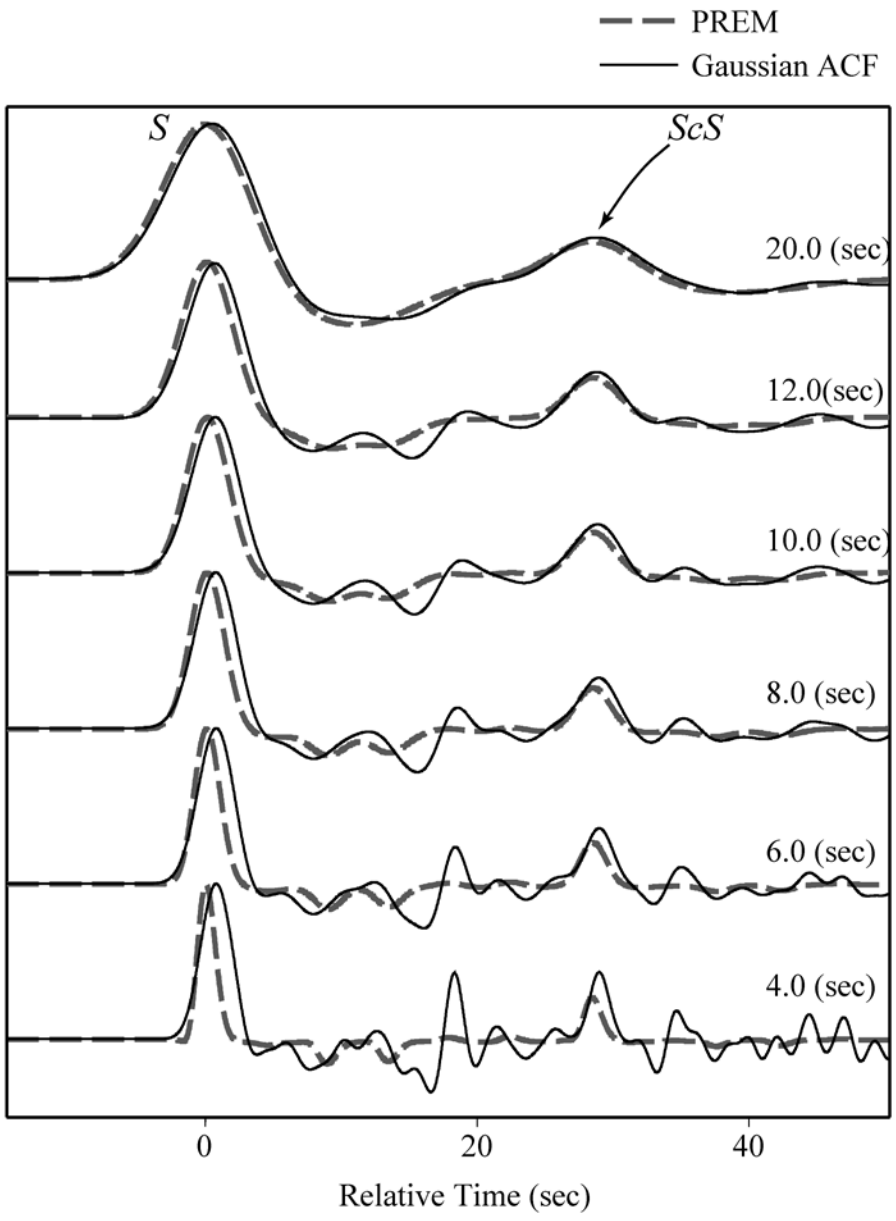

Figure 4.19 Frequency dependence of scattering. Shown are displacement synthetics for PREM (dashed line) and for a random media with a Gaussian autocorrelation function (solid line) created with RMS velocity perturbation of 3% and 16 km autocorrelation length superimposed on PREM. Seismograms are normalized to unity on the *S* arrival.

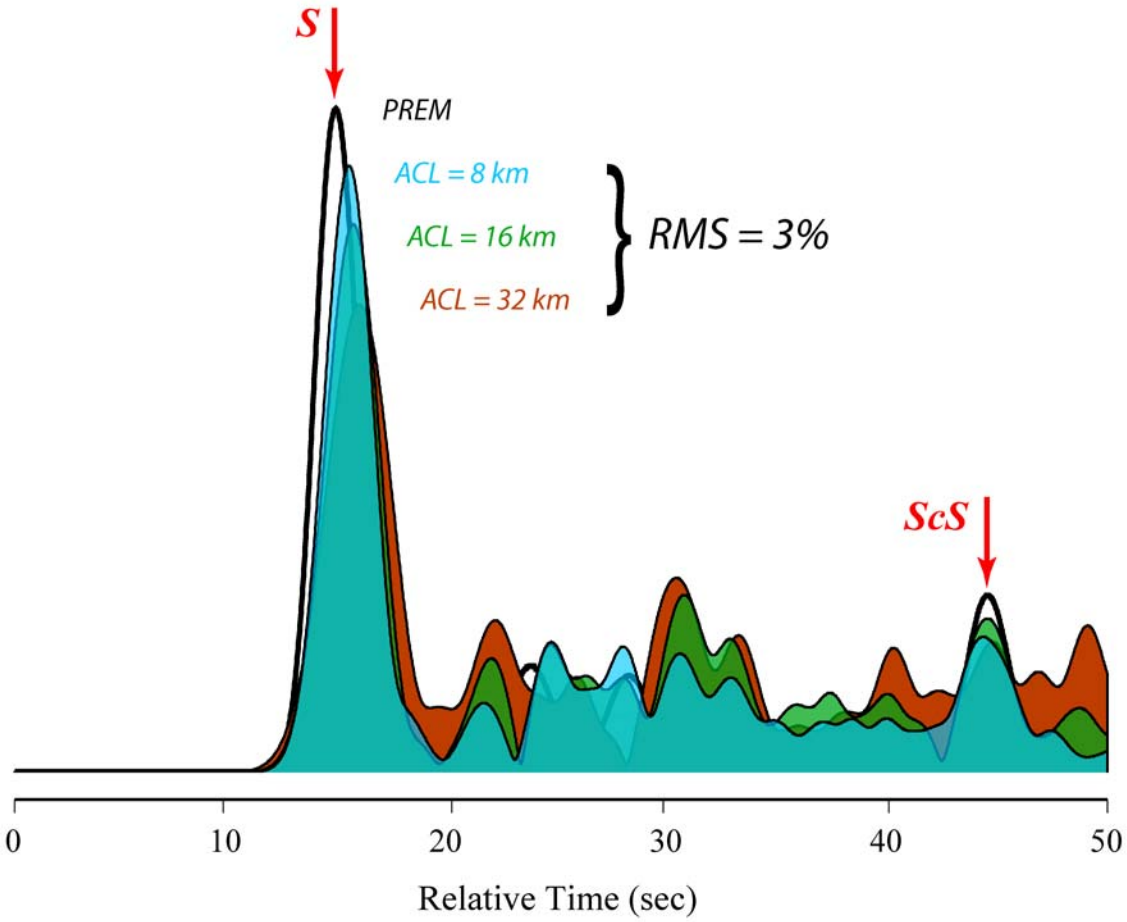

Figure 4.20 The dependence of autocorrelation length (ACL) on *SH*-wave envelopes. Envelopes of displacement seismograms are shown for the PREM model (black line) and for the PREM model with three realizations of random *S*-wave velocity perturbations applied. The perturbations are produced for a Gaussian autocorrelation function with 3% RMS velocity perturbations. Envelopes are shown for random perturbations with ACL's of 8 km (blue), 16 km (green) and 32 km (red).

CHAPTER 5

3-D SEISMIC IMAGING OF THE D" REGION BENEATH THE COCOS PLATE

Michael S. Thorne[1], Thorne Lay[2], Edward J. Garnero[1], Gunnar Jahnke[3,4], Heiner Igel[3]

[1]*Department of Geological Sciences, Arizona State University, Tempe, AZ 85287-1404, USA. E-mail: mthorne@asu.edu*
[2]*Department of Earth Sciences, University of California Santa Cruz, Santa Cruz, CA 95064, USA.*
[3]*Department of Earth and Environmental Sciences, Ludwig Maximilians Universität, Theresienstrasse 41, 80333 Munich, Germany.*
[4]*now at: Federal Institute of Geosciences and Natural Resources, Stilleweg 2, 30655 Hanover, Germany.*

SUMMARY

We use a 3-D axi-symmetric finite difference algorithm to model *SH*-wave propagation through cross-sections of 3-D lower mantle models beneath the Cocos Plate derived from recent data analyses. Synthetic seismograms with dominant periods as short as 4 sec are computed for several models: (1) a D" reflector 264 km above the CMB with laterally varying *S*-wave velocity increases of 0.9% to 2.6%, based on localized structures from a 1-D double-array stacking method; (2) an undulating D" reflector with large topography and uniform velocity increase obtained using a 3-D migration method; and (3) cross-sections through the 3-D mantle *S*-wave velocity tomography model TXBW. We apply double-array stacking to assess model predictions of data. Of the models explored, the *S*-wave tomography model TXBW displays the best overall agreement with data. The undulating reflector produces a double *Scd* arrival that may be useful in future studies for distinguishing between D" volumetric heterogeneity and D" discontinuity topography. 3-D model predictions show waveform variability not observed in 1-D model predictions. It is challenging to predict 3-D structure based on localized 1-D models when lateral structural variations are on the order of a few wavelengths of the energy used, particularly for the grazing geometry of our data. Iterative approaches of computing 3-D

synthetic seismograms and adjusting 3-D model characteristics by considering path integral effects are necessary to accurately model fine-scale D" structure.

5.1 Introduction

5.1.1 Lower Mantle Discontinuities

Ever since the designation of the D" region (Bullen 1949), which consists of heterogeneous velocity structure in the lowermost 200-300 km of the mantle, researchers have sought to characterize the detailed nature of this boundary layer. The mechanisms responsible for D" heterogeneity, manifested in strong arrival time fluctuations of seismic phases sampling the region, are still poorly constrained. It is important to characterize the D" region because its role as a major internal thermal boundary layer of Earth affects many disciplines, including mineral physics, global geodynamics, geochemistry, and geomagnetism (see Lay *et al.* 2004a for a review). The existence of a D" shear velocity discontinuity, discovered by Lay & Helmberger (1983), has added further complexity to creating a detailed picture of the D" region.

Only a handful of seismological techniques directly detect the D" discontinuity. The discontinuity is most commonly detected by observations of a travel-time triplication in *S*- and/or *P*- waves bottoming in the lower mantle. The structure has also been detected by observations of a strong arrival in the coda of $PKKP_{AB}$ (Rost & Revenaugh 2003). Studies of differential travel times between pairs of seismic phases (e.g., *ScS-S*, *PcP-P,* $PKKP_{AB}$-$PKKP_{DF}$) support the presence of a relatively abrupt increase in deep mantle wave-speeds in the lowermost mantle (e.g., Creager & Jordan 1986; Woodward &

Masters 1991; Zhu & Wysession 1997). Although the differential travel time studies are compatible with a D" discontinuity, they do not resolve its presence.

During the past two decades, the D" discontinuity has been detected in numerous seismic investigations (see Wysession *et al.* 1998 for a review). These studies have characterized the D" discontinuity as being a sharp *P*- and/or *S*- wave velocity (V_P and/or V_S) increase (~0.5 to 3.0% for V_P and ~0.9 to 3.0% for V_S) ranging in height from 150 to 350 km above the core-mantle boundary (CMB) with an average height of 250 km.

The *P*-wave observations most convincingly associated with a D" discontinuity are for paths beneath northwestern Siberia (e.g., Weber & Davis 1990; Houard & Nataf 1993). Other studies using *P*-wave data fail to find strong evidence for the discontinuity at many locations (e.g., Ding & Helmberger 1997). However, a lack of observations of *P*-wave reflections does not necessarily indicate non-existence of a velocity increase in D". For example, the sharpness, or depth extent, of the boundary plays an important role in its reflectivity. At grazing angles, where the wavefield triplicates, a velocity increase spread out over roughly 100 km can match most triplication data as accurately as for a sharp discontinuity (e.g., Young & Lay 1987; Gaherty & Lay 1992). However; pre-critical and high-frequency *P*-waves will be only weakly reflected by such a gradient increase. An undulating boundary may produce intermittent reflections or scattering that confuse detections of reflections. Additionally, a relatively low amplitude V_P jump at the D" discontinuity appears to be common, yielding reflections below the detection limit of routine seismic techniques. In general, past studies have not established whether a D" *P*-wave velocity discontinuity is ubiquitous or intermittent.

In contrast, *S*-wave reflections from a D" discontinuity are more commonly observed. A number of studies have revealed three regions of the deep mantle where the existence of a D" *S*-wave velocity discontinuity is particularly well supported by *S*-wave observations. These three regions are:

1. Beneath Siberia (e.g., Lay & Helmberger 1983; Weber & Davis 1990; Gaherty & Lay 1992; Weber 1993; Garnero & Lay 1997; Valenzuela & Wysession 1998; Thomas et al. 2004b),
2. Beneath Alaska (e.g., Lay & Helmberger 1983; Young & Lay 1990; Lay & Young 1991; Kendall & Shearer 1994; Matzel et al. 1996; Garnero & Lay 1997; Lay et al. 1997), and
3. Beneath Central America (e.g., Lay & Helmberger 1983; Zhang & Lay 1984; Kendall & Shearer 1994; Kendall & Nangini 1996; Ding & Helmberger 1997; Reasoner & Revenaugh 1999; Ni *et al.* 2000; Garnero & Lay 2003; Lay *et al.* 2004b; Thomas *et al.* 2004a; Hutko *et al.* 2005).

Some locations in the deep mantle where seismic observations do not show evidence for a shear wave discontinuity are adjacent to regions where observations do indicate the presence of a discontinuity. Explanations of why the discontinuity may appear or disappear over small spatial scales (e.g., < 100 km Lay *et al.* 2004b) are still debated. Strong topographic relief on the discontinuity and/or rapid 3-D velocity variations beneath the discontinuity have been invoked as possible explanations (e.g., Kendall & Nangini 1996; Thomas *et al.* 2004a).

Additional studies using *S*-waves have shown evidence for the discontinuity beneath the Central Pacific (Garnero *et al.* 1993; Avants *et al.* 2005). This has motivated speculation that the feature is global (e.g., Sidorin *et al.* 1999). Nevertheless, further probing of the deep mantle, especially under the Southern Pacific and Atlantic Ocean regions, is needed before the lateral extent of the feature can be ascertained.

5.1.2 S-wave Triplication Behavior

Because the D" discontinuity increase for V_S appears to be greater than for V_P, studies utilizing triplications in the *S*-wave field have been the preferred method for detecting the discontinuity. In this paper we restrict our attention to *S*-waves observed on transverse component (*SH*) recordings at epicentral distances ranging from roughly 70º to 85º. Fig. 5.1 shows synthetic *SH* displacement seismograms computed using a finite difference axi-symmetric method for *SH*-waves (SHaxi). This method is described in (Jahnke *et al.* 2005) and is used to compute synthetic seismograms for D" discontinuity models.

In Fig. 5.1 synthetic seismograms for the PREM (Dziewonski & Anderson 1981) shear velocity structure, which does not contain a D" discontinuity, are shown with dotted lines. Synthetic seismograms for a D" discontinuity model with a 1.3% V_S increase (relative to PREM) 264 km above the CMB are shown in black. Neither model has crustal layers, as discussed below. Synthetics for the discontinuity model exhibit a travel-time triplication with extra arrivals between *S* and *ScS*. We use the nomenclature of Lay & Helmberger (1983) to describe the triplication phases labeled in Fig 5.1. The direct *S*-

wave turning above the discontinuity is termed *Sab* whereas the *S*-wave energy turning below the discontinuity is termed *Scd*. *Sbc* denotes arrivals reflecting off the discontinuity. The post-critical *Sbc* arrival is progressively phase shifted, producing a small negative overshoot of the combined *Scd* + *Sbc* arrival. In Fig. 5.1 distinct *Scd* and *Sbc* arrivals are discernible at larger distances; however the *Scd* and *Sbc* arrivals are generally not separately distinguishable in broadband data. Hence, we refer to the combined (*Scd* + *Sbc*) arrival as *SdS*. Most studies reference *SdS* travel-times and amplitudes to *ScS* (also shown in Fig. 5.1). Because the synthetics shown in Fig. 5.1 were created for a 500 km deep source, the seismic phase *s400S,* an underside reflection from the 400 km discontinuity above the source, is also observed. The amplitude of *s400S* is usually too low to be observed in broadband data without stacking records (e.g., Flanagan & Shearer 1998).

Fig. 5.2 shows the ray path geometry of the seismic phases in Fig. 5.1 for a receiver at an epicentral distance of 75º. The ray path geometry is for the same discontinuity model used to create the synthetic seismograms in Fig. 5.1. Also shown in Fig. 5.2 is the *SH*- velocity wavefield at one instance in time through a cross-section of the Earth computed with the SHaxi method. The relationship between spherical wave fronts and geometrical rays, which are perpendicular to the wave fronts, can be seen. Infinite frequency ray paths are useful for visualizing the path that seismic energy takes through the mantle, however, the seismic energy interaction with Earth structure surrounding the geometric ray must be considered because it also contributes energy to the seismic phases recorded at the surface (e.g., Dahlen *et al.* 2000).

5.1.3 Study region and objectives

The D" discontinuity beneath the Central American region has been investigated extensively because of excellent data coverage provided by South American events and North American receivers. Three recent studies have focused on mapping the D" discontinuity structure in 3-D beneath the Cocos Plate subset of the Central American region (Lay *et al.* 2004b; Thomas *et al.* 2004a; Hutko *et al.* 2005). A recent tomographic inversion including *SdS* arrivals has also imaged the lower 500 km of the mantle beneath Central America (Hung *et al.* 2005). These regional studies have produced models for the structure of the discontinuity in the Cocos Plate region and will be discussed in detail in Section 3.

The variability in seismic differential travel-time (e.g., *ScS-Scd* or *Scd-Sab* differential travel-times – referred to hereafter as $T_{ScS\text{-}Scd}$ and $T_{Scd\text{-}Sab}$ respectively) or amplitude ratio (e.g., *Scd*/S*cS*) observations relative to optimal 1-D model predictions indicate the presence of 3-D D" structure (e.g., Lay & Helmberger 1983; Kendall & Nangini 1996). Because D" discontinuity topography and V_S heterogeneity are both likely to be 3-D in nature (e.g., Tackley 2000; Farnetani & Samuel 2005), there are major challenges in resolving discontinuity topography from surrounding volumetric velocity heterogeneity. Moreover, many D" discontinuity structures have been inferred based on using localized 1-D processing techniques, without it being clear how to generalize those models to 3-D structures. This is particularly problematic for triplication arrivals that graze the deep mantle, with extensive horizontal averaging of the structure. 3-D models have been obtained using migration approaches that assume homogeneous reference

structures and point-scattering assumptions, which intrinsically bias the model images. Tomography methods usually do not account for abrupt velocity discontinuities, and incur errors by incorrect back-projection of travel-times on incorrect raypaths.

In order to progress from 1-D processing and modeling techniques that use simplifying assumptions for 3-D modeling, seismologists must use advanced synthetic seismogram techniques. Numerical techniques for computing synthetic seismograms in 2- or 3-D are now becoming practical because of the recent availability and processing power of cluster computing. In this paper, we produce 3-D synthetic seismograms for our versions of 3-D models based on various D" discontinuity modeling results beneath the Cocos Plate. We also create synthetic seismograms through cross-sections of a recent *S*-wave tomography models (Grand 2002). The models we construct and compute synthetics for are summarized in Table 5.1. We compare waveforms and travel-time differentials from the computed synthetic seismograms with each other and with broadband data used in the studies of Lay *et al.* (2004b) and Thomas *et al.* (2004a). Furthermore, we analyze the limits of using localized 1-D processing techniques and lateral interpolations to infer 3-D D" discontinuity structure.

5.2 3-D axi-symmetric finite difference method and verification

Constraining models of 3-D D" structure requires computation of synthetic seismograms for 3-D geometries (hereafter referred to as 3-D synthetic seismograms) for comparison to original data. This also allows an assessment of if and how localized 1-D modeling results or migration methods should be extrapolated to predict actual 3-D structure. We use the 3-D axi-symmetric finite difference method (SHaxi) (based after

Igel & Weber 1995, 1996; and extended in Jahnke *et al.* 2005) to explore the 3-D model extrapolations based on recent models of heterogeneous D" structure beneath the Cocos Plate obtained from several distinct procedures. This is the first application of the SHaxi method to original data.

The SHaxi method does not incorporate full 3-D Earth models as in some other numerical techniques (e.g., the spectral element method of Komatitsch & Tromp 2002). Instead the model defined on a grid in the vertical plane containing the great circle arc is expanded to 3-D by (virtually) rotating the grid around the vertical axis. As a consequence the computation on a 2-D grid provides seismogram with the correct geometrical spreading, but only for axi-symmetric geometries. Nonetheless, this axi-symmetric method has several advantages for computing synthetic seismograms. Because it computes the wave field on a 2-D grid, synthetic seismograms can be generated for much shorter dominant periods (e.g., down to 1 sec) than with full 3-D techniques. SHaxi also maintains the correct 3-D geometrical spreading, which is an advantage over purely 2-D techniques that do not.

The main restriction in using the SHaxi method is that structures incorporated on the 2-D axi-symmetric grid act as 3-D ring-like structures (see Jahnke *et al.* 2005). This makes it impossible to model focusing and defocusing effects due to variations off the great circle plane. Additionally the source acts as a strike-slip with a fixed SH source radiation pattern proportional to the sine of the takeoff angle. This fixed radiation pattern makes direct comparison of amplitudes between synthetics and data from arbitrary

oriented sources slightly complicated. In this study we are primarily concerned with differential travel time effects and we place less emphasis on amplitude effects.

In order to produce synthetic seismograms at relatively high frequencies we used 16 nodes (128 processors) of the Hitachi SR8000 super computer at the Leibniz-Rechenzentrum, Munich, Germany. These computations require 42,000 (lateral) × 6,000 (radial) finite difference grid-points. This grid spacing corresponds to roughly 0.5 km between grid-points radially, and varies between 0.5 km (Earth's surface) and 0.25 km (CMB) laterally. Calculations are run to 1700.0 seconds of simulation time, which takes approximately 24 hours to compute. For these input parameters, synthetic seismograms with a dominant period of 4 sec are produced. This is suitable for comparisons with our *SH* observations which have been low-pass filtered with a cut-off of 3.3 sec.

In order to ensure that our computations are accurate for the time and epicentral distance windows used in this study, we used the Gemini (Greens Function of the Earth by Minor Integration) method of Friederich & Dalkolmo (1995) to compute 1-D PREM synthetics for comparison to our finite-difference results. The window containing *Sab* and *ScS* that we use starts 20 sec before and ends 100 sec after the *Sab* arrival in epicentral distance ranging from 70º – 85º. The Gemini method was chosen because it has previously been used for verification of other synthetic seismogram techniques (Igel *et al.* 2000). We produced 10 sec dominant period synthetics with the Gemini method for use in our comparisons. Overlaying individual traces display excellent agreement between the SHaxi and Gemini methods, as demonstrated by a minimum cross-correlation coefficient between records of 0.9982 at 85º.

In synthetics created for PREM [Supplemental Fig. 6A], crustal and mid-crustal reverberations interfere with the *SdS* arrival. The average crustal structure represented in PREM is not a realistic estimate of the complex crustal structure beneath southern California recording stations (e.g., Zhu & Kanamori 2000). In order to compare our synthetics to data from southern California stations, we remove the crustal layers from PREM before computing synthetic seismograms.

5.3 Study region and model construction

5.3.1 D" structure beneath the Cocos Plate

The D" discontinuity structure beneath the Cocos Plate region has been the focus of numerous seismological studies. Thomas *et al.* (2004a) provide a review of these studies, finding that a D" *S*-wave velocity discontinuity has been consistently inferred at a height ranging between 150 – 300 km above the CMB with a velocity increase ranging from 0.9 – 3.0%. There is little evidence for a corresponding *P*-wave velocity D" discontinuity (e.g., Ding & Helmberger 1997; Rost, private communication, 2005) other than the work of Reasoner & Revenaugh (1999) who stack many short-period signals and infer a weak reflector (0.5 – 0.6% *P*-wave velocity increase) about 190 km above the CMB.

Five recent studies have attempted to assess possible small-scale 2- or 3-D variability of the D" discontinuity beneath the Cocos Plate. Lay *et al.* (2004b), Thomas *et al.* (2004a), and Hutko *et al.* (2005) produced D" discontinuity models for the Cocos Plate region using various stacking and migration methods. We compute synthetic seismograms through cross-sections of our 3-D constructions of the models produced by

Lay *et al.* (2004b) and Thomas *et al.* (2004a). Ni *et al.* (2000) computed synthetic seismograms through cross-sections of the tomography model of Grand (1994) to determine whether that shear velocity structure helped to improve 1-D D" discontinuity models. We similarly compute synthetic seismograms for the most recent tomography model of Grand (2002) for comparison. Hung *et al.* (2005) presented a lower mantle tomography model of the Central American region that overlaps the Cocos Plate region. However, consideration of the Hung *et al.* (2005) model suggests that it lacks adequate data sampling in our study region and we do not analyze it further here. We summarize below how we produced model cross-sections for use in the SHaxi method, and the results of comparing data to the resulting 3-D synthetics.

5.3.2 Double-array stacking model

Lay *et al.* (2004b) analyzed broadband transverse component seismic seismograms including *SdS* and *ScS* arrivals from 14 deep South American events recorded by Californian regional networks. Fig. 5.3a shows the source-receiver geometries used. The study employed the double-array stacking technique of Revenaugh & Meyer (1997) to obtain apparent reflector depths of *SdS* energy for localized bins of data with nearby *ScS* CMB reflection points. Fig. 5.3b shows detailed outlines of the four geographic bins in which Lay *et al.* (2004b) grouped their data. *SdS* energy was detected in stacks throughout the region, however the area delimited by Bin 2 showed weak *SdS* energy and some individual seismic traces did not show clear *SdS* arrivals between *Sab* and *ScS*, as previously noted by Garnero & Lay (2003). If the shear velocity within the

D" layer (i.e., between the D" discontinuity and the CMB) is laterally uniform, the stacks imply localized topography of the discontinuity ranging over 150 km, in which case the amplitude variations might arise due to reflection from an undulating reflector. However, Rokosky *et al.* (2004) and most mantle tomography models suggest a general south-to-north increase in D" V_S from Bin 1 to Bin 4, based primarily on *ScS* arrival times. Lay *et al.* (2004b) modeled the data using localized 1-D models, allowing the average velocity in the D" layer to vary as needed to match the amplitude of *SdS*. They found that the variations required to match the amplitude kept the depth of the discontinuity almost constant. Their final model involved a 264 km thick D" layer with varying V_S increase across the D" layer ranging from 0.9 to 2.6%. The resulting structures match the general trend of the *ScS* arrival time data, except for the model in Bin 1, which predicts earlier *ScS* arrivals than observed. Reconciling the *SdS* amplitudes and *ScS* arrival times requires a model with a large discontinuity about 100 km deeper than in bins to the north.

To create models for use with the SHaxi method based on the localized 1-D results of Lay *et al*. (2004b), we construct cross-sections through four average great circle paths from source clusters to station clusters (Path 1 – Path 4, Fig. 5.3b). These great circle paths are based on the average event-receiver location for events that have *ScS* bounce-points in each of the four geographic bins. For each cross-section, we use PREM velocities above the D" discontinuity. A brief description of models and their naming convention are outlined in Table 5.1. We constructed models with two end-member scenarios: (1) the velocity structure in each bin is block-like (model LAYB) [Supplemental Fig. 6B]; and (2) the velocity structure is linearly interpolated between the

center of each bin (model LAYL). We use the same great circle paths (Paths 1-4) to construct cross-sections for the models listed in Table 5.1. We note that this process assumes very localized sensitivity of the 1-D modeling as implied by the fine binning used; as found below this results in very small scale variations that are at odds with the intrinsic resolution of the nearly horizontally grazing ray geometry.

5.3.3 Point-scattering migration model

Thomas *et al.* (2004a) employed a pre-critical point-scattering migration technique (Thomas *et al.* 1999) to image the deep mantle beneath the Cocos Plate using the same data set as Lay *et al.* (2004b). The imaged model space was roughly 700 km in length and 150 km wide (study region T shown in Fig. 5.3b). The migration study used the 1-D background model ak135 (Kennett *et al.* 1995) to provide travel-times for stacking windows of seismogram subsets compatible with scattering from a specified 3-D grid of scattering positions. V_S was not allowed to vary laterally, which projects all travel time variations into apparent scattering locations within the background model. A smoothed version of the resultant scattering image gives a topographically varying D" discontinuity surface with a south-to-north increase in discontinuity height above the CMB from 150 to 300 km. This apparent topography is similar to the double-array stacking results of Lay *et al.* (2004b) for a 1-D stacking model. The 150 km increase in discontinuity height occurs in the center of the image region (near Bin2 of Lay *et al.* (2004b)), over a lateral distance of roughly 200 km. The central region, containing the transition in discontinuity depth, does not reflect strong coherent energy and there is

uncertainty in the continuity of the structure. The topography in this model is completely dependent on the assumption of 1-D background structure.

The migration approach used by Thomas *et al.* (2004a) does not model the amplitudes and like all Kirchhoff migrations, simply images a reflector embedded in the background model without accounting for wave interactions with the structure. In order to compute synthetic seismograms for this structure, it is necessary to prescribe the V_S increase across the imaged reflector. Previous 1-D modeling efforts for the region suggested a 2.75% (Lay & Helmberger 1983; Kendall & Nangini 1996) or 2.0% (Ding & Helmberger 1997) V_S increase, but Lay *et al.* (2004b) suggest the region has strong lateral variability ranging from 0.9 to 2.6%. As initial estimates, we chose V_S increases of 2.0% (model THOM2.0) and 1.0% (model THOM1.0).

Recent studies of a lower mantle phase transition from magnesium silicate perovskite to a post-perovskite (ppv) structure indicate that the phase transition should involve 1.5% V_S and 1% density increases (Tsuchiya *et al.* 2004a), providing a possible explanation for the D" discontinuity. This phase transition also is predicted to have a steep Clapeyron slope of ~7-10 MPa K^{-1} (Oganov & Ono 2004; Tsuchiya *et al.* 2004b), which could account for significant topography on the D" discontinuity. Because the study of Thomas *et al.* (2004a) suggests rapidly varying topography, as may accompany a ppv phase transition in the presence of lateral thermal and compositional gradients (e.g., Hernlund *et al.* 2005), we also create synthetic seismograms with 1.5% V_S and 1% density increases (model THOM1.5). Model cross-sections are shown in Supplemental Fig. 6B for model THOM2.0.

5.3.4 Tomography model

A consistent feature of recent *S*-wave tomography models (e.g., Masters *et al.* 1996; Kuo *et al.* 2000; Megnin & Romanowicz 2000; Ritsema & van Heijst 2000; Gu *et al.* 2001; Grand 2002) is the presence of relatively high shear velocities beneath the Central America and Cocos Plate region. Model TXBW (parameterized with 2.5º × 2.5º bins – roughly 150 km on a side) from Grand (2002) was not developed using triplication arrivals and resolves longer wavelength structure than models produced by Lay *et al.* (2004b) and Thomas *et al.* (2004a). The reference model for TXBW has relatively high D" velocities, and the lowest layer (bottom 220 km of the mantle) in model TXBW contains high V_S perturbations (up to ~2.3% increases) relative to PREM beneath the Cocos Plate, with a general south-to-north velocity increase. This is consistent with the results of Lay *et al.* (2004b).

Ni *et al.* (2000) utilized the WKM method (a modification of the WKBJ method of Chapman 1978) to produce synthetic seismograms through 2-D cross-sections of block-style tomography models. As an application of their method, Ni *et al.* (2000) produced synthetics through two cross-sections of Grand's (1994) tomography model, with great-circle paths passing through the Central American region. Ni *et al.* (2000) were not able to observe the *SdS* phase in Grand's model for the chosen great-circle paths without arbitrarily increasing the velocity perturbations in the lowermost layer of Grand's model by a factor of 3. Their synthetics then compare favorably to broadband *Scd* waveforms of Ding & Helmberger (1997) for the Cocos Plate region.

We created four cross-sections through Grand's most recent tomography model TXBW (Grand 2002) for synthetic seismogram construction with the SHaxi method. To create cross-sections, we mapped the heterogeneity in TXBW onto our finite difference grid using four-point inverse distance weighted interpolation between the V_S values given in the model. Our cross-section through great circle Path 1 (Fig. 5.3) is identical to one of the cross-sections used in the study of Ni *et al.* (2000).

Model TXBW is parameterized in layers of blocks with constant *S*-wave velocity perturbations (δV_S). We observe a noticeable increase in average V_S between the two lowermost layers along each of our reference great-circle paths (Path1: +1.5%; Path 2: +1.75%; Path 3: +1.75%; Path 4: +2.0% - Supplemental Fig. 6C). Ni *et al.* (2000) referenced the heterogeneity in Grand's tomography model directly to PREM (S. Ni, private communication, 2005) rather than to the 1-D reference model actually used in Grand's inversion. When we use the 1-D reference model of Grand, with its velocity increase in the lowermost mantle, the tomographic models produces significant *SdS* energy from the boundary between the two lowermost layers and we find no need to arbitrarily enhance the structure [Cross-sections are shown in Supplemental Fig. 6C and D]. Cross-sections through model TXBW show moderate variation in V_S progressing between Paths 1-2-3-4. The strongest variation in velocity structure is observed between Path 1 and 4.

5.4 Synthetic seismogram results

We computed synthetic seismograms for each great-circle path through the three models described in the preceding section. Significant variability in waveform shape and

differential travel-times between seismic phases is found in the synthetic seismograms for the various models, as we discuss below. We consider $T_{ScS-Scd}$ and $T_{ScS-Sab}$, *Scd*/*ScS* amplitude ratios, and waveform characteristics between the different predictions.

5.4.1 Models LAYB and LAYL

Synthetic seismograms were computed for models LAYB and LAYL which have block-like or linearly interpolated V_S structures, respectively. Differences in waveform shape or travel-time of arrivals between LAYB and LAYL are not observable for the 4-s dominant period of our synthetic seismograms. This is because the geographic bin size used by Lay *et al.* (2004b) is small compared with the wavelength of *S*-wave energy in the D" region (bins are ~2.5º wide in the great circle arc direction, or ~5 wavelengths of a 4 sec dominant period wave at the CMB). The effect of bin size on $T_{ScS-Scd}$ and $T_{ScS-Sab}$ will be discussed in Section 7.

We also compute synthetic seismograms for the 1-D models from Lay *et al*. (2004b) to compare with our synthetics for the 3-D interpolation of those models. Overlaying synthetics for model LAYB with synthetics for the 1-D models illuminates the 3-D structural effects on waveform shape and timing [Supplemental Fig. 6E]. 3-D synthetics for model LAYB show simple *SdS* waveforms, similar to the 1-D predictions, with $T_{Scd-Sab}$ between the 1-D and 3-D models unchanged. However, there exists large variability in $T_{ScS-Scd}$ between the synthetics. This is not unexpected since *ScS* samples several bins in the 3-D computation, and thereby averages the laterally varying D" structure. For example, 3-D predictions for Path 2 of LAYB show reduced $T_{ScS-Scd}$ (~1.5

sec decrease for 70º-80º) from those for the optimal 1-D model for Bin 2. This discrepancy is due to *ScS* having its central bounce-point in Bin 2 (with a 0.4% V_S increase in the 1-D model), but the *ScS* wave also travels through Bins 1 and 3 (which have 0.9% and 0.7% V_S increases throughout D", respectively). Thus the 3-D $T_{ScS\text{-}Scd}$ is relatively reduced, since *ScS* is advanced by the neighboring bins. Path 3 similarly has a smaller $T_{ScS\text{-}Scd}$ (~1.5 sec decrease). This illustrates the challenge of how to interpret a suite of localized 1-D model results; the models need to be projected and averaged along the ray paths in a manner akin to tomography when constructing a 3-D model rather than being treated as local blocks as we have done

In addition to the large variations between 1-D and 3-D predicted $T_{ScS\text{-}Scd}$ significant variations in *Scd*/*ScS* amplitude ratios are present. Only minor discrepancies exist in predicted *ScS*/*Sab* amplitude ratios implying that differences in 1-D and 3-D *Scd/ScS* predictions are due to 3-D effects on *Scd*. In general, increasing V_S below the D" discontinuity increases *Scd* amplitudes. *Scd* amplitudes in the 3-D synthetics are sensitive to D" velocities in the neighboring bins because of the grazing ray geometry and the large resultant Fresnel zone. For example, synthetics for Path 2 of LAYB show an increase in the *Scd*/*ScS* amplitude ratio over synthetics for the 1-D Bin 2 model (ratio increase from 0.07 to 0.15), owing to Bin 2 being juxtaposed with two higher velocity bins. This suggests that mapping of localized 1-D structure into a 3-D model requires attention to the effective Fresnel zone as well. This is intrinsic to migration and finite-frequency tomography approaches.

5.4.2 Models THOM1.0, THOM1.5, and THOM2.0

We constructed three models based on Thomas *et al.* (2004a), one for each of three distinct D" velocities (see Table 5.1). Larger D" velocity increases produce smaller $T_{ScS\text{-}Scd}$ and larger *Scd/ScS* amplitude ratios, which accounts for the main differences in synthetics for models THOM1.0, THOM1.5, and THOM2.0. Model THOM1.5 also included a 1% density increase, which produced indistinguishable synthetics from those either lacking or containing greater density increases (up to 5%).

Although differences between models THOM1.0 – THOM2.0 are straightforward, *ScS-Scd* differential timing and *Scd*/*ScS* amplitude ratio effects between Paths 1-4 are complex [Supplemental Fig. 6F]. Here, we restrict the discussion on variable Path effect to model THOM2.0.

Along Path 1, the wavefield encounters the deepest D" discontinuity (~130 km above the CMB) (see Supplemental Fig. 6B). Consequently, $T_{ScS\text{-}Scd}$ are the smallest. Along Path 4, the wavefield encounters the shallowest D" discontinuity (~290 km above the CMB). Although $T_{ScS\text{-}Scd}$ for Path 4 are greater than for Path 1 (ranging between 1.5 sec larger at 80º to 9 sec larger at 71º), the largest $T_{ScS\text{-}Scd}$ are sometimes observed for paths 2 and 3. Along Paths 2 and 3 the wave field encounters the transition from a deep to shallow D" discontinuity. Three snapshots of the *SdS* and *ScS* energy are shown for Path 3 (Fig. 5.4), which displays the development of a double *Scd* arrival. In Fig. 5.4(a) as the wave field interacts with the deepest D" discontinuity structure the *Scd* phase is already apparent. 50 sec later the wavefield interacts with the transition from a deep to shallow discontinuity (Fig. 5.4b), showing more *Scd* complexity due to multipathing with

the shallower and deeper discontinuities. A double *Scd* arrival is fully developed 50 sec later, apparent as two distinct *Scd* peaks in the synthetic seismograms.

At closer epicentral distances (from 70º-72º for Path 3) the *Scd* arrival originating from the deeper discontinuity contains higher amplitudes. At the further epicentral distances (> 72º for path 3) the *Scd* arrival originating from the shallower discontinuity contains the higher amplitudes. Arrival times based on *Scd* peak amplitudes imply an abrupt jump in $T_{ScS\text{-}Scd}$ at the epicentral distance where *Scd* amplitudes from the shallower discontinuity overtake *Scd* amplitudes from the deeper discontinuity. For Path 3 a 3 sec change in $T_{ScS\text{-}Scd}$ occurs at 72º.

5.4.3 Model TXBW

Fig. 5.5 shows overlain synthetic seismograms computed for model TXBW for Paths 1 and 4. A clear *SdS* arrival between *Sab* and *ScS*, as well as arrivals between *Sab* and *SdS* caused by crustal reverberations, are apparent for both models. Because of the layered block-style inversion used to create TXBW, other small arrivals are present from discontinuous jumps between layers.

Decreases in $T_{ScS\text{-}Sab}$ (generally < 1 sec on average, but up to 2 sec between paths 1 and 4) are observed moving from Path 1 to 4, due to progressively increasing V_S toward the north in the D" region. This also decreases $T_{ScS\text{-}Scd}$ (by <1 sec on average between Path 1 and 4). 3-D structure elsewhere along the paths likely plays an important role in timing and amplitude anomalies (e.g., Zhao & Lei 2004), but our focus here is on D"

structure. Nonetheless, we note variable *Scd/ScS* amplitude ratios that are not easily understandable in terms of D" structure alone.

5.5 Synthetic seismograms compared with data

The most direct assessment of a model's performance is to compare the synthetic predictions with data. We compare synthetic predictions for Path 1 with the data set used in the studies of Lay *et al.* (2004b) and Thomas *et al.* (2004a). The four Bins used by Lay *et al.* (2004b) contained records spanning limited epicentral distance ranges. The ranges are: Bin 1: 79º-82º; Bin 2: 71º-79º; Bin 3: 75º-82º; Bin 4: 70º-77º. It is difficult to detect *SdS* in individual records for epicentral distances less than roughly 78º, because *Scd* amplitudes are relatively low at shorter distances and are often obscured by noise in the traces. The inferred small D" discontinuity V_S increase (e.g., 0.4% for Bin 2, or 0.7% for Bin 3) also makes detection of *SdS* energy in individual traces problematic. These two factors make direct comparison of data with synthetics challenging for Paths 2, 3, and 4. Data grouped into Bin 1 show *SdS* energy in individual traces, allowing us to compare these recordings with synthetic seismograms for Path 1.

Fig. 5.6 shows synthetics seismograms for models LAYB, THOM1.5, THOM2.0 and TXBW along with data from the April 23, 2000, Argentina event. Although some scatter exists in travel-times and amplitudes of *SdS* energy for signals grouped into Bin 1, the event shown in Fig. 5.6 is representative. As previously mentioned, the SHaxi method has a fixed source radiation pattern, so amplitude differences in the phases shown in Fig. 5.6 are not exactly comparable, with the synthetics expected to show relatively low *ScS/Sab* amplitude ratios due to the effective source radiation pattern.

Model LAYB (Fig. 5.6a) adequately explains $T_{ScS\text{-}Scd}$, although $T_{ScS\text{-}Sab}$ are slightly too long. Model THOM1.0 (not shown in Fig. 5.6) reproduces $T_{ScS\text{-}Scd}$ the best amongst the models based on Thomas *et al*. (2004a) but does not predict $T_{ScS\text{-}Scd}$ as well as model LAYB. Model THOM1.5 (Fig. 5.6b) performs better than model THOM2.0 in reproducing $T_{ScS\text{-}Scd}$; however, model THOM1.5 does worse than THOM2.0 in predicting the $T_{ScS\text{-}Sab}$ differential times. Model THOM2.0 (Fig. 5.6c) predicts $T_{ScS\text{-}Sab}$ differential times accurately, but under-predicts $T_{ScS\text{-}Scd}$ by as much as 2.5 sec. The best agreement between synthetics and data for Path 1 is observed for model TXBW (Fig. 5.6d). $T_{ScS\text{-}Sab}$ and $T_{ScS\text{-}Scd}$ are in excellent agreement particularly for distances greater than ~80º. TXBW slightly over-predicts $T_{ScS\text{-}Sab}$ for distances less than 80º, however, $T_{ScS\text{-}Scd}$ is well matched.

5.6 Double-array stacking comparisons

Because it is difficult to observe the *Scd* phase in individual records for distances less than 78º, the studies of Lay *et al.* (2004b) and Thomas *et al.* (2004a) employed data stacking techniques to infer D" discontinuity properties. Here we stack synthetic seismograms using the double-array stacking technique of Revenaugh & Meyer (1997) to obtain apparent reflector depths of the *SdS* energy (as in Lay *et al.* 2004b). The SHaxi method has a fixed source radiation pattern, and we can predict its effect on the amplitudes of resulting stacks. All that is needed is to slightly scale *ScS* relative to *SdS* in the stacking of synthetics by normalizing *ScS* in the synthetics on a value less than unity by an amount corresponding to the ratio of the radiation pattern coefficient for *ScS*

divided by that for *SdS*. The actual data are not scaled for source radiation pattern because for each bin the average *SdS/ScS* corrections are very close to 1.0.

Fig. 5.7 shows double-array stacks of data compared to synthetic predictions, as functions of target depth relative to the CMB. PREM is used as the reference stacking velocity model for both data and synthetics, so apparent *SdS* reflector depths are biased to the same extent. We stack synthetics for ranges of epicentral distances that correspond to those of the corresponding data. *ScS* energy stacks coherently at the CMB, because the *ScS* peaks are aligned on the reference *ScS* arrival times. *SdS* energy is clearly apparent in the data stacks at the apparent depths indicated by the arrows. Saw tooth irregularities at shallower depths occur as a result of individual waveform truncation before the *Sab* arrival. This is done because there tends to be a rise in amplitude of the traces in the *Sab* coda.

Double-beam stacking results are summarized in Table 5.2. Model THOM1.0 predicts the D" discontinuity height best, however, it under predicts the *SdS/ScS* amplitude ratio most severely. Overall, models LAYB and TXBW predict apparent D" discontinuity height and *SdS/ScS* amplitude ratios the best. Model THOM2.0 often predicts the *SdS/ScS* amplitude ratio as well as models LAYB and TXBW, but it under predicts the discontinuity height the most, and the *SdS* waveform shapes are irregular. None of the matches are as good as for the 1-D models for each bin obtained by Lay *et al.* (2004b).

Although synthetics for model TXBW compare well with data, the fit is not perfect, especially for Path 2 (Fig. 5.7). D" V_S likely varies on shorter scale lengths than

TXBW is able to resolve, as suggested by the short-scale velocity variation of Lay *et al.* (2004b). It may be possible to obtain better synthetic-data agreement by slightly modifying model TXBW. The models of Lay *et al.* (2004b) may guide the direction such enhancements take, however, we found no simple procedure to map the structures suggested by Lay *et al.* (2004b) onto TXBW. Significant trial-and-error forward modeling, guided by the 1-D stacking results and the spatial distribution of the tomography model appears to be the best way to formulate the search for a best-fitting model.

The stacks shown in Fig. 5.7(a) are in agreement with the results of comparing individual synthetics to data records as in Fig. 5.6. That is, we can see that model TXBW indicates a reflector at the same height above CMB as the data, while model LAYB suggests the height above CMB to be slightly higher than the data suggest. The LAYB result can be understood in that the model produced a slight over-prediction of the *ScS-Scd* differential travel-times. The under-predicted *ScS-Scd* differential travel-times of models THOM1.0-THOM2.0 are manifested in the stacks of Fig. 5.7(a) as deeper D" discontinuity reflectors than what these data suggest.

5.7 Discussion

In this paper, we presented 3-D synthetic seismograms for recent models of deep mantle *S*-wave tomography and D" discontinuity structure beneath the Cocos Plate region. We compared these synthetics with broadband data. Our main focus has been to assess how well the 3-D models inferred from various analysis procedures actually account for the original observations. In this section, we discuss important sources of

uncertainty and difficulties associated with the models for which we computed synthetic seismograms.

Lay *et al.* (2004b) produced 1-D models of the D" discontinuity structure with excellent agreement to data stacks. However, our 3-D synthetics for model LAYB compared less favorably to data stacks. The main issue here is how best to develop a 3-D structure from the 'local' characterization provided by small bin processing given the grazing nature of the seismic waves which must laterally average the structure. The *SdS* features in the data stacks are remarkably discrete; even small overlap of the bins leads to appearance of double peaks in the stacks, as noted by Lay *et al.* (2004b). But the grazing ray geometry argues that this cannot be interpreted as resolving spatial heterogeneities on the scale of the actual binning. What is needed is an understanding of the mapping of the locally characterized wavefield into heterogeneous structure. This is undoubtedly a non-linear mapping given that volumetric heterogeneity and reflector topography can trade-off.

We explore the effects of V_S heterogeneity wavelength on $T_{ScS\text{-}Scd}$ and $T_{ScS\text{-}Sab}$ in Fig. 5.8. We construct a suite of models with a base model containing a D" discontinuity at a height of 264 km above the CMB and a V_S increase of 2.33%. Synthetic seismograms are computed for a source 500 km deep at an epicentral distance of 78º. The *ScS* bounce-point for this source-receiver geometry is located at 38.12º from the source. Centered on this *ScS* bounce-point we introduce a domain with higher V_S (+3% increase). This higher velocity domain is given a width along the great-circle path in varying multiples of the *ScS* wavelength for a dominant period of 7 sec (1 wavelength ≈

50 km). In Fig. 5.8, the *ScS-Sab* differential travel times are shown as a function of domain size for the high velocity region. For $T_{ScS-Sab}$, a domain width of 2-3 wavelengths already affects the differential travel-times by a few tenths of seconds. However it is not until a domain width of roughly 30 wavelengths (~1500 km for a 7 sec dominant period wave) is reached that $T_{ScS-Sab}$ converges to the travel-time prediction for a 1-D model with a 3.0% V_S increase beneath the discontinuity. This is consistent with the long path length of *ScS* within the D" layer and the large effective Fresnel zone for wide-angle reflections as indicated in Figure 5.2.

The Bin sizes used in the Lay *et al.* (2004b) study are on average roughly 3 wavelengths in length along the great circle path. Fig. 5.8 demonstrates that differential travel-times may be significantly dominated by the neighboring bin structure. *ScS-Scd* times suffer a similar lack of path isolation. These experiments argue that 1-D travel time modeling results are biased if along path lateral variability is shorter scale than about 30-wavelengths. However, our *SdS* data clearly display strong variation over distances of much less than 30-wavelengths, thus 3-D techniques must be employed to reliably map the required heterogeneous structure. It is unrealistically optimistic to believe that fine binning resolves fine scale structure when grazing rays are being used; the wave propagation effects may be spatially rapidly varying but the responsible structure is likely to be large scale. Since tomography intrinsically distributes path integral effects over large scale, it can provide a good starting basis for initial modeling, as demonstrated by Ni *et al*. (2000) and by the modeling in this paper.

We also calculated $T_{ScS\text{-}Sab}$ and $T_{ScS\text{-}Scd}$ using 3-D ray tracing for the same model geometries as used for Fig. 5.8. The 3-D ray tracing solutions coincide with the travel-times shown in Fig. 5.8 to within a couple tenths of seconds. However, significant variations between ray tracing and waveform predictions occur when imaging low-velocity layers.

Paths 2 and 3 of models THOM1.0-2.0 show a rapid transition in D" discontinuity thickness (e.g., Fig 5.4 and Supplemental Fig. 6B) producing a double *Scd* peak in the synthetic predictions. This double *Scd* peak has not been reported in observations, but comes to light with the calculation of 3-D synthetic seismograms. Given the possibility of the post-perovskite phase transition being responsible for the D" discontinuity, it is interesting to establish whether models with rapid variations in topography can account for the data. Future efforts seeking to resolve topographic variation on the D" discontinuity should consider the prediction of a double *Scd* arrival.

For the SHaxi approach, out of great circle plane variations in D" discontinuity topography cannot be modeled, so we do not model the exact scattering of energy that the full 3-D model of Thomas *et al.* (2004a) would produce. Because our models are axi-symmetric more *SdS* energy may be backscattered from the transition from thin to thick D" layering in models THOM1.0-2.0 than would be scattered in fully 3-D models. Models THOM1.0-2.0 have relatively small *SdS*/*Scd* amplitudes, though we are not able to constrain the degree of *Scd* amplitude misfit due to our geometry. Perhaps the greatest challenge for interpreting migration images is that they do not resolve velocity contrasts (at least for Kirchhoff point-scattering migrations), and the reflector images are

highly dependent on the reference velocity structure. Volumetric heterogeneity as needed to match *ScS* arrival times suggests that apparent topography is likely to be incorrect, and in this case, exaggerated. Thus, the poor agreement of resulting synthetics is not a clear indication that the models are flawed; the mapping to 3-D may simply be in significant error. This uncertainty extends to any effort to infer dynamical features based on the migration images.

If V_S gradients perpendicular to our 2-D cross-sections for model TXBW are insignificant over a distance of a couple of wavelengths our synthetics should be adequate. Because there was only slight change in our synthetic predictions between individual paths, lateral variation does appears to be minor for our geometry and full 3-D synthetics may not be necessary to predict the waveforms. Not having to compute full 3-D synthetics for the present class of whole Earth tomography models would drastically save computational resources and time, and is currently feasible using low-cost cluster computing. We are currently exploring differences between synthetics computed for tomography models with fully 3-D codes and the SHaxi method, which will be reported on soon.

5.8 Conclusions

We have demonstrated that important 3-D wavefield effects are predicted for models of 3-D structure built upon underlying 1-D modeling assumptions. We have investigated recent models of D" discontinuity structure beneath the Cocos Plate region using 3-D synthetic seismograms calculated with the finite-difference SHaxi method. We made synthetic predictions for 3-D models inferred from results of several recent “high

resolution" imaging studies, including D" discontinuity mapping by stacking and migration, and tomographically derived volumetric heterogeneity. We focused our comparison on seismic phases predominantly used to image D" discontinuity structure: *S*, *ScS* and the intermediate arrival *SdS* which is present if a high velocity D" layer exists. We found significant discrepancies between observations and 3-D synthetic predictions, which highlight the need for 3-D tools in the process of mapping localized imaging results into 3-D structure. 1-D tools are unable to accurately predict 3-D structure if structural variations are on the order of wavelength of the energy used; the problem is particularly severe for grazing ray geometries. 3-D ray tracing techniques may aid in constructing 3-D models by providing improved reference seismic arrival times. However, methods utilizing 3-D synthetic seismograms, such as the SHaxi approach, are better suited for this purpose as important waveform effects can be synthesized. In order to model fine-scale 3-D D" structure, we believe future efforts should incorporate methods of synthesizing 3-D seismograms in an iterative approach. Reasonable starting models may be constructed by migration or double-array stacking techniques, which may be improved if tomographic models are used as the reference structure. Initial models can be improved in an iterative fashion by computing 3-D synthetic seismograms, comparing the synthetics with data, and adjusting the model. However, it will be challenging to determine the best way to adjust the model in the forward sense, requiring significant trial and error. In the inverse sense, low cost methods such as SHaxi may allow reasonable full waveform inversions to be calculated along corridors densely sampled with data.

ACKNOWLEDGEMENTS

Most figures were generated using the Generic Mapping Tools freeware package (Wessel & Smith 1998). M. T. and E. G. were partially supported by NSF grant EAR-0135119. T. L. was supported by NSF Grant EAR-0125595. Thanks to the Leibniz Computing Center, Munich, for access to their computational facilities. Support is also acknowledged from the German Academic Exchange Service (IQN-Georisk), the German Research Foundation, and the Human Resources and Mobility Programme of the European Union (SPICE-Project). The SHaxi source code is openly available at http://www.spice-rtn.org/.

REFERENCES

Avants, M. S., Lay, T., Russell S.A., & Garnero, E.J., 2005. Shear-velocity variation within the D" region beneath the central Pacific, *Journal of Geophysical Research - Solid Earth*, in review.

Bullen, K. E., 1949. Compressibility-pressure hypothesis and the Earth's interior, *Monthly Notes of the Royal Astronomical Society*, Geophysics Supplement, 355-368.

Chapman, C.H., 1978. A new method for computing synthetic seismograms, *Geophys. J. R. astr. Soc.,* **54**, 481-518.

Creager, K. C. & Jordan, T. H., 1986. Aspherical structure of the core-mantle boundary from PKP Travel-Times, *Geophysical Research Letters*, **13**, 1497-1500.

Dahlen, F. A., Hung, S. H. & Nolet, G., 2000. Frechet kernels for finite-frequency traveltimes - I. Theory, *Geophysical Journal International*, **141**, 157-174.

Ding, X. M. & Helmberger, D. V., 1997. Modelling D" structure beneath Central America with broadband seismic data, *Physics of the Earth and Planetary Interiors*, **101**, 245-270.

Dziewonski, A. M. & Anderson, D. L., 1981. Preliminary Reference Earth Model, *Physics of the Earth and Planetary Interiors*, **25**, 297-356.

Farnetani, C. G., and H. Samuel, 2005. Beyond the thermal plume paradigm, *Geophys. Res. Lett.*, **32**, No.7, L07311, 10.1029/2005GL022360.

Flanagan, M. P. & Shearer, P. M., 1998. Topography on the 410-km seismic velocity discontinuity near subduction zones from stacking of sS, sP, and pP precursors, *Journal of Geophysical Research-Solid Earth*, **103**, 21165-21182.

Friederich, W. & Dalkolmo, J., 1995. Complete synthetic seismograms for a spherically symmetrical Earth by a numerical computation of the Greens-function in the frequency-domain, *Geophysical Journal International*, **122**, 537-550.

Gaherty, J. B. & Lay, T., 1992. Investigation of laterally heterogeneous shear velocity structure in D" beneath Eurasia, *Journal of Geophysical Research-Solid Earth*, **97**, 417-435.

Garnero, E. J., Helmberger, D. V. & Grand, S., 1993. Preliminary evidence for a lower mantle shear-wave velocity discontinuity beneath the Central Pacific, *Physics of the Earth and Planetary Interiors*, **79**, 335-347.

Garnero, E. J. & Lay, T., 1997. Lateral variations in lowermost mantle shear wave anisotropy beneath the north Pacific and Alaska, *Journal of Geophysical Research-Solid Earth*, **102**, 8121-8135.

Garnero, E. J. & Lay, T., 2003. D " shear velocity heterogeneity, anisotropy and discontinuity structure beneath the Caribbean and Central America, *Physics of the Earth and Planetary Interiors*, **140**, 219-242.

Grand, S. P., 1994. Mantle shear structure beneath the America and surrounding oceans, *Journal of Geophysical Research-Solid Earth*, **99**, 11591-11621.

Grand, S. P., 2002. Mantle shear-wave tomography and the fate of subducted slabs, *Philosophical Transactions of the Royal Society of London Series a-Mathematical Physical and Engineering Sciences*, **360**, 2475-2491.

Gu, Y. J., Dziewonski, A. M., Su, W. J. & Ekstrom, G., 2001. Models of the mantle shear velocity and discontinuities in the pattern of lateral heterogeneities, *Journal of Geophysical Research-Solid Earth*, **106**, 11169-11199.

Hernlund, J.W, C. Thomas, P.J. Tackley, A doubling of the post-perovskite phase boundary and structure of the Earth's lowermost mantle, *Nature*, **434**, 883-886, 2005.

Houard, S. & Nataf, H. C., 1993. Laterally varying reflector at the top of D" beneath Northern Siberia, *Geophysical Journal International*, **115**, 168-182.

Hung, S.-H., Garnero, E., Chiao, L.-Y., Lay, T. & Kuo, B. Y., 2005. Finite frequency tomography of D" shear velocity heterogeneity beneath the Caribbean, *Journal of Geophysical Research*, **110**, doi: 10.1029/2004JB003373.

Hutko, A., Lay, T., Garnero, E. & Revenaugh, J. R., 2005. A folded slab at the core-mantle boundary beneath the Cocos Plate imaged by Kirchoff migration, *Nature*, submitted.

Igel, H. & Weber, M., 1995. SH-wave propagation in the whole mantle using high-order finite differences, *Geophys. Res. Let.*, **22**, 731-734.

Igel, H. & Weber, M., 1996. P-SV wave propagation in the Earth's mantle using finite differences: Application to heterogeneous lowermost mantle structure, *Geophys. Res. Let.*, **23**, 415-418.

Igel, H., Takeuchi, N., Geller, R. J., Megnin, C., Bunge, H. P., Clevede, E., Dalkolmo, J. & Romanowicz, B., 2000. The COSY Project: verification of global seismic modeling algorithms, *Physics of the Earth and Planetary Interiors*, **119**, 3-23.

Jahnke, G., Thorne, M.S., Cochard, A., & Igel, H., 2005. Global SH wave propagation with an axi-symmetric finite-difference scheme, *Geophysical Journal International*, submitted 2005.

Kendall, J. M. & Shearer, P. M., 1994. Lateral Variations in D" thickness from long-period shear-wave data, *Journal of Geophysical Research-Solid Earth*, **99**, 11575-11590.

Kendall, J. M. & Nangini, C., 1996. Lateral variations in D" below the Caribbean, *Geophysical Research Letters*, **23**, 399-402.

Kennett, B. L. N., Engdahl, E. R. & Buland, R., 1995. Constraints on seismic velocities in the Earth from travel-times, *Geophysical Journal International*, **122**, 108-124.

Komatitsch, D. & Tromp, J., 2002. Spectral-element simulations of global seismic wave propagation - I. Validation, *Geophysical Journal International*, **149**, 390-412.

Kuo, B. Y., Garnero, E. J. & Lay, T., 2000. Tomographic inversion of S-SKS times for shear velocity heterogeneity in D ": Degree 12 and hybrid models, *Journal of Geophysical Research-Solid Earth*, **105**, 28139-28157.

Lay, T. & Helmberger, D. V., 1983. A lower mantle S-wave triplication and the shear velocity structure of D", *Geophysical Journal of the Royal Astronomical Society*, **75**, 799-837.

Lay, T. & Young, C. J., 1991. Analysis of seismic SV waves in the core's penumbra, *Geophysical Research Letters*, **18**, 1373-1376.

Lay, T., Garnero, E. J., Young, C. J. & Gaherty, J. B., 1997. Scale lengths of shear velocity heterogeneity at the base of the mantle from S wave differential travel times, *Journal of Geophysical Research-Solid Earth*, **102**, 9887-9909.

Lay, T., Garnero, E. J. & William, Q., 2004a. Partial melting in a thermo-chemical boundary layer at the base of the mantle, *Physics of the Earth and Planetary Interiors*, **146**, 441-467.

Lay, T., Garnero, E. J. & Russell, S. A., 2004b. Lateral variation of the D " discontinuity beneath the Cocos Plate, *Geophysical Research Letters*, **31**, doi:10.1029/2004GL020300.

Masters, G., Johnson, S., Laske, G. & Bolton, H., 1996. A shear-velocity model of the mantle, *Philosophical Transactions of the Royal Society of London Series a-Mathematical Physical and Engineering Sciences*, **354**, 1385-1410.

Matzel, E., Sen, M. K. & Grand, S. P., 1996. Evidence for anisotropy in the deep mantle beneath Alaska, *Geophysical Research Letters*, **23**, 2417-2420.

Megnin, C. & Romanowicz, B., 2000. The three-dimensional shear velocity structure of the mantle from the inversion of body, surface and higher-mode waveforms, *Geophysical Journal International*, **143**, 709-728.

Ni, S. D., Ding, X. M. & Helmberger, D. V., 2000. Constructing synthetics from deep earth tomographic models, *Geophysical Journal International*, **140**, 71-82.

Oganov, A. R. & Ono, S., 2004. Theoretical and experimental evidence for a post-perovskite phase of MgSiO3 in Earth's D " layer, *Nature*, **430**, 445-448.

Reasoner, C. & Revenaugh, J., 1999. Short-period P wave constraints on D " reflectivity, *Journal of Geophysical Research-Solid Earth*, **104**, 955-961.

Revenaugh, J. & Meyer, R., 1997. Seismic evidence of partial melt within a possibly ubiquitous low-velocity layer at the base of the mantle, *Science*, **277**, 670-673.

Ritsema, J. & van Heijst, H.-J., 2000. Seismic imaging of structural heterogeneity in Earth's mantle: Evidence for Large-Scale Mantle Flow, *Science Progress*, **83**, 243-259.

Rokosky, J. M., Lay, T., Garnero, E. J. & Russell, S. A., 2004. High-resolution investigation of shear wave anisotropy in D " beneath the Cocos Plate, *Geophysical Research Letters*, **31**, L07605.

Rost, S. & Revenaugh, J., 2003. Detection of a D " discontinuity in the south Atlantic using PKKP, *Geophysical Research Letters*, **30**, 1840.

Sidorin, I., Gurnis, M., & Helmberger, D. V., 1999. Evidence for a ubiquitous seismic discontinuity at the base of the mantle, Science, **286**, 1326-1331.

Tackley, P.J., 2000. Mantle convection and plate tectonics: Towards an integrated physical and chemical theory, *Science*, 288, 2002-2007, 2000.

Thomas, C., Weber, M., Wicks, C. W. & Scherbaum, F., 1999. Small scatterers in the lower mantle observed at German broadband arrays, *Journal of Geophysical Research-Solid Earth*, **104**, 15073-15088.

Thomas, C., Garnero, E. J. & Lay, T., 2004a. High-resolution imaging of lowermost mantle structure under the Cocos plate, *Journal of Geophysical Research-Solid Earth*, **109**, doi:10.1029/2004JB003013.

Thomas, C., Kendall, J., Lowman, J., 2004b. Lower-mantle seismic discontinuities and the thermal morphology of subducted slabs, *Earth Planet. Sci. Lett.*, **225**, 105–113.

Tsuchiya, T., Tsuchiya, J., Umemoto, K. & Wentzcovitch, R. A., 2004a. Phase transition in MgSiO3 perovskite in the earth's lower mantle, *Earth and Planetary Science Letters*, **224**, 241-248.

Tsuchiya, T., Tsuchiya, J., Umemoto, K. & Wentzcovitch, R. M., 2004b. Elasticity of post-perovskite MgSiO3, *Geophysical Research Letters*, **31**, L14603, doi:10.1029/2004GL020278.

Valenzuela, R. W. & Wysession, M. E., 1998. Illuminating the Base of the Mantle with Diffracted Waves, *in The Core-Mantle Boundary Region*, pp. 57-71, ed., Gurnis, M., Wysession, M. E., Knittle, E. & Buffet, B. A., American Geophysical Union, Washington, D.C.

Weber, M. & Davis, J. P., 1990. Evidence of a laterally variable lower mantle structure from P-waves and S-waves, *Geophysical Journal International*, **102**, 231-255.

Weber, M., 1993. P-wave and S-wave reflections from anomalies in the lowermost mantle, *Geophysical Journal International*, **115**, 183-210.

Wessel, P., and W. H. F. Smith, 1998. New, improved version of the Generic Mapping Tools released, *Eos Trans. AGU*, **79**, 579.

Woodward, R. L. & Masters, G., 1991. Lower-mantle structure from ScS-S differential travel-times, *Nature*, **352**, 231-233.

Wysession, M. E., Lay, T., Revenaugh, J., Williams, Q., Garnero, E., Jeanloz, R. & Kellogg, L. H., 1998. The D" discontinuity and its implications, *in The Core-Mantle Boundary Region*, pp. 273-297, ed., Gurnis, M., Wysession, M. E., Knittle, E. & Buffet, B. A., American Geophysical Union, Washington, D.C.

Young, C. J. & Lay, T., 1987. Evidence for a shear velocity discontinuity in the lower mantle beneath India and the Indian-Ocean, *Physics of the Earth and Planetary Interiors*, **49**, 37-53.

Young, C. J. and T. Lay (1990). Multiple phase analysis of the shear velocity structure in the D" region beneath Alaska, *J. Geophys. Res.*, **95**, 17385-17402.

Zhang, J. J. & Lay, T., 1984. Investigation of a lower mantle shear-wave triplication using a broad-band array, *Geophysical Research Letters*, **11**, 620-623.

Zhao, D. & Lei, J., 2004. Seismic ray path variations in a 3D global velocity model, *Physics of the Earth and Planetary Interiors*, **141**, 153-166.

Zhu, A. N. & Wysession, M. E., 1997. Mapping global D" P velocities from ISC PcP-P differential travel times, *Physics of the Earth and Planetary Interiors*, **99**, 69-82.

Zhu, L. P. & Kanamori, H., 2000. Moho depth variation in southern California from teleseismic receiver functions, *Journal of Geophysical Research-Solid Earth*, **105**, 2969-2980.

TABLES

Table 5.1 Models

Model	Description	Model based on:
LAYB[a]	Block style bins	Lay *et al.* 2004b
LAYL[a]	Linear interpolation between bins	Lay *et al.* 2004b
THOM1.0[b]	1% Vs increase beneath discontinuity	Thomas *et al.* 2004a
THOM1.5[b]	1.5% Vs & 1% ρ increase beneath discontinuity	Thomas *et al.* 2004a
THOM2.0[b]	2% Vs increase beneath discontinuity	Thomas *et al.* 2004a
TXBW	Tomographically derived δV_S heterogeneity	Grand 2002

[a]Fixed D" thickness, variable D" δV_S
[b]Variable D" thickness, fixed D" δV_S

Table 5.2 D" thickness (km)* from double-beam stacking for data and models

Path	Data	LAYB	THOM1.0	THOM1.5	THOM2.0	TXBW
Path 1	160	185	115	95	80	167
Path 2	270	227	234	215	200	210
Path 3	250	196	230	202	182	198
Path 4	220	229	213	193	172	199

*Thickness refers to *Scd* peak in Fig. 5.7.

FIGURES

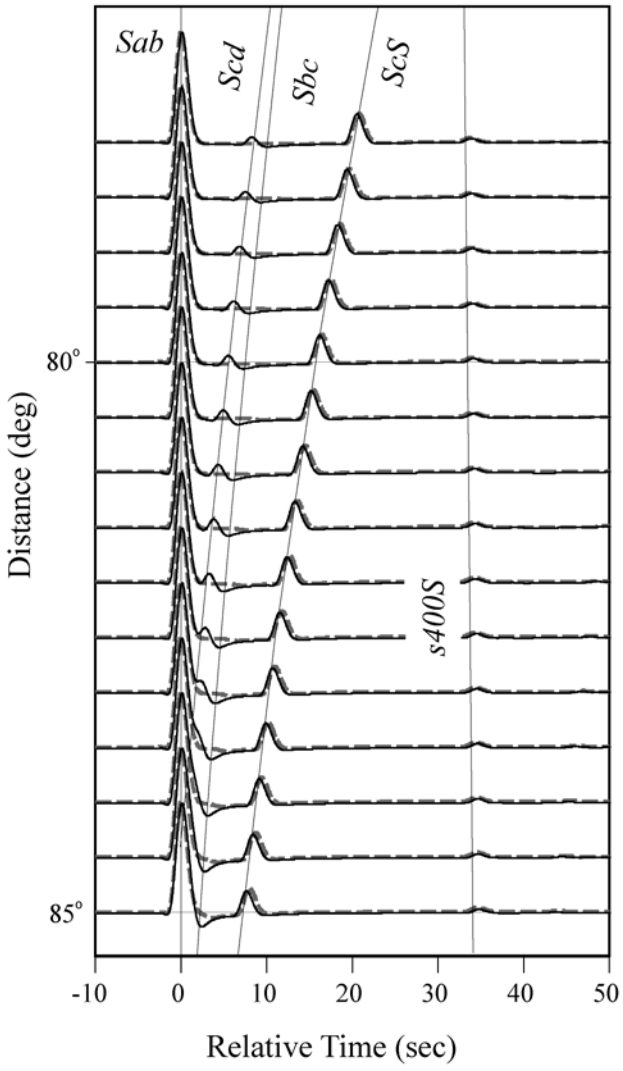
Sab
Scd
Sbc
ScS
s400S
80°
85°
Distance (deg)
-10
0
10
20
30
40
50
Relative Time (sec)

Figure 5.1 Transverse component displacement synthetics are shown for a 500 km deep event at teleseismic ranges. The calculation is done for a D" discontinuity model with a 1.3% V_S increase located 264 km above the CMB (solid lines), and synthetics for PREM (dashed lines). Synthetics are aligned and normalized to unity on the phase *S*, and calculated for a dominant period of 4 sec. Phase labels are given for the D" model, noting that the PREM model does not display the triplication phase *SdS*. Note, the phase *SdS* is composed of the two arrivals *Scd* (positive peak) and *Sbc* (positive and negative peak immediately following *Scd*).

a) Wavefield and Ray Geometry

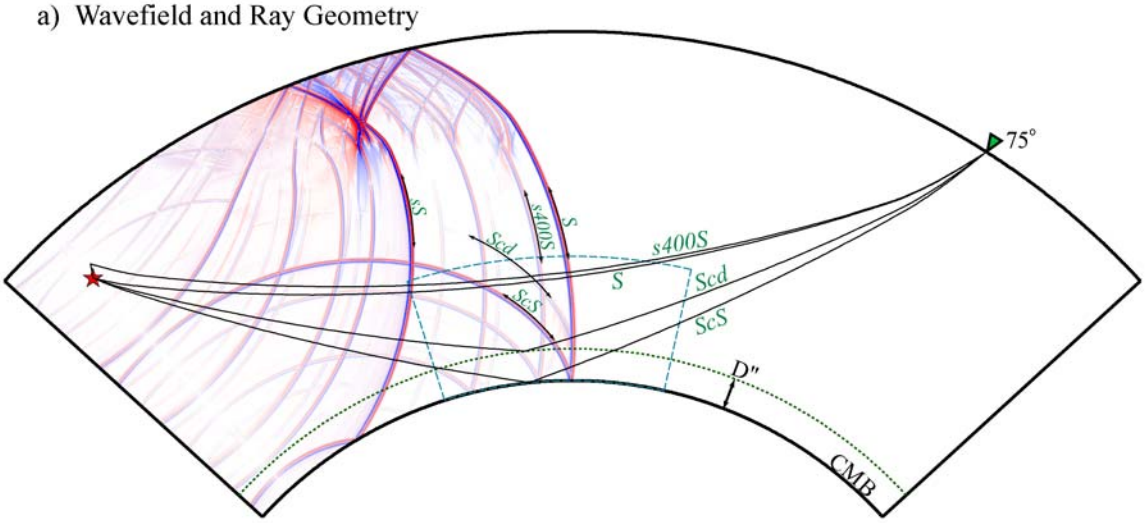

b) Wavefield and Ray Geometry - Detail

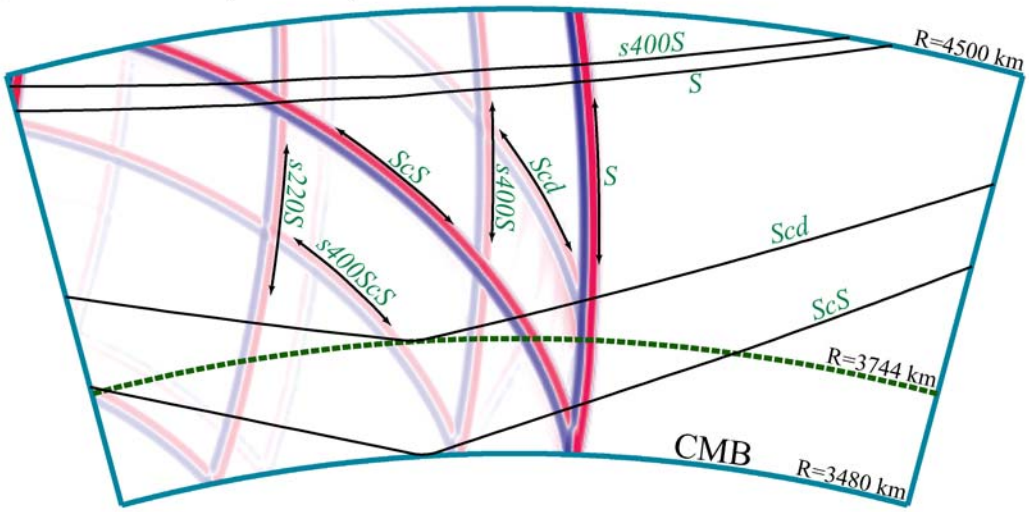

Figure 5.2 a) The *SH*- velocity wave field is shown at propagation time of 600 sec for a 500 km deep event with dominant source period of 6 sec. Selected wave fronts are labeled with black double-sided arrows. Ray paths are drawn in black for an epicentral distance of 75º. The calculation is done for the D" discontinuity (indicated with a dashed green line) model of Fig. 5.1. Non-linear scaling was applied to the wavefield amplitudes to magnify lower amplitude phases. b) Detail of wavefield shown in panel a. The region displayed is indicated by a dashed blue box in panel a.

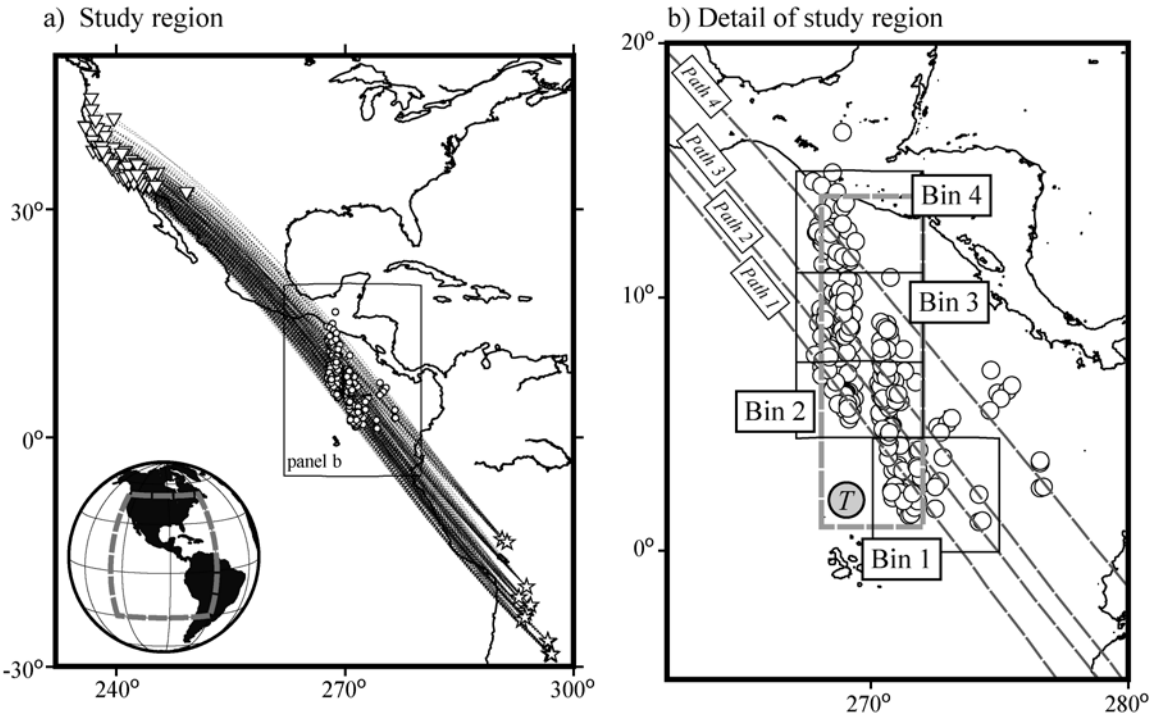

Figure 5.3 Location of study region. Panel a) shows the general location of the study region. Shown are events (stars), receivers (triangles) event-receiver great circle paths (dashed lines) and *ScS* bounce-points (circles) used in the studies of Lay *et al.* (2004b) and Thomas *et al.* (2004a). *ScS* bounce-points are calculated from the PREM model. Both studies utilize the same data set. Panel b) displays a detailed section of the study region. This panel shows the *ScS* bounce-points as white circles. 1-D models were produced in the study of Lay *et al.* (2004b) for 4 distinct bins outlined in this plot by black rectangles (labeled Bins 1-4). The dashed gray lines (labeled Paths 1-4) represent the average great circle paths of source-receiver pairs for these four Bins, and are also the Paths for which we calculate synthetics in this study. The dashed gray rectangle (labeled with a gray-shaded T) represents the area modeled in the study of Thomas *et al.* (2004a).

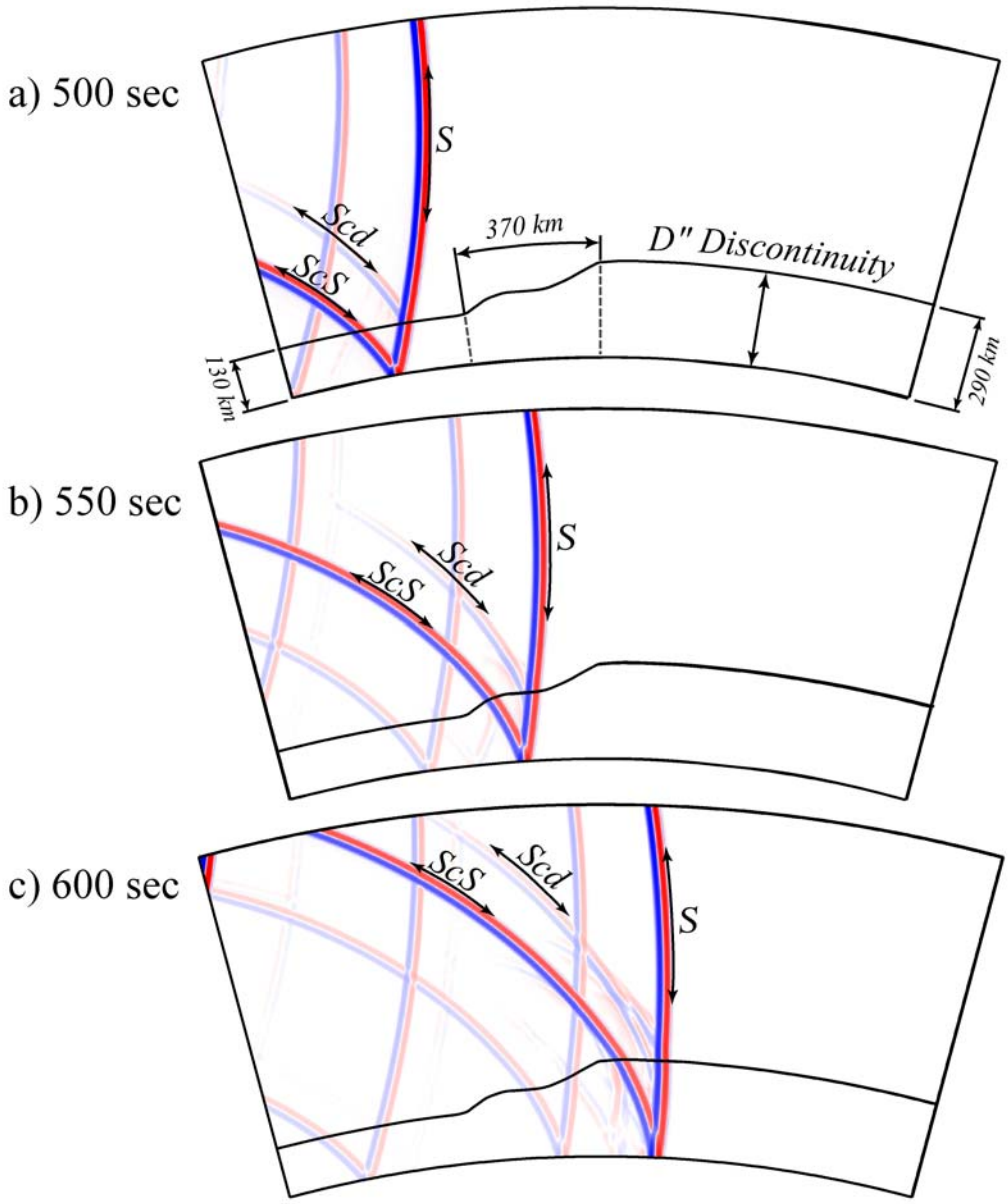
a) 500 sec
S
Scd
ScS
370 km
D" Discontinuity
130 km
290 km
b) 550 sec
S
Scd
ScS
c) 600 sec
ScS
Scd
S

Figure 5.4 Snapshots at three time intervals are shown for model THOM2.0 for Path 3. The view displayed includes a section of the lower-most mantle between radii 3480 - 4500 km and between epicentral distances 25º - 55º. The amplitude of the *SH*- velocity wavefield is shown in red and blue. The top of the D" discontinuity in model THOM2.0 is drawn with a solid black line. Select seismic phases are labeled with double-sided arrows. These snapshots show the evolution of the wave field as it encounters a D" discontinuity with topographic variation. The topographic variation is observed to produce two distinct *Scd* arrivals.

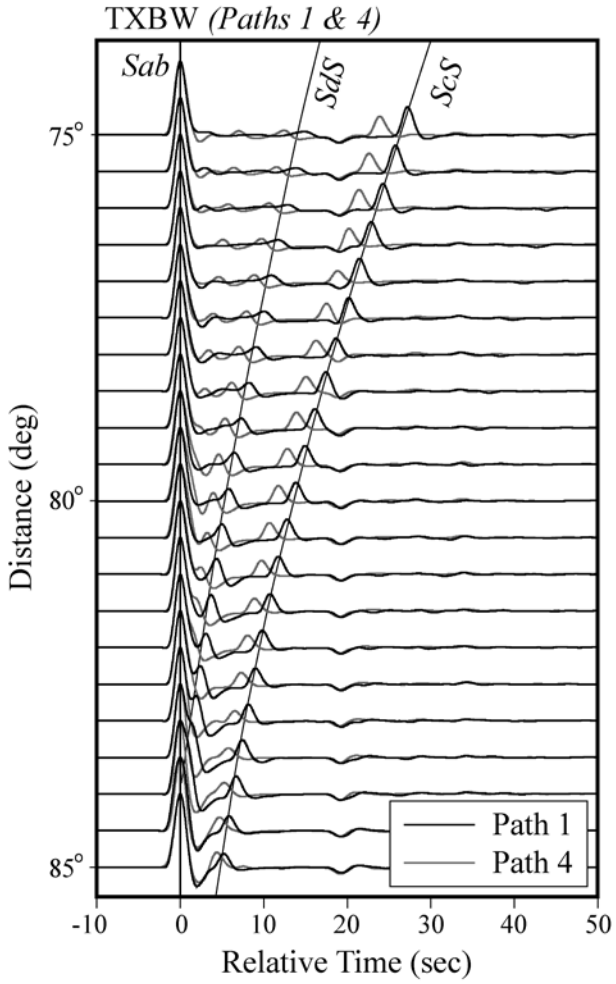

Figure 5.5 Comparison of synthetics for model TXBW for Paths 1 (black) and 4 (gray). Transverse component displacement synthetics are shown. Synthetics are aligned and normalized to unity on the phase *Sab*, and calculated for a dominant period of 4 sec. For clarity, lines are drawn at the peak *SdS* and *ScS* arrival time for Path 1.

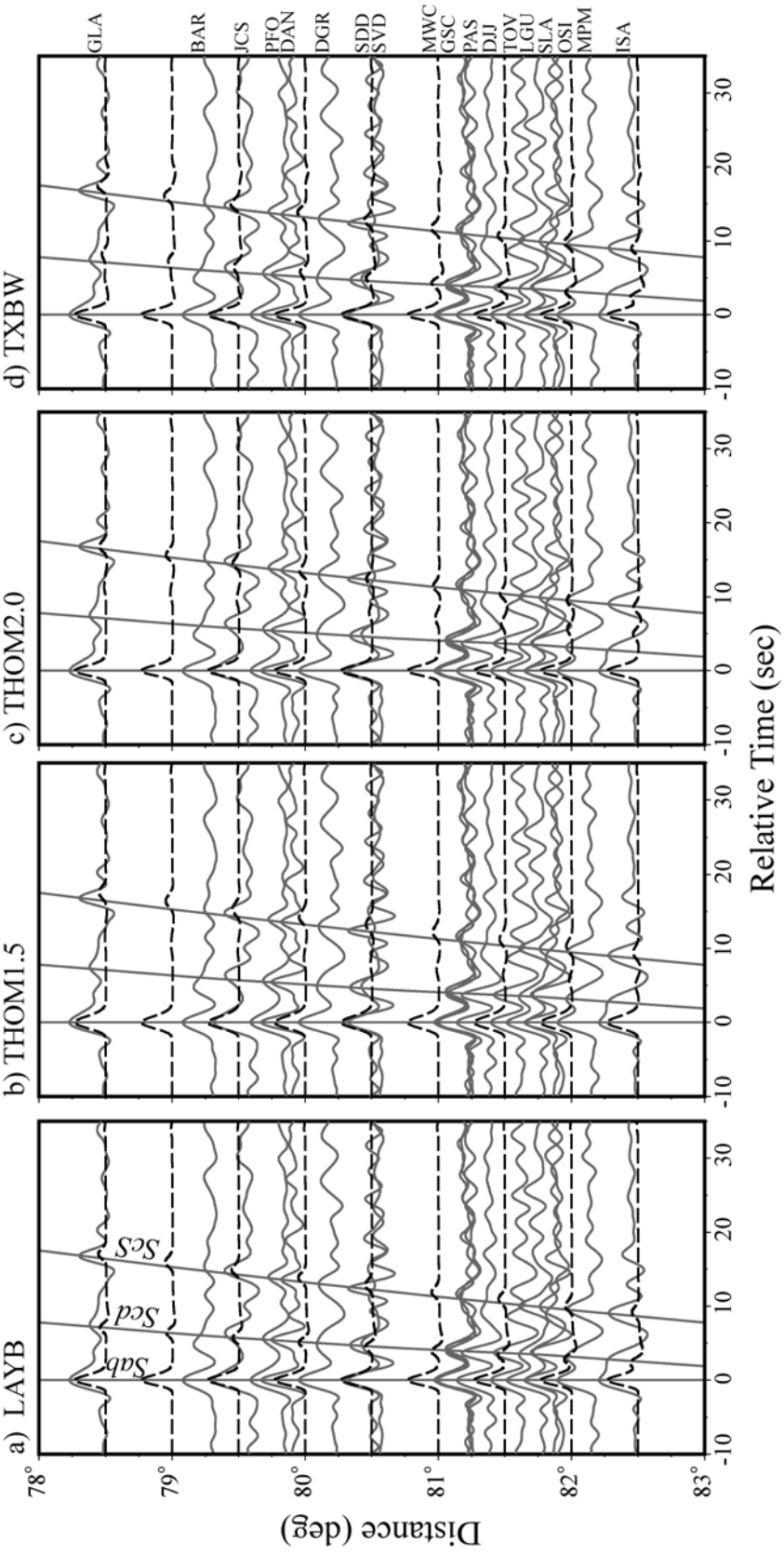
a) LAYB
b) THOM1.5
c) THOM2.0
d) TXBW
Sab
Scd
ScS
GLA
BAR
JCS
PFO
DAN
DGR
SDD
SVD
MWC
GSC
PAS
DJJ
TOV
LGU
SLA
OSI
MPM
ISA
78°
79°
80°
81°
82°
83°
Distance (deg)
-10
0
10
20
30
Relative Time (sec)

Figure 5.6 Comparison of synthetics created for Path 1 (solid lines) with data (dashed lines, April 23, 2000 Argentina 600 km deep event). Transverse component displacement synthetics and data are shown. Data are distance shifted to a source depth of 500 km. Approximate arrival times (peak amplitude) for the phases *Sab*, *Scd*, and *ScS* for data are indicated by solid lines so that differences between data and synthetic differential travel-times can be easily inspected visually. Receiver names are listed to the right of data traces.

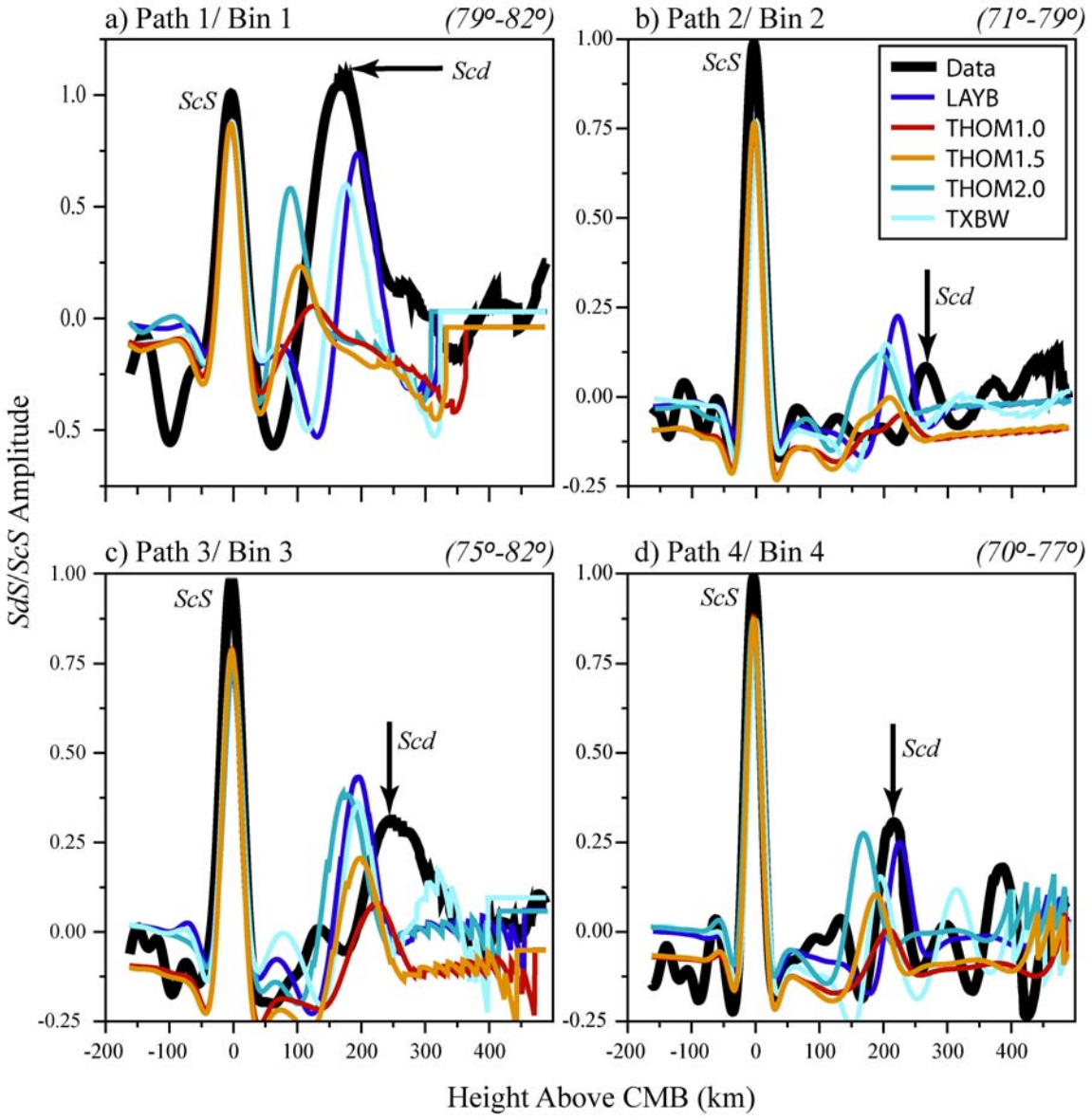

Figure 5.7 Stacking results for each Path (1-4) of synthetic prediction and Bin (1-4) of data are shown. Data stacks from Lay *et al.* (2004b) are drawn in black. The epicentral distance range of these data is displayed in the upper right corner of each panel. We stacked synthetic seismograms for the same epicentral distance range as these data.

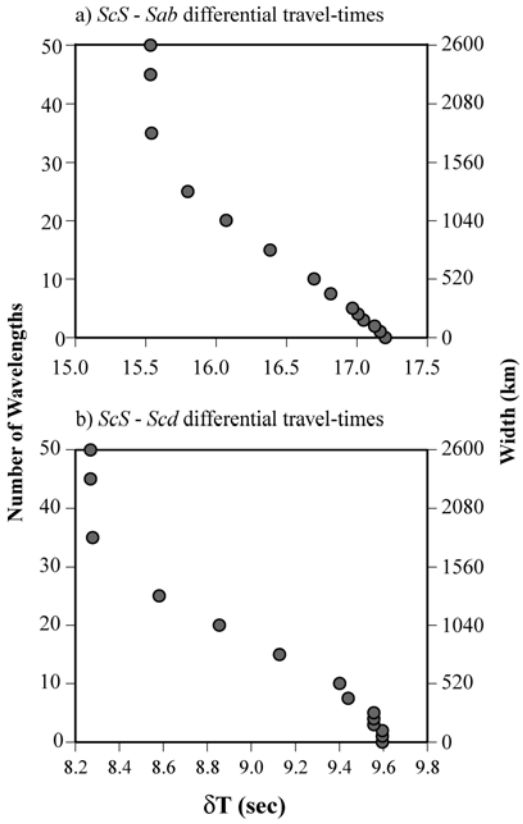

Figure 5.8 3-D effects of D" lateral V_S heterogeneity on $T_{ScS–Sab}$ (panel a) and $T_{ScS-Scd}$ (panel b) is shown. These differential travel-times are computed for a D" model with a constant V_S = 7.375 km/sec (+2.33% jump) except in a box centered on the *ScS* bounce point for source-receiver epicentral distance of 78º and source depth of 500 km (central bounce-point = 38.12º). Inside this box the V_S is 7.431 km/sec (+3% jump). The D" thickness is fixed at 264 km corresponding with the study of Lay *et al.* (2004b). The width of the inner box is shown on the right axis in km and on the left axis in multiples of the wavelength of *ScS* in the box. The wavelength multiples are shown for a *ScS* dominant period of 7 sec for which the synthetics were computed.

SUPPLEMENTAL FIGURES

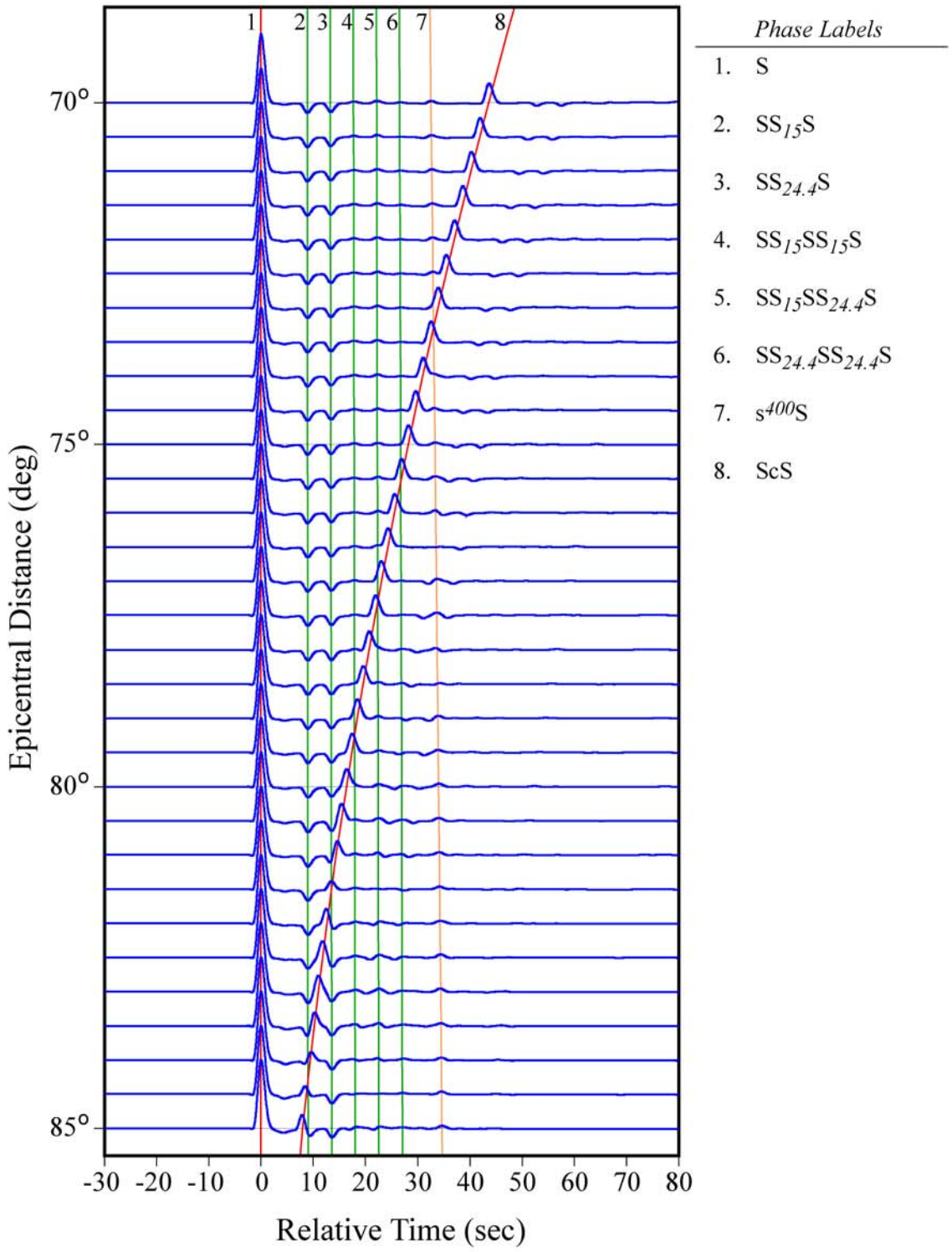

Supplement 5A Transverse component displacement synthetics are shown. Synthetics for PREM with a 500 km source depth are drawn in blue. Synthetics are aligned and normalized to unity on the phase *S*, and calculated for a dominant period of 4 sec. Crustal and mid-crustal phases that interfere with the *SdS* and *ScS* wavefield are labeled with green lines. *S* and *ScS* are labeled with red lines. The yellow line labels the underside reflection of the 400 km depth discontinuity in PREM ($s^{400}S$).

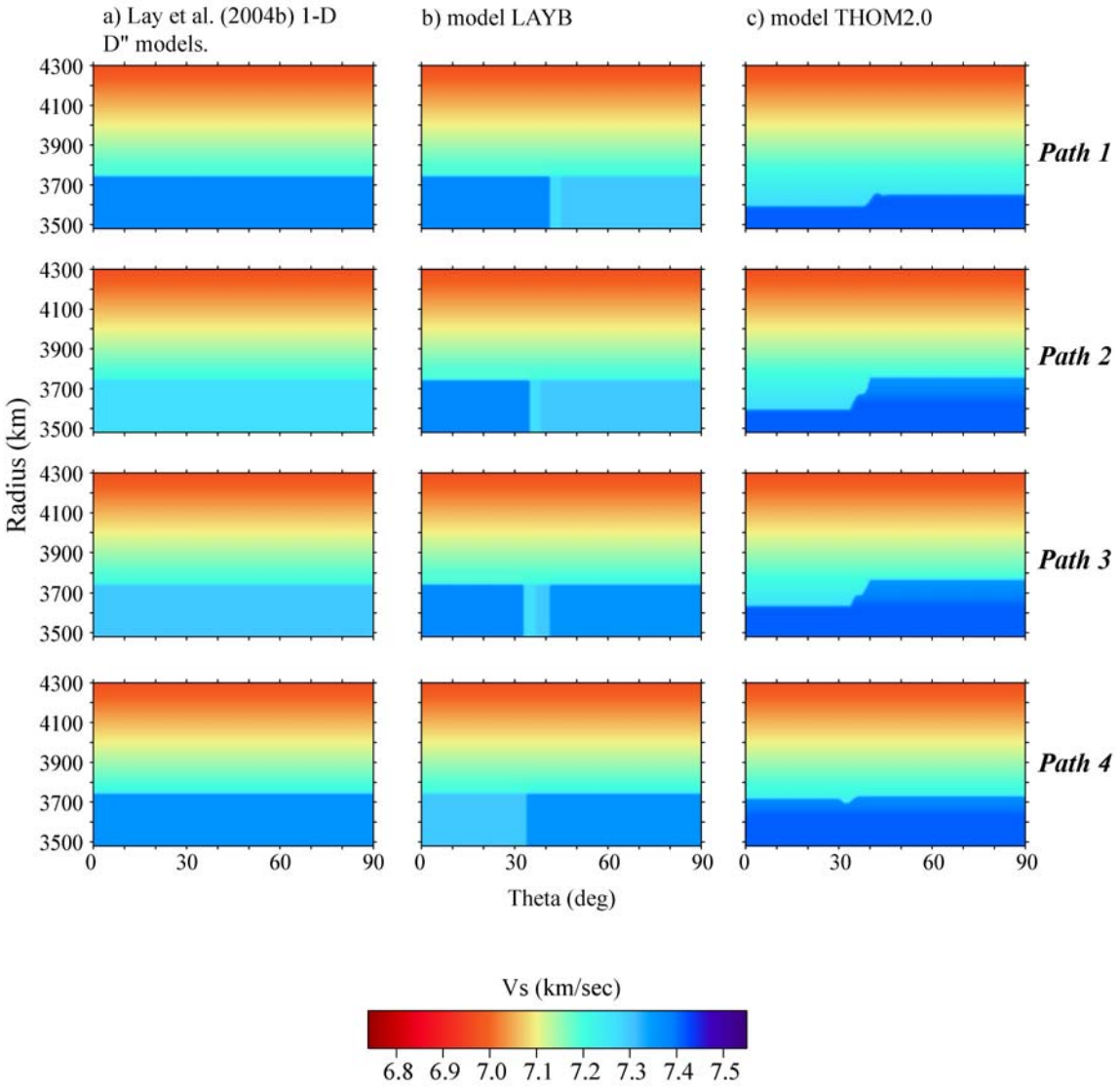

Supplement 5B Lower mantle cross-sections for a) 1-D D" discontinuity models of Lay *et al.* (2004b), b) model LAYB, and c) model THOM2.0. Cross-sections for each of the four Paths we computed synthetic seismograms for are shown. Color scaling is based on absolute V_S in each model.

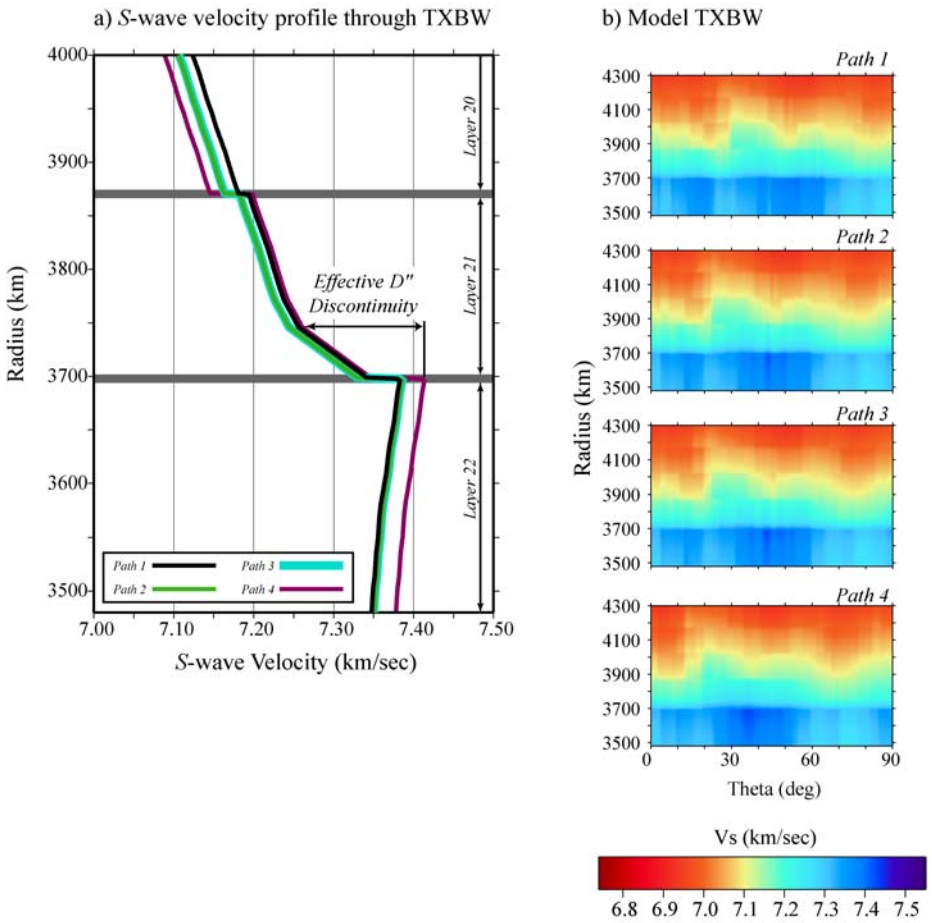

Supplement 5C a) Lower mantle cross-sections for model TXBW. Cross-sections for each of the four Paths we computed synthetic seismograms for are shown. Color scaling is based on V_S. b) V_S profile in the lower mantle through model TXBW. Shown is the 1-D V_S profile at an epicentral distance of 40º. This distance is chosen as approximating the central bounce point of *ScS* recorded at an epicentral distance of 80º. The profile is shown for Paths 1-4. Layer 20-22 refers to the number of layer in the tomographic inversion of Grand (2002). The phase *SdS* observes an effective D" discontinuity as indicated.

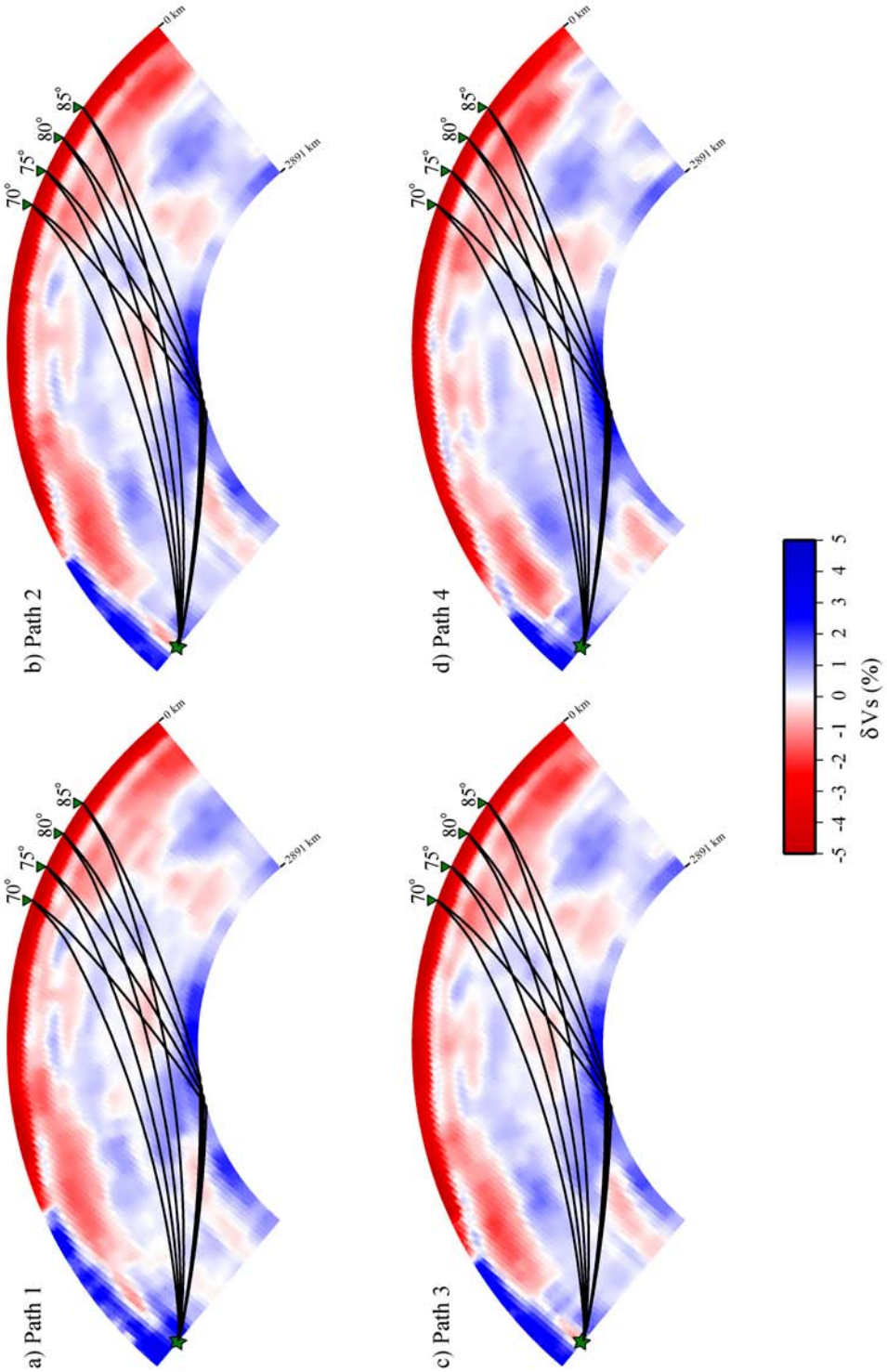
a) Path 1
b) Path 2
c) Path 3
d) Path 4
70°
75°
80°
85°
0 km
2891 km
-5 -4 -3 -2 -1 0 1 2 3 4 5
δVs (%)

Supplement 5D Whole mantle cross-sections for model TXBW. Cross-sections for each of the four Paths we computed synthetic seismograms for are shown. Color scaling is based on δV_S. Ray path geometry is shown for the phases *S* and *ScS* for a 500 km deep event (green star) recorded at receivers (green triangles) with epicentral distances 70º, 75º, 80º, and 85º.

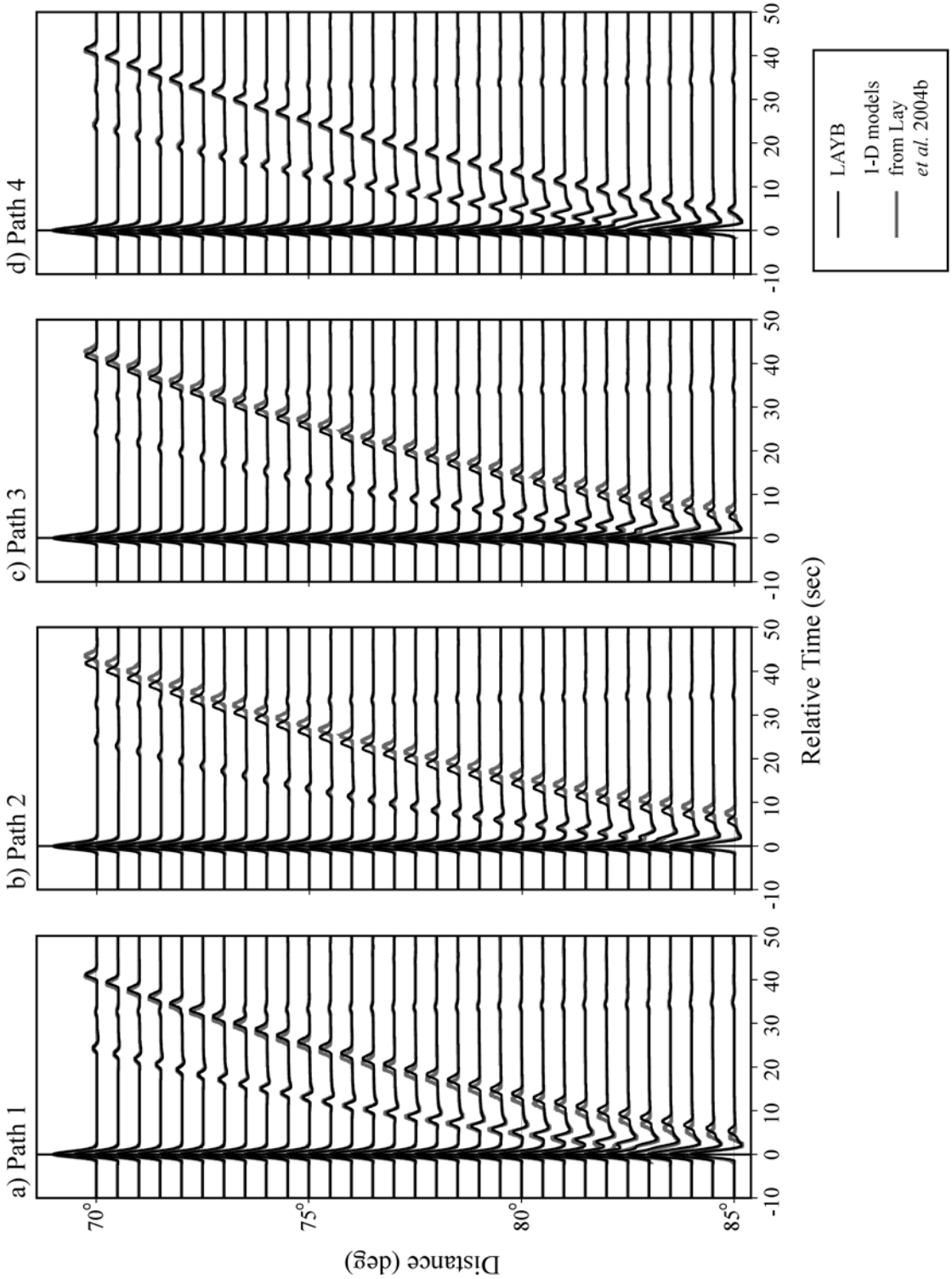
a) Path 1
b) Path 2
c) Path 3
d) Path 4
70°
75°
80°
85°
Distance (deg)
-10
0
10
20
30
40
50
Relative Time (sec)
LAYB
1-D models from Lay et al. 2004b

Supplement 5E Comparison of synthetics computed for the 1-D D" models of Lay *et al.* (2004b, drawn in gray) with synthetics created for model LAYB (drawn in black). Each panel displays synthetics for the labeled Path. Synthetics are aligned and normalized to unity on the phase *S*, and calculated for a dominant period of 4 sec.

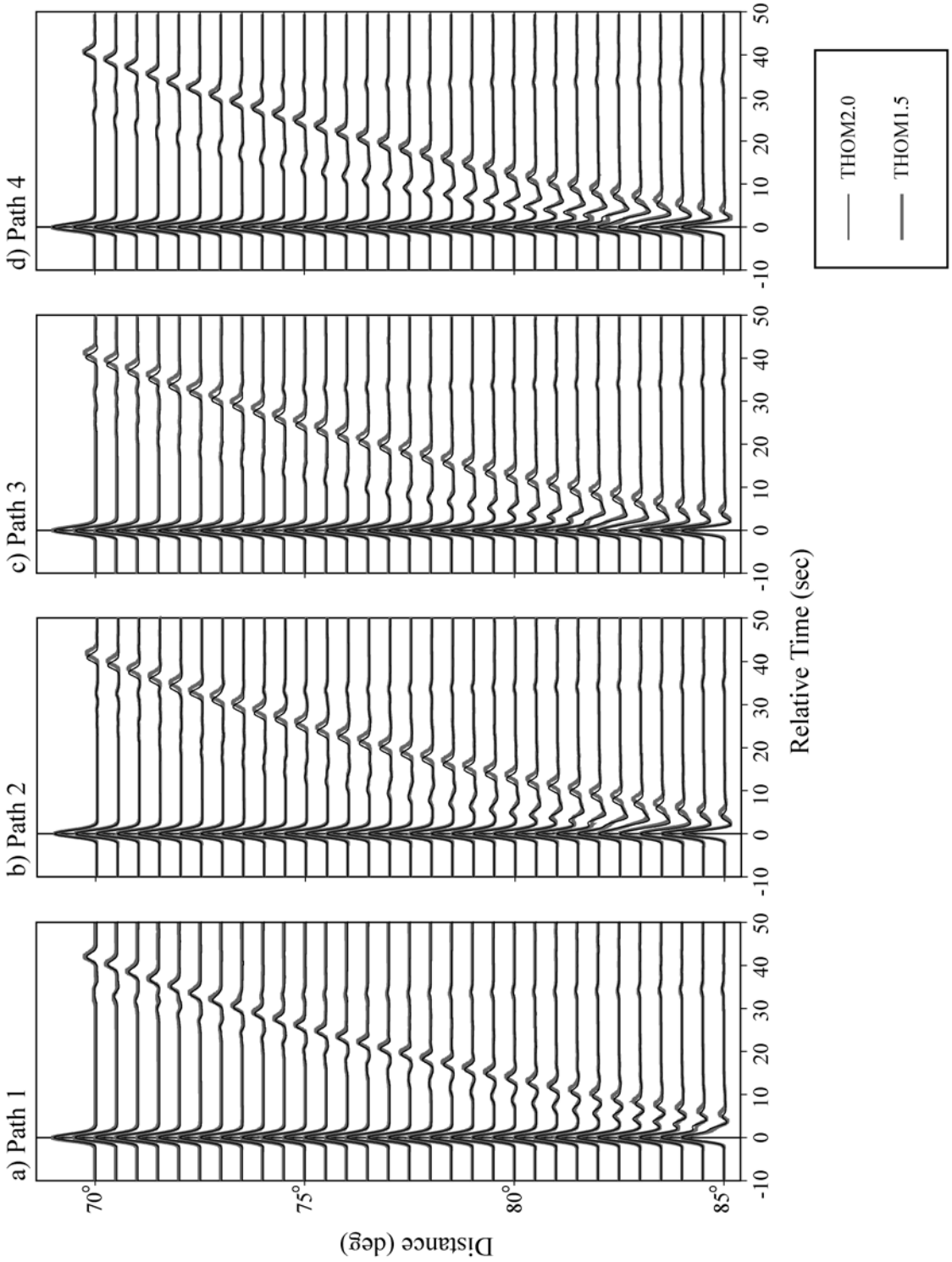
a) Path 1
b) Path 2
c) Path 3
d) Path 4
Distance (deg)
70°
75°
80°
85°
-10
0
10
20
30
40
50
Relative Time (sec)
THOM2.0
THOM1.5

Supplement 5F Comparison of synthetics computed for models THOM1.5 (drawn in gray) and THOM2.0 (drawn in black). Each panel displays synthetics for the labeled Path. Synthetics are aligned and normalized to unity on the phase *S*, and calculated for a dominant period of 5 sec.

APPENDIX A

COMPANION CD

A.1 SACLAB

SACLAB is the integration of the standard in solid earth seismic signal processing, Seismic Analysis Code (SAC), with the standard in technical computing, MATLAB®, making the computational and programming power of MATLAB® easily available for use with SAC data files. SACLAB allows one to read SAC data files into MATLAB® and perform some useful SAC operations in MATLAB®. SACLAB utilities complement the MATLAB® signal processing toolbox, which has become widely used in the industry. With SACLAB, programs and data files are portable to any platform that runs MATLAB® (e.g., Windows, Unix, Linux, etc.). SACLAB foster interdisciplinary collaboration since MATLAB® can be found in most departments. Also, the extensive documentation in MATLAB® provides a better understanding of the algorithms used, and makes it easy to alter a program for a different use.

The Companion CD contains the core SACLAB routines stored in *function m-file* format. These routines are located in the *saclab* directory of the CD. The routines available on this disc and their primary function are listed below in Table A.1.

Table A.1 Core SACLAB routines and function.

Utility Name	Function
MATLAB indexing utilities	
Contents.m	SACLAB contents*
Reading and writing utilities	
rsac.m	Read SAC binary
wsac.m	Write SAC binary
bsac.m	Be SAC – convert MATLAB array to SAC format.
Header evaluation utilities	
lh.m	List SAC header
ch.m	Change SAC header
Filtering Utilities	
bp.m	Band pass filter SAC file
hp.m	High pass filter SAC file
lp.m	Low pass filter SAC file
mavg.m	Moving average filter SAC file
Misc. Utilities	
add.m	Add constant value to SAC file
cut.m	Cut SAC file
deriv.m	Calculate derivatives of SAC file
envelope.m	Calculate envelope of SAC file
integrate.m	Integrate SAC file by trapezoidal rule
mul.m	Multiply SAC file by constant value
rmean.m	Remove mean of SAC file
rtrend.m	Remove trend of SAC file
taper.m	Taper SAC file
Plotting Utilities	
p1.m	Plot traces (one trace per subplot)
p2.m	Plot traces (overlay traces)
Function Generation	
boxfun.m	Create boxcar signal
kupper.m	Create kupper signal
refl.m	Create reflectivity-like signal
ricker.m	Create ricker signal
triangle.m	Create triangle/truncated triangle signal

*Uses MATLAB®'s ability to search for available utilities. e.g., if the SACLAB utilities are stored in the directory *saclab* typing 'help saclab' in the MATLAB® command window will retrieve a list of all available SACLAB utilities and their function in a fashion similar to this table.

A.2 Animations of seismic wave propagation

In Chapter's 4 and 5 we introduce the SHaxi method for computation of seismic wave propagation. One of the nicer features of finite difference simulations is the ability to produce snapshots of the wave propagation. These snapshots can be processed into animations of wave propagation. On the companion CD the directory *shaxi* contains animations of whole mantle *SH*-wave propagation. The animations contained are in the QuickTime format. To view animations in QuickTime format the QuickTime player is required (http://www.apple.com/quicktime/download/). Because of the large size of the files best playback performance is obtained by downloading the animations off the CD onto your hard drive before playing. The animations contained on the CD and the model parameters for each animation are listed below.

A.2.1 Homogeneous Velocity Models

1. homogeneous_earth_0km.mov

Model type:	Homogeneous velocity model
Vs:	2.0 km/sec
Density:	4.0 g/cm^3
Source depth:	0 km
Dominant period:	30 sec
Plot range:	$-60° \leq \theta \leq 60°$
Non-linear Scale:	0.5
Radial grid points:	2,000
Lateral grid points:	10,000

2. homogeneous_earth_0km_Vs5.mov

Model type:	Homogeneous velocity model
Vs:	5.0 km/sec
Density:	4.0 g/cm^3
Source depth:	0 km
Dominant period:	30 sec
Plot range:	$-90° \leq \theta \leq 90°$
Non-linear scale:	0.5
Radial grid points:	2,000
Lateral grid points:	10,000

3. homogeneous_earth_500km.mov

Model type:	Homogeneous velocity model
Vs:	2.0 km/sec
Density:	4.0 g/cm^3
Source depth:	500 km
Dominant period:	30 sec
Plot range:	$-60° \leq \theta \leq 60°$
Non-linear scale:	0.5
Radial grid points:	2,000
Lateral grid points:	10,000

4. homogeneous_earth_1400km.mov

Model type:	Homogeneous velocity model
Vs:	2.0 km/sec
Density:	4.0 g/cm^3
Source depth:	1400 km
Dominant period:	30 sec
Plot range:	$-60° \leq \theta \leq 60°$
Non-linear scale:	0.5
Radial grid points:	2,000
Lateral grid points:	10,000

5. LowV_Layer.mov

Model type:	Homogeneous velocity model with a low-velocity layer. Model has density 4.0 g/cm^3 throughout entire model. Velocity is 3.5 km/sec throughout model except in the low velocity layer. The low velocity layer is contained between the radii 5200 and 5800 km and has a velocity of 2.5 km/sec.
Source depth:	0 km
Dominant period:	30 sec
Plot range:	$-70° \leq \theta \leq 70°$
Non-linear scale:	0.5
Radial grid points:	2,000
Lateral grid points:	10,000

6. mega_low.mov

Model type:	Homogeneous velocity model with an extreme low-velocity layer. Model has density 4.0 g/cm^3 throughout entire model. Velocity is 3.5 km/sec throughout model except in the low velocity layer. The low velocity layer has a velocity of 0.5 km/sec.
Source depth:	0 km
Dominant period:	30 sec
Plot range:	$-60° \leq \theta \leq 60°$
Non-linear scale:	0.5
Radial grid points:	2,000
Lateral grid points:	10,000

7. HiV_layer.mov

Model type:	Homogeneous velocity model with a high velocity layer. Model has density 4.0 g/cm^3 throughout entire model. Velocity is 3.5 km/sec throughout model except in the high velocity layer. The high velocity layer is contained between the radii 5200 and 5800 km and has a velocity of 4.5 km/sec.
Source depth:	0 km
Dominant period:	30 sec
Plot range:	$-85° \leq \theta \leq 85°$
Non-linear scale:	0.5
Radial grid points:	2,000
Lateral grid points:	10,000

8. Low_Vbody_50km.mov

Model type:	Homogeneous velocity model with a low-velocity body. Model has Density 4.0 g/cm^3 throughout entire model. Velocity is 3.5 km/sec throughout model except in the low-velocity body which has a *S*-wave velocity reduction of 5% (Velocity = 3.325 km/sec). The low-velocity body has a radius of 50.0 km, and is centered at a depth of 1371 km, and at an epicentral distance of 30°. A 30 sec dominant period corresponds to a wavelength of 105 km in the homogeneous velocity model. Thus, the size of the low velocity body is on the order of 1-dominant wavelength.
Source depth:	0 km
Dominant period:	30 sec
Plot range:	$-10° \leq \theta \leq 75°$
Non-linear scale:	0.5
Radial grid points:	2,000
Lateral grid points:	10,000

9. Low_Vbody_150km.mov

Model type:	Homogeneous velocity model with a low-velocity body. Model has Density 4.0 g/cm^3 throughout entire model. Velocity is 3.5 km/sec throughout model except in the low-velocity body. The low-velocity body has a *S*-wave velocity reduction of 5% (Velocity = 3.325 km/sec) The low-velocity body has a radius of 150.0 km, and is centered at a depth of 1371 km, and at an epicentral distance of 30°. A 30 sec Dominant Period corresponds to a wavelength of 105 km in the homogeneous velocity model. Thus, the size of the low-velocity body is on the order of 3-dominant wavelengths.
Source depth:	0 km
Dominant period:	30 sec
Plot range:	$-10° \leq \theta \leq 75°$
Non-linear scale:	0.5
Radial grid points:	2,000
Lateral grid points:	10,000

A.2.2 PREM Models

1. prem_500km.mov

Model type:	PREM
Source depth:	500 km
Dominant period:	20 sec
Plot range:	$-180° \leq \theta \leq 180°$
Non-linear scale:	0.3
Radial grid points:	2,000
Lateral grid points:	10,000

2. prem_500km_12s.mov

Model type:	PREM
Source depth:	500 km
Dominant period:	12 sec
Plot range:	$-10° \leq \theta \leq 140°$
Non-linear scale:	0.3
Radial grid points:	Never recorded
Lateral grid points:	Never recorded

3. shinjuku.mov

Model type:	PREM
Source depth:	500 km
Dominant period:	15 sec
Plot range:	$-180° \leq \theta \leq 180°$
Non-linear scale:	Color scale modified beyond non-linear scaling.
Radial grid points:	Never recorded
Lateral grid points:	Never recorded

A.2.3 Other Reference Models

1. txbw_500km.mov

Model type:	TXBW (Steve Grand 2002 tomography model)
Source depth:	500 km
Source location:	Lat: -27.7°; Lon: 296.7°
Receiver location:	Lat: 34.0°; Lon: 243.1°
Dominant period:	6 sec
Plot range:	$-5° \leq \theta \leq 90°$
Non-linear scale:	0.3
Radial grid points:	3,000
Lateral grid points:	30,000
Reference:	Grand, S.P., 2002. Mantle shear-wave tomography and the fate of subducted slabs. *Philos. Trans. R. Soc. Lond. Ser. A-Math. Phys. Eng. Sci.*, **360** (1800), 2475-2491.

A.2.4 D" discontinuity models

1. thom2.mov

Model type:	PREM w/ D" discontinuity based on Thomas *et al.* (2004)
Source depth:	500 km
Dominant period:	10 sec
Plot range inset:	$-5° \leq \theta \leq 90°$
Plot range zoom:	$25° \leq \theta \leq 55°$; 3480 km $\leq r \leq$ 4500 km
Non-linear scale:	0.3
Radial grid points:	2,750
Lateral grid points:	20,000
Reference:	Thomas, C., Garnero, E.J., & Lay, T., 2004. High-resolution imaging of lowermost mantle structure under the Cocos plate, *Journal of Geophysical Research-Solid Earth*, **109** (B8).